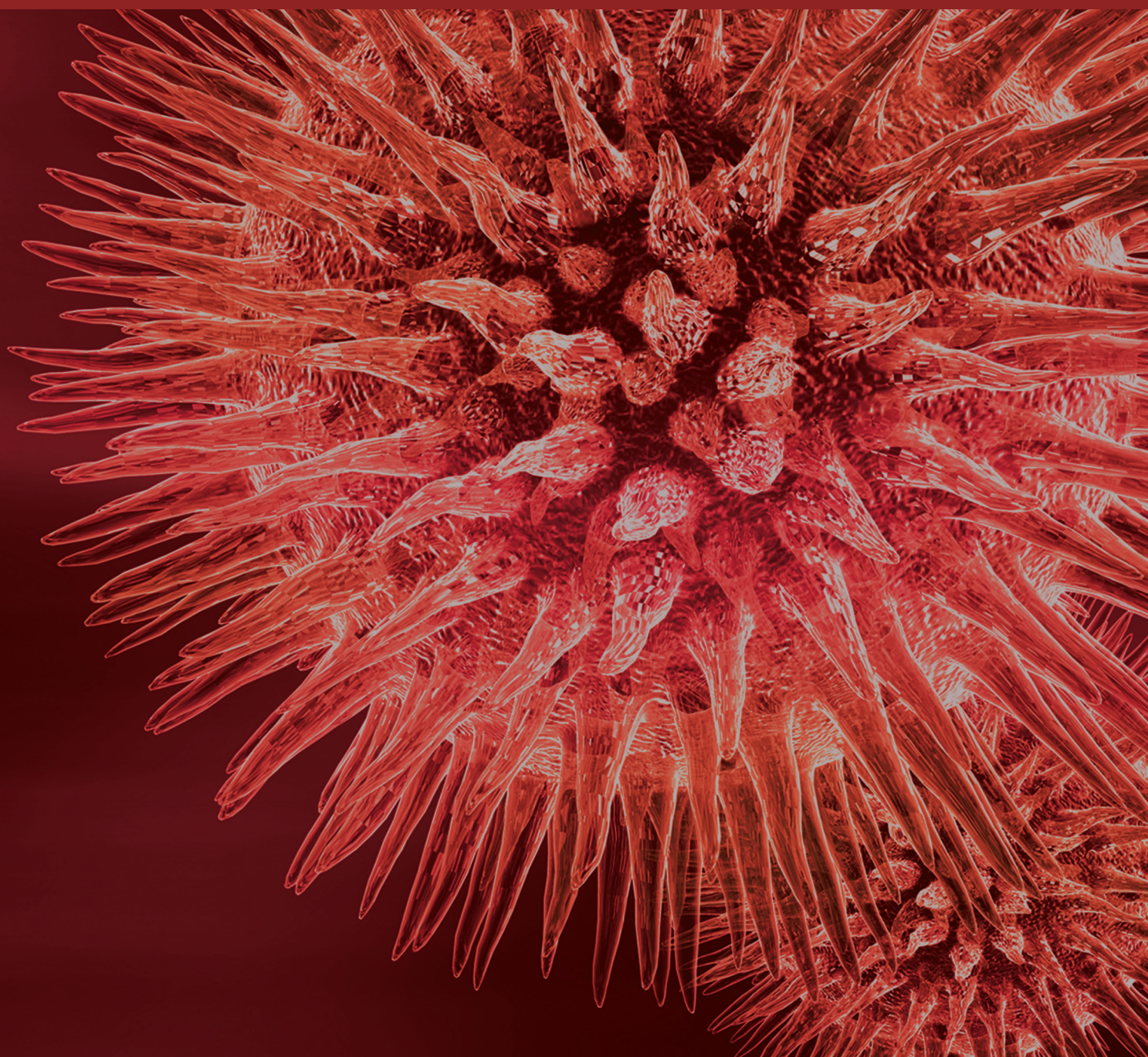


BioMed Research International

# Cell and Molecular Mechanics in Health and Disease

Guest Editors: Keiko Kawauchi, Hideaki Fujita, Daisuke Miyoshi, Evelyn K. F. Yim, and Hiroaki Hirata





---

# **Cell and Molecular Mechanics in Health and Disease**

BioMed Research International

---

## **Cell and Molecular Mechanics in Health and Disease**

Guest Editors: Keiko Kawauchi, Hideaki Fujita, Daisuke Miyoshi,  
Evelyn K. F. Yim, and Hiroaki Hirata



---

Copyright © 2017 Hindawi Publishing Corporation. All rights reserved.

This is a special issue published in “BioMed Research International.” All articles are open access articles distributed under the Creative Commons Attribution License, which permits unrestricted use, distribution, and reproduction in any medium, provided the original work is properly cited.

# Contents

## **Cell and Molecular Mechanics in Health and Disease**

Keiko Kawauchi, Hideaki Fujita, Daisuke Miyoshi, Evelyn K. F. Yim, and Hiroaki Hirata  
Volume 2017, Article ID 2860241, 2 pages

## **Directional Transport of a Bead Bound to Lamellipodial Surface Is Driven by Actin Polymerization**

Daisuke Nobezawa, Sho-ichi Ikeda, Eitaro Wada, Takashi Nagano, and Hidetake Miyata  
Volume 2017, Article ID 7804251, 14 pages

## **Hyperforin/HP- $\beta$ -Cyclodextrin Enhances Mechanosensitive $\text{Ca}^{2+}$ Signaling in HaCaT Keratinocytes and in Atopic Skin Ex Vivo Which Accelerates Wound Healing**

Hiroya Takada, Jun Yonekawa, Masami Matsumoto, Kishio Furuya, and Masahiro Sokabe  
Volume 2017, Article ID 8701801, 9 pages

## **Substrate Stiffness Influences Doxorubicin-Induced p53 Activation via ROCK2 Expression**

Takahiro Ebata, Yasumasa Mitsui, Wataru Sugimoto, Miho Maeda, Keigo Araki, Hiroaki Machiyama, Ichiro Harada, Yasuhiro Sawada, Hideaki Fujita, Hiroaki Hirata, and Keiko Kawauchi  
Volume 2017, Article ID 5158961, 10 pages

## **Dynamics of Actin Stress Fibers and Focal Adhesions during Slow Migration in Swiss 3T3 Fibroblasts: Intracellular Mechanism of Cell Turning**

Michiko Sugawara, Hiromi Miyoshi, Takuya Miura, Hiroto Tanaka, Ken-ichi Tsubota, and Hao Liu  
Volume 2016, Article ID 5749749, 16 pages

## **A Two-Dimensional Numerical Investigation of Transport of Malaria-Infected Red Blood Cells in Stenotic Microchannels**

Tong Wang, Yong Tao, Uwitije Rongin, and Zhongwen Xing  
Volume 2016, Article ID 1801403, 16 pages

## **The Hedgehog Signaling Networks in Lung Cancer: The Mechanisms and Roles in Tumor Progression and Implications for Cancer Therapy**

Yoshinori Abe and Nobuyuki Tanaka  
Volume 2016, Article ID 7969286, 11 pages

## **Voltage-Dependent Inactivation of MscS Occurs Independently of the Positively Charged Residues in the Transmembrane Domain**

Takeshi Nomura, Masahiro Sokabe, and Kenjiro Yoshimura  
Volume 2016, Article ID 2401657, 6 pages

## **Roles of pRB in the Regulation of Nucleosome and Chromatin Structures**

Chiharu Uchida  
Volume 2016, Article ID 5959721, 11 pages

## **Functions of the Tumor Suppressors p53 and Rb in Actin Cytoskeleton Remodeling**

Takahiro Ebata, Hiroaki Hirata, and Keiko Kawauchi  
Volume 2016, Article ID 9231057, 10 pages

## **Proliferation-Related Activity in Endothelial Cells Is Enhanced by Micropower Plasma**

Kotaro Suzuki and Daisuke Yoshino  
Volume 2016, Article ID 4651265, 11 pages



---

**The Circadian NAD<sup>+</sup> Metabolism: Impact on Chromatin Remodeling and Aging**

Yasukazu Nakahata and Yasumasa Bessho

Volume 2016, Article ID 3208429, 7 pages

## Editorial

# Cell and Molecular Mechanics in Health and Disease

**Keiko Kawauchi,<sup>1</sup> Hideaki Fujita,<sup>2</sup> Daisuke Miyoshi,<sup>1</sup>  
Evelyn K. F. Yim,<sup>3</sup> and Hiroaki Hirata<sup>4</sup>**

<sup>1</sup>*Frontiers of Innovative Research in Science and Technology, Konan University, 7-1-20 Minatojima-Minamimachi, Chuo-ku, Kobe, Hyogo 650-0047, Japan*

<sup>2</sup>*Laboratory for Comprehensive Bioimaging, Riken Qbic, 6-2-3 Furuedai, Suita, Osaka 565-0874, Japan*

<sup>3</sup>*Department of Chemical Engineering, University of Waterloo, 200 University Avenue West, Waterloo, ON, Canada N2L 3G1*

<sup>4</sup>*Nagoya University Graduate School of Medicine, 65 Tsurumai, Showa-ku, Nagoya, Aichi 466-8550, Japan*

Correspondence should be addressed to Keiko Kawauchi; [kawauchi@center.konan-u.ac.jp](mailto:kawauchi@center.konan-u.ac.jp)

Received 15 January 2017; Accepted 16 January 2017; Published 13 February 2017

Copyright © 2017 Keiko Kawauchi et al. This is an open access article distributed under the Creative Commons Attribution License, which permits unrestricted use, distribution, and reproduction in any medium, provided the original work is properly cited.

A growing body of research has revealed that not only chemical stimuli, but also the mechanical stimuli in the microenvironment surrounding cells have a significant impact on cell behaviors. Mechanical stimuli from the environment are detected by various mechanosensing biomolecules including mechanosensitive ion channels and nonion channel type mechanosensors, leading to modulation of intracellular signaling. Notably, while subcellular structures—including cytoskeletons, membranous organelles, and the nucleus— influence and determine mechanical properties of cells, the mechanical properties of both cells and their microenvironment are altered in cancer or other diseases such as infections, chronic inflammation, and degenerative diseases. The abnormal expression and activation of mechanosensing biomolecules and/or components of the subcellular structures, which are sometimes accompanied by gene mutations, have been observed in many disease states. Such alterations potentially tune the chemical and physical interactions between cells and their environments and thereby contribute to disease progression. Therefore, the mechanical properties of individual subcellular structures (e.g., the actin cytoskeleton, cell adhesion complexes, and chromosomes) and the signaling molecules regulating these structures are emerging as targets in the research seeking mechanistic understanding of disease development or potential therapies for the diseases.

The original and review papers in this special issue provide novel insights into the mechanical cue-dependent regulation of cellular functions in various types of cells including bacterial cells, erythrocytes, fibroblasts, endothelial cells, and cancer cells. The topics range from the mechanosensing

element at the plasma membrane to mechanical-induced intracellular signaling and structural remodeling and the mechanical modulation of the cancer therapy.

T. Nomura et al. addressed an inactivation mechanism of the mechanosensing biomolecule, MscS ion channel and revealed the contributions of positively charged residues in the channel molecule to the membrane potential-dependent inactivation of MscS.

Using numerical simulations, T. Wang et al. systematically examined how malaria infection-induced changes in mechanical properties of the erythrocyte membrane affect the blood flow in microvessels with stenosis. They showed that both deformability and adhesiveness of the erythrocyte membrane are critical factors characterizing the blood flow, which may provide the mechanical basis for microcirculatory obstruction in severe malaria.

D. Nobezawa et al. showed that, in contrast to the classical view, actin polymerization, rather than myosin II activity, plays a dominant role in driving the retrograde movement of the actin cytoskeleton at the protruding edge of a migrating cell.

Using detailed live-cell imaging, M. Sugawara et al. examined the mechanism that regulates the directional change in cell migration. They showed that, during the directional change, a migrating cell exhibits spatial coordination of three distinct dynamics of focal adhesion and the actin cytoskeleton, which potentially contributes to the change of cell polarity.

H. Takada et al. reported that while mechanical stretch of wounded skin accelerates the wound repair, this effect

of mechanical stretch is enhanced by treating the skin with hyperforin, a major component of a traditional herbal medicine.

Several other outstanding papers showed and discussed that the physical properties of mechanical environments or mechanical stimuli alter the cell characters via intracellular signaling pathways including NF- $\kappa$ B and p53 signaling pathways.

K. Suzuki and D. Yoshino reported that the treatment of endothelial cells with micropower plasma at gas-liquid interface promotes their proliferation. Furthermore, the plasma-induced NF- $\kappa$ B activation is shown to be involved as underlying intracellular signaling.

The group of K. Kawauchi, who is one of the Editorial team members, showed that stiffness of the extracellular matrix (ECM) modulates the effect of chemotherapy on cancer cell growth. Soft ECM attenuates chemotherapeutic agent-induced activation of the tumor suppressor p53 in breast cancer cells, leading to cell growth resistance against chemotherapy.

In addition to original research papers, four interesting review papers discuss the relationship of mechanosensing and various diseases. K. Kawauchi's group reviewed the roles of the tumor suppressors p53 and retinoblastoma protein (pRb), whose signaling pathways are disrupted in many types of cancers, in the regulation of mechanosensing biomolecules and the actin cytoskeleton.

C. Uchida focused on the role of pRb in the regulation of chromatin structures. The paper reviewed how physical interactions of pRb with histone modifiers and chromatin factors control nucleosome/chromatin structures and discussed a potent strategy of cancer therapies that target these protein factors.

Y. Nakahata and Y. Bessho described an overview of the role of NAD<sup>+</sup> metabolism in circadian changes of mechanical properties of chromosome/chromatin. Furthermore, they discussed the possibility that aging-associated diseases may be treated by interfering with NAD<sup>+</sup> metabolism.

Y. Abe and N. Tanaka reviewed how the abnormal activation of the hedgehog signaling pathway, which plays a critical role in development and tissue homeostasis, leads to progression of lung cancer. In particular, they pointed out that physical interaction of non-small cell lung cancer (NSCLC) cells with cancer-associated fibroblasts enhances metastatic potential of NSCLC cells by activating the hedgehog signaling pathway.

The papers in this special issue illustrate that modulations of mechanosignaling pathways may provide novel approaches for development of new therapeutic methods which are distinctive from the conventional chemical therapies. The new discoveries will potentially lead to further in-depth studies on mechanochemical transduction mechanisms at molecular and supramolecular levels in the future.

*Keiko Kawauchi  
Hideaki Fujita  
Daisuke Miyoshi  
Evelyn K. F. Yim  
Hiroaki Hirata*

## Research Article

# Directional Transport of a Bead Bound to Lamellipodial Surface Is Driven by Actin Polymerization

**Daisuke Nobezawa, Sho-ichi Ikeda, Eitaro Wada, Takashi Nagano, and Hidetake Miyata**

*Department of Physics, Tohoku University, Aramaki, Aoba-ku, Sendai, Miyagi 980-8578, Japan*

Correspondence should be addressed to Hidetake Miyata; [miyata@bio.phys.tohoku.ac.jp](mailto:miyata@bio.phys.tohoku.ac.jp)

Received 27 August 2016; Revised 31 October 2016; Accepted 30 November 2016; Published 26 January 2017

Academic Editor: Keiko Kawauchi

Copyright © 2017 Daisuke Nobezawa et al. This is an open access article distributed under the Creative Commons Attribution License, which permits unrestricted use, distribution, and reproduction in any medium, provided the original work is properly cited.

The force driving the retrograde flow of actin cytoskeleton is important in the cellular activities involving cell movement (e.g., growth cone motility in axon guidance, wound healing, or cancer metastasis). However, relative importance of the forces generated by actin polymerization and myosin II in this process remains elusive. We have investigated the retrograde movement of the poly-D-lysine-coated bead attached with the optical trap to the edge of lamellipodium of Swiss 3T3 fibroblasts. The velocity of the attached bead drastically decreased by submicromolar concentration of cytochalasin D, latrunculin A, or jasplakinolide, indicating the involvement of actin turnover. On the other hand, the velocity decreased only slightly in the presence of 50  $\mu\text{M}$  (–)-blebbistatin and Y-27632. Comparative fluorescence microscopy of the distribution of actin filaments and that of myosin II revealed that the inhibition of actin turnover by cytochalasin D, latrunculin A, or jasplakinolide greatly diminished the actin filament network. On the other hand, inhibition of myosin II activity by (–)-blebbistatin or Y-27632 little affected the actin network but diminished stress fibers. Based on these results, we conclude that the actin polymerization/depolymerization plays the major role in the retrograde movement, while the myosin II activity is involved in the maintenance of the dynamic turnover of actin in lamellipodium.

## 1. Introduction

When the cell crawls on surfaces, it first protrudes the leading edge, and the protruded edge adheres to the surface. This is followed by a contraction of the cell body and subsequent dissociation of its rear [1]. The repetition of these steps makes the cell advance. The leading edge is a thin, veil-like membranous structure called lamellipodium that is filled with a dense, crisscrossed network of actin filaments (actin cytoskeleton). Between the lamellipodium and the nucleus is a region called lamellum. This region contains actin filaments and bipolar myosin mini-filaments; lamellipodium and lamellum are mechanically connected to each other by actin filaments [2, 3].

In lamellipodium, actin moves at a constant velocity toward the nucleus [4, 5]. This movement, called retrograde (actin) flow, continues to the end of lamellipodium, slowing down in lamellum. When a small object is bound to the surface near the edge of the cell, it is transported on the surface toward the nucleus [6]. The velocities of the retrograde

movements of actin in the cell and the small object attached to the surface of the cell have been found to be the same [7–9]. Hence, it has been postulated that the object is coupled to the actin network through its interaction with transmembrane proteins. An example is the transport of a bead coated with glutamate receptor (mGluR5): the bead is initially executing a Brownian motion, but once engaged to the underlying cytoskeleton, it is transported toward nucleus [10]. Another example is a fibronectin receptor, integrin. Thus, when integrin beta-1 is bound by gold particles coated by fibronectin, it binds to the cytoskeleton and is transported rearward. The retrograde flow will exert a tensile force on the linkage between integrin and actin cytoskeleton strengthening the linkage [11]. This positive feedback must be important in the crawling of the cell.

The origin of the force driving the retrograde movement has been attributed to the polymerization of actin and/or the motor function of nonmuscle myosin II. In lamellipodium, the fast-growing (barbed) end of an actin filament is facing

toward the front edge of lamellipodium [12–14]. Actin filaments growing toward the leading edge eventually hit and push the leading edge. Then, the filaments will receive a reaction force from the leading edge. If the actin cytoskeleton is firmly linked to the adhesion substrate through integrin, the lamellipodial membrane will protrude; if the link is disconnected or slips, the reaction force will push back the actin network, resulting in the retrograde flow. In neuronal growth cone the link (clutch) involves the immunoglobulin superfamily cell adhesion molecule [15] or the L1 cell adhesion molecule [16]. The latter molecule indirectly interacts with the actin cytoskeleton through a molecule, ankyrin<sub>b</sub>. The regulation of the linkage between the cytoskeleton and the adhesion substrate by the clutch mechanism is thought to be important in growth cone steering [17] or initiation of neurogenesis [16].

In lamellum, myosin II forms bipolar filaments and those filaments together with actin filaments generate a contractile force in lamellum [18]. This force is transmitted to lamellipodium, because lamellum is mechanically coupled to lamellipodium by actin filaments, and the force will pull the actin filament network in the lamellipodium, causing the retrograde flow. The myosin-dependent retrograde flow has been experimentally shown [19]. When the actin filament network is linked to the adhesion substrate, the contraction of lamellum will pull the cell body thereby contributing to the forward translocation of the cell body. As described below, the actin-based or myosin II-based mechanisms seem to operate in the retrograde flow in cell-dependent fashion.

A study using a highly motile fish epidermal keratocyte has demonstrated that the cell speed is regulated by the linkage of cell adhesion molecules to the adhesion substrate as well as that of actin cytoskeleton to the clutch [20]. Thus, a firm linkage of the adhesion molecule to the adhesion substrate plus full engagement of the clutch will result in the fast protrusion and the fast movement of the cell. In the slow moving cell the receptor-adhesion linkage is weak and slips, resulting in the backward transport of the actin cytoskeleton. This will reduce the velocity of the protrusion of the leading edge, resulting in the slower advancing motion. In keratocyte, the sum of the rate of the protrusion and that of the retrograde flow is almost the same between the fast-moving and slow moving keratocytes, suggesting the regulation of the coupling between the polymerization rate and retrograde flow rate by the engagement of the clutch and the strength of cell adhesion. In a subtype of sea urchin coelomocyte, independent contribution of the actin polymerization and myosin II activity to the retrograde flow has been demonstrated [21]. When this cell was treated with an inhibitor of myosin II light chain kinase to reduce the activity of myosin II, the retrograde movement was halted in the cell interior but continued near the cell peripheral region. Inhibition of actin polymerization with cytochalasin D (CytD) partially slowed down the retrograde flow of actin cytoskeleton with the appearance of a cell fringe devoid of actin filaments. Based on these observations, the authors concluded that the two mechanisms, the pushing by actin polymerization at the front and the pulling by myosin-driven contraction of more central part of the cell, independently contribute to the retrograde flow.

In the present study, we measured the velocity of the polystyrene bead, which had been coated with poly-D-lysine and attached to the tip of lamellipodium of Swiss 3T3 fibroblast. Swiss 3T3 fibroblast has been used for several decades in the study of cell motility; its motility is between that of keratocyte and coelomocyte. With this system, we evaluated the relative contribution of the actin-dependent and myosin II-dependent mechanisms in the retrograde flow by using inhibitors specific to actin turnover and myosin II activity.

## 2. Materials and Methods

**2.1. Chemicals.** Dulbecco's modified Eagle medium (DMEM) was obtained from Nissui Pharmaceutical Co., Ltd. (Tokyo, Japan). DMEM without glucose, fetal bovine serum (FBS), penicillin-streptomycin, and L-glutamine were obtained from Thermo Fisher Scientific (Yokohama, Japan). Carboxylated polystyrene beads (1  $\mu$ m) were obtained from Polysciences, Inc. (Warrington, PA, USA). Poly-D-lysine, mouse monoclonal anti-myosin light chain antibody, formaldehyde, poly(oxyethylene) octylphenyl ether (Triton X-100), and jasplakinolide (Jasp) were obtained from Sigma-Aldrich Japan (Shinagawa, Tokyo, Japan). Plasmid of the red fluorescence protein (pDsRed monomer) fused to actin (hereafter called RFP-actin) was obtained from Clontech (Kusatsu, Shiga, Japan). The transfection reagent (Lipofectamine<sup>®</sup> 2000), rhodamine-conjugated phalloidin, and Alexa 488-labeled anti-mouse IgG were obtained from Invitrogen (Yokohama, Kanagawa, Japan). The (–)-blebbistatin, Y-27632, CytD, latrunculin A (LatA), and concanavalin A were obtained from Wako Chemical Co. (Osaka, Japan). A 2-[4-(2-hydroxyethyl)piperazin-1-yl]ethanesulfonic acid (HEPES) and biotin N-hydroxysulfosuccinimide ester (biotin-Sulfo-OSu) were obtained from Dojindo Laboratories (Kumamoto, Japan). Fibronectin fragment III (7–10) was obtained from Ito Life Science (Moriya City, Ibaraki, Japan). A 1  $\mu$ m, microsphere labeled with neutravidin (avidin-beads) was obtained from Molecular Probes (Eugene, OR, USA).

**2.2. Cell and Cell Culture.** Swiss3T3 fibroblast was obtained from JCRB Cell Bank (Ibaraki, Osaka, Japan). Cells were cultured in DMEM supplemented with 5% FBS, 1% penicillin-streptomycin, and 2 mM L-glutamine. Cells were placed in a CO<sub>2</sub> incubator (NAPCO model 5410, Precision Scientific, Chicago, IL, USA) at 37°C, 5% CO<sub>2</sub>, and 90% humidity. Prior to the experiment, cells were subcultured overnight in the fresh cell culture medium; cells were plated in a custom-made chamber (Hirata chamber; see below) and the chamber was placed in the incubator.

Figure 1(a) summarizes the process of the construction of Hirata chamber. A no. 1 coverslip (24 mm  $\times$  60 mm) was coated with 3-aminopropyltriethoxysilane (2% in ethanol; Shin-Etsu Chemical Co., Ltd., Tokyo) at room temperature for 30 min. The silane-coating was activated by heating at 180°C for 30 min, and a fluorocarbon-based amorphous polymer (Cytop<sup>®</sup> CTX-809A, Asahi Technoglass, Shizuoka, Japan) was placed ring-wise at the center of the coverslip. After Cytop was dried at room temperature overnight, the coverslip was placed in an oven and was heated first at 50°C

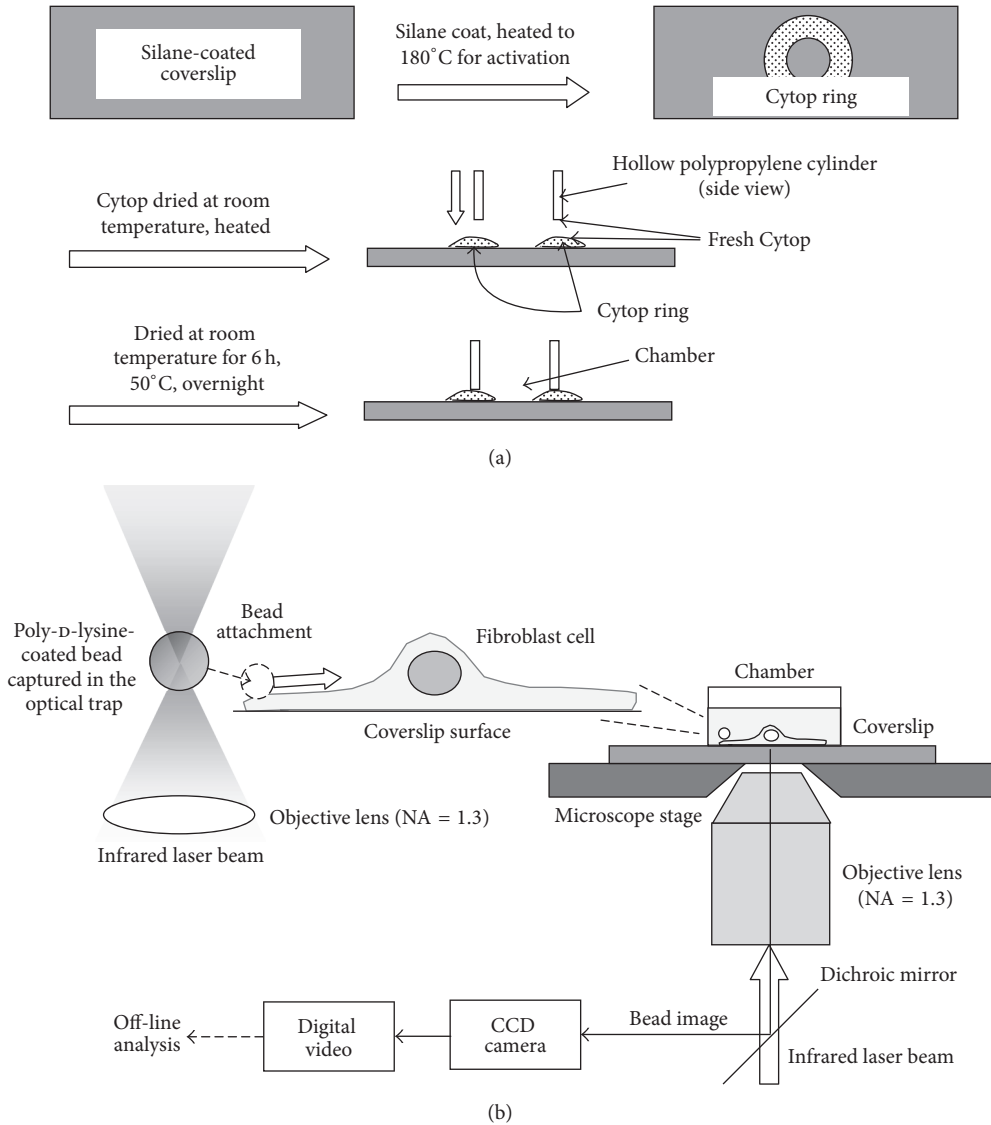


FIGURE 1: (a) Process of the construction of the Hirata chamber. The process after the coating of the coverslip with aminopropyltriethoxysilane is shown. See Section 2.2 for details. (b) The experimental set-up. An optical trap was generated in Zeiss inverted phase-contrast microscope by focusing an infrared laser beam (thick vertical arrow) with an objective lens (NA = 1.3). A poly-D-lysine-coated bead was captured in the trap and was attached to the edge of lamellipodium (the dashed arrow). As soon as the stable contact between the bead and the lamellipodium was achieved, the laser was turned off and the bead was allowed to move on the cell surface (bold horizontal arrow). The phase-contrast image of the bead was acquired with a CCD camera and was recorded on a digital video tape at 30 frames/sec. Video sequences were transferred to a hard disk for the off-line analysis (see Section 2.5). The figure is not drawn to scale.

for 1.5 h and then at 180°C for 1 h. The mouth portion of a 15 mL polypropylene centrifuge tube (~10 mm height) was cut out, the bottom rim of which was applied with fresh Cytop; fresh Cytop was also applied to the top of the Cytop ring, and the tube was placed on the ring. Final drying process was carried out at room temperature for 6 h followed by an overnight incubation at 50°C.

**2.3. Bead Coating.** Polystyrene beads were coated with poly-D-lysine in 1 mg/mL poly-D-lysine aqueous solution at 4°C overnight. The coated beads were washed once in Milli-Q water to remove excess poly-D-lysine and were suspended

in cell culture medium without FBS or phenol red but were supplemented with 10 mM HEPES (pH 7.2). Concanavalin A (50 µg/mL~1000 µg/mL) was covalently coupled to the polystyrene beads with 1-ethyl-3-(3-dimethylaminopropyl) carbodiimide. Amino groups of fibronectin III (7-10) were labeled with biotin-Sulfo-OSu and the modified fibronectin was bound to the avidin-bead through the biotin-avidin linkage.

**2.4. Imaging of the Bead and the Cell.** To measure the retrograde movement of the cell-bound bead, an inverted phase-contrast microscope (ICM401, Carl Zeiss, Tokyo, Japan),

which was equipped with a 100x, NA = 1.3 objective lens, was used (Figure 1(b)). The optical trapping system implemented in this microscope [22] was utilized to attach the bead to the edge of lamellipodium, because it has been shown that the retrograde movement at the back of lamellipodium slowed down [23]. Phase-contrast image of the bead was acquired with a charge-coupled device (CCD) camera (C2400-7, Hamamatsu, Hamamatsu, Japan) and was recorded on a digital video tape. The recorded images were transferred to a hard disk for off-line analysis.

To visualize fluorescently stained cells, an inverted epifluorescence microscope (IX71, Olympus, Tokyo) equipped with a 100x, NA = 1.3 objective lens and a cooled CCD camera (C4742-96-12ERG, Hamamatsu, Hamamatsu, Japan) was used. The same camera was also used to acquire the phase-contrast images of the fluorescently stained cells (see below). The images were directly recorded on a hard disk for later analysis.

**2.5. Measurement of the Retrograde Movement of the Bead and Analysis of the Bead-Trajectory with Mean-Square-Displacement Plot.** In each experiment, the suspension of the poly-D-lysine-coated bead was added to the cell culture medium (1/1000~1/500 volume of the culture medium) in the Hirata chamber. The chamber was then transferred onto the stage of the microscope. To measure the retrograde movement, a bead was captured with the optical trap and the microscope stage was maneuvered to achieve the contact of the bead with the cell edge (within  $\sim 1 \mu\text{m}$  from the edge of lamellipodium; Figure 1(b)). The use of the optical trap has an advantage, because one could choose the closest location to the lamellipodial edge as the attachment site. Usually within a few sec (at most 10 sec), the bead was firmly bound to the lamellipodium, and the laser was turned off to allow the bead to move on the surface of the lamellipodium. The whole sequence (bead capture, attachment, and transport) was recorded, as described above, and the trajectory of the bead was analyzed (see below).

We attempted to attach beads coated with concanavalin A or fibronectin III but could not achieve the firm binding; in both cases beads seemed to be only tethered to the cell and the turning off of the laser of the optical trap resulted in the movement of the bead away from the cell surface. Therefore, we used the poly-D-lysine beads.

Video image of the bead was used to determine the position of the bead every 33 ms with a program ("optical tweezers" written by Shoichi Ikeda) running on ImageJ (ver. 1.46) and was represented with  $(x(t_j), y(t_j))$ , where  $t_j = (j - 1) \tau$  and  $j$  varies from 1 (unity) to  $N$  (total number of the analyzed video frames) and  $\tau = 33$  ms, the minimum time interval, as described [22]. The  $N$  varied from 600 to 1400 depending on the experiment. The bead movements were not analyzed, if shrinkage of the lamellipodium or ruffling occurred during the observation ( $\sim 25\%$  of total experiments).

To analyze the bead motion, the mean-square-displacement (MSD) value was calculated from the bead position as follows:

$$\text{MSD}(k\tau) = \left[ \frac{1}{N-k} \cdot \sum_{j=k+1}^N \left[ \{x((j-1)\cdot\tau) - x((j-k-1)\cdot\tau)\}^2 + \{y((j-1)\cdot\tau) - y((j-k-1)\cdot\tau)\}^2 \right] \right] \quad (1)$$

Here,  $\tau = 33$  ms and  $N$  and  $k$  represents integer  $\geq 1$ . We assumed that the bead movement is a superposition of the two-dimensional lateral diffusion and a one-dimensional drift with  $D$  as the diffusion constant and  $V$  the time-independent velocity. On this assumption, MSD value is represented with the following equation:

$$\text{MSD} = 4D\Delta t + V^2(\Delta t)^2, \quad (2)$$

where  $\Delta t \equiv k\tau$  is the duration [24]. Thus, the bead movement is parametrized with two quantities,  $D$  and  $V$ .

Fluorescence speckle microscopy has been developed and applied to measure the turnover dynamics of actin filaments as well as the retrograde flow [25, 26]. With this technique hundreds of actin speckles can be analyzed with a spatiotemporal resolution of 270 nm and  $\sim 1$  s, from which spatial variation of the rate of retrograde flow and that of actin turnover are derived. The bead analysis cannot provide the information of many moving objects, but the spatiotemporal resolution of the bead analysis is 10 nm and 33 ms, respectively, and is higher than that of the speckle microscopy. This feature is utilized to analyze the movement of the bead within  $\Delta t < 0.1$  s (Figure 3(d)).

**2.6. Transient Expression of RFP-Actin Fusion Protein.** To transiently express the RFP-actin in the cell, the plasmid was introduced into the cell with the transfection reagent, Lipofectamine 2000, according to the manufacturer's instruction.

**2.7. Kymograph Analysis.** Kymograph is also used to analyze the movements of cellular objects including the surface-bound bead, fluorescently-labeled actin filaments, or lamellipodia [22, 27]. We analyzed the dynamics of RFP-actin with this method: in lamellipodia containing RFP-actin, retrograde movements of the fluorescent spots were observed. From the video sequence the direction of the movement of the spots was identified and the kymograph was made along a straight line parallel to this direction. The unidirectional steady movement provided a straight line in the kymograph. With the calibration of the temporal and spatial axis, the slope of the straight line provided the velocity of the analyzed object. In an independent experiment, we also measured the velocity of the  $1 \mu\text{m}$  poly-D-lysine-coated bead attached to the cell expressing RFP-actin by the kymograph technique.

**2.8. Inhibition of Actin Turnover and Myosin II Activity.** To inhibit actin turnover, we used CytD, LatA, and Jasp. CytD

binds to the fast-growing end of actin filament and inhibits the elongation of the filament [28]; LatA binds to actin monomer and sequesters it, thereby decreasing the rate of association of the monomer to the filament end [29]; Jasp inhibits the depolymerization of actin filaments [30]. For inhibition of myosin II, (-)-blebbistatin and Y-27632 were used. The mechanisms of the action of two inhibitors are different [31, 32]: the former inhibits the release of phosphate from the active site and the latter inhibits Rho-dependent kinase (ROCK), but both inhibit the actomyosin ATPase activity.

Quantification of the effect of inhibitors on  $V_{\text{fit}}$  was done as follows. After the addition of the inhibitor, cells were incubated for 30 min in the CO<sub>2</sub> incubator. They were then subjected to the measurements and the analysis, as described in Section 2.5. The measurements of  $V_{\text{fit}}$  values of the untreated cells were carried out on the same day as the measurement with inhibitors, and the velocities obtained with inhibitors were always normalized to the average of the  $V_{\text{fit}}$  value of the untreated cells, because of the considerable variation of the  $V_{\text{fit}}$  values (see Section 3.1).

### 2.9. Cell Fixation and Fluorescent Staining of Actin Filaments.

Fixation of the cell and fluorescent staining of actin filaments had been carried out according to the previously described method [25, 33, 34]: cells were fixed with 4% formaldehyde and then permeabilized with 0.1% Triton X-100. Actin filaments were visualized with 0.1  $\mu$ M rhodamine-phalloidin. Myosin II in the same cell was visualized by indirect immunofluorescence technique: mouse monoclonal antibody against myosin II light chain and Alexa488-labeled anti-mouse IgG were sequentially applied to the cell after fixation and permeabilization.

Profiles of the intensity of the fluorescence from actin filaments and that from myosin II were analyzed using ImageJ plugin “plot profile”. The numerical data were transferred to Microsoft Excel 2007 and were manipulated as follows. The intensity values of the fluorescence intensity obtained under each experimental condition were normalized to the maximum value in each profile. To determine the position where the profile exhibits a rapid rise, the derivative of the intensity profile was numerically determined and the position corresponding to the maximum value was assigned as the position of the rapid rise (see Section 3.3).

## 3. Results

**3.1. Characterization of the Retrograde Movement of the Bead Attached to Lamellipodia.** An example of the  $xy$  trace of the bead obtained over 33 s is shown in Figure 2(a). Figure 2(b) shows the  $xy$  trace of the bead bound to the glass surface, which was determined over 50 sec: this movement was due to the mechanical drift of the stage and the total distance traveled in this particular example was  $\sim 1/6$  of that of the trajectory shown in Figure 2(a); the range of the movement of the fixed beads was always much smaller than the cell-bound beads (see below). Figure 2(c) shows an example of the MSD plot. The curve-fitting provided  $D$  and  $V$  values as fitting parameters (represented with  $D_{\text{fit}}$  and  $V_{\text{fit}}$ ). In the example

shown in Figure 2(c),  $D_{\text{fit}} = 272.3 \text{ nm}^2/\text{s}$  and  $V_{\text{fit}} = 52.7 \text{ nm/s}$ , respectively.

Figure 3(a) shows that the  $V_{\text{fit}}$  values measured on different days varied considerably. Figure 3(b) shows the histogram of  $V_{\text{fit}}$  values obtained from the same set of the data as shown in Figure 3(a). A minor population of the data distributed  $>100 \text{ nm/s}$ , but the major population distributed around 30–70 nm/s with the average value of  $46.6 \pm 23.3 \text{ nm/s}$  (average  $\pm$  standard deviation, 160 samples). The  $V_{\text{fit}}$  values were within the range of the velocities of the surface-bound beads, fluorescently-labeled actin, or intracellular vesicular bodies [7, 10, 23]. The average  $V_{\text{fit}}$  value of the beads fixed to the bottom of the chamber was  $2.7 \pm 1.8 \text{ nm/s}$  (14 samples obtained in 5 independent experiments), which was much smaller than that of the control cells.

As shown in Figure 3(c), the distribution of the  $D_{\text{fit}}$  values skewed toward small values, implying that the diffusive movements very rarely occurred. Majority of the  $D_{\text{fit}}$  values were smaller than  $10^3 \text{ nm}^2/\text{s}$  and were almost two orders of magnitude smaller than the lateral diffusion coefficient of integrin  $\alpha 5\beta 1$  ( $5.3 \pm 4.4 \times 10^4 \text{ nm}^2/\text{s}$  [34]). Previous studies have reported values of two-dimensional diffusion coefficient of a similar order of magnitude [10, 35]. Thus in the present case, the two-dimensional movement of the bead seemed to be restricted.

Figure 3(d) shows the plots of  $\log_{10}(\text{MSD})$  versus  $\log_{10}(\Delta t)$  for two samples (samples 1 and 2). The slopes of these plots for large  $\Delta t$  ( $>1 \text{ s}$ , or  $\text{Log}_{10}\Delta t > 3$ ) were  $\sim 2$ , which is expected for the movement at a constant velocity, but the slope of the plot for small  $\Delta t$  ( $<0.1 \text{ s}$ ;  $\text{Log}_{10}\Delta t < 2$ ) was  $\sim 1$  for sample 1 and  $\sim 0$  for sample 2. Thus, in the latter sample, the bead seemed to execute subdiffusion, not Brownian movement. The subdiffusion is described with a relation between MSD and  $\Delta t$ ;  $\text{MSD} = A\Delta t^b$ , where  $A$  and  $b$  (between 0 and 1) are time-independent constants [36]. We speculate that the small  $D_{\text{fit}}$  values reflect the subdiffusional movements, which was not apparent from the MSD plot. At present, it is not possible to obtain more details of the movement for  $\Delta t < 0.1 \text{ s}$ , because 33 ms is the highest temporal resolution we can achieve. Hence, the reason for the variation is a theme of the future study.

We next compared the velocity of the bead, which was attached to the cell expressing RFP-actin, with the velocity of the RFP-actin in lamellipodium. Two measurements were carried out in different cells, because in our hand it was not possible to bring two objects simultaneously into the focus. Similar comparison has been made in several previous studies [7–9]. Figure 4(a) represents an example of the kymograph generated from a sequence of phase-contrast image of the bead. The black line was drawn to trace the kymograph. This kymograph curved toward the end of the record, because the bead gradually went out of focus; the curved part was not used for the analysis. Figure 4(b) shows a lamellipodium of the cell expressing RFP-actin. The white line indicates the direction along which the kymograph was generated. Figure 4(c) represents an example of the kymograph, in which two movements are apparent: one is the retrograde movement of the actin spot (indicated with the horizontal white

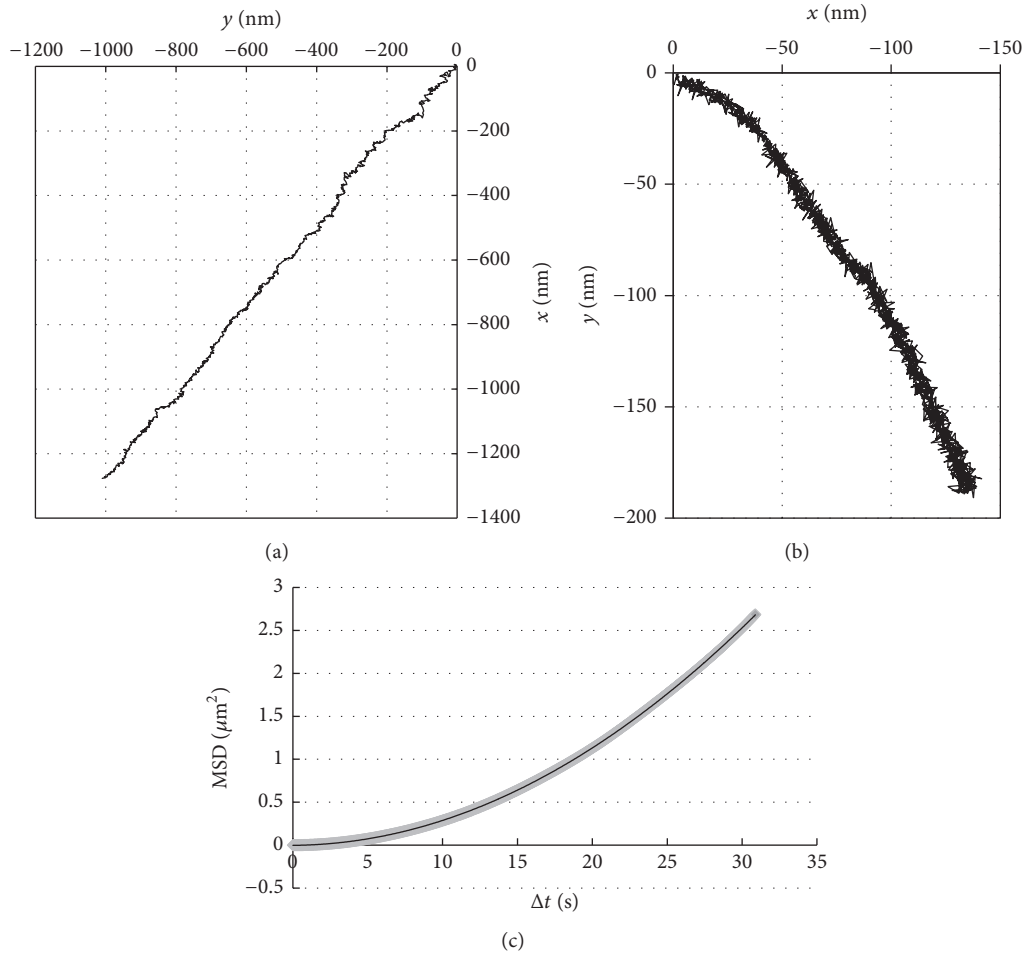


FIGURE 2: (a) The  $(x(t_j), y(t_j))$  plots of a bead bound to lamellipodium of the untreated cell. The recording duration was 33 s. (b) The  $(x(t_j), y(t_j))$  plots of a bead bound to the glass surface (fixed bead), representing the mechanical drift of the experimental system; the recording duration was 50 s. (c) The MSD plot of the bead moving on lamellipodium (see Section 2.5). The data were the same as that shown in (a); this curve was fit with a quadratic function of the time,  $\Delta t$ :  $\text{MSD} = 0.002769\Delta t^2 + 0.001304\Delta t - 0.001659$ ,  $R^2 = 0.999988$ .

arrow) and the other is the protrusive movement of the cell edge (horizontal gray arrow). The velocity of the retrograde movement of RFP-actin was calculated from the straight line drawn below the white arrow. Figure 4(d) shows the comparison of the velocity of the bead and that of the RFP-actin: the velocity of the bead was  $46.1 \pm 23.3$  nm/s (average  $\pm$  standard deviation; 62 samples), and that of the RFP-actin was  $51.2 \pm 32.9$  nm/s (87 samples). The difference between the two values was not statistically significant ( $p > 0.05$ , two-tailed  $t$ -test). Thus, we conclude that the velocity of the retrograde movement of actin filaments was the same as that of the surface-bound bead.

**3.2. Effect of the Inhibition of Actin Turnover/Myosin II Activity on the Retrograde Movement.** We investigated how the inhibition of actin dynamics affected the retrograde movement of the bead. Figure 5(a) shows  $V_{\text{fit}}$  of the bead bound to the surface of the cell treated with CytD (open bars) or LatA (gray bars). The  $V_{\text{fit}}$  values were normalized to the  $V_{\text{fit}}$  values of the untreated cells measured on the same day as the

day of the inhibitor experiment to compensate for the day-to-day variability of the  $V_{\text{fit}}$  values (Figure 3(a)). In the presence of CytD  $\geq 20$  nM, the  $V_{\text{fit}}$  values were significantly lower than the control values ( $p < 0.05$ , indicated with asterisks). The  $V_{\text{fit}}$  values in the presence of LatA  $\geq 100$  nM were significantly lower than the control values ( $p < 0.05$ , indicated with asterisks). As shown in Figure 5(b),  $0.5 \mu\text{M}$  Jasp strongly lowered the velocity of the retrograde bead movement: the average  $V_{\text{fit}}$  value in the presence of Jasp was  $15 \pm 13$  nm/s and was significantly lower than the control value ( $68 \pm 29$  nm/s;  $p < 0.05$ , 6 samples). These results altogether indicate that the actin turnover plays an important role in the retrograde movement of the surface-bound bead.

We next examined the effect of the inhibitors of myosin II activity ((-)-blebbistatin and Y-27632) on the  $V_{\text{fit}}$  values (Figure 5(c)). The average  $V_{\text{fit}}$  value in the presence of  $50 \mu\text{M}$  (-)-blebbistatin was lower than the control value by  $\sim 11\%$ , but the difference was not statistically significant ( $p > 0.05$ ). The  $V_{\text{fit}}$  obtained at  $50 \mu\text{M}$  Y-27632 was significantly lower than that of the control value by  $\sim 27\%$  ( $p < 0.05$ ). Thus,

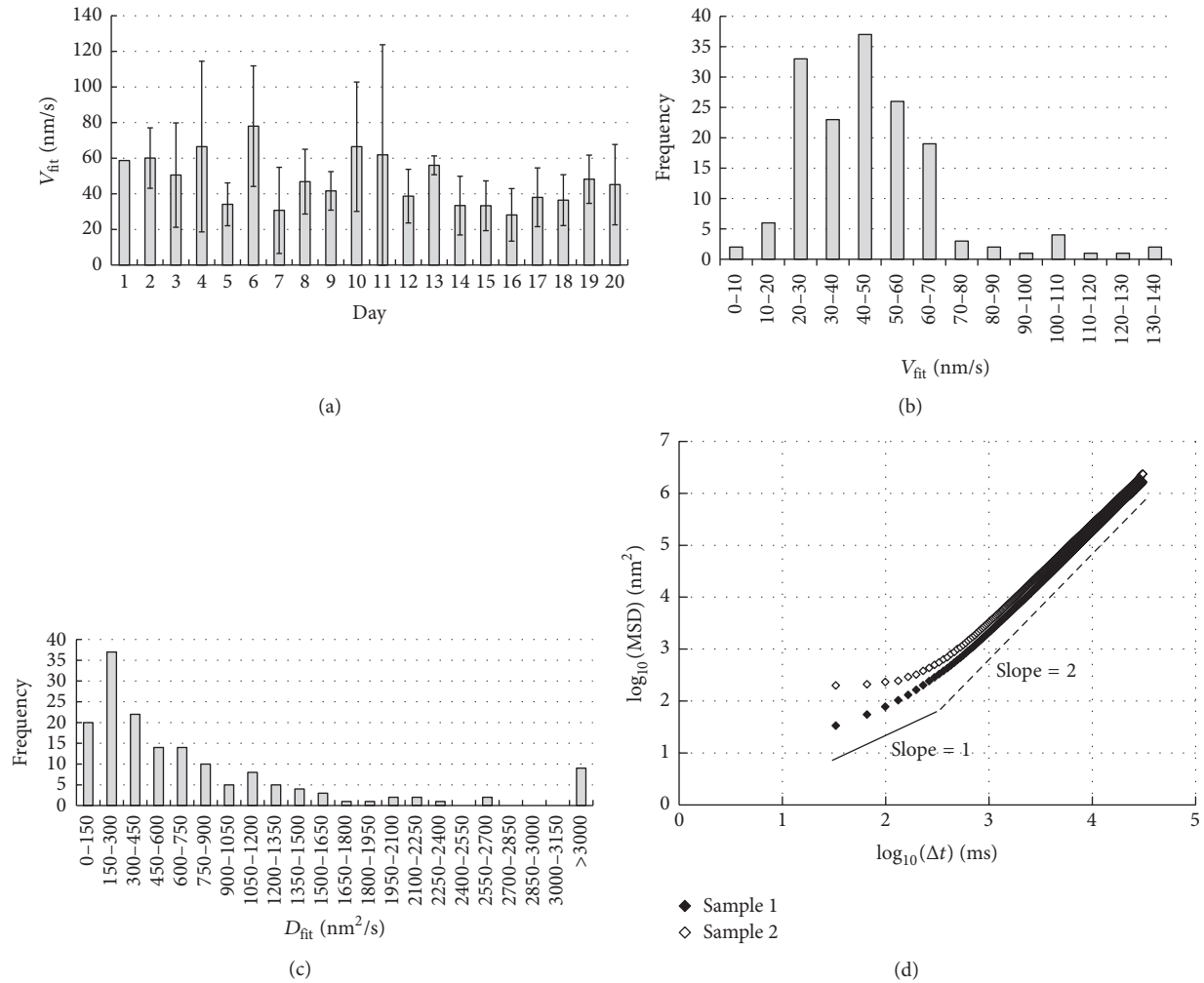


FIGURE 3: (a) Day-to-day variation of  $V_{fit}$  values of untreated cells. Total 160 measurements were carried out over 20 different days (on day 1 a single measurement was carried out). The average  $\pm$  standard deviation of all the data was  $46.6 \pm 23.3$  nm/s. (b) Distribution of the  $V_{fit}$  values shown in (a); majority of the  $V_{fit}$  values are  $<100$  nm/s. (c) Distribution of  $D_{fit}$  values; the distribution is strongly skewed toward left and is quite broad. (d)  $\log_{10}(MSD)$  versus  $\log_{10}(\Delta t)$  plot of an untreated cell (sample 1, closed symbols) and that of another untreated cell (sample 2, open symbols). The continuous straight line has a slope = 1 and the dashed straight line has a slope = 2, each of which represents a diffusion and a unidirectional movement with a constant velocity.

the inhibition of myosin II activity only slightly slowed the retrograde movement of the surface-bound beads.

**3.3. Effect of Actin or Myosin II Inhibitors on the Intracellular Distribution of Actin Filaments and Myosin II.** Figure 6(a) shows the fluorescence micrograph of an untreated cell stained for actin, and Figure 6(b) shows the same cell but immuno-stained for myosin II. Comparison of the two panels indicates that the pattern of the distribution of actin filaments and myosin II was different especially in lamellipodium. Figure 6(a) shows that actin in the lamellipodium exhibits somewhat graded, vague staining (arrows). Actin bundles (arrowheads) are penetrating through the vague staining. The vague staining of actin in lamellipodium of fibroblasts and B16-F1 mouse melanoma cells has been attributed to the dense meshwork of actin filaments, which has been supported by the electron microscopic observation [3, 12]. Lamellipodia of the

cells transiently expressing RFP-actin exhibited similar pattern of fluorescence in lamellipodium (not shown). As shown in Figure 6(b), myosin II appeared as spots. Some spots were on the actin bundles and the rest of the spots were at the back of lamellipodium (arrowheads in Figure 6(b)). The latter observation is consistent with the previous observation that myosin II was distributed mostly in lamella as bipolar mini-filaments [18]. Colocalization of myosin II with the actin bundle demonstrates that the bundle is a stress fiber [27].

The different distribution of actin filaments and myosin II in lamellipodium is clearly demonstrated in the different position of the rapid rise of line profiles (Figure 6(c); black line for actin, gray line for myosin II). The position of rapid rise of the actin intensity, as determined by the method described in Section 2.9, is shown with the arrow in Figure 6(d) and that of myosin II intensity is shown with the dashed arrow. The black arrow indicates the position of the

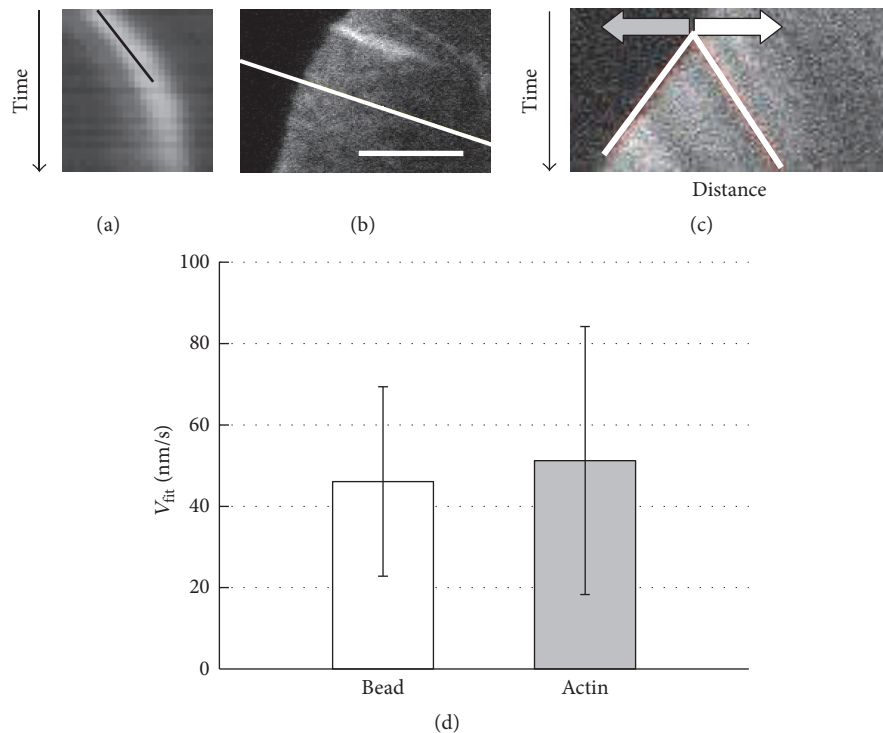


FIGURE 4: (a) A kymograph of  $1\ \mu\text{m}$  bead moving on the surface of the cell expressing RFP-actin. The width of the vertical edge of the kymograph is  $2.5\ \mu\text{m}$  and that of the horizontal edge is  $27\ \text{s}$ ; the slope of the black line represents the velocity of the bead; for this particular example, the velocity was  $87.5\ \text{nm/s}$ . (b) Part of a lamellipodium of the cell expressing RFP-actin; kymograph of RFP-actin was generated along the white line. Horizontal bar,  $5\ \mu\text{m}$ . (c) The kymograph; gray arrow indicates the forward motion of the lamellipodial edge, and white arrow indicates the retrograde movement of the fluorescence pattern of RFP-actin. The width of the vertical edge is  $60\ \text{sec}$  and that of the horizontal edge is  $16\ \mu\text{m}$ . In this case, protrusion of lamellipodium and retrograde flow of actin occurred at the same time. The slopes of two white lines represent the velocity of the bead and the cell edge. (d) The average of the velocity of the bead bound to the lamellipodium of the cell expressing RFP-actin (62 measurements) and that of RFP-actin (87 measurements), both estimated by kymograph method. Error bar, standard deviation.

most rapid rise of actin intensity, and the dashed arrow indicates that of myosin II intensity. The different positions of these arrows demonstrate the difference in the distribution of actin and myosin filament. Similar differential distribution has been previously reported [37, 38]. Immediately behind the position of the rapid rise of actin profile, a plateau (indicated with  $\wedge$ ) appears; this corresponds to the vague staining of actin near the cell edge.

Figure 6(e) shows that  $100\ \text{nM}$  CytD drastically altered the distribution of actin filaments. The vague staining along the edge of lamellipodium disappeared; instead, the edge was rimmed by actin filaments (arrowheads). Number of stress fibers seemed to be decreased, and the remaining actin bundles (arrows) made spikes. The region where myosin II existed overlapped the region where actin was populated (Figure 6(f); arrows indicate the same actin bundles as those in Figure 6(e)). As demonstrated in the line-profile plot (Figure 6(g)), the rise of the actin and myosin profiles started at almost the same positions (arrow for actin and dashed arrow for myosin II, determined in the same manner as described above; the arrowhead indicates the position of the actin rim). Similar distributions of actin and myosin II were observed in the cell treated with LatA (not shown).

Majority of the cells treated with  $5\ \mu\text{M}$  (-)-blebbistatin or  $5\ \mu\text{M}$  Y-27632 (Figures 6(h) and 6(i)) possessed lamellipodia (asterisks). Individual lamellipodia were narrower and longer than those of the untreated cells, and the number of lamellipodia in individual cells increased. Elongated lamellipodia of *Aplysia* bag-cell neuronal growth cone treated with  $70\ \mu\text{M}$  (-)-blebbistatin had been demonstrated [23]. The vague staining of actin along the cell edge was observed (white arrows in Figures 6(h) and 6(i)), as in the untreated cell. The number of stress fibers seemed to be decreased and many of them were thinner than those in the untreated cells (Figures 6(h) and 6(i), arrowheads). The stress fibers behind the lamellipodia (arrowheads) are longer than those in the untreated cell; elongation of stress fibers has been observed in the *Aplysia* growth cone treated with (-)-blebbistatin, which has been interpreted as the decrease in the severing activity of myosin II (see Section 4).

Figures 6(j) and 6(k) show the distribution of actin filaments and myosin II in the cell treated with  $50\ \mu\text{M}$  (-)-blebbistatin. The peripheral vague staining still existed, but the stress fibers penetrating the lamellipodium almost disappeared (Figure 6(j); arrowhead indicates very faint line) as compared with the cell treated with  $5\ \mu\text{M}$  (-)-blebbistatin.

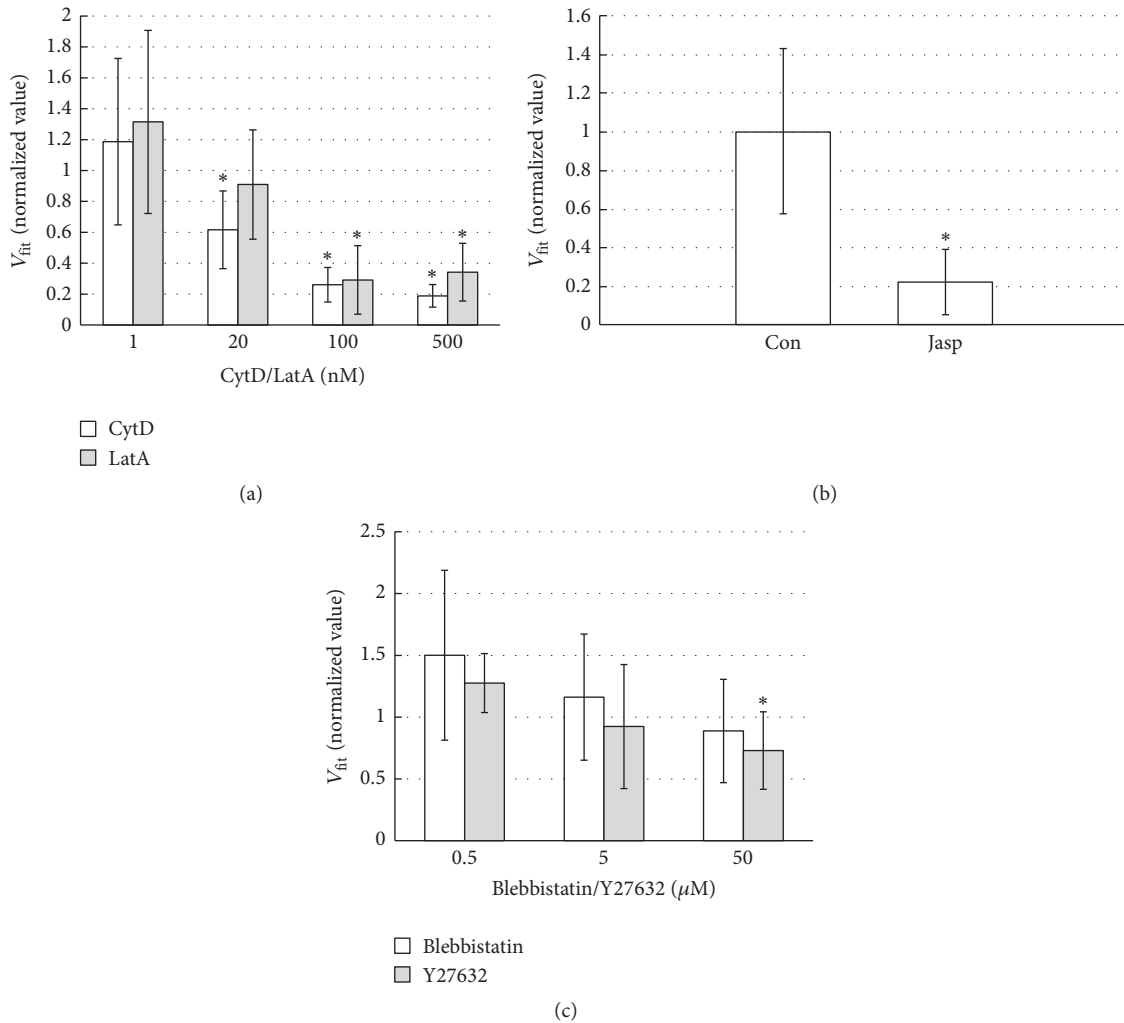


FIGURE 5: (a) The effect of CytD/LatA on the average  $V_{fit}$  values; error bar, standard deviation. (b) Comparison of the average  $V_{fit}$  values of the control cells and the cells treated with  $0.5 \mu\text{M}$  Jasp. (c) The effect of (-)-blebbistatin/Y-27632 on  $V_{fit}$  values; error bar, standard deviation. In (a) and (c),  $V_{fit}$  values were normalized to the control values, which were determined on the same day when each inhibitor experiment was carried out. Asterisks in (a) to (c) indicate the statistically significant change ( $p < 0.05$ ) of the average  $V_{fit}$  values from that of the untreated cells.

On the other hand, the distribution of myosin II was quite similar to that in the untreated cell and did not overlap that of actin. Thus, the line profiles of actin and myosin (see Figure 6(l)) measured along the white line shown in Figures 6(j) and 6(k) demonstrate that the distribution of actin started rising at the cell periphery, whereas that of myosin II rose slowly and exhibited a sharp rise only at the back of lamellipodium (arrow in Figure 6(l)). The plateau in the profile plot is evident between  $\sim 3.5 \mu\text{m}$  and  $\sim 5.5 \mu\text{m}$  from the start of the profile. We note that the (-)-blebbistatin at  $50 \mu\text{M}$ , which is ten times higher concentration than that used for the cell shown in Figure 6(h), provided similar narrow and elongated morphology of lamellipodia; we consider that this argues against the possibility of the photoinactivation of (-)-blebbistatin [39] or of insufficient concentration of the drug. The possibility is also remote that the concentration of Y-27632 was not sufficiently high, because we previously

showed that  $10 \mu\text{M}$  Y-27632 strongly inhibited the contraction of stress fibers in Swiss 3T3 fibroblast [27].

#### 4. Discussion

It has been postulated that the retrograde movements occur as a result of either the reaction of the pushing of the growing actin filament network against the edge of lamellipodium, myosin II-based contraction of actin filament network in a lamellum behind lamellipodium, or both. To investigate the relative contribution of actin polymerization and myosin II activity, we measured the velocity of the retrograde movement of the poly-D-lysine-coated bead attached to the tip of lamellipodium and compared the velocities in the presence and absence of the inhibitors of actin turnover or myosin II activity.

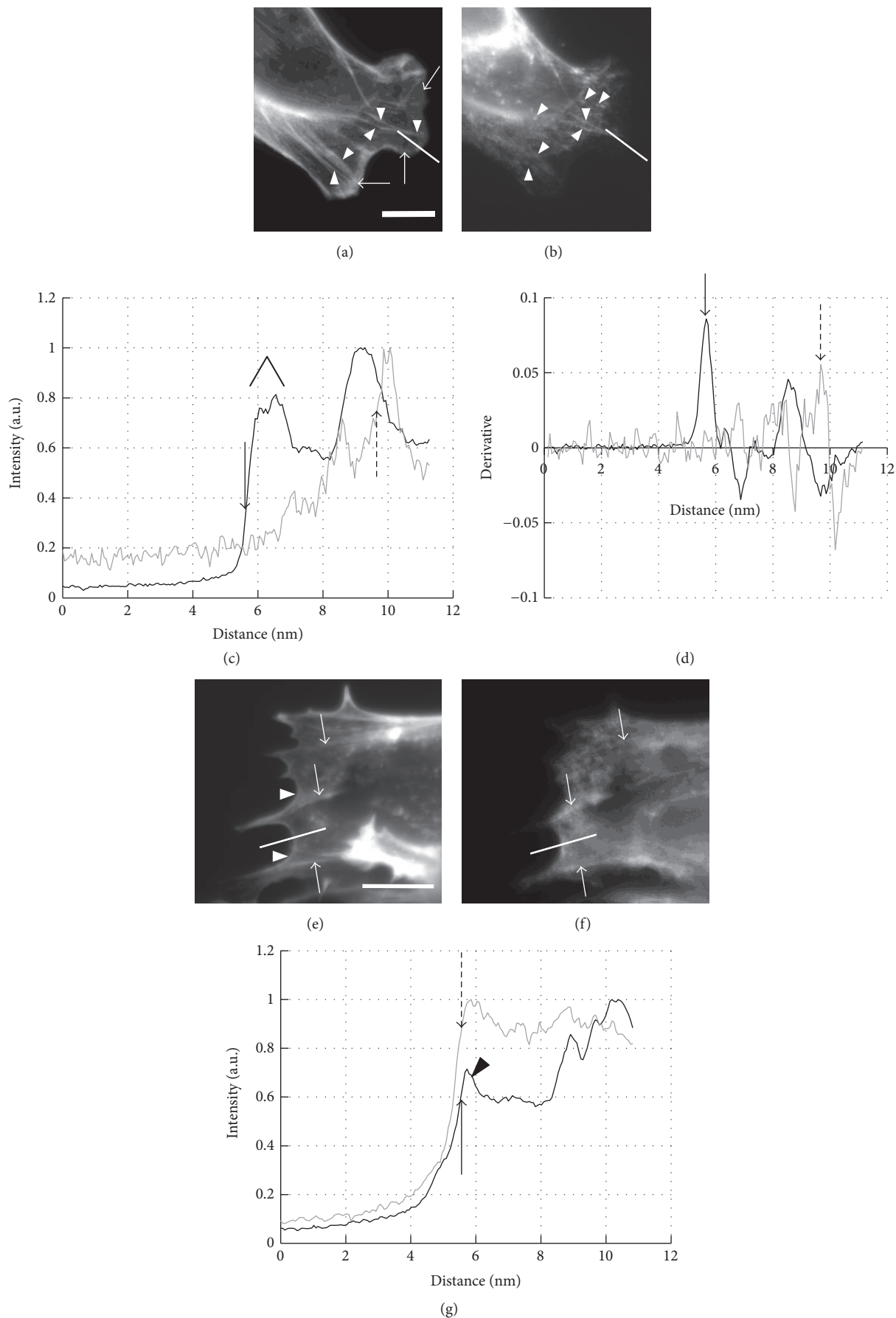
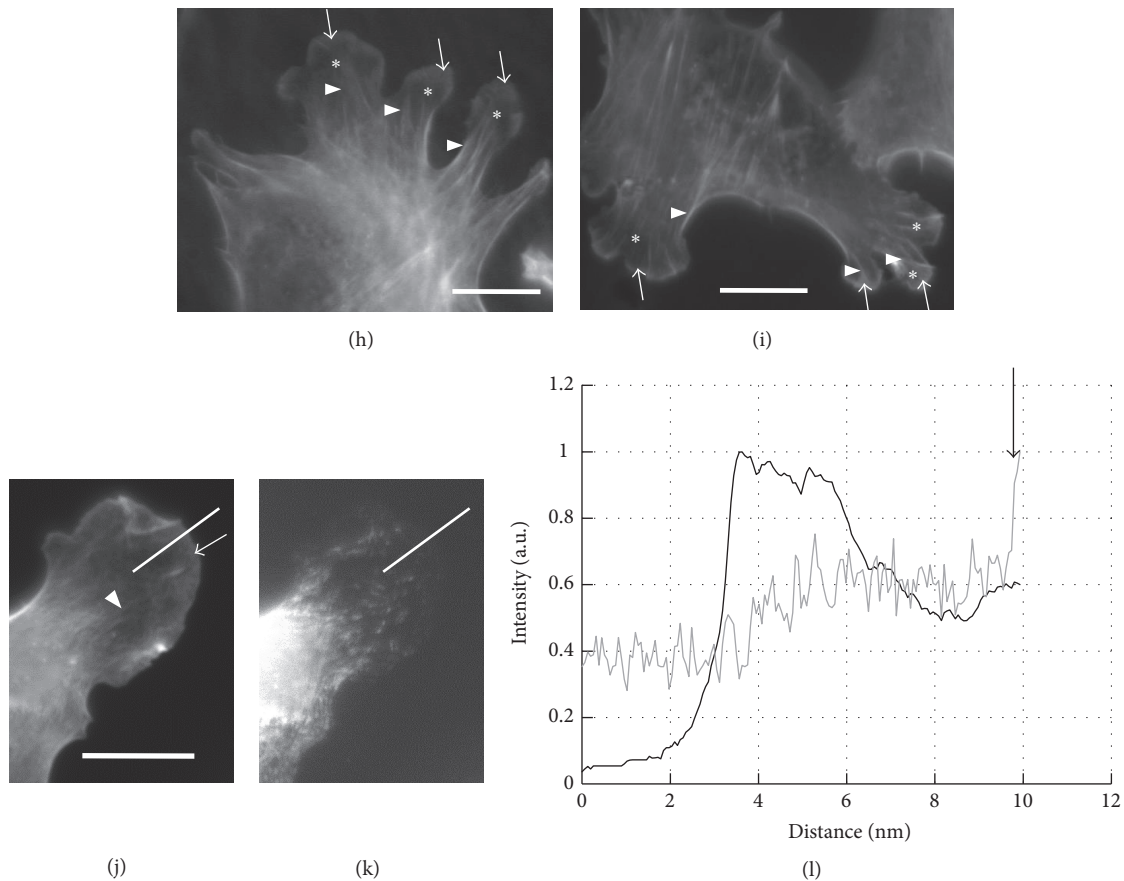


FIGURE 6: Continued.



**FIGURE 6:** Effect of the inhibitors of actin turnover or those of myosin II activity on the distribution of actin filaments and myosin II. Under each condition, distributions of actin and myosin II are compared in the same cell. (a) Actin filaments in the control cell; arrows, vague staining of actin filament network in the lamellipodium; arrowheads, actin bundles. (b) Myosin II in the same cell; arrowheads indicate the spot-like fluorescence attributed to myosin II mini-filaments, some of which reside along the actin bundles. Unlike actin, distribution of myosin II along the cell periphery was hardly observed. (c) Comparison of fluorescence intensity of actin filaments and that of myosin II measured along the white lines shown in (a) and (b). The fluorescence intensity was normalized as described in Section 2.9. The arrow and the dashed arrow indicate the start of the rapid rise of the profile of actin and that of myosin II, respectively. The symbol ( $\wedge$ ) indicates the plateau corresponding to the vague actin staining. (d) Derivative of the intensity profiles shown in (a) and (b); the arrow and the dashed arrow indicate the positions of local maxima of the derivative of the profiles of actin and that of myosin II, each of which corresponds to the rapid rise of each profile. (e) Actin filaments in the cell treated with 100 nM CytD; arrows indicate the distribution of actin bundles (i.e., stress fibers); arrowheads indicate the cell edge where rim-like distribution of actin filaments is seen. (f) The same cell stained for myosin II; there is some colocalization of myosin II with actin bundles (arrows). (g) Line profiles of fluorescence intensity for actin (black line) and myosin II (gray line) measured along the white lines shown in (d) and (e). The arrow and the dashed arrow indicate the start of the rapid rise of the profiles of actin and myosin II, respectively. The arrowhead indicates a peak of the fluorescence profile corresponding to the actin rim. ((h) and (i)) Distribution of actin filaments in the cell treated with 5  $\mu$ M (-)-blebbistatin or with 5  $\mu$ M Y-27632, respectively. Asterisks indicate lamellipodia; arrows in both panels indicate the vague staining of actin in lamellipodia; arrowheads in both panels indicate actin stress fibers. ((j) and (k)) Distributions of actin filaments and myosin II in the cell treated with 50  $\mu$ M (-)-blebbistatin. Arrows indicate the vague staining of actin and arrowheads indicate actin bundles. (l) Line profiles of the intensity of actin filaments (black line) and that of myosin II (gray line) measured along the white lines shown in (i) and (j), respectively; the background (outside the cell) of the image field for myosin (k) was higher than that of actin probably because of the nonspecific binding of the secondary antibody to the glass surface. The wide plateau corresponding to the vague actin fluorescence is evident between  $\sim 3.5 \mu$ m and  $\sim 5.5 \mu$ m from the start of the profile plot. White thick bar in (j) indicates 10  $\mu$ m.

Inhibition of actin turnover with CytD, LatA, or Jasp greatly slowed down the retrograde movement of the bead. On the other hand, inhibition of myosin II ATPase activity slightly lowered the velocity. Thus, in Swiss 3T3 fibroblasts actin turnover played a major role in the retrograde movement, whereas myosin II activity played secondary or some other roles.

As a result of the inhibition of the actin polymerization by CytD or LatA, the vague staining of actin filament network at the edge of lamellipodium disappeared. This was because the actin polymerization was inhibited by either the barbed-end capping activity of CytD [28] or the actin-sequestering action of LatA [29], whereas the depolymerization of actin at the back of lamellipodium was not affected by these inhibitors

[14]. The significant decrease of the  $V_{fit}$  value in the presence of these inhibitors can be explained as a result of the loss of actin network structure.

In the CytD- or LatA-treated cells rim of actin appeared along the cell edge. A previous study [3] has proposed a mechanism of the generation of similar structure: during a pause of the protrusion of lamellipodium, short filaments disappear as a result of the depolymerization activity. Longer filaments that have survived the depolymerization form bundles with myosin II. As some of the actin filaments in this bundle are connected to the actomyosin network in lamella, the contraction of the actomyosin will pull the cell edge. With the attachment of both ends of the bundle to the cell adhesion sites, an inward curvature of the bundle will be generated. We presume that the rim observed in the present study was formed in an analogous process, because actin polymerization was halted by actin inhibitors, but both the cell-specific depolymerization activity and myosin II activity were not changed.

After the treatment of the cell with CytD or LatA, stress fibers seemed to be diminished but did not totally disappear. It has been suggested that stress fibers are formed by a connection between actin filaments that elongated by polymerization from the cell adhesion site and those formed at the cell periphery and joined together by myosin II filaments [40] or those formed by bundling of actin filaments severed in lamellipodium (a cytoplasmic pool of actin filaments) [41]. Thus, CytD/LatA, by inhibiting the formation of new filament, would have depleted the filament pool, and, hence, the formation of stress fibers by the coalition process was inhibited, leading to the diminution. On the other hand, it has been shown that mutual interaction between adjacent actin filaments in a stress fiber is stabilized by multiple proteins such as  $\alpha$ -actinin, Arp2/3, or bipolar myosin filament [42]. Probably because of this, the on-and-off rates of actin monomer to and from a stress fiber are low [40]. As a result, some stress fibers remained after CytD/LatA treatment. A study with MTF24 fibroblast has shown that stress fibers remained after the treatment of the cell with 100 nM CytD for 2 h [43].

The inhibition of myosin II activity by (-)-blebbistatin or Y-27632 resulted in only a small decrease of  $V_{fit}$  values even at the highest concentration (50  $\mu$ M) of these drugs. The actin network structure along the cell edge still existed, which is represented with the wide plateau in the line profile of actin staining. We assume that the remaining actin network was driving the retrograde movements. On the other hand, stress fibers in the cells treated with these drugs were progressively lost (Figure 6(h) for 5  $\mu$ M (-)-blebbistatin and Figure 6(j) for 50  $\mu$ M (-)-blebbistatin). This was probably due to the decrease in contractility of the stress fiber [44, 45]. The development of longer lamellipodia in the cells treated with (-)-blebbistatin/Y-27632 was a combined result of the decreased contractility and the elongation of actin by polymerization that was not affected by the myosin II inhibitors [14, 23]. The reason for the narrowing of lamellipodia and the increase in their number is not clear.

Our experimental results collectively suggest that the actin polymerization is the major source of the driving force

of the retrograde flow, while the contractile activity of myosin II may play some other roles. It has been suggested that filament formation by actin polymerization at the front of the actin network and the depolymerization at the back, which follows the severing of filaments, is balanced [46]. These two processes are mediated by the retrograde flow of actin network with severing and the forward transport of actin monomer [47]. It has been suggested that the contractile force generated by myosin II filaments promotes the severing and/or depolymerization of actin filaments [23]. If this occurs in our system, the inhibition of the activity of myosin II will decrease the amount of the actin returned to the leading edge. As a result, the polymerization rate and hence the velocity of retrograde flow will be decreased. We propose that the slight decrease in the  $V_{fit}$  in the presence of 50  $\mu$ M (-)-blebbistatin or Y-27632 was due to the impairment of the severing function.

Previous studies have demonstrated that the retrograde flow depends on the activity of myosin [9, 21, 48]. Involvement of myosin 1c [9] or myosin IIA [48] in the retrograde flow has been demonstrated. In these studies the pulling action of myosin is considered to be the most important. Our study has suggested that myosin II participates in the process of retrograde flow in a way different from what has been demonstrated in the above studies. However, it is also possible that some intricate mechanism exists that compensates the loss of myosin II activity in the retrograde flow. Further study is necessary to fully understand the relative importance of the two mechanisms in the retrograde flow.

## Competing Interests

The authors declare no conflict of interests.

## Acknowledgments

This work was supported by a grant-in-aid from MEXT, Japan.

## References

- [1] D. A. Lauffenburger and A. F. Horwitz, "Cell migration: a physically integrated molecular process," *Cell*, vol. 84, no. 3, pp. 359–369, 1996.
- [2] A. Ponti, M. Machacek, S. L. Gupton, C. M. Waterman-Storer, and G. Danuser, "Two distinct actin networks drive the protrusion of migrating cells," *Science*, vol. 305, no. 5691, pp. 1782–1786, 2004.
- [3] S. A. Koestler, S. Auinger, M. Vinzenz, K. Rottner, and J. V. Small, "Differentially oriented populations of actin filaments generated in lamellipodia collaborate in pushing and pausing at the cell front," *Nature Cell Biology*, vol. 10, no. 3, pp. 306–313, 2008.
- [4] J. P. Heath and B. F. Holifield, "On the mechanisms of cortical actin flow and its role in cytoskeletal organizations of fibroblasts," *Symposia of the Society for Experimental Biology*, vol. 47, pp. 35–56, 1993.
- [5] D. Bray and J. G. White, "Cortical flow in animal cells," *Science*, vol. 239, no. 4842, pp. 883–888, 1988.

- [6] A. Grebecki, "Membrane and cytoskeleton flow in motile cells with emphasis on the contribution of free-living amoebae," *International Review of Cytology*, vol. 148, pp. 37–80, 1994.
- [7] G. W. Fisher, P. A. Conrad, R. L. DeBiasio, and D. L. Taylor, "Centripetal transport of cytoplasm, actin, and the cell surface in lamellipodia of fibroblasts," *Cell Motility and the Cytoskeleton*, vol. 11, no. 4, pp. 235–247, 1988.
- [8] M. E. Brown and P. C. Bridgman, "Retrograde flow rate is increased in growth cones from myosin IIB knockout mice," *Journal of Cell Science*, vol. 116, no. 6, pp. 1087–1094, 2003.
- [9] T. J. Diefenbach, V. M. Latham, D. Yimlamai, C. A. Liu, I. M. Herman, and D. G. Jay, "Myosin 1c and myosin IIB serve opposing roles in lamellipodial dynamics of the neuronal growth cone," *Journal of Cell Biology*, vol. 158, no. 7, pp. 1207–1217, 2002.
- [10] A. Sergé, L. Fourgeaud, A. Hémar, and D. Choquet, "Active surface transport of metabotropic glutamate receptors through binding to microtubules and actin flow," *Journal of Cell Science*, vol. 116, no. 24, pp. 5015–5022, 2003.
- [11] D. P. Felsenfeld, D. Choquet, and M. P. Sheetz, "Ligand binding regulates the directed movement of  $\beta 1$  integrins on fibroblasts," *Nature*, vol. 383, no. 6599, pp. 438–440, 1996.
- [12] V. C. Abraham, V. Krishnamurthi, D. L. Taylor, and F. Lanni, "The actin-based nanomachine at the leading edge of migrating cells," *Biophysical Journal*, vol. 77, no. 3, pp. 1721–1732, 1999.
- [13] A. Narita, J. Mueller, E. Urban, M. Vinzenz, J. V. Small, and Y. Maéda, "Direct determination of actin polarity in the cell," *Journal of Molecular Biology*, vol. 419, no. 5, pp. 359–368, 2012.
- [14] T. D. Pollard and G. G. Borisy, "Cellular motility driven by assembly and disassembly of actin filaments," *Cell*, vol. 112, no. 4, pp. 453–465, 2003.
- [15] D. M. Suter, L. D. Errante, V. Belotserkovsky, and P. Forscher, "The Ig superfamily cell adhesion molecule, apCAM, mediates growth cone steering by substrate-cytoskeletal coupling," *Journal of Cell Biology*, vol. 141, no. 1, pp. 227–240, 1998.
- [16] K. Nishimura, F. Yoshihara, T. Tojima et al., "LI-dependent neuritogenesis involves ankyrin<sub>B</sub> that mediates LI-CAM coupling with retrograde actin flow," *Journal of Cell Biology*, vol. 163, no. 5, pp. 1077–1088, 2003.
- [17] T. Mitchison and M. Kirschner, "Cytoskeletal dynamics and nerve growth," *Neuron*, vol. 1, no. 9, pp. 761–772, 1988.
- [18] A. B. Verkhovskiy, T. M. Svitkina, and G. G. Borisy, "Myosin II filament assemblies in the active lamella of fibroblasts: their morphogenesis and role in the formation of actin filament bundles," *Journal of Cell Biology*, vol. 131, no. 4, pp. 989–1002, 1995.
- [19] C. H. Lin, E. M. Espreafico, M. S. Mooseker, and P. Forscher, "Myosin drives retrograde F-actin flow in neuronal growth cones," *Neuron*, vol. 16, no. 4, pp. 769–782, 1996.
- [20] C. Jurado, J. R. Haserick, and J. Lee, "Slipping or gripping? Fluorescent speckle microscopy in fish keratocytes reveals two different mechanisms for generating a retrograde flow of actin," *Molecular Biology of the Cell*, vol. 16, no. 2, pp. 507–518, 2005.
- [21] J. H. Henson, T. M. Svitkina, A. R. Burns et al., "Two components of actin-based retrograde flow in sea urchin coelomocytes," *Molecular Biology of the Cell*, vol. 10, no. 12, pp. 4075–4090, 1999.
- [22] K. Sakai, S. Kohmoto, D. Nobezawa, S.-I. Ikeda, and H. Miyata, "Measurement of lamellipodial protrusion by optical trapping," *Journal of the Physical Society of Japan*, vol. 84, no. 2, Article ID 024802, 2015.
- [23] N. A. Medeiros, D. T. Burnette, and P. Forscher, "Myosin II functions in actin-bundle turnover in neuronal growth cones," *Nature Cell Biology*, vol. 8, no. 3, pp. 215–226, 2006.
- [24] H. Qian, M. P. Sheetz, and E. L. Elson, "Single particle tracking. Analysis of diffusion and flow in two-dimensional systems," *Biophysical Journal*, vol. 60, no. 4, pp. 910–921, 1991.
- [25] C. Waterman-Storer, A. Desai, and E. D. Salmon, "Fluorescent speckle microscopy of spindle microtubule assembly and motility in living cells," in *Methods in Cell Biology*, vol. 61, pp. 155–173, 1999.
- [26] N. Watanabe and T. J. Mitchison, "Single-molecule speckle analysis of actin filament turnover in lamellipodia," *Science*, vol. 295, no. 5557, pp. 1083–1086, 2002.
- [27] Y. Senju and H. Miyata, "The role of actomyosin contractility in the formation and dynamics of actin bundles during fibroblast spreading," *Journal of Biochemistry*, vol. 145, no. 2, pp. 137–150, 2009.
- [28] J. A. Cooper, "Effects of cytochalasin and phalloidin on actin," *Journal of Cell Biology*, vol. 105, no. 4, pp. 1473–1478, 1987.
- [29] I. Spector, N. R. Shochet, Y. Kashman, and A. Groewiss, "Latrunculin: novel marine toxins that disrupt microfilament organization in cultured cells," *Science*, vol. 219, no. 4584, pp. 493–495, 1983.
- [30] L. P. Cramer, "Role of actin-filament disassembly in lamellipodium protrusion in motile cells revealed using the drug jasplakinolide," *Current Biology*, vol. 9, no. 19, pp. 1095–1105, 1999.
- [31] M. Kovács, J. Tóth, C. Hetényi, A. Málnási-Csizmadia, and J. R. Sellers, "Mechanism of blebbistatin inhibition of myosin II," *Journal of Biological Chemistry*, vol. 279, no. 34, pp. 35557–35563, 2004.
- [32] A. Masamune, K. Kikuta, M. Satoh, K. Satoh, and T. Shimosegawa, "Rho kinase inhibitors block activation of pancreatic stellate cells," *British Journal of Pharmacology*, vol. 140, no. 7, pp. 1292–1302, 2003.
- [33] H. Hirata, K. Ohki, and H. Miyata, "Change of the topography of ventral cell surface during spreading of fibroblasts as revealed by evanescent wave-excited fluorescence microscopy: effect of contractility and microtubule integrity," *JSME International Journal, Series C: Mechanical Systems, Machine Elements and Manufacturing*, vol. 46, no. 4, pp. 1208–1217, 2003.
- [34] H. Hirata, K. Ohki, and H. Miyata, "Mobility of integrin  $\alpha 5 \beta 1$  measured on the isolated ventral membranes of human skin fibroblasts," *Biochimica et Biophysica Acta (BBA)—General Subjects*, vol. 1723, no. 1–3, pp. 100–105, 2005.
- [35] D. F. Kucik, T. E. O'Toole, A. Zheleznyak, D. K. Busettini, and E. J. Brown, "Activation-enhanced  $\alpha (IIb) \beta (3)$ -integrin-cytoskeleton interactions outside of focal contacts require the  $\alpha$ -subunit," *Molecular Biology of the Cell*, vol. 12, no. 5, pp. 1509–1518, 2001.
- [36] M. J. Saxton and K. Jacobson, "Single-particle tracking: applications to membrane dynamics," *Annual Review of Biophysics and Biomolecular Structure*, vol. 26, pp. 373–399, 1997.
- [37] L. P. Cramer and T. J. Mitchison, "Myosin is involved in post-mitotic cell spreading," *Journal of Cell Biology*, vol. 131, no. 1, pp. 179–189, 1995.
- [38] M. S. Shutova, A. Y. Alexandrova, and J. M. Vasiliev, "Regulation of polarity in cells devoid of actin bundle system after treatment with inhibitors of myosin II activity," *Cell Motility and the Cytoskeleton*, vol. 65, no. 9, pp. 734–746, 2008.
- [39] T. Sakamoto, J. Limouze, C. A. Combs, A. F. Straight, and J. R. Sellers, "Blebbistatin, a myosin II inhibitor, is photoinactivated by blue light," *Biochemistry*, vol. 44, no. 2, pp. 584–588, 2005.

- [40] P. Hotulainen and P. Lappalainen, "Stress fibers are generated by two distinct actin assembly mechanisms in motile cells," *Journal of Cell Biology*, vol. 173, no. 3, pp. 383–394, 2006.
- [41] J. V. Small, K. Rottner, I. Kaverina, and K. I. Anderson, "Assembling an actin cytoskeleton for cell attachment and movement," *Biochimica et Biophysica Acta—Molecular Cell Research*, vol. 1404, no. 3, pp. 271–281, 1998.
- [42] S. Tojkander, G. Gateva, and P. Lappalainen, "Actin stress fibers—assembly, dynamics and biological roles," *Journal of Cell Science*, vol. 125, no. 8, pp. 1855–1864, 2012.
- [43] J. D. Rotty, C. Wu, E. M. Haynes et al., "Profilin-1 serves as a gatekeeper for actin assembly by Arp2/3-dependent and -independent pathways," *Developmental Cell*, vol. 32, no. 1, pp. 54–67, 2015.
- [44] M. Chrzanowska-Wodnicka and K. Burridge, "Rho-stimulated contractility drives the formation of stress fibers and focal adhesions," *Journal of Cell Biology*, vol. 133, no. 6, pp. 1403–1415, 1996.
- [45] H. Hirata, H. Tatsumi, C. T. Lim, and M. Sokabe, "Force-dependent vinculin binding to talin in live cells: a crucial step in anchoring the actin cytoskeleton to focal adhesions," *American Journal of Physiology—Cell Physiology*, vol. 306, no. 6, pp. C607–C620, 2014.
- [46] C. Le Clainche and M.-F. Carrier, "Regulation of actin assembly associated with protrusion and adhesion in cell migration," *Physiological Reviews*, vol. 88, no. 2, pp. 489–513, 2008.
- [47] D. Zicha, I. M. Dobbie, M. R. Holt et al., "Rapid actin transport during cell protrusion," *Science*, vol. 300, no. 5616, pp. 142–145, 2003.
- [48] Y. Cai, N. Biais, G. Giannone et al., "Nonmuscle myosin IIA-dependent force inhibits cell spreading and drives F-actin flow," *Biophysical Journal*, vol. 91, no. 10, pp. 3907–3920, 2006.

## Research Article

# Hyperforin/HP- $\beta$ -Cyclodextrin Enhances Mechanosensitive $\text{Ca}^{2+}$ Signaling in HaCaT Keratinocytes and in Atopic Skin Ex Vivo Which Accelerates Wound Healing

Hiroya Takada,<sup>1,2</sup> Jun Yonekawa,<sup>1</sup> Masami Matsumoto,<sup>2</sup>  
Kishio Furuya,<sup>3</sup> and Masahiro Sokabe<sup>3</sup>

<sup>1</sup>Department of Physiology, Nagoya University Graduate School of Medicine, 65 Tsurumai, Nagoya 466-8550, Japan

<sup>2</sup>Pixy Central Research Institute, 3-7-1 Kamitsuchidananaka, Ayase, Kanagawa 252-1113, Japan

<sup>3</sup>Mechanobiology Laboratory, Nagoya University Graduate School of Medicine, 65 Tsurumai, Nagoya 466-8550, Japan

Correspondence should be addressed to Kishio Furuya; [furuya@med.nagoya-u.ac.jp](mailto:furuya@med.nagoya-u.ac.jp)

Received 16 September 2016; Accepted 29 November 2016; Published 22 January 2017

Academic Editor: Adam Reich

Copyright © 2017 Hiroya Takada et al. This is an open access article distributed under the Creative Commons Attribution License, which permits unrestricted use, distribution, and reproduction in any medium, provided the original work is properly cited.

Cutaneous wound healing is accelerated by mechanical stretching, and treatment with hyperforin, a major component of a traditional herbal medicine and a known TRPC6 activator, further enhances the acceleration. We recently revealed that this was due to the enhancement of ATP- $\text{Ca}^{2+}$  signaling in keratinocytes by hyperforin treatment. However, the low aqueous solubility and easy photodegradation impede the topical application of hyperforin for therapeutic purposes. We designed a compound hydroxypropyl- $\beta$ -cyclodextrin- (HP- $\beta$ -CD-) tetracapped hyperforin, which had increased aqueous solubility and improved photoprotection. We assessed the physiological effects of hyperforin/HP- $\beta$ -CD on wound healing in HaCaT keratinocytes using live imaging to observe the ATP release and the intracellular  $\text{Ca}^{2+}$  increase. In response to stretching (20%), ATP was released only from the foremost cells at the wound edge; it then diffused to the cells behind the wound edge and activated the P2Y receptors, which caused propagating  $\text{Ca}^{2+}$  waves via TRPC6. This process might facilitate wound closure, because the  $\text{Ca}^{2+}$  response and wound healing were inhibited in parallel by various inhibitors of ATP- $\text{Ca}^{2+}$  signaling. We also applied hyperforin/HP- $\beta$ -CD on an ex vivo skin model of atopic dermatitis and found that hyperforin/HP- $\beta$ -CD treatment for 24 h improved the stretch-induced  $\text{Ca}^{2+}$  responses and oscillations which failed in atopic skin.

## 1. Introduction

Epidermal keratinocytes are located at the surface of the skin and are exposed to various environmental stimuli including mechanical and physical stimuli and are susceptible to these stimuli. During the wound healing process, these exogenous stimuli and the endogenous stimuli, such as the tension and traction forces generated between the migration of the foremost cells and the cells that are located behind them, may affect the rate of wound closure. Our earlier study demonstrated that mechanical stretching facilitated wound closure in bovine aortic endothelial cells [1]. We recently reported that wound healing in HaCaT keratinocytes was accelerated by stretching and treatment with hyperforin, which is a major component of a traditional herbal medicine and which is

known to be a TRPC6 activator, further accelerated wound closure [2]. We revealed that the facilitation of wound closure by mechanical stretching and hyperforin occurs due to the release of ATP via mechanosensitive hemichannels at the wound edge and the P2Y receptor-mediated  $\text{Ca}^{2+}$  influx via TRPC6 in the cells located behind the wound edge using real-time ATP luminescence imaging and  $\text{Ca}^{2+}$  fluorescence measurement [2]. The influx of  $\text{Ca}^{2+}$  through TRPC6 channels was also reported to be essential for wound healing in vivo in TRPC6 knockout mice [3].

Hyperforin is a major active constituent of St. John's wort (*Hypericum perforatum* L.) extract, which is widely used in traditional herbal medicines, to promote wound healing [4–9]. The use of hyperforin-rich cream as a topical

medication for atopic dermatitis was recently reported [10–14]. In spite of its potential therapeutic activities, the extreme sensitivity of hyperforin to photodegradation has impeded its topical application. The complexation of St. John's wort extract with  $\beta$ - and  $\gamma$ -cyclodextrin (CD) was reported to enhance the photoprotection and solubility of hyperforin in aqueous solutions [15–17]. In the present study, we aimed to develop a novel formation of encapsulated hyperforin with hydroxypropyl- $\beta$ -cyclodextrin (HP- $\beta$ -CD) to improve its aqueous solubility and photostability, because HP- $\beta$ -CD has been shown to possess the highest solubility not only in water but also in ethanol among several of the CD compounds that are commonly used. We also assessed the effects of the compound on the wound healing and ATP- $\text{Ca}^{2+}$  signaling in HaCaT keratinocytes.

Atopic dermatitis is a chronic inflammatory skin disease that develops due to various factors that are associated with epidermal barrier dysfunction [18]. It is known that the  $\text{Ca}^{2+}$  gradient in the epidermis is necessary for maintaining the barrier function; however, the  $\text{Ca}^{2+}$  dynamics of atopic skin remain to be elucidated. We herein measured the stretch-induced  $\text{Ca}^{2+}$  responses *ex vivo* in atopic skin using a confocal microscope. We found that the  $\text{Ca}^{2+}$  responses were impaired in the atopic epidermis and that the responses recovered after the application of hyperforin/HP- $\beta$ -CD. The data suggested that hyperforin/HP- $\beta$ -CD is a potent targeted therapeutic agent that can be used to promote epidermal wound healing and treat atopic dermatitis.

## 2. Material and Methods

**2.1. Reagents.** Hyperforin/hydroxypropyl- $\beta$ -cyclodextrin was prepared by the complexation of hyperforin (Cayman Chemical, Ann Arbor, MI) and hydroxypropyl- $\beta$ -cyclodextrin (HP- $\beta$ -CD; CycloChem, Tokyo, Japan) as described below. The other chemicals and reagents were as follows: carbenoxolone disodium salt (CBX), apyrase (from potato),  $\text{GdCl}_3$ , U73122, and Cremophor EL (Sigma-Aldrich, St. Louis, MO); ionomycin (Calbiochem, San Diego, CA); suramin hexasodium (RBI, Natick, MA); GsMTx-4 (Peptide Institute, Osaka, Japan); diC8-PIP<sub>2</sub> (Echelon Biosciences, Salt Lake City, UT); dispase (Godo Shusei, Tokyo, Japan); Fluo-8 AM (AAT Bioquest, Sunnyvale, CA); Cellmatrix type IA (Nitta Gelatin, Osaka, Japan); Lipofectamine (18324, Invitrogen, Carlsbad, CA); DME/F12 (D9785; Sigma-Aldrich, St. Louis, MO); FBS (12483; Gibco, Carlsbad, CA).

**2.2. The Preparation of Hydrophilic and Stable Hyperforin/HP- $\beta$ -CD.** Solutions of  $4.66 \times 10^{-4}$  M hyperforin (in 1 mL methanol) and  $1.86 \times 10^{-3}$  M HP- $\beta$ -CD (in 1 mL ethanol) were mixed and then stirred for 30 min. The solvents were then removed *in vacuo* with a centrifugal evaporator (0.1 Mpa, 2800 rpm, 90 min, WKN-PV-1200, Wakenyaku, Kyoto, Japan) at ambient temperature. The obtained white solid was dissolved in Milli-Q water by ultrasonication for at least 10 min. The resulting aqueous solution of hyperforin/HP- $\beta$ -CD was syringe-filtered with a 0.20  $\mu\text{m}$  pore size and kept

in a freezer until use. All of the procedures were performed under light-shielded conditions.

Stoichiometry of the reaction between hyperforin and HP- $\beta$ -CD was spectroscopically determined. The concentration of hyperforin in these studies was  $4.66 \times 10^{-4}$  M whereas the HP- $\beta$ -CD concentration was used in the range of 0–8.0 equivalents. The UV spectra of hyperforin were recorded using a UV/VIS scanning spectrophotometer (Gene Spec III, Hitachi Naka Instruments, Hitachinaka, Japan). The changes in the absorbance of hyperforin following the addition of various concentrations of the HP- $\beta$ -CD complexing agent were measured at  $\lambda_{\text{max}} 281 \pm 7$  nm.

**2.3. The Analysis of Irradiated Hyperforin Solution by HPLC.** An irradiation test was performed using a 6-watt LED light bulb (total luminous flux 480 lm, color temperature: 6700 K, Panasonic, Osaka, Japan) that was placed 14 cm above the samples. Irradiation was conducted in a dark room under temperature control (25°C). Aliquots of 40  $\mu\text{L}$  were taken every 30 min for the analysis. All of the quantitative measurements were conducted using a Hitachi LaChrom Elite HPLC system (Hitachi High-Technologies, Tokyo, Japan) equipped with a quaternary pump (L-2130), an autosampler (L-2200), a column oven (L-2300), and a diode array detector (DAD/L-2450). Separation was performed using a TSKgel ODS-100Z reversed phase column (4.6 mm  $\times$  250 mm, 5  $\mu\text{m}$ , Tosho, Tokyo, Japan) with a mobile phase composed of acetonitrile-water-methanol-trifluoroacetic acid (72 : 18 : 10 : 0.5, v/v/v/v). The flow rate was 1.6 mL/min. The UV detector was set at 270 nm. Curve fitting was performed using Excel (MS Office 2013) to minimize the  $R^2$  value.

**2.4. Cell Culture.** HaCaT human keratinocyte cells [19] at passages 36 and 37 were purchased from Cell Lines Services (CLS, Heidelberg, Germany) and were grown in DME/F12 (0.07 mM  $\text{Ca}^{2+}$ ) supplemented with 2% FBS at 37°C in a humidified atmosphere of 5%  $\text{CO}_2$ . The growth medium was prepared from DME/F12 (D9785; Sigma-Aldrich) by adding 0.07 mM  $\text{Ca}^{2+}$ , 365 mg/L L-glutamine, 59.05 mg/L L-leucine, 91.25 mg/L L-lysine-HCl, 61.2 mg/L  $\text{MgCl}_2 \cdot 6\text{H}_2\text{O}$ , 48.84 mg/L  $\text{MgSO}_4$  (anhydrous), 17.2 mg/L L-methionine, and 1.2 g/L  $\text{NaHCO}_3$  and was adjusted to pH 7.4 with 1 mM NaOH. For the experiments, the cells were seeded on a collagen-coated (Cellmatrix type IA) silicone stretch chamber (see the following) or 15 mm round glass coverslips (Matsunami, Osaka, Japan) and cultured in DME/F12 (1.05 mM  $\text{Ca}^{2+}$ ) supplemented with 10% FBS to allow cell attachment. After 1 day, the medium was replaced with DME/F12 (0.07 mM  $\text{Ca}^{2+}$ ) supplemented with 2% FBS, and the cells were further incubated for 1 day to achieve confluence.

The physiological experiments were performed as described previously [2]. A brief explanation follows.

**2.5. Cell Stretch Experiments and Wound Closure Assay.** The cells were cultured in a stretch chamber molded out of Silpot 184 W/C silicone elastomers (Dow Corning Toray, Tokyo, Japan). A chamber with cultured cells was attached to a stretching machine (NS-600W or ST-600W, STREX, Osaka,

Japan) mounted on the stage of an inverted microscope (IX-70, Olympus, Tokyo, Japan) for intracellular  $\text{Ca}^{2+}$  imaging or an upright microscope (BX51WI, Olympus) for extracellular ATP imaging. HaCaT cells were seeded on collagen-coated silicone stretch chambers or 15 mm round glass coverslips at  $3 \times 10^5$  cells/cm<sup>2</sup> and grown to confluence. A narrow cell-free gap (about 250  $\mu\text{m}$ ) was created in a fully confluent monolayer by removing a silicone strip that was attached to the bottom of the stretch chamber during cell seeding. The wound closure process was monitored every 3 h after making the scratch using an inverted microscope (IX-70 Olympus) with a 4x (UPlanFL N, 0.13) objective. The wound closure speed was defined as the percentage of the wound closure area, which was calculated from the ratio of the final migrated area to the initial cell-free area.

**2.6. Intracellular  $\text{Ca}^{2+}$  Measurement and Real-Time Imaging of the Released ATP.** At 3 h after making a scratch, the HaCaT cells in the stretch chamber were loaded with 1  $\mu\text{M}$  Fluo-8 AM using 0.1–0.2% of Cremophor EL (Sigma-Aldrich) for 40–60 min in an incubator at 37°C. After washing away the dye with DME/F12 containing 2.0 mM  $\text{Ca}^{2+}$ , the chamber with the cells was attached to the stretching device on the stage of an inverted microscope with 4x (UPlanFL N, 0.13) or 10x (UPlanFL 0.30) objectives. Time-lapse Fluo-8 fluorescence images were acquired at 0.5 s intervals using MetaMorph software (v6.3 and 7.5, Molecular Devices, Downingtown, PA).

The stretch-induced release of ATP was measured in real-time using the imaging system, as described previously [20]. Briefly, the luciferin-luciferase ATP bioluminescence was detected using a high-sensitivity camera system simultaneously with infrared DIC imaging to monitor exact cell locations and extension during stretching. At 3 h after making a scratch, the cells in the stretching chamber were attached to the stretching device on the stage of an upright microscope (BX51WI, Olympus) with a 4x objective (340 Fluor XL, 0.28) and the medium was replaced with DME/F12 medium (2.0 mM  $\text{Ca}^{2+}$  and 10 mM HEPES, pH 7.4) containing high-sensitivity luciferin-luciferase solution (60315; Lucifer HS Set, Kikkoman Biochemifa, Tokyo, Japan). Images were acquired using the MetaMorph software with a stream acquisition mode (exposure time 100 ms).

**2.7. The Knockdown of TRPC6 by shRNA.** TRPC6 shRNA plasmids that coexpressed RFP (TF308626; OriGene Technologies, Rockville, MD) were used. The shTRPC6 targeting sequence was 59-AAGCAGGACATCTCAAGT-CTCCGCTATGA-39. A scrambled noneffective plasmid with the same nucleotide content was used as a negative control. Each shRNA at a concentration of 45 nM was transfected into HaCaT cells using Lipofectamine reagent, according to the manufacturer's instructions.

**2.8. Ex Vivo Skin Preparation and Live  $\text{Ca}^{2+}$  Imaging of the Epidermis.** Biopsies were taken from the outer forearm of a volunteer with atopic skin. Written informed consent was obtained from the volunteer. The study was approved by the

Pixy Central Institute Ethics Committee, 2009. The sample of skin tissue was placed in PBS prior to treatment with dispase. After overnight digestion with 500 U/mL dispase in serum-free F12/DME with or without hyperforin/HP- $\beta$ -CD at 4°C, the epidermis was peeled off from the dermis with forceps. The detached pieces of epidermis were fixed with intradermal needles on an elastic silicone chamber and were further incubated at 37°C in a humidified 5%  $\text{CO}_2$  atmosphere for 12 h. Epidermis tissue was loaded with 1  $\mu\text{M}$  Fluo-8 AM using 0.2% of Cremophor EL in culture media for 1 h at 37°C. After washing away the dye with DME/F12 containing 2.0 mM  $\text{Ca}^{2+}$ , the chamber containing the cells was attached to a pulse-motor-driven stretching machine (NS-600W or ST-600W, STREX) mounted on the stage of an inverted laser scanning confocal microscope (LSM510 with a 10x lens, Carl Zeiss, Jena, Germany). Time-lapse Fluo-8 fluorescence and Nomarski differential interference contrast images were acquired at 1 s intervals. The  $\text{Ca}^{2+}$  imaging experiments were performed at room temperature ( $24 \pm 2^\circ\text{C}$ ).

### 3. Results

**3.1. Preparation of Stable Hydrophilic Hyperforin Encapsulated in HP- $\beta$ -CD and Its Effect on Wound Closure.** To improve the photostability and aqueous solubility of hyperforin, it was molecularly encapsulated in cyclodextrin. Hyperforin was complexed with hydroxypropyl- $\beta$ -cyclodextrin (HP- $\beta$ -CD) at different molar ratios using the solvent evaporation method. The hyperforin/HP- $\beta$ -CD complexes were investigated with UV/Vis spectroscopy in aqueous solution. The molar ratio method was used to determine the stoichiometry of the inclusion complex formed by hyperforin and HP- $\beta$ -CD.  $\Delta A$ , the difference in the absorbance of hyperforin with and without HP- $\beta$ -CD, was plotted against the molar ratio of HP- $\beta$ -CD to hyperforin at 280 nm (Figure 1(a)). The curve for hyperforin/HP- $\beta$ -CD showed an inflexion point at a ratio of 1 : 4, suggesting that the inclusion complex formed HP- $\beta$ -CD tetracapped hyperforin at hemiterpene terminal moieties (Figure 1(b)). Next, we checked the light stability of a 1 : 4 complex of hyperforin/HP- $\beta$ -CD using HPLC. Figure 1(c) shows the visible light-induced degradation curves of hyperforin and the hyperforin/HP- $\beta$ -CD complex. The apparent half-life of hyperforin was 30 min, while that of the hyperforin/HP- $\beta$ -CD complex was prolonged to 180 min. A curve fitting analysis by single exponential decay with a baseline showed a large baseline (44%) in the curve for hyperforin/HP- $\beta$ -CD, suggesting the existence of a nondegraded (photoprotected) form in the complex (Figure 1(c) fitting line).

We previously demonstrated that the wound closure of keratinocytes was accelerated by stretching and that hyperforin treatment further enhanced the effect [2] (Figure 1(d)). In the present study, we examined the effect of hyperforin/HP- $\beta$ -CD on wound closure. A confluent monolayer of HaCaT cells cultured on silicone membrane was linearly scratched to create a cell-free gap of  $\sim 250 \mu\text{m}$  width, and the wound was allowed to heal under various conditions. Figure 1(d) shows representative wound closing

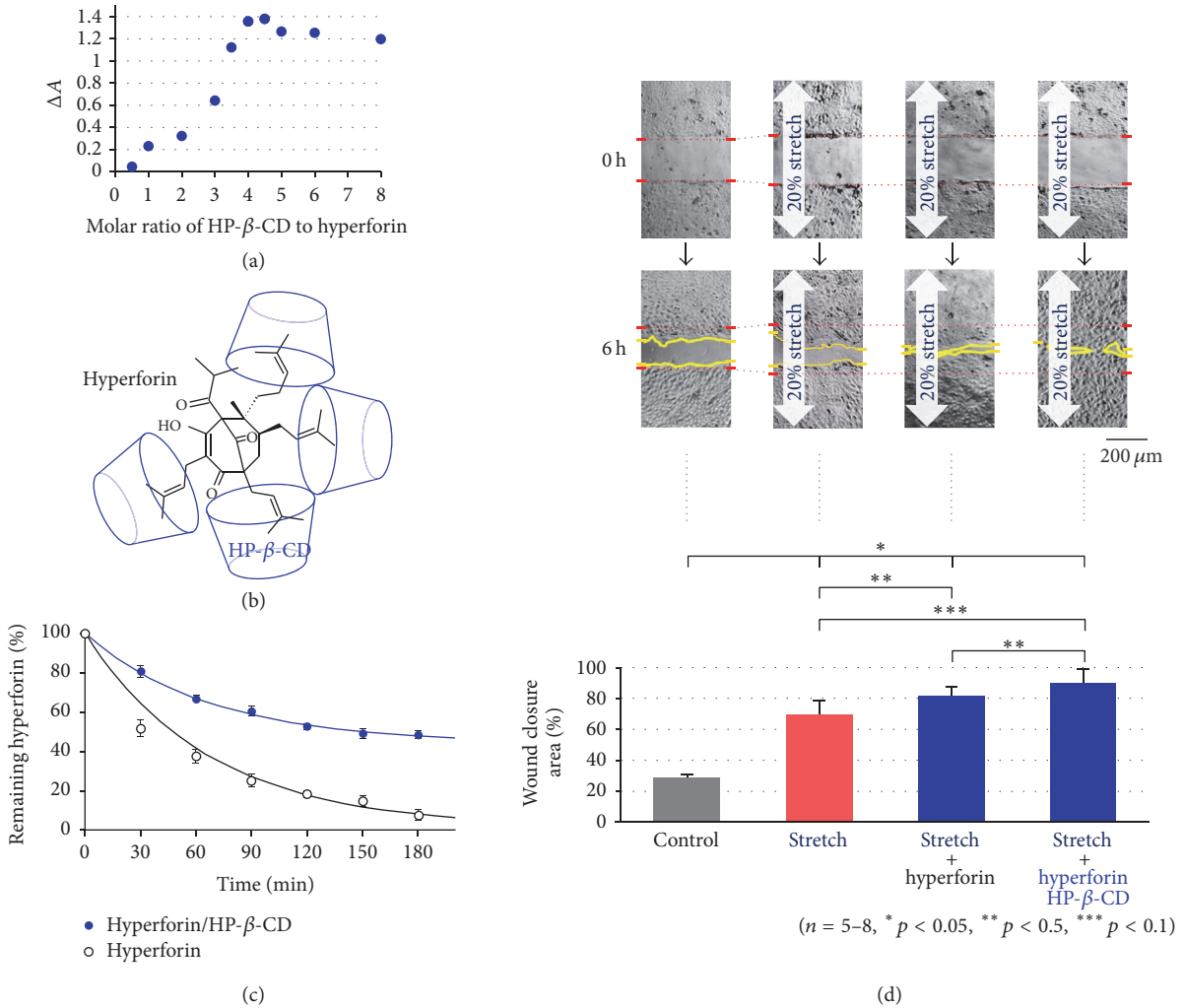


FIGURE 1: The complexation of hyperforin with hydroxypropyl-β-cyclodextrin (HP-β-CD) and its effects on wound closure in HaCaT cells. (a) The molar ratio graph obtained by UV/Vis spectra measurements of the inclusion complex formed by hyperforin ( $4.66 \times 10^{-4}$  M) and HP-β-CD (0–8.0 equivalents) at 25°C. (b) A possible model of the 1:4 complex of hyperforin/HP-β-CD. (c) The photodegradation of hyperforin/HP-β-CD in aqueous solution and hyperforin in methanol induced by LED light exposure. Curve fitting was performed by single exponential decay with a baseline. The baselines obtained for hyperforin/HP-β-CD and hyperforin were 44% and 1.4%, respectively. (d) The effects of hyperforin and hyperforin/HP-β-CD treatments on wound closure in keratinocytes under sustained stretching. Stretch stimulation (20%) facilitated wound closure in HaCaT keratinocytes (stretch). Treatment with hyperforin ( $1 \mu\text{M}$ ) further accelerated the wound closure (stretch + hyperforin) and the wound gap was nearly closed at 6 h after scratching. Hyperforin/HP-β-CD ( $1 \mu\text{M}$  as hyperforin) showed equal or greater efficacy to hyperforin (stretch + hyperforin/HP-β-CD) in promoting wound closure. The data are shown as representative DIC images (upper pictures at 0 h and 6 h) and by the averages of the calculated percentage of the wound closure areas (lower graph). The quantitative data in (c) and (d) are shown as the mean  $\pm$  SEM.

images captured at 0 and 6 h after scratching and the average of the calculated percentage of the wound closure area. A 20% sustained stretch facilitated wound closure in comparison to nonstretched cells (control) and hyperforin ( $1 \mu\text{M}$ ) treatment further enhanced the effect of stretching, as shown previously. Hyperforin/HP-β-CD ( $1 \mu\text{M}$ ) was equally (or more) effective in facilitating wound closure.

**3.2. The Stretch-Induced ATP Release and the Initiation of  $\text{Ca}^{2+}$  Waves from the Leading Cells on the Wound Gap.** It was reported that stretch stimulation induced intercellular  $\text{Ca}^{2+}$  waves in hyperforin-treated HaCaT cells, which were

initiated from the leading cells on the wound edge and that this occurred due to the release of ATP from the leading cells and the activation of TRPC6 on the cells behind the leading edge through the activation of P2Y with the spread ATP [2]. We assessed whether hyperforin/HP-β-CD also has the same effects on HaCaT keratinocytes. At 3 h after making a narrow scar on the confluent monolayer of hyperforin/HP-β-CD-treated cells, stretching (20% for 1 s, perpendicular to the linear gap) induced an increase in the intracellular  $\text{Ca}^{2+}$  in almost all of the leading cells on the wound edge and the  $\text{Ca}^{2+}$  increase propagated towards the rear cells behind the edge in a wave-like pattern

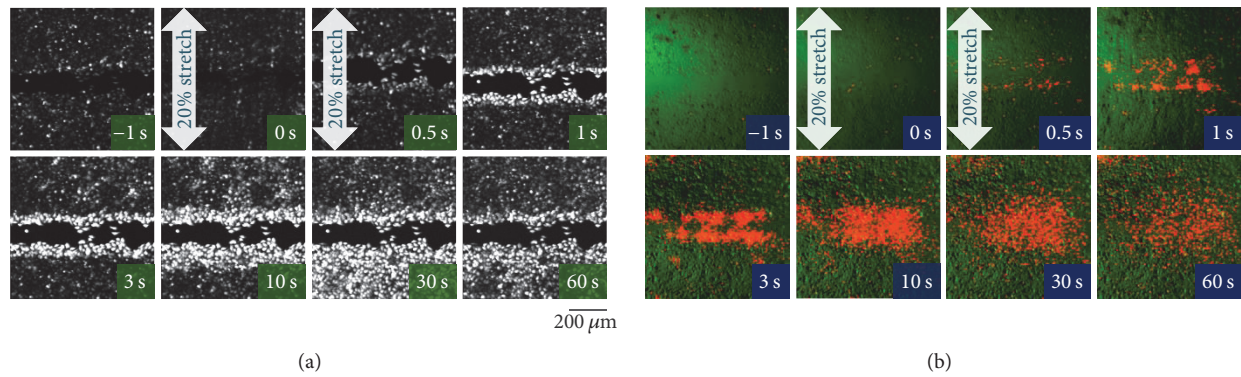


FIGURE 2: Stretch-induced  $\text{Ca}^{2+}$  wave propagation from the wound edge and ATP release from the leading cells. Hyperforin/HP- $\beta$ -CD-treated HaCaT cells at 3 h after scratching were subjected to a single stretch (20% for 1 s), which was applied perpendicular to the linear gap. (a) The intracellular  $\text{Ca}^{2+}$  responses were measured using the  $\text{Ca}^{2+}$  fluorescence indicator, Fluo-8. In response to the stretch, the cells at the leading edge exhibited a remarkably long-lasting increase in intracellular  $\text{Ca}^{2+}$ , and the  $\text{Ca}^{2+}$  increase subsequently propagated to the cells located behind the edge (Movie S1 online). (b) The release of ATP was visualized using a real-time luciferin-luciferase bioluminescence imaging system. Representative overlay images of the ATP-dependent luminescence (red) and infrared DIC images (green) are shown. Following stretching, the release of ATP was only observed in the cells at the leading edge. The released ATP diffused into the entire area and remained at a high concentration for several minutes (Movie S2 online).

(Figure 2(a); Movie S1) (see Supplementary Material available online at <https://doi.org/10.1155/2017/8701801>). The  $\text{Ca}^{2+}$  waves occurred due to the release of ATP from the leading cells and its diffusion to the surrounding cells behind the edge, as shown in Figure 2(b) (Movie S2). The stretch applied parallel to the linear gap had essentially the same effect on ATP- $\text{Ca}^{2+}$  signaling and wound healing in HaCaT cells [2].

One notable advantage of hyperforin/HP- $\beta$ -CD was that the effects on the stretch-induced ATP and  $\text{Ca}^{2+}$  signaling were more reproducible than those obtained simple hyperforin. This may be attributed to the improvement of photostability and the aqueous solubility of hyperforin/HP- $\beta$ -CD.

**3.3. The Pharmacological Analysis of the Stretch-Induced  $\text{Ca}^{2+}$  Responses and Wound Closure in Hyperforin/HP- $\beta$ -CD-Treated Cells.** To analyze the characteristics of the stretch-induced  $\text{Ca}^{2+}$  response, the effects of various inhibitors on the  $\text{Ca}^{2+}$  response were evaluated in hyperforin/HP- $\beta$ -CD-treated HaCaT cells. The time course of the intracellular  $\text{Ca}^{2+}$  response induced by a 20% stretch was measured at different distances (0–240  $\mu\text{m}$ ) from the scar (Figure 3(a), control; hyperforin/HP- $\beta$ -CD-treated cells). At 0  $\mu\text{m}$  (wound edge), the  $\text{Ca}^{2+}$  response was evoked immediately after stretching and it was prolonged by several min. When the distance from the edge was increased, a longer time lag was found before the onset of the activity; however, the amplitudes of the plateau phase were nearly the same. These results were consistent with the idea that  $\text{Ca}^{2+}$  waves caused by the simple diffusion of ATP released from the leading cells at wound edge and the activation of P2Y in the surrounding cells behind the wound edge. When  $\text{Gd}^{3+}$  (10  $\mu\text{M}$ ), an inhibitor of the stretch-activated channel, was applied, the  $\text{Ca}^{2+}$  response in the peak was reduced and the

rate of decay was obviously faster, especially at the distant regions (Figure 3(b)). The  $\text{Ca}^{2+}$  responses were similarly measured under various conditions and inhibitors and were evaluated by the peak response in an averaged trace of the responses at different distances (Figure 3(c)). The suppression observed in  $\text{Ca}^{2+}$ -free medium, in hyperforin/HP- $\beta$ -CD-untreated cells and in shTRPC6-treated cells, suggested the involvement of the influx of  $\text{Ca}^{2+}$  via TRPC6. The inhibition by the treatments with suramin (P2-receptor antagonist, 100  $\mu\text{M}$ ), apyrase (ATP-hydrolyzing enzyme, 20 U/mL), and CBX (hemichannel blocker, 100  $\mu\text{M}$ ) suggested the contribution of ATP signaling in this process. The reduction by each treatment with U73122 (PLC inhibitor, 10  $\mu\text{M}$ ) and diC8-PIP2 (a water-soluble PIP<sub>2</sub> analog that suppresses the activity of PLC by competing with PIP<sub>2</sub>, 10  $\mu\text{M}$ ) suggested that the P2Y receptor-Gq-PLC-DAG-mediated signaling cascade was involved in the activation of TRPC6. These results were the same as those obtained by treatment with hyperforin (nonencapsulate) and stretch stimulation [2]. This suggests the involvement of the release of ATP via hemichannels in the leading cells and that the activation of P2Y in the cells behind the wound edge prolonged the influx of  $\text{Ca}^{2+}$  via TRPC6 through the Gq-PLC-DAG cascade.

To confirm whether hyperforin/HP- $\beta$ -CD facilitates wound closure by amplifying ATP- $\text{Ca}^{2+}$  signaling, we assessed the effects of the various inhibitors that were used above on the wound closure during sustained stretching. The wound gap was almost closed at approximately 6 h (Figure 3(d), control) after scratching, while treatment with  $\text{Ca}^{2+}$  depletion (nominally  $\text{Ca}^{2+}$ -free), CBX (100  $\mu\text{M}$ ), apyrase (20 U/mL), suramin (100  $\mu\text{M}$ ),  $\text{Gd}^{3+}$  (10  $\mu\text{M}$ ), GsMTx-4 (5  $\mu\text{M}$ ), and shTRPC6 treatment delayed wound closure (Figure 3(d)). This suggested that the wound closure process required ATP- $\text{Ca}^{2+}$  signaling, especially the influx of  $\text{Ca}^{2+}$  through TRPC6.

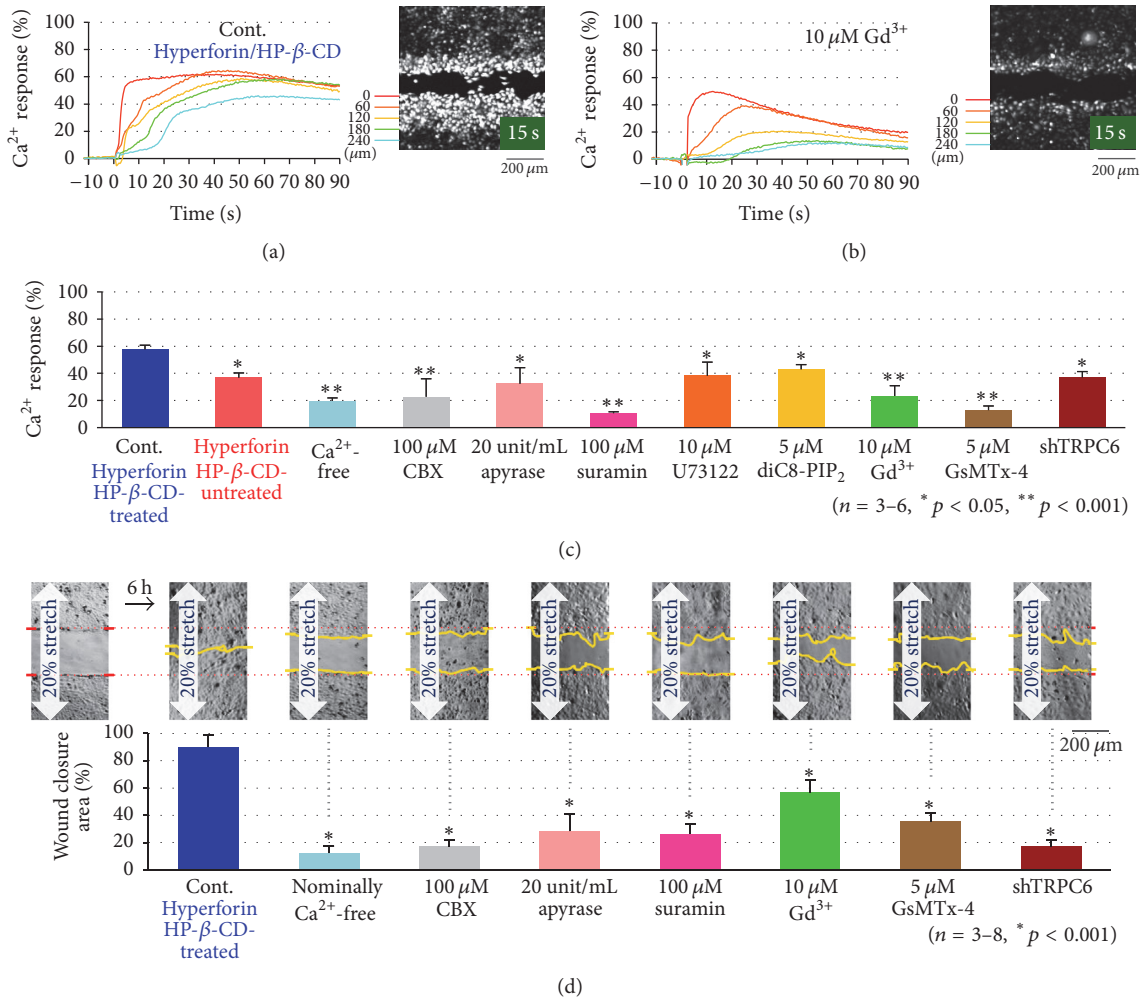


**FIGURE 3:** The effects of various inhibitors on the stretch-induced  $\text{Ca}^{2+}$  responses and wound closure. (a) The time course of changes in the fluorescence intensity of Fluo-8 due to a transient 20% stretch in hyperforin/HP- $\beta$ -CD-treated HaCaT cells (control). Each color trace indicated the data at different distances of 0, 60, 120, 180, and 240 from the wound edge (inset image). The intensity was normalized to the peak value obtained with ionomycin treatment at the end of each experiment. (b) The effects of  $\text{Gd}^{3+}$  on the stretch-induced  $\text{Ca}^{2+}$  response as a typical example of the blocking effects of the inhibitors.  $\text{Gd}^{3+}$  ( $10 \mu\text{M}$ ) was applied at 10 min before the application of a 20% stretch. (c) The effects of various inhibitors on 20% transient stretch-induced  $\text{Ca}^{2+}$  responses in hyperforin/HP- $\beta$ -CD-treated HaCaT cells. The intensity traces at each distance from the wound edge were averaged and normalized to the peak intensity obtained with ionomycin treatment. The data show the average of the peak values obtained in 3-6 separate experiments. Various inhibitors, including CBX ( $100 \mu\text{M}$ ), apyrase (20 Unit/mL), suramin ( $100 \mu\text{M}$ ), U73122 ( $10 \mu\text{M}$ ), diC8-PIP<sub>2</sub> ( $5 \mu\text{M}$ ),  $\text{Gd}^{3+}$  ( $10 \mu\text{M}$ ), and GsMTx-4 ( $5 \mu\text{M}$ ), were applied at 10 min before the stretch stimulation. A  $\text{Ca}^{2+}$ -free condition was achieved by changing the medium to  $\text{Ca}^{2+}$ -free medium that contained  $0.5 \mu\text{M}$  EGTA. All of the quantitative data are shown as the mean ( $\pm$ SEM). (d) The effects of various inhibitors on the stretch facilitated wound closure in hyperforin/HP- $\beta$ -CD-treated HaCaT cells. Confluent cell cultures were scratched and allowed to migrate for 6 h under a sustained 20% stretch in a medium that contained various inhibitors, including CBX ( $100 \mu\text{M}$ ), apyrase (20 Unit/mL), suramin ( $100 \mu\text{M}$ ),  $\text{Gd}^{3+}$  ( $10 \mu\text{M}$ ), and GsMTx-4 ( $5 \mu\text{M}$ ) or in nominally  $\text{Ca}^{2+}$ -free medium. shTRPC6 was applied to the cells for 3 h; the cells were then grown to confluence. Representative DIC images (upper panel) and the means of 3-8 wound closure experiments at 6 h after scratching (lower panel) are shown. All of the quantitative data are shown as the mean ( $\pm$ SEM).

**3.4. The Effects of Hyperforin/HP- $\beta$ -CD Treatment on the  $\text{Ca}^{2+}$  Responses in the Ex Vivo Skin of Atopic Dermatitis.** Next, we assessed the effects of hyperforin/HP- $\beta$ -CD treatment and stretch mechanical stimulation on an ex vivo epidermis of atopic dermatitis. The epidermis, which was detached from the dermis after overnight treatment with dispase, was loaded with Fluo-8AM and observed with a laser confocal

microscope. Normal skin exhibited frequent spontaneous  $\text{Ca}^{2+}$  oscillations and a large  $\text{Ca}^{2+}$  response to stretch stimulation (1 s single) and subsequent  $\text{Ca}^{2+}$  waves with the long-lasting elevation of  $\text{Ca}^{2+}$  (Figure 4(a), Movie S3). In contrast, the epidermis of atopic dermatitis showed few oscillations and only a small response to stretching without any waves (Figure 4(b), Movie S4). In contrast, atopic skin

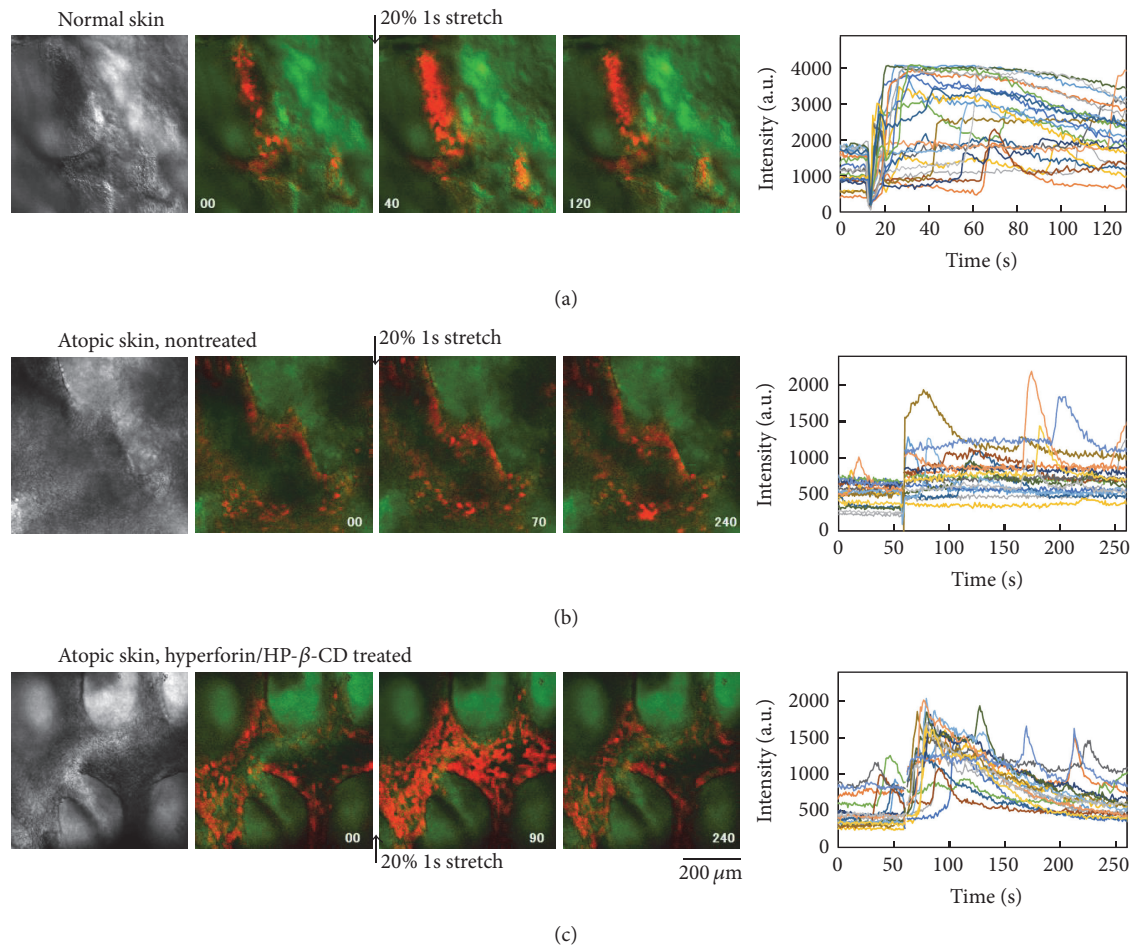


FIGURE 4: The effects of hyperforin/HP- $\beta$ -CD treatment on the Ca<sup>2+</sup> dynamics in the epidermis of atopic skin ex vivo. The epidermis was detached from the dermis by dispase treatment and fixed on a stretch chamber with intradermal needles. The fluorescence of the Ca<sup>2+</sup> indicator, Fluo-8AM, was observed with a laser confocal microscope (left image panels) and the changes in intensity in several cells were plotted in the right panels. (a) The Ca<sup>2+</sup> oscillation and the Ca<sup>2+</sup> response to stretch stimulation (20%, 1s, transient) in the epidermis of normal skin ex vivo. Frequent Ca<sup>2+</sup> oscillation and a large Ca<sup>2+</sup> response to stretching and subsequent Ca<sup>2+</sup> waves were prominent (see also Movie S3). (b) In the atopic epidermis, little Ca<sup>2+</sup> oscillation and a very weak Ca<sup>2+</sup> response to stretching were observed (see also Movie S4). (c) The 24 h treatment of atopic skin with hyperforin/HP- $\beta$ -CD drastically induced autonomous Ca<sup>2+</sup> oscillation and led to a transient, long-lasting Ca<sup>2+</sup> increase induced by stretching (see also Movie S5).

that had been treated with hyperforin/HP- $\beta$ -CD for 24 h exhibited autonomous Ca<sup>2+</sup> oscillation, and a transient long-lasting increase in Ca<sup>2+</sup> and more frequent Ca<sup>2+</sup> oscillations following stretch stimulation (Figure 4(c), Movie S5). The application of hyperforin/HP- $\beta$ -CD-treatment to atopic skin for 24 h led to the recovery of the mechanosensitive ATP-Ca<sup>2+</sup> signaling, which was dysfunctional in the untreated atopic epidermis.

#### 4. Discussion

The topical application of hyperforin, which is a traditional folk remedy, has anti-inflammatory, antioxidative, antibacterial, antinociceptive, and wound healing effects. Recently, accumulating evidence indicates that hyperforin facilitates the keratinocyte differentiation caused by the uptake of

Ca<sup>2+</sup> through TRPC6 [11]. Our previous studies showed that hyperforin-treated HaCaT keratinocytes could accelerate wound closure in conjunction with exogenous and endogenous mechanical stretching through the facilitation of the ATP-Ca<sup>2+</sup> signaling cascade [2]. The impact of hyperforin on mechanosensitivity remains unclear, but hyperforin certainly amplifies ATP-Ca<sup>2+</sup> signaling and facilitates reepithelialization during wound healing. However, due to the photostability of hyperforin, daylight initiates its facile oxidative degradation [21]. Prenyl side chains (hemiterpene moieties) containing conjugated double bonds are generally prone to oxidation. In order to enhance the stability of hyperforin and exert its topical therapeutic potential, hyperforin was encapsulated by forming a supramolecular complexation with HP- $\beta$ -CD. The solubility of HP- $\beta$ -CD is highest in ethanol as well as water among the CD compounds,  $\alpha$ -CD,  $\beta$ -CD,

methylated- $\beta$ -CD, sulfoethyl ethyl- $\beta$ -CD,  $\gamma$ -CD, and HP- $\beta$ -CD. This amphipathic property was a major advantage when making the inclusion complex with hydrophobic hyperforin. The molar ratio method indicated that the optimal ratio of the hyperforin/HP- $\beta$ -CD complex was 1:4. This meant the formation of HP- $\beta$ -CD-tetracapped hyperforin, where the hyperforin was encapped with HP- $\beta$ -CD at each hemiterpene moiety [22] as shown in Figure 1(b). The novel inclusion complex showed obvious photostability in comparison to hyperforin (Figure 1(c)). The curve fitting of the decay time course of hyperforin/HP- $\beta$ -CD indicated the existence of a large nondecayed component that corresponded to photostable hyperforin. This modification can contribute to both pharmaceutical application and topical medication.

We assessed the effects of hyperforin/HP- $\beta$ -CD on wound healing and ATP- $\text{Ca}^{2+}$  signaling in keratinocytes. Hyperforin/HP- $\beta$ -CD enhanced the acceleration of wound closure by stretching with a similar efficiency to hyperforin (Figure 1(d)). In hyperforin/HP- $\beta$ -CD-treated keratinocytes, stretching induced a conspicuous increase in the  $\text{Ca}^{2+}$  levels in the leading cells facing the wound edge and the  $\text{Ca}^{2+}$  waves slowly propagated to the cells behind the wound edge (Figure 2(a)). These propagating  $\text{Ca}^{2+}$  waves were entirely due to the release of ATP from the leading cells (Figure 2(b)). The pathway of ATP release was CBX sensitive (Figure 3(c)) and presumably pannexin hemichannels from our previous study [2]. The migrating cells at the wound edge represented morphological changes that were similar to those observed at the epithelial-to-mesenchymal transition and might be more susceptible to endogenous and exogenous mechanical stress [2, 23]. The increase in  $\text{Ca}^{2+}$  in the cells behind the wound edge was dependent on the influx of  $\text{Ca}^{2+}$  via the TRPC6 channels, which were activated by the activation of P2Y through the Gq-PLC-DAG-mediated signaling cascade (Figure 3(c)) [2] and lasted for a relatively long period. The concentration and duration of the  $\text{Ca}^{2+}$  increase were dependent on the distance from the wound edge, making a  $\text{Ca}^{2+}$  gradient from the leading cells to the following cells. This  $\text{Ca}^{2+}$  gradient may be essential for organized wound healing, including cell migration, molecular relocation, and gene expression. The cell traction of the cells located behind the edge by migrating leading cells is also an important mechanical cue for wound healing that is controlled by  $\text{Ca}^{2+}$  dependent cell-cell interaction molecules such as E-cadherin. This  $\text{Ca}^{2+}$  signaling is enhanced by treatment with hyperforin/HP- $\beta$ -CD.

Interestingly, the reagents that blocked the increase in  $\text{Ca}^{2+}$  also suppressed the acceleration of wound closure in response to stretching in hyperforin/HP- $\beta$ -CD-treated cells (Figure 3(d)). Thus, the hyperforin/HP- $\beta$ -CD complex shows a similar efficiency to hyperforin in inducing mechanosensitive ATP- $\text{Ca}^{2+}$  signaling and wound closure in keratinocytes. In fact, hyperforin/HP- $\beta$ -CD seems to be superior due to the reproducibility of the data concerning stretch-induced ATP and  $\text{Ca}^{2+}$  signaling, which may be attributed to the photostability and aqueous solubility of hyperforin/HP- $\beta$ -CD.

In our experimental design, HaCaT keratinocytes were cultured under low extracellular  $\text{Ca}^{2+}$  conditions (0.07 mM), which mimicked the extracellular  $\text{Ca}^{2+}$  environment for barrier-perturbed epidermis, such as the environment that would result from skin stripping or the use of surfactants. Atopic dermatitis is also a skin barrier dysfunction. Topical medication of hyperforin-rich St. John's wort cream has been shown to be effective in patients with atopic dermatitis [10–14]. The analysis of the laser scanning microscopy images has shown that the hyperforin-rich cream reduces the skin surface dryness and improves the moisture level of the stratum corneum [14]. However, the mechanism underlying the improvement of symptoms in atopic skin remains unclear. Our present study is the first to demonstrate how the  $\text{Ca}^{2+}$  dynamics of atopic skin behave under mechanical environments such as wound healing and reepithelialization. We observed the  $\text{Ca}^{2+}$  dynamics induced by the stretching of epidermis *ex vivo* using a confocal microscope (Figure 4). In atopic epidermis, there was a remarkable decrease in the  $\text{Ca}^{2+}$  responses and oscillations induced by stretching (Figure 4(b)). Treatment with hyperforin/HP- $\beta$ -CD for 24 h restored the  $\text{Ca}^{2+}$  responses and oscillations, even in atopic skin (Figure 4(c)). These results suggest that the pathogenesis of atopic dermatitis is related to ATP- $\text{Ca}^{2+}$  signaling and that hyperforin/HP- $\beta$ -CD may have therapeutic application in the treatment of atopic dermatitis.

## 5. Conclusions

Cutaneous wound healing is accelerated by mechanical stress both exogenously and endogenously, and treatment with hyperforin enhances the acceleration through the facilitation of ATP- $\text{Ca}^{2+}$  signaling in keratinocytes. We succeeded in making HP- $\beta$ -CD-tetracapped hyperforin (hyperforin/HP- $\beta$ -CD), which possessed increased aqueous solubility and improved photoprotection. Treatment with hyperforin/HP- $\beta$ -CD enhanced the mechanically induced ATP- $\text{Ca}^{2+}$  signaling and accelerated wound closure in HaCaT keratinocytes with equal (or greater) efficacy to hyperforin. We also applied hyperforin/HP- $\beta$ -CD on atopic skin *ex vivo* and found that hyperforin/HP- $\beta$ -CD treatment for 24 h improved the stretch-induced  $\text{Ca}^{2+}$  responses and oscillations, which reduced in atopic skin. The data suggest that hyperforin/HP- $\beta$ -CD is a potent targeted therapeutic agent that can be used to promote epidermal wound healing and to treat atopic dermatitis.

## Competing Interests

The authors declare that there is no conflict of interests regarding the publication of this paper.

## Acknowledgments

The authors thank K. Uekama (Professor Emeritus, Kumamoto University) for his kind help in characterizing the hyperforin/HP- $\beta$ -CD complex. This work was supported by funds from the Japan Society for the Promotion of Science

(JSPS) Institutional Program for Young Researcher Overseas Visits (to Hiroya Takada); by a Medical Research Grant of Kyousaidan (to Hiroya Takada); by JSPS KAKENHI Grant nos. JP24590274 and JP15K09174 (to Kishio Furuya).

## References

- [1] T. Tanaka, K. Naruse, and M. Sokabe, "Effects of mechanical stresses on the migrating behavior of endothelial cells," in *Biomechanics at Micro- and Nanoscale Levels*, H. Wada, Ed., vol. 1, pp. 75–87, World Scientific, Singapore, 2005.
- [2] H. Takada, K. Furuya, and M. Sokabe, "Mechanosensitive ATP release from hemichannels and Ca<sup>2+</sup> influx through TRPC6 accelerate wound closure in keratinocytes," *Journal of Cell Science*, vol. 127, no. 19, pp. 4159–4171, 2014.
- [3] J. Davis, A. R. Burr, G. F. Davis, L. Birnbaumer, and J. D. Molkentin, "A TRPC6-dependent pathway for myofibroblast transdifferentiation and wound healing in vivo," *Developmental Cell*, vol. 23, no. 4, pp. 705–715, 2012.
- [4] S. Samadi, T. Khadivzadeh, A. Emami, N. S. Moosavi, M. Tafaghodi, and H. R. Behnam, "The effect of hypericum perforatum on the wound healing and scar of cesarean," *Journal of Alternative and Complementary Medicine*, vol. 16, no. 1, pp. 113–117, 2010.
- [5] Z. Saddiqe, I. Naeem, and A. Maimoona, "A review of the antibacterial activity of *Hypericum perforatum* L.," *Journal of Ethnopharmacology*, vol. 131, no. 3, pp. 511–521, 2010.
- [6] I. Süntar, E. K. Akkol, H. Keleş, A. Oktem, K. H. C. Başer, and E. Yeşilada, "A novel wound healing ointment: a formulation of *Hypericum perforatum* oil and sage and oregano essential oils based on traditional Turkish knowledge," *Journal of Ethnopharmacology*, vol. 134, no. 1, pp. 89–96, 2011.
- [7] M. Dikmen, Y. Öztürk, G. Sagratini, M. Ricciutelli, S. Vittori, and F. Maggi, "Evaluation of the wound healing potentials of two subspecies of *hypericum perforatum* on cultured NIH3T3 fibroblasts," *Phytotherapy Research*, vol. 25, no. 2, pp. 208–214, 2011.
- [8] U. Wölflle, G. Seelinger, and C. M. Schempp, "Topical application of St. John's Wort (*Hypericum perforatum*)," *Planta Medica*, vol. 80, no. 2-3, pp. 109–120, 2014.
- [9] M. Marrelli, G. Statti, F. Conforti, and F. Menichini, "New potential pharmaceutical applications of hypericum species," *Mini-Reviews in Medicinal Chemistry*, vol. 16, no. 9, pp. 710–720, 2016.
- [10] C. M. Schempp, T. Windeck, S. Hezel, and J. C. Simon, "Topical treatment of atopic dermatitis with St. John's wort cream—a randomized, placebo controlled, double blind half-side comparison," *Phytomedicine*, vol. 10, no. 4, pp. 31–37, 2003.
- [11] M. Müller, K. Essin, K. Hill et al., "Specific TRPC6 channel activation, a novel approach to stimulate keratinocyte differentiation," *Journal of Biological Chemistry*, vol. 283, no. 49, pp. 33942–33954, 2008.
- [12] S. Arndt, S. F. Haag, A. Kleemann, J. Lademann, and M. C. Meinke, "Radical protection in the visible and infrared by a hyperforin-rich cream—in vivo versus ex vivo methods," *Experimental Dermatology*, vol. 22, no. 5, pp. 354–357, 2013.
- [13] U. Wölflle, G. Seelinger, and C. M. Schempp, "Topical application of St. John's wort (*Hypericum perforatum*)," *Planta Medica*, vol. 80, no. 2-3, pp. 109–120, 2014.
- [14] M. C. Meinke, H. Richter, A. Kleemann et al., "Characterization of atopic skin and the effect of a hyperforin-rich cream by laser scanning microscopy," *Journal of Biomedical Optics*, vol. 20, no. 5, Article ID 051013, 2015.
- [15] H. C. J. Orth and P. C. Schmidt, "Stability and stabilization of hyperforin," *Pharmazeutische Industrie*, vol. 62, no. 1, pp. 60–63, 2000.
- [16] B. Isacchi, N. Galeotti, M. C. Bergonzi, C. Ghelardini, A. R. Bilia, and F. F. Vincieri, "Pharmacological in vivo test to evaluate the bioavailability of some St John's wort innovative oral preparations," *Phytotherapy Research*, vol. 23, no. 2, pp. 197–205, 2009.
- [17] J. Hatanaka, Y. Shinme, K. Kuriyama et al., "In vitro and in vivo characterization of new formulations of st. john's wort extract with improved pharmacokinetics and anti-nociceptive effect," *Drug Metabolism and Pharmacokinetics*, vol. 26, no. 6, pp. 551–558, 2011.
- [18] M. J. Cork, S. G. Danby, Y. Vasilopoulos et al., "Epidermal barrier dysfunction in atopic dermatitis," *Journal of Investigative Dermatology*, vol. 129, no. 8, pp. 1892–1908, 2009.
- [19] P. Boukamp, R. T. Petrussevska, D. Breitkreutz, J. Hornung, A. Markham, and N. E. Fusenig, "Normal keratinization in a spontaneously immortalized aneuploid human keratinocyte cell line," *Journal of Cell Biology*, vol. 106, no. 3, pp. 761–771, 1988.
- [20] K. Furuya, M. Sokabe, and R. Grygorczyk, "Real-time luminescence imaging of cellular ATP release," *Methods*, vol. 66, no. 2, pp. 330–344, 2014.
- [21] C. Y. W. Ang, L. Hu, T. M. Heinze et al., "Instability of St. John's wort (*Hypericum perforatum* L.) and degradation of hyperforin in aqueous solutions and functional beverage," *Journal of Agricultural and Food Chemistry*, vol. 52, no. 20, pp. 6156–6164, 2004.
- [22] I. Clarot, D. Clédât, S. Battu, and P. J. P. Cardot, "Chromatographic study of terpene derivatives on porous graphitic carbon stationary phase with  $\beta$ -cyclodextrin as mobile phase modifier," *Journal of Chromatography A*, vol. 903, no. 1-2, pp. 67–76, 2000.
- [23] N. D. Evans, R. O. C. Oreffo, E. Healy, P. J. Thurner, and Y. H. Man, "Epithelial mechanobiology, skin wound healing, and the stem cell niche," *Journal of the Mechanical Behavior of Biomedical Materials*, vol. 28, pp. 397–409, 2013.

## Research Article

# Substrate Stiffness Influences Doxorubicin-Induced p53 Activation via ROCK2 Expression

**Takahiro Ebata,<sup>1</sup> Yasumasa Mitsui,<sup>1</sup> Wataru Sugimoto,<sup>1</sup> Miho Maeda,<sup>1</sup> Keigo Araki,<sup>2</sup> Hiroaki Machiyama,<sup>3,4</sup> Ichiro Harada,<sup>5</sup> Yasuhiro Sawada,<sup>6</sup> Hideaki Fujita,<sup>3,4</sup> Hiroaki Hirata,<sup>7</sup> and Keiko Kawauchi<sup>1,8</sup>**

<sup>1</sup>Frontiers of Innovative Research in Science and Technology, Konan University, 7-1-20 Minatojima-Minamimachi, Chuo-ku, Kobe, Hyogo 650-0047, Japan

<sup>2</sup>Department of Bioscience, School of Science and Technology, Kwansai Gakuin University, 2-1 Gakuen, Sanda, Hyogo 669-1337, Japan

<sup>3</sup>Laboratory for Comprehensive Bioimaging, Riken Qbic, 6-2-3 Furuedai, Suita, Osaka 565-0874, Japan

<sup>4</sup>WPI, Immunology Frontier Research Center, Osaka University, 1-3 Yamadaoka, Suita, Osaka 565-0871, Japan

<sup>5</sup>Laboratory for Mechanical Medicine, Nadogaya Research Institute, Nadogaya Hospital, 687-4 Kashiwa, Chiba 277-0032, Japan

<sup>6</sup>Department of Rehabilitation for the Movement Functions, Research Institute, National Rehabilitation Center for Persons with Disabilities 4-1 Namiki, Tokorozawa, Saitama 359-8555, Japan

<sup>7</sup>Nagoya University Graduate School of Medicine, 65 Tsurumai, Showa-ku, Nagoya, Aichi 466-8550, Japan

<sup>8</sup>Department of Molecular Oncology, Institute for Advanced Medical Sciences, Nippon Medical School, 1-396 Kosugi-cho, Nakahara-ku, Kawasaki, Kanagawa 211-8533, Japan

Correspondence should be addressed to Keiko Kawauchi; [kawauchi@center.konan-u.ac.jp](mailto:kawauchi@center.konan-u.ac.jp)

Received 30 July 2016; Revised 3 December 2016; Accepted 12 December 2016; Published 16 January 2017

Academic Editor: Esmail Jabbari

Copyright © 2017 Takahiro Ebata et al. This is an open access article distributed under the Creative Commons Attribution License, which permits unrestricted use, distribution, and reproduction in any medium, provided the original work is properly cited.

The physical properties of the extracellular matrix (ECM), such as stiffness, are involved in the determination of the characteristics of cancer cells, including chemotherapy sensitivity. Resistance to chemotherapy is often linked to dysfunction of tumor suppressor p53; however, it remains elusive whether the ECM microenvironment interferes with p53 activation in cancer cells. Here, we show that, in MCF-7 breast cancer cells, extracellular stiffness influences p53 activation induced by the antitumor drug doxorubicin. Cell growth inhibition by doxorubicin was increased in response to ECM rigidity in a p53-dependent manner. The expression of Rho-associated coiled coil-containing protein kinase (ROCK) 2, which induces the activation of myosin II, was significantly higher when cells were cultured on stiffer ECM substrates. Knockdown of ROCK2 expression or pharmacological inhibition of ROCK decreased doxorubicin-induced p53 activation. Our results suggest that a soft ECM causes downregulation of ROCK2 expression, which drives resistance to chemotherapy by repressing p53 activation.

## 1. Introduction

One of the major causes of resistance to cancer therapies, such as chemotherapy and radiation, is dysfunction of p53 [1–3]. Under low stress conditions, the expression of p53 is maintained at a low level due to Mdm-2-mediated degradation [4]. In response to DNA damage caused by genotoxic drugs, PI3 kinase-like kinase family members (ATM, ATR, and DNA-PK) are activated and then phosphorylate p53 [5, 6]. Subsequently, they phosphorylate and stabilize p53 by attenuating its dissociation from Mdm2-mediated degradation [7]. p53

then induces cell cycle arrest and apoptosis by inducing the expression of various target genes, including  $p21^{WAF1}$ , NOXA, and PIG6, leading to growth inhibition of damaged cells [8]. p53 dysfunction is frequently caused by mutation(s) in TP53 encoding p53 [9].

Accumulating evidence has shown that extracellular matrix (ECM) stiffness, a tumor microenvironment factor, contributes to chemotherapy sensitivity [10]. Stiffness of the ECM secreted by stroma cells, such as cancer-associated fibroblasts and myofibroblasts, is increased in most solid

tumors [11, 12]. For example, mammary gland tumors, whose elastic modulus is approximately 1–4 kPa, are stiffer than healthy mammary glands (<1 kPa). Notably, stiffer tumors are associated with a higher aggressiveness of cancer cells [11, 13, 14]. However, it remains elusive whether ECM stiffness modulates p53 function and chemotherapy sensitivity in cancer cells.

Cells sense ECM stiffness at integrin-mediated cell-ECM adhesion structures termed focal adhesions (FAs) [15]. The rigidity of the ECM modulates the recruitment and phosphorylation of FA proteins, leading to actin polymerization via the activation of Rho GTPases, including Rho, Rac, and Cdc42 [16]. Rho also activates ROCK, which induces the activation of the actin-based motor protein myosin and increases the generation of actin-myosin contractile forces [11].

Treatment with the genotoxic drug doxorubicin typically induces remodeling of actin cytoskeleton architecture; however, its effects appear somewhat controversial [17–21]. In mouse embryonic fibroblasts, doxorubicin impairs the formation of contractile actomyosin bundles, that is, stress fibers, but induces the formation of cortical actomyosin rings [19, 20]. Conversely, other studies have reported that the formation of stress fibers is promoted by doxorubicin prior to the onset of apoptosis in several cell lines, including MCF-7 cells [17, 21]. While the formation of stress fibers as well as FAs is impaired in suspended cells, the efficacy of doxorubicin to induce apoptosis is increased in these cells [17, 18], suggesting that the formation of stress fibers and FAs may help to protect cells from apoptosis. In addition, it has also been reported that, in mouse embryonic fibroblasts, the formation of filopodia, which are thin finger-like cell protrusions generated by actin polymerization, is diminished upon doxorubicin treatment [22]. Since filopodia protrusions promote the survival of disseminated carcinoma cells [23], the doxorubicin-induced attenuation of filopodia formation may contribute to the low viability of doxorubicin-treated cells.

In this study, we examined whether matrix stiffness affects the doxorubicin-induced growth inhibition of MCF-7 breast cancer cells expressing wild-type p53. We found that doxorubicin treatment reduced cell viability to a larger extent on a stiff substrate (30 kPa) than on a soft one (2 kPa) and that this stiffness-dependent decrease in the viability of doxorubicin-treated cells required p53 activation. ROCK2 expression was increased in response to ECM rigidity, and ROCK2 knockdown diminished doxorubicin-induced p53 activation. The ectopic expression of p53 prevented doxorubicin-induced filopodia formation in cells cultured on soft substrates. Our findings suggest that the upregulation of ROCK2-mediated actomyosin contractility on a stiff ECM confers the chemotherapy response of cancer cells via the substantial activation of p53.

## 2. Materials and Methods

**2.1. Cell Culture.** MCF-7 human breast cancer cells and 293T human embryonic kidney cells obtained from the American

Type Culture Collection were cultured in Dulbecco's modified Eagle's medium (Nissui Pharmaceutical) supplemented with 10% fetal bovine serum and 1% penicillin/streptomycin. N-Acryloyl-6-aminocaproic acid- (ACA-) copolymerized acrylamide gels for polyacrylamide culture substrates were prepared as described previously [24, 25]. The cells were seeded on the substrates at  $2.2 \times 10^5$  cells/cm<sup>2</sup> and treated with doxorubicin (DOXO; 1  $\mu$ g/mL) after incubation for 24 h.

**2.2. MTT Assay.** Cell growth was assessed by an MTT assay according to the manufacturer's instructions (Dojindo, Inc.).

**2.3. Retroviral Vectors and Retroviral Infection.** To generate retroviruses encoding small hairpin RNAs (shRNAs) against human p53 and human ROCK2, the p53 target sequence [26] 5'-GACTCCAGTGGTAATCTAC-3' and ROCK2 target sequence [27] 5'-GGTTTATGCTATGAAGCTT-3' were cloned into the pSuper retro puro vector (Oligoengine). Retroviral infection was performed as described previously [28]. Briefly, the retrovirus vector encoding shRNA was cotransfected with the pAmpho plasmid into 293T cells using the HilyMax transfection reagent (Dojindo). At 48 h after transfection, the supernatant was collected and then used to infect MCF-7 cells in the presence of 8  $\mu$ g/mL Polybrene. Infected cells were selected using puromycin (1.5  $\mu$ g/mL) for 3 days.

**2.4. Antibodies and Materials.** Anti-p53 mouse monoclonal (DO-1; Santa Cruz Biotechnology), anti-HDAC1 mouse monoclonal (2E10; Merck Millipore), anti- $\alpha$ -tubulin mouse monoclonal (DM1A; Sigma-Aldrich), anti-p21 rabbit monoclonal (EPR3993; Abcam), and anti-Lamin B1 rabbit polyclonal (Abcam) antibodies were used for immunoblot analyses. Anti-pMLC2 (Ser19) rabbit polyclonal (Cell Signaling Technology) and anti-HA mouse monoclonal (16B12; Covance) antibodies were used for immunofluorescence analyses. Doxorubicin and Y-27632 were purchased from Merck Millipore.

**2.5. Quantitative Real-Time PCR.** Quantitative real-time PCR analysis was performed as described previously [29]. The following primers were used: human p21<sup>waf1</sup> forward 5'-GGCTTCATGCCAGCTACTTC-3' and reverse 5'-CCCTAGGCTGTGCTCACTTC-3'; human NOXA forward 5'-AGCTGGAAGTCGAGTGTGCT-3' and reverse 5'-ACGTGCACCTCCTGAGAAAA-3'; human PIG6 forward 5'-TTTTTCACCCACACTTGCAGA-3' and reverse 5'-TGTCCCAGGCAGGTATCAGGTT-3'; human ROCK2 forward 5'-CAACTGTGAGGCTTGTATGAAG-3' and reverse 5'-TGCAAGGTGCTATAATCTCCTC-3'; and human ubiquitin forward 5'-TGACTACAACATCCAGAA-3' and reverse 5'-ATCTTTGCCTTGACATTC-3' [24].

**2.6. Immunoblot Analysis.** MCF-7 cells were solubilized with the lysis buffer (50 mM Tris pH 7.4, 150 mM NaCl, 1% Triton X-100, 1% SDS, 10 mM EDTA, 1 mM Na<sub>3</sub>VO<sub>4</sub>, 10 mM NaF, and protease inhibitor cocktail [PIC; Nacalai Tesque]) and then centrifuged at 20,000  $\times$ g for 20 min after sonication. The

supernatants were used as total cell extracts and subjected to sodium dodecyl sulfate-polyacrylamide gel electrophoresis (SDS-PAGE). For fractionation of nuclear and cytosol extracts, the cells were solubilized in buffer A (10 mM HEPES pH 7.2, 10 mM KCl, 0.1 mM EDTA, 0.1 mM EGTA, 0.4% NP-40, and PIC) and then centrifuged at  $10,000 \times g$  for 10 min after incubation on ice for 5 min. The supernatants were used as cytosol extracts. The pellets were washed with buffer A and subsequently resuspended in buffer B (20 mM HEPES pH 7.9, 400 mM NaCl, 1 mM EDTA, 1 mM EGTA, and PIC) in a vortex mixer for 10 min. The supernatants obtained after centrifugation at  $20,000 \times g$  for 15 min were used as nuclear extracts. The extracts were subjected to SDS-PAGE. To obtain the Triton X-100 soluble and insoluble fractionations, the cells were solubilized with the lysis buffer (50 mM Tris pH 7.4, 150 mM NaCl, 1% Triton X-100, 10 mM EDTA, 1 mM  $\text{Na}_3\text{VO}_4$ , 10 mM NaF, and PIC) and then at  $20,000 \times g$  for 15 min after incubation on ice for 15 min. The supernatants were used as Triton X soluble fractions. The pellets were resuspended in the SDS sample buffer after washing with the buffer and subsequently sonicated. The lysates were used as Triton X insoluble fractions. The extracts were subjected to SDS-PAGE.

**2.7. Fluorescence Microscopy.** To immunostain for MLC2 phosphorylated at Ser19, the cells were fixed with 10% formaldehyde in phosphate-buffered saline (PBS) supplemented with 0.1 M HEPES pH 7.4 and then permeabilized with 0.2% Triton X-100. After blocking with 5% goat serum in PBS, the cells were incubated with the anti-pMLC2 (Ser19) antibody. Alexa Fluor 633-conjugated goat anti-rabbit IgG (Molecular Probes) was used as a secondary antibody. Alexa Fluor 488 phalloidin (Molecular Probes) and DAPI (Vector Laboratories) were used to stain F-actin and nuclei, respectively. To visualize p53 and F-actin simultaneously in single cells within spheroids, cells cultured overnight on the 2 kPa substrate were transfected with the Lifeact-GFP expression vector (a gift from Roland Wedlich-Söldner, University of Munster, Munster, Germany [30]) together with the control or HA-tagged p53 expression vector. After 24 h, the cells were treated with doxorubicin for 16 h. The cells were fixed with 10% formaldehyde in PBS containing 0.1 M HEPES pH 7.4. Doxorubicin incorporated into the cells was visualized using its autofluorescence (e.g., ex: 488 nm/em: >580 nm [31]). Images were acquired using a confocal microscope (LSM700; Zeiss) and then analyzed with ImageJ software (NIH).

**2.8. Statistical Analysis.** Statistical analysis of data was performed using the unpaired Student's two-sided *t*-test.

### 3. Results and Discussion

We cultured MCF-7 cells on gelatin-coated ACA gels with elasticities of 2 kPa and 30 kPa as well as on plastic dishes (elastic modulus  $\sim 10^6$  kPa). The cells on the 2 kPa substrate aggregated and formed spheroid structures (Figure 1(a)).

Conversely, the cells cultured on the 30 kPa substrate exhibited flat and spread morphologies, although they were flatter and more spread out when cultured on plastic dishes. While activation of integrin signaling in response to a rigid ECM can prevent antitumor drug-induced cell death [32], spheroid formation, which is typically observed on a soft ECM (Figure 1(a)), also reportedly makes cancer cells resistant to antitumor drugs [33, 34]. Given these apparently opposing results, we examined how the inhibitory effect of doxorubicin on cell growth was influenced by ECM stiffness using trypan blue exclusion-based cell staining. When the cells were cultured on the 2 kPa substrate, doxorubicin treatment reduced the relative number of viable cells by  $\sim 35\%$  (Figure 1(b)). Conversely, when the cells were cultured on the 30 kPa substrate, the relative number of viable cells was reduced further (by  $\sim 54\%$ ) upon doxorubicin treatment. We further investigated the effect of ECM stiffness on cell proliferation in the presence or absence of doxorubicin using an MTT assay. The number of cells cultured on the 30 kPa substrate was significantly more than that cultured on the 2 kPa substrate (see Figure S1 in Supplementary Material available online at <https://doi.org/10.1155/2017/5158961>), indicating that substrate stiffening promotes cell proliferation. By contrast, the number of doxorubicin-treated cells cultured on the 30 kPa substrate was similar to that cultured on the 2 kPa substrate. The doxorubicin-induced attenuation of cell proliferation was also more significant on the 30 kPa substrate than on the 2 kPa substrate.

While MCF-7 cells cultured on the soft substrate form spheroids (Figure 1(a)), spheroid formation provides hypoxic microenvironments and attenuates drug penetration [33, 34]. These effects associated with spheroid formation potentially contribute to the chemotherapeutic resistance of cancer cells, in which downregulation of p53 activation is reportedly involved [33]. However, the following results suggest that downregulation of p53 activation on the soft substrate is unlikely to be caused by spheroid-associated hypoxia or limited drug penetration in our system. First, although hypoxia typically occurs in tissue located at a distance of  $100\text{--}150 \mu\text{m}$  from blood vessels [35], the width of spheroids formed in our experimental condition was much smaller ( $40 \pm 10 \mu\text{m}$  in radius,  $n = 214$ ). Second, the concentration of penetrated doxorubicin was not apparently different between the central region and outer edge of the spheroids (Figures 1(c) and 1(d)).

We next investigated the contribution of p53 to the ECM stiffness-dependent regulation of cellular morphology and doxorubicin-induced cell growth inhibition. MCF-7 cells with shRNA-mediated depletion of p53 expression (Figure 1(e)) were spread out on the 30 kPa and plastic substrates but formed spheroids on the 2 kPa substrate, albeit these spheroids had irregular shapes compared with those of control cells (Figure 1(a)). This suggests that the p53-depleted cells retain the ability to sense differences in substrate elasticity. However, the rigidity-dependency of the doxorubicin-induced reduction of cell viability (Figure 1(b)) and cell proliferation (Fig. S1) was abrogated upon p53 knockdown.

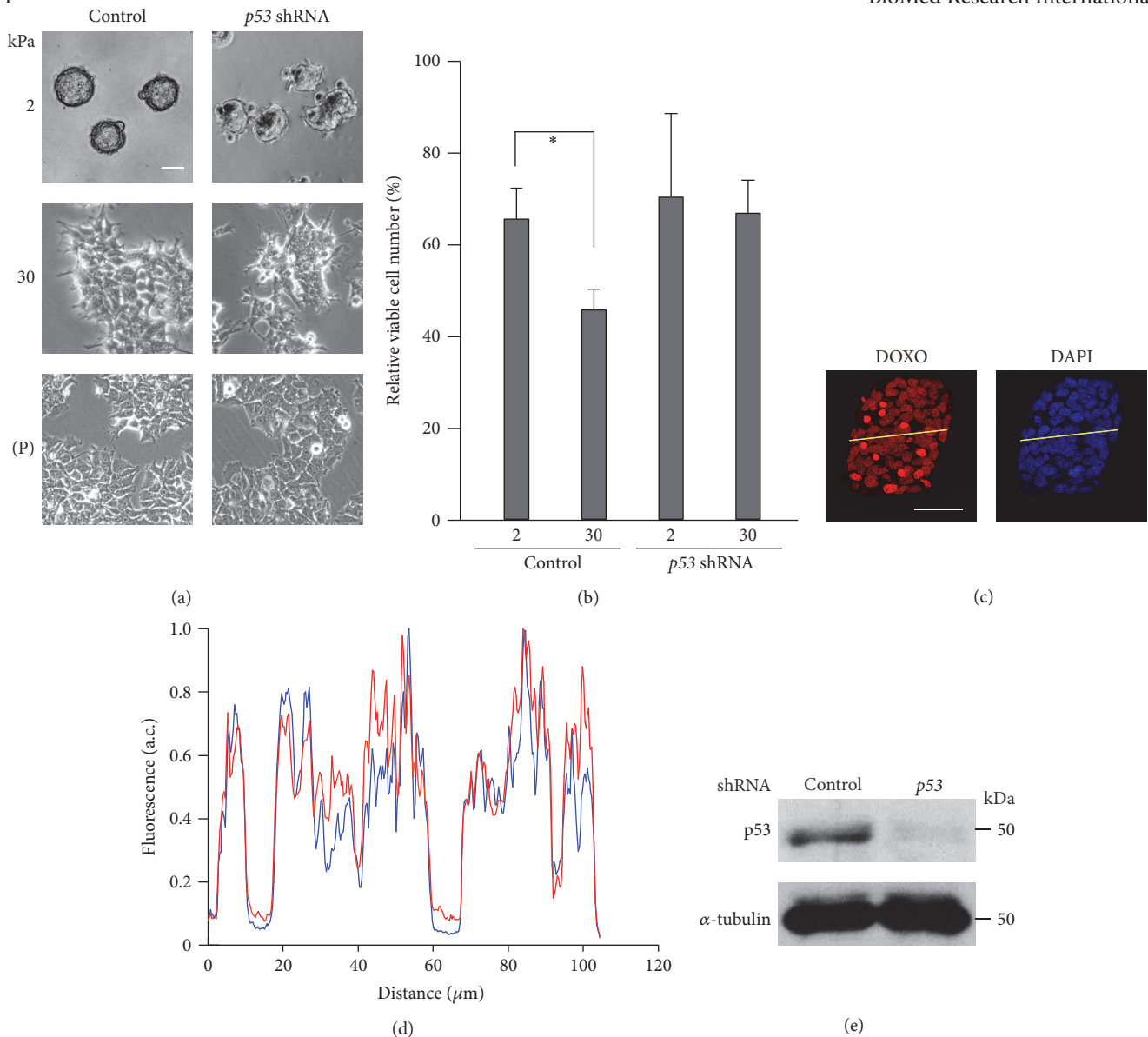


**FIGURE 1:** Rigid substrates enhance the inhibitory effect of doxorubicin on cell growth in a p53-dependent manner. (a-b) MCF-7 cells infected with a control or *p53* shRNA-expressing retrovirus were cultured on substrates with elasticities of 2 and 30 kPa or on plates (P;  $\sim 10^6$  kPa). (a) Phase contrast images of the cells were obtained with an inverted microscope (Olympus CKX41). Scale bar, 50  $\mu\text{m}$ . (b) The cells were treated with doxorubicin (DOXO; 1  $\mu\text{g}/\text{mL}$ ) for 24 h, and the number of viable cells was counted using trypan blue exclusion-based cell staining. In each condition, the number of doxorubicin-treated cells was normalized to that of nontreated cells. Each bar represents the mean  $\pm$  standard deviation (SD);  $n = 4$ . Asterisks,  $p < 0.05$ . (c-d) Accumulation of doxorubicin into cells cultured on a substrate with an elasticity of 2 kPa was evaluated. (c) Doxorubicin incorporated into cells was visualized using its autofluorescence. Z-stack images with an interval of 1.0  $\mu\text{m}$  were obtained using a confocal microscope. Projected images for doxorubicin (red) and nuclei (DAPI) are shown. Scale bar, 50  $\mu\text{m}$ . (d) The fluorescence intensity of the yellow line drawn across the spheroid was plotted. Intensity values were normalized with respect to the maximum value in each profile. (e) Extracts from control and *p53* shRNA-expressing cells cultured on plates were subjected to immunoblot analysis with antibodies against p53 and  $\alpha$ -tubulin as a loading control.

To dissect whether p53 activation was involved in the ECM rigidity-dependent modulation of doxorubicin-induced cell growth inhibition, we examined p53 transcriptional activity by evaluating the expression of its well-known target genes, *p21<sup>Waf1</sup>*, which encodes a cyclin-dependent kinase inhibitor, and *NOXA* and *PIG6*, whose products induce apoptosis by activating caspases [8]. The expression of *p21<sup>Waf1</sup>* was drastically increased by doxorubicin treatment

in a p53-dependent manner, and its doxorubicin-induced expression was significantly higher on the 30 kPa substrate than on the 2 kPa substrate (Figures 2(a) and 2(b)). We observed similar effects of substrate stiffness and p53 on the gene expression of *NOXA* and *PIG6*. Consistent with the increased gene expression of these apoptosis-inducing factors (Figure 2(a)), cleavage of the caspase substrate Lamin B1 [36–40] was also increased by doxorubicin treatment in a

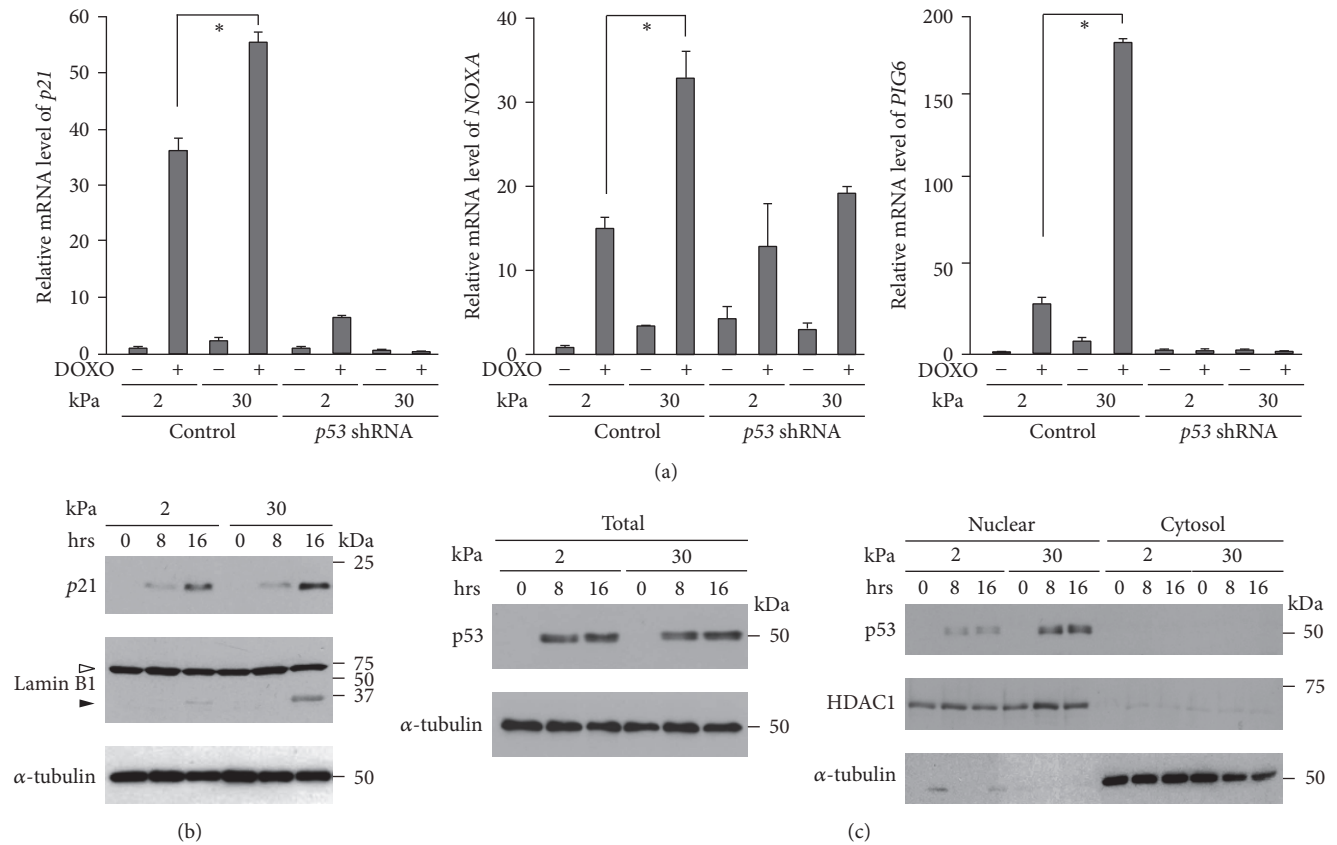


FIGURE 2: Soft substrates diminish doxorubicin-induced p53 activation. (a–c) Cells infected with a control or *p53* shRNA-expressing retrovirus were cultured on substrates with elasticities of 2 and 30 kPa. (a) The expression of *p21<sup>Waf1</sup>*, *NOXA*, and *PIG6* in cells cultured in the presence or absence of DOXO (1  $\mu$ g/mL) for 24 h was evaluated by quantitative real-time PCR. Each bar represents the mean  $\pm$  SD;  $n = 3$ . Asterisks,  $p < 0.01$ . (b–c) Control and *p53* shRNA-expressing cells were treated with DOXO for the indicated time periods. (b) Total cell lysates were subjected to immunoblot analysis with antibodies against p21, Lamin B1, and  $\alpha$ -tubulin as a loading control. The white arrowhead indicates full-length Lamin B1, while the black arrowhead indicates a cleaved fragment. (c) Total cell extracts, nuclear extracts, and cytosol extracts were subjected to immunoblot analysis with antibodies against p53, HDAC1 as a nuclear marker, and  $\alpha$ -tubulin as a loading control or cytosol marker.

substrate rigidity-dependent manner (Figure 2(b)). Thus, a stiff ECM has a promoting effect on doxorubicin-induced p53 activation, which would underlie the observation that cell growth inhibition following doxorubicin treatment is enhanced on a stiff ECM in a p53-dependent manner (Figure 1(b)).

We next examined whether p53 protein levels following doxorubicin treatment were influenced by ECM stiffness. The expression of p53 increased upon doxorubicin treatment, which was not affected by substrate rigidity (Figure 2(c) left). Conversely, the amount of p53 in the nuclear fraction was larger when the cells were cultured on the stiffer substrate (Figure 2(c) right). By contrast, the amount of p53 in the Triton X-100 insoluble cytoskeleton fraction [41] of doxorubicin-treated cells was lower on the 30 kPa substrate than on the 2 kPa substrate (Fig. S2). These results suggest that a soft ECM attenuates the nuclear accumulation of p53 through the interaction of p53 with the cytoskeleton.

Stiff substrates have been shown to increase actomyosin contraction [11, 42, 43]. We have also shown that the expression of the actomyosin activator ROCK2 is downregulated

in fibroblasts when the cells are cultured on soft (<4 kPa) substrates [44]. Consistent with these previous reports, phosphorylation of myosin light chain (MLC), a critical step in the activation of nonmuscle myosin, was higher in cells cultured on stiffer substrates (Figure 3(a)). Since it has been reported that the doxorubicin-induced stabilization and concomitant nuclear accumulation of p53 are suppressed by the myosin II ATPase inhibitor blebbistatin or the ROCK inhibitor Y-27632 in keratinocytes [45], we asked whether rigidity-dependent ROCK2 expression and concomitant actomyosin activation were involved in the enhanced activation of p53 on the stiff substrate. Consistent with the case of fibroblasts [44], *ROCK2* expression in MCF-7 cells was significantly higher on the 30 kPa substrate than on the 2 kPa substrate (Figure 3(b)). While doxorubicin treatment induced the accumulation of p53 in nuclei (Figure 2(b)), both ROCK inhibition (Figure 3(c)) and ROCK2 knockdown (Figures 3(d) and 3(e)) diminished the doxorubicin-induced nuclear accumulation of p53. Concomitantly, the expression of the p53 target gene *p21<sup>Waf1</sup>*, which was induced upon doxorubicin treatment, was largely decreased by ROCK2 knockdown (Figure 3(f)). Taken

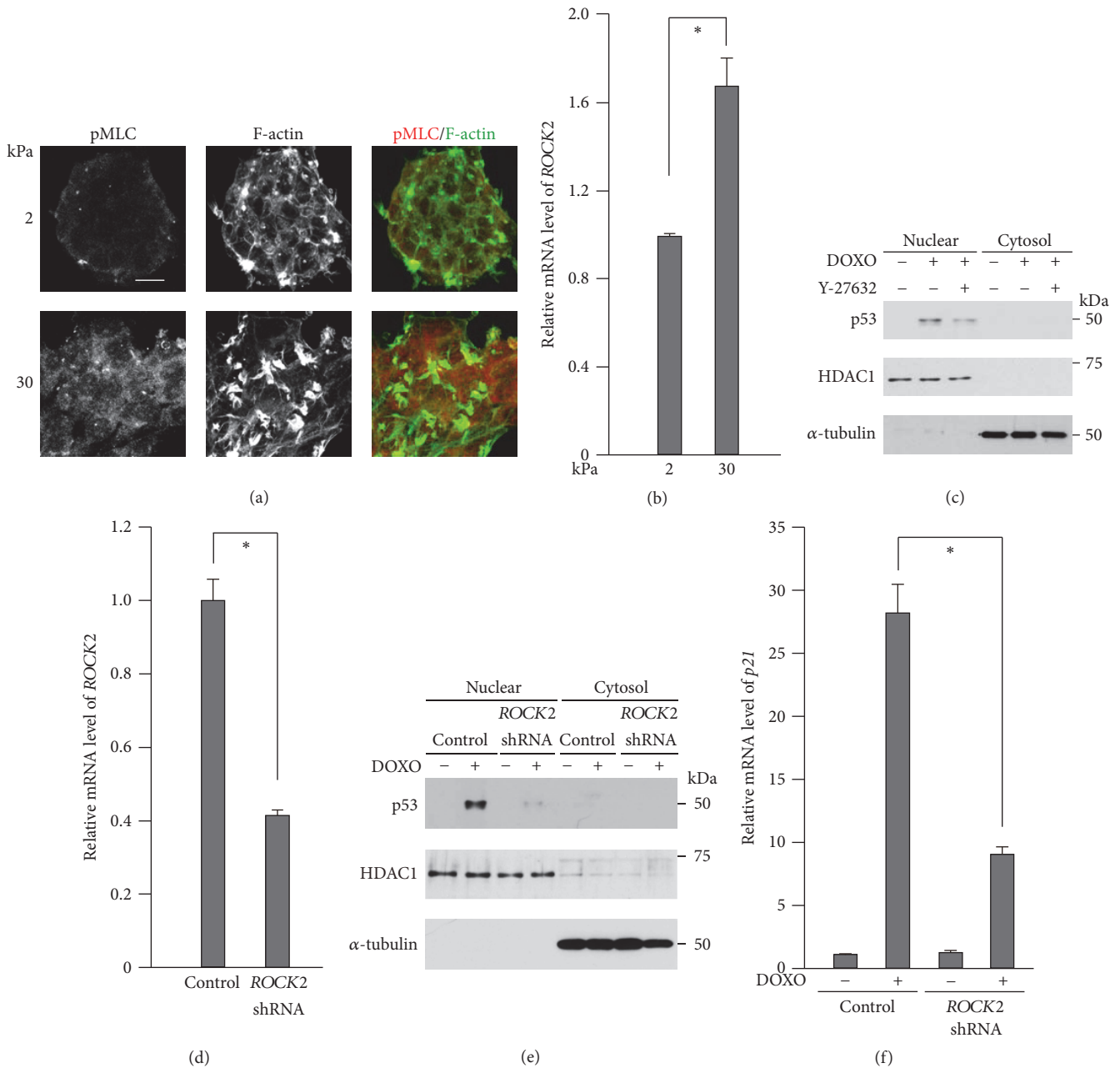


FIGURE 3: ROCK2 is involved in doxorubicin-induced p53 activation. (a) Cells were cultured on substrates with elasticities of 2 and 30 kPa. Confocal images of cells stained for phosphorylated MLC (pMLC2; red) and F-actin (green). Scale bars, 20  $\mu\text{m}$ . Z-stack images with an interval of 1.0  $\mu\text{m}$  were obtained using a confocal microscope, and projected images are shown. (b) ROCK2 expression in cells cultured on substrates with elasticities of 2 and 30 kPa was evaluated by quantitative real-time PCR. Each bar represents the mean  $\pm$  SD;  $n = 3$ . Asterisks,  $p < 0.02$ . (c) Nuclear extracts and cytosol extracts from cells cultured in the presence or absence of DOXO (1  $\mu\text{g}/\text{mL}$ ) and/or Y-27632 (10  $\mu\text{M}$ ) for 16 h were subjected to immunoblot analysis with antibodies against p53, HDAC1 as a nuclear marker, and  $\alpha$ -tubulin as a cytosol marker. (d–f) The cells were infected with a control or ROCK2 shRNA-expressing retrovirus. (d) ROCK2 expression was evaluated as in (b). (e) Nuclear extracts and cytosol extracts from cells cultured in the presence or absence of DOXO for 16 h were subjected to immunoblot analysis with antibodies against p53, HDAC1 as a nuclear marker, and  $\alpha$ -tubulin as a loading control or cytosol marker. (f) p21<sup>Waf1</sup> expression in cells cultured in the presence or absence of DOXO for 24 h was evaluated by quantitative real-time PCR. Each bar represents the mean  $\pm$  SD;  $n = 3$ . Asterisks,  $p < 0.01$ .

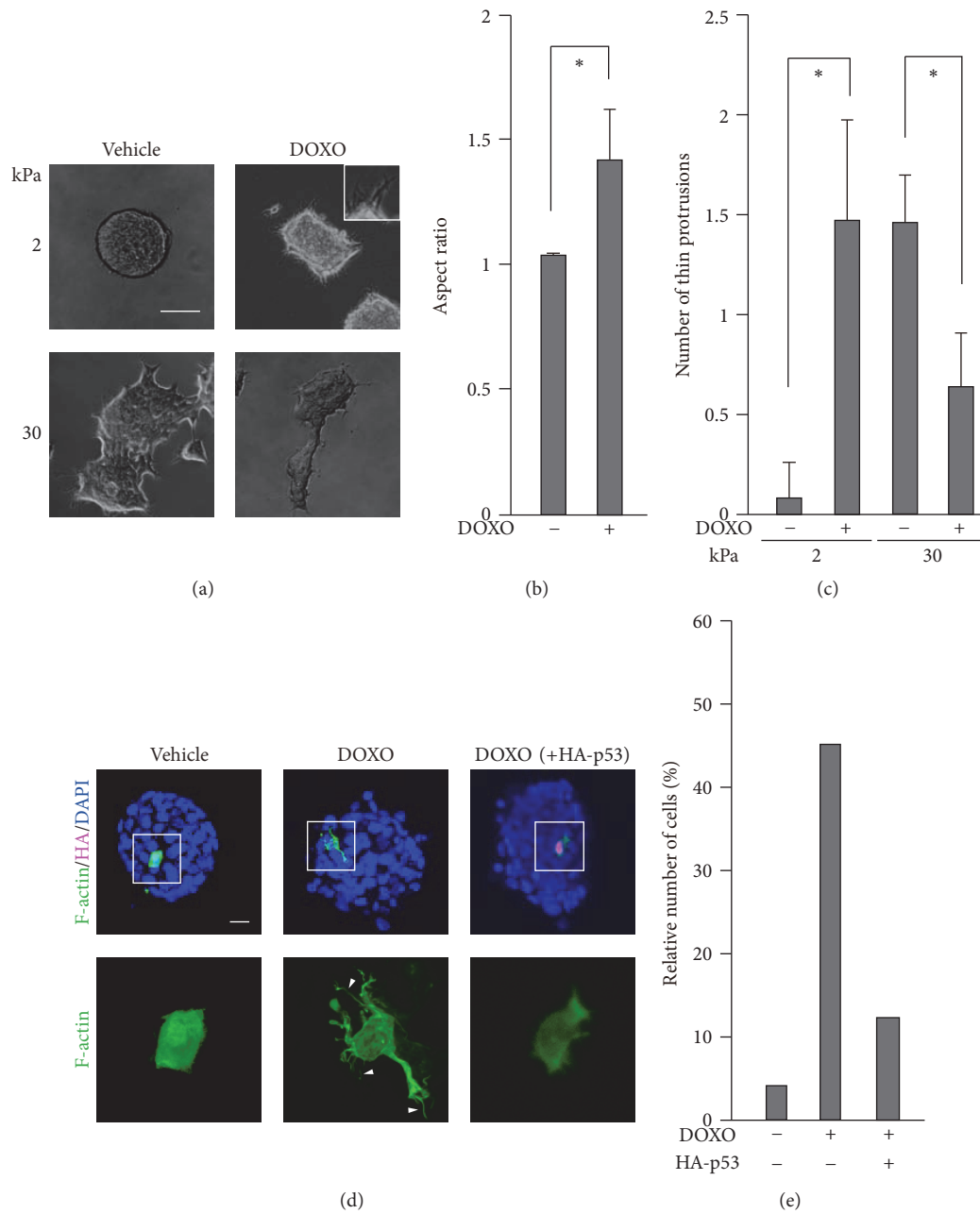


FIGURE 4: Doxorubicin treatment induces protrusion formation in cells cultured on soft substrates. (a, d) Cells cultured on substrates with elasticities of 2 kPa (a, d) and 30 kPa (d) were treated with or without DOXO (1  $\mu\text{g}/\text{mL}$ ) for 16 h. (a) Phase contrast images of the cells were obtained with an inverted microscope. Scale bar, 100  $\mu\text{m}$ . (b) The aspect ratio of spheroids cultured on 2 kPa was calculated from the major length to the minor length of an ellipse that fitted each spheroid using ImageJ software. Each bar represents the mean  $\pm$  SD;  $n = 10$ . Asterisks,  $p < 0.01$ . (c) The number of thin protrusions ( $\geq 20 \mu\text{m}$ ) along the periphery of a cell cluster was quantified using ImageJ software. Data indicate the number of protrusions per 100  $\mu\text{m}$  of the periphery of a cell cluster. Each bar represents the mean  $\pm$  SD;  $n = 5$ . Asterisks,  $p < 0.01$ . (d) The cells were transfected with the Lifeact-GFP expression vector to label F-actin together with the HA-tagged p53 expression vector before treatment with DOXO. Confocal images of F-actin (green), HA (magenta), and nuclei (DAPI; blue) are shown. Z-stack images with an interval of 1.0  $\mu\text{m}$  were obtained using a confocal microscope, and projected images are shown. Magnified images of F-actin in the boxed regions are also shown. Scale bar, 20  $\mu\text{m}$ . The white arrowheads indicate filopodia-like protrusions ( $\geq 10 \mu\text{m}$ ). (e) The relative number of cells, which have more than three filopodia-like protrusions ( $\geq 10 \mu\text{m}$ ), to total cell number ( $n = 24$ ), is shown.

together, these results suggest that the substrate stiffness-dependent increase in the expression and activity of ROCK2 contributes to p53 activation.

The ROCK family consists of ROCK1 and ROCK2. Both isoforms have redundant functions and are implicated in MLC2 phosphorylation upon doxorubicin treatment [19, 20]. While we have shown here that ROCK2 activity potentiates the doxorubicin-induced activation of p53, previous studies have suggested that p53 activation can, in turn, lead to the enhanced activation of ROCK1. While ROCK1 is constitutively activated during apoptosis upon its cleavage by caspase-3 and caspase-7 [46], p53 activates these caspases [47]. Therefore, ROCKs and p53 potentially form a positive feedback loop in cells undergoing apoptosis. This positive feedback mechanism would accelerate cell depletion upon doxorubicin treatment, and ECM rigidity may affect the efficacy of doxorubicin on cell depletion by modulating this feedback mechanism. However, the actual mechanism by which ROCK regulates p53 activity remains unclear. Since p53 shuttles dynamically between the nucleus and cytoplasm [48], ROCK may modulate the import/export of p53 into/from the nucleus to regulate the nuclear localization of p53, which needs to be examined in future studies.

p53 alters cell behavior through remodeling of the actin cytoskeleton [49], and actin remodeling is involved in the determination of cell fate upon doxorubicin treatment [17, 19–22, 50]. While actin remodeling plays a central role in the morphological changes of cells [51], we noticed that the spheroids that formed on the 2 kPa substrate spread out with thin protrusions after treatment with doxorubicin (Figures 4(a)–4(c)). By contrast, cell clusters on the 30 kPa substrate became less spread out upon doxorubicin treatment, which accompanied a decrease in the formation of thin protrusions (Figures 4(a) and 4(c)). We then examined how doxorubicin modulated the actin cytoskeleton to induce protrusion formation in cells cultured on the 2 kPa substrate. Doxorubicin treatment caused the formation of long filopodia-like protrusions in cells residing in spheroids (Figures 4(d) and 4(e)). Importantly, while p53 activity was relatively low on the 2 kPa substrate compared with the stiffer substrate (Figure 2), the ectopic expression of p53 in cells on the 2 kPa substrate abrogated the doxorubicin-induced formation of protrusions (Figures 4(d) and 4(e)). This inhibitory effect of p53 on protrusion formation is consistent with the previously reported functions of p53; p53 decreases the activity of Cdc42, a small GTPase that promotes the formation of filopodia, as well as the expression of fascin, a major actin-bundling protein in filopodia [22, 52, 53]. Considering that filopodia protrusions promote cell survival [23], our results imply that the reduced activity of p53 in spheroids may make cells resistant to chemotherapy by promoting protrusion formation.

The stemness of cancer cells is a contributing factor to the metastasis, recurrence, and chemotherapy resistance of cancers [54–57]. p53 reduces stemness by repressing the expression of various stem cell markers and by activating the DNA excision repair pathway [49, 58]. Conversely, ROCK inhibition and soft substrates promote the self-renewal of stem cells and reprogramming of fibroblasts into stem cells

[50–54]. Given these previous results, downregulation of the ROCK-p53 axis on soft substrates, which we have revealed in this study, may contribute to the production of cancer stem cells.

#### 4. Conclusions

Our study provides novel insights into the mechanism underlying the environment-mediated drug resistance of breast cancer cells. Stiffer substrates make breast cancer cells more susceptible to doxorubicin treatment in a p53-dependent manner. It is of note that while advanced cancer cells are associated with stiffer tumors [9, 11, 12], they typically bear somatic mutations of *TP53* at a high rate [9]. Therefore, due to p53 dysfunction by its mutation, advanced cancer cells may exhibit chemotherapeutic resistance even in rigid tumors. Conversely, cancer cells at early stages, in which the *TP53* gene does not typically suffer severe mutations, reside in relatively soft environments that may reduce the inhibitory effect of genotoxic drugs on cell growth. Treatment of early stage cancer cells with genotoxic drugs combined with a drug or physical method that increases extracellular stiffness and/or myosin II activity may provide an effective approach for cancer therapy.

#### Competing Interests

The authors declare that there is no conflict of interests regarding the publication of this paper.

#### Acknowledgments

The authors thank Dr. Roland Wedlich-Söldne for the Lifeact-GFP expression vector and Drs. Koji Nagahama, Takahito Nishikata, Junji Kawakami, Shota Yamauchi, Kiyonao Sada, and Mr. Toshiya Kotari for discussion. This work was supported by Astellas Pharma Inc., Japan, Hyogo Science and Technology Association, and Naito Foundation.

#### References

- [1] M. Weller, "Predicting response to cancer chemotherapy: the role of p53," *Cell and Tissue Research*, vol. 292, no. 3, pp. 435–445, 1998.
- [2] J. S. Fridman and S. W. Lowe, "Control of apoptosis by p53," *Oncogene*, vol. 22, no. 56, pp. 9030–9040, 2003.
- [3] W. A. Freed-Pastor and C. Prives, "Mutant p53: one name, many proteins," *Genes and Development*, vol. 26, no. 12, pp. 1268–1286, 2012.
- [4] K. H. Vousden and X. Lu, "Live or let die: the cell's response to p53," *Nature Reviews Cancer*, vol. 2, no. 8, pp. 594–604, 2002.
- [5] E. Appella and C. W. Anderson, "Post-translational modifications and activation of p53 by genotoxic stresses," *European Journal of Biochemistry*, vol. 268, no. 10, pp. 2764–2772, 2001.
- [6] B. Gu and W.-G. Zhu, "Surf the post-translational modification network of p53 regulation," *International Journal of Biological Sciences*, vol. 8, no. 5, pp. 672–684, 2012.

- [7] Y. Haupt, R. Maya, A. Kazaz, and M. Oren, "Mdm2 promotes the rapid degradation of p53," *Nature*, vol. 387, no. 6630, pp. 296–299, 1997.
- [8] K. K. Hoe, C. S. Verma, and D. P. Lane, "Drugging the p53 pathway: understanding the route to clinical efficacy," *Nature Reviews Drug Discovery*, vol. 13, no. 3, pp. 217–236, 2014.
- [9] N. Rivlin, R. Brosh, M. Oren, and V. Rotter, "Mutations in the p53 tumor suppressor gene: important milestones at the various steps of tumorigenesis," *Genes and Cancer*, vol. 2, no. 4, pp. 466–474, 2011.
- [10] M. Castells, B. Thibault, J.-P. Delord, and B. Couderc, "Implication of tumor microenvironment in chemoresistance: tumor-associated stromal cells protect tumor cells from cell death," *International Journal of Molecular Sciences*, vol. 13, no. 8, pp. 9545–9571, 2012.
- [11] M. J. Paszek, N. Zahir, K. R. Johnson et al., "Tensional homeostasis and the malignant phenotype," *Cancer Cell*, vol. 8, no. 3, pp. 241–254, 2005.
- [12] K. R. Levental, H. Yu, L. Kass et al., "Matrix crosslinking forces tumor progression by enhancing integrin signaling," *Cell*, vol. 139, no. 5, pp. 891–906, 2009.
- [13] J. I. Lopez, I. Kang, W.-K. You, D. M. McDonald, and V. M. Weaver, "In situ force mapping of mammary gland transformation," *Integrative Biology*, vol. 3, no. 9, pp. 910–921, 2011.
- [14] I. Levental, K. R. Levental, E. A. Klein et al., "A simple indentation device for measuring micrometer-scale tissue stiffness," *Journal of Physics Condensed Matter*, vol. 22, no. 19, Article ID 194120, 2010.
- [15] S. V. Plotnikov, A. M. Pasapera, B. Sabass, and C. M. Waterman, "Force fluctuations within focal adhesions mediate ECM-rigidity sensing to guide directed cell migration," *Cell*, vol. 151, no. 7, pp. 1513–1527, 2012.
- [16] S. Huvneers and E. H. J. Danen, "Adhesion signaling—crosstalk between integrins, Src and Rho," *Journal of Cell Science*, vol. 122, no. 8, pp. 1059–1069, 2009.
- [17] M. J. van Nimwegen, M. Huigsloot, A. Camier, I. B. Tjeldens, and B. van de Water, "Focal adhesion kinase and protein kinase B cooperate to suppress doxorubicin-induced apoptosis of breast tumor cells," *Molecular Pharmacology*, vol. 70, no. 4, pp. 1330–1339, 2006.
- [18] M. Desouza, P. W. Gunning, and J. R. Stehn, "The actin cytoskeleton as a sensor and mediator of apoptosis," *BioArchitecture*, vol. 2, no. 3, pp. 75–87, 2014.
- [19] J. Shi, M. Surma, L. Zhang, and L. Wei, "Dissecting the roles of ROCK isoforms in stress-induced cell detachment," *Cell Cycle*, vol. 12, no. 10, pp. 1492–1500, 2013.
- [20] J. Shi, X. Wu, M. Surma et al., "Distinct roles for ROCK1 and ROCK2 in the regulation of cell detachment," *Cell Death and Disease*, vol. 4, no. 2, article no. e483, 2013.
- [21] D. R. Croft, D. Crighton, M. S. Samuel et al., "p53-Mediated transcriptional regulation and activation of the actin cytoskeleton regulatory RhoC to LIMK2 signaling pathway promotes cell survival," *Cell Research*, vol. 21, no. 4, pp. 666–682, 2011.
- [22] G. Gadéa, L. Lapasset, C. Gauthier-Rouvière, and P. Roux, "Regulation of Cdc42-mediated morphological effects: a novel function for p53," *The EMBO Journal*, vol. 21, no. 10, pp. 2373–2382, 2002.
- [23] G. Jacquemet, H. Hamidi, and J. Ivaska, "Filopodia in cell adhesion, 3D migration and cancer cell invasion," *Current Opinion in Cell Biology*, vol. 36, pp. 23–31, 2015.
- [24] A. K. Guo, Y. Y. Hou, H. Hirata et al., "Loss of p53 enhances NF- $\kappa$ B-dependent lamellipodia formation," *Journal of Cellular Physiology*, vol. 229, no. 6, pp. 696–704, 2014.
- [25] A. K. Yip, K. Iwasaki, C. Ursekar et al., "Cellular response to substrate rigidity is governed by either stress or strain," *Biophysical Journal*, vol. 104, no. 1, pp. 19–29, 2013.
- [26] T. R. Brummelkamp, R. Bernards, and R. Agami, "A system for stable expression of short interfering RNAs in mammalian cells," *Science*, vol. 296, no. 5567, pp. 550–553, 2002.
- [27] T. Yugawa, K. Nishino, S.-I. Ohno et al., "Noncanonical NOTCH signaling limits self-renewal of human epithelial and induced pluripotent stem cells through ROCK activation," *Molecular and Cellular Biology*, vol. 33, no. 22, pp. 4434–4447, 2013.
- [28] K. Kawauchi, K. Araki, K. Tobiume, and N. Tanaka, "p53 Regulates glucose metabolism through an IKK-NF- $\kappa$ B pathway and inhibits cell transformation," *Nature Cell Biology*, vol. 10, no. 5, pp. 611–618, 2008.
- [29] K. Kawauchi, W. W. Tan, K. Araki et al., "p130Cas-dependent actin remodelling regulates myogenic differentiation," *Biochemical Journal*, vol. 445, no. 3, pp. 323–332, 2012.
- [30] J. Riedl, A. H. Crevenna, K. Kessenbrock et al., "Lifeact: a versatile marker to visualize F-actin," *Nature Methods*, vol. 5, no. 7, pp. 605–607, 2008.
- [31] P. Swietach, A. Hulikova, S. Patiar, R. D. Vaughan-Jones, and A. L. Harris, "Importance of intracellular pH in determining the uptake and efficacy of the weakly basic chemotherapeutic drug, doxorubicin," *PLoS ONE*, vol. 7, no. 4, Article ID e35949, 2012.
- [32] J. S. Desgrosellier and D. A. Cheresh, "Integrins in cancer: biological implications and therapeutic opportunities," *Nature Reviews Cancer*, vol. 10, no. 1, pp. 9–22, 2010.
- [33] J.-P. Cosse, M. Ronvaux, N. Ninane, M. J. Raes, and C. Michiels, "Hypoxia-induced decrease in p53 protein level and increase in c-jun DNA binding activity results in cancer cell resistance to etoposide," *Neoplasia*, vol. 11, no. 10, pp. 976–986, 2009.
- [34] X. Gong, C. Lin, J. Cheng et al., "Generation of multicellular tumor spheroids with microwell-based agarose scaffolds for drug testing," *PLoS ONE*, vol. 10, no. 6, Article ID e0130348, 2015.
- [35] R. H. Thomlinson and L. H. Gray, "The histological structure of some human lung cancers and the possible implications for radiotherapy," *British Journal of Cancer*, vol. 9, no. 4, pp. 539–549, 1955.
- [36] L. Rao, D. Perez, and E. White, "Lamin proteolysis facilitates nuclear events during apoptosis," *The Journal of Cell Biology*, vol. 135, no. 6, part 1, pp. 1441–1455, 1996.
- [37] S. Ruchaud, N. Korfali, P. Villa et al., "Caspase-6 gene disruption reveals a requirement for lamin A cleavage in apoptotic chromatin condensation," *EMBO Journal*, vol. 21, no. 8, pp. 1967–1977, 2002.
- [38] N. Morishima, "Changes in nuclear morphology during apoptosis correlate with vimentin cleavage by different caspases located either upstream or downstream of Bcl-2 action," *Genes to Cells*, vol. 4, no. 7, pp. 401–414, 1999.
- [39] A. H. Stegh, H. Herrmann, S. Lampel et al., "Identification of the cytolinker plectin as a major early in vivo substrate for caspase 8 during CD95- and tumor necrosis factor receptor-mediated apoptosis," *Molecular and Cellular Biology*, vol. 20, no. 15, pp. 5665–5679, 2000.
- [40] E. A. Slee, C. Adrain, and S. J. Martin, "Executioner caspase-3, -6, and -7 perform distinct, non-redundant roles during the

- demolition phase of apoptosis,” *Journal of Biological Chemistry*, vol. 276, no. 10, pp. 7320–7326, 2001.
- [41] Y. Sawada and M. P. Sheetz, “Force transduction by Triton cytoskeletons,” *Journal of Cell Biology*, vol. 156, no. 4, pp. 609–615, 2002.
- [42] C.-M. Lo, H.-B. Wang, M. Dembo, and Y.-L. Wang, “Cell movement is guided by the rigidity of the substrate,” *Biophysical Journal*, vol. 79, no. 1, pp. 144–152, 2000.
- [43] A. Saez, A. Buguin, P. Silberzan, and B. Ladoux, “Is the mechanical activity of epithelial cells controlled by deformations or forces?” *Biophysical Journal*, vol. 89, no. 6, pp. L52–L54, 2005.
- [44] S. Higuchi, T. M. Watanabe, K. Kawauchi, T. Ichimura, and H. Fujita, “Culturing of mouse and human cells on soft substrates promote the expression of stem cell markers,” *Journal of Bioscience and Bioengineering*, vol. 117, no. 6, pp. 749–755, 2014.
- [45] D. Schramek, A. Sendoel, J. P. Segal et al., “Direct in vivo RNAi screen unveils myosin IIa as a tumor suppressor of squamous cell carcinomas,” *Science*, vol. 343, no. 6168, pp. 309–313, 2014.
- [46] J. G. Walsh, S. P. Cullen, C. Sheridan, A. U. Lüthi, C. Gerner, and S. J. Martin, “Executioner caspase-3 and caspase-7 are functionally distinct proteases,” *Proceedings of the National Academy of Sciences of the United States of America*, vol. 105, no. 35, pp. 12815–12819, 2008.
- [47] M. Schuler, E. Bossy-Wetzler, J. C. Goldstein, P. Fitzgerald, and D. R. Green, “p53 induces apoptosis by caspase activation through mitochondrial cytochrome c release,” *Journal of Biological Chemistry*, vol. 275, no. 10, pp. 7337–7342, 2000.
- [48] D. R. Green and G. Kroemer, “Cytoplasmic functions of the tumour suppressor p53,” *Nature*, vol. 458, no. 7242, pp. 1127–1130, 2009.
- [49] K. Araki, T. Ebata, A. K. Guo, K. Tobiume, S. J. Wolf, and K. Kawauchi, “P53 Regulates cytoskeleton remodeling to suppress tumor progression,” *Cellular and Molecular Life Sciences*, vol. 72, no. 21, pp. 4077–4094, 2015.
- [50] O. T. Fackler and R. Grosse, “Cell motility through plasma membrane blebbing,” *Journal of Cell Biology*, vol. 181, no. 6, pp. 879–884, 2008.
- [51] E. S. Chhabra and H. N. Higgs, “The many faces of actin: matching assembly factors with cellular structures,” *Nature Cell Biology*, vol. 9, no. 10, pp. 1110–1121, 2007.
- [52] P. K. Mattila and P. Lappalainen, “Filopodia: molecular architecture and cellular functions,” *Nature Reviews Molecular Cell Biology*, vol. 9, no. 6, pp. 446–454, 2008.
- [53] X. Sui, J. Zhu, H. Tang et al., “p53 controls colorectal cancer cell invasion by inhibiting the NF- $\kappa$ B-mediated activation of Fascin,” *Oncotarget*, vol. 6, no. 26, pp. 22869–22879, 2015.
- [54] N. A. Lobo, Y. Shimono, D. Qian, and M. F. Clarke, “The biology of cancer stem cells,” *Annual Review of Cell and Developmental Biology*, vol. 23, pp. 675–699, 2007.
- [55] C. A. O’Brien, A. Pollett, S. Gallinger, and J. E. Dick, “A human colon cancer cell capable of initiating tumour growth in immunodeficient mice,” *Nature*, vol. 445, no. 7123, pp. 106–110, 2007.
- [56] E. Monzani, F. Facchetti, E. Galmozzi et al., “Melanoma contains CD133 and ABCG2 positive cells with enhanced tumorigenic potential,” *European Journal of Cancer*, vol. 43, no. 5, pp. 935–946, 2007.
- [57] A. S. Adhikari, N. Agarwal, and T. Iwakuma, “Metastatic potential of tumor-initiating cells in solid tumors,” *Frontiers in Bioscience*, vol. 16, no. 5, pp. 1927–1938, 2011.
- [58] M. Maugeri-Saccà, M. Bartucci, and R. De Maria, “DNA damage repair pathways in cancer stem cells,” *Molecular Cancer Therapeutics*, vol. 11, no. 8, pp. 1627–1636, 2012.

## Research Article

# Dynamics of Actin Stress Fibers and Focal Adhesions during Slow Migration in Swiss 3T3 Fibroblasts: Intracellular Mechanism of Cell Turning

Michiko Sugawara,<sup>1</sup> Hiromi Miyoshi,<sup>2,3</sup> Takuya Miura,<sup>1</sup> Hiroto Tanaka,<sup>4</sup>  
Ken-ichi Tsubota,<sup>1</sup> and Hao Liu<sup>1</sup>

<sup>1</sup>Department of Mechanical Engineering, Graduate School of Engineering, Chiba University, 1-33 Yayoi-cho, Inage-ku, Chiba 263-8522, Japan

<sup>2</sup>Pathophysiological and Health Science Team, RIKEN Center for Life Science Technologies, 6-7-3 Minatojima-minamimachi, Chuo-ku, Kobe, Hyogo 650-0047, Japan

<sup>3</sup>Health Metrics Development Team, RIKEN Compass to Healthy Life Research Complex Program, 6-7-1 Minatojima-minamimachi, Chuo-ku, Kobe, Hyogo 650-0047, Japan

<sup>4</sup>Department of Mechanical and Control Engineering, Graduate School of Science and Engineering, Tokyo Institute of Technology, 2-12-1 Ookayama, Meguro-ku, Tokyo 152-8550, Japan

Correspondence should be addressed to Michiko Sugawara; [msugawara@chiba-u.jp](mailto:msugawara@chiba-u.jp)

Received 9 September 2016; Revised 23 November 2016; Accepted 6 December 2016

Academic Editor: Hiroaki Hirata

Copyright © 2016 Michiko Sugawara et al. This is an open access article distributed under the Creative Commons Attribution License, which permits unrestricted use, distribution, and reproduction in any medium, provided the original work is properly cited.

To understand the mechanism regulating the spontaneous change in polarity that leads to cell turning, we quantitatively analyzed the dynamics of focal adhesions (FAs) coupling with the self-assembling actin cytoskeletal structure in Swiss 3T3 fibroblasts. Fluorescent images were acquired from cells expressing GFP-actin and RFP-zyxin by laser confocal microscopy. On the basis of the maximum area, duration, and relocation distance of FAs extracted from the RFP-zyxin images, the cells could be divided into 3 regions: the front region, intermediate lateral region, and rear region. In the intermediate lateral region, FAs appeared close to the leading edge and were stabilized gradually as its area increased. Simultaneously, bundled actin stress fibers (SFs) were observed vertically from the positions of these FAs, and they connected to the other SFs parallel to the leading edge. Finally, these connecting SFs fused to form a single SF with matured FAs at both ends. This change in SF organization with cell retraction in the first cycle of migration followed by a newly formed protrusion in the next cycle is assumed to lead to cell turning in migrating Swiss 3T3 fibroblasts.

## 1. Introduction

Directional cell migration plays an essential role in embryonic development [1], tissue regeneration [2], development and remodeling of the nervous system [3], wound healing in multicellular organisms [4, 5], and biomedical applications such as tissue formation [6]. During these processes, cells generate, maintain, and change front-back polarity by integrating chemical and mechanical stimuli from the extracellular environment [7, 8].

The mechanism of polarity control of migrating cells has been studied extensively in chemotactic neutrophils and

*Dictyostelium* amoeba in response to and movement along a gradient of chemoattractant [9, 10]. Polarized chemotactic cell migration is associated with the formation of polarized networks of actin filaments and microtubules together with the asymmetric distribution of signaling molecules including PI3Ks, PTEN, and Rho GTPases [10, 11]. It is also reported that local temperature gradients induce neurite outgrowth due to the enhanced microtubule and actin dynamics [12]. Intensive studies show that mechanical stimuli, such as stiffness [13–15] and topography [16, 17] of the extracellular matrix, and chemical and thermal stimuli are critical

factors controlling the polarity of migrating cells. Mechanically responding cells modulate the delicate force balance between contractility of the actin cytoskeleton and exogenous mechanical forces transmitted across the focal adhesions (FAs) [6] and change their migratory direction [15, 18, 19]. Thus, self-organization of the actin cytoskeletal system involving FAs is a key factor to understand the polarity control of migrating cells in relation to mechanical stimuli in the extracellular environment.

The details on polarity maintenance through self-assembling actin cytoskeletal structure coupling with the dynamics of FAs, which are known to be regulated by Rho family GTPases [20, 21], have been studied extensively in relation to the key steps: protrusion at the leading edge, adhesion to the extracellular matrix via FAs, and detachment and retraction at the cell rear. Protrusion at the leading edge is driven by actin polymerization to form a lamellipodium, which is a dynamic dendritic network with actin binding proteins such as Arp2/3 for nucleation and branching of actin filaments [22, 23], capping proteins for terminating actin polymerization [24] and ADF/cofilin for severing actin filaments [25]. Some actin filaments in the lamellipodium are depolymerized and recycled again for polymerization to actin filaments. Others including filopodia, which are rod-like projections that extend from the lamellipodium and are composed of bundles of actin filaments, are delivered to the lamella by the actin retrograde flow to assemble a contractile network for traction, consisting of bundled filaments, myosin II, and FAs [26–29]. The contractile forces generated in the actomyosin network are required for retrograde flow to assemble the contractile network, as well as cell body translocation and disassembling FAs at the cell rear [30, 31].

Self-assembly of actin cytoskeleton for polarity generation has been reported in physically pushed lamellipodial fragments, in which the physical stimulus leads to local compression of the bundled actin filaments with myosin II, resulting in a positive feedback loop that initiates polarization and persistent migration [32]. Furthermore, this polarity generation was shown to be dependent on Rho kinase-mediated reorganization of the actomyosin network based on the detailed analysis of the spatiotemporal reorganization of the F-actin network [33].

Clarification of the mechanism of polarity change is the next challenge to understand the control of migrating cells in response to mechanical stimuli since extensive studies have demonstrated the self-assembling actin cytoskeletal structure and dynamics of FAs for polarity generation and maintenance. Our aim here was to demonstrate the mechanism regulating the change in polarity that leads to cell turning by focusing on the dynamics of FAs and bundled actin filaments called stress fibers (SFs) [34]. We combined precise observations of FAs and SFs with quantitative analyses of FA assembly-disassembly in relation to spatiotemporal changes in SFs. These observations and analyses demonstrated the spatiotemporal coordination of intracellular cytoskeletal reorganization due to an actin self-assembly mechanism and dynamics of FA formation.

## 2. Materials and Methods

**2.1. Cell Culture, Transfection, and Sample Preparation.** Swiss 3T3 fibroblasts (Riken Cell Bank, Tsukuba, Japan) were cultured in 5% CO<sub>2</sub> at 37°C in Dulbecco's modified Eagle's medium (Low-glucose DMEM; GIBCO, USA) supplemented with 10% fetal bovine serum (Nacalai Tesque, Japan) and penicillin/streptomycin (50 units/mL and 50 µg/mL, resp.) (GIBCO). For long-term observations of cell migration, the cells were plated on 35 mm glass-bottom dishes (Matsunami, Japan). For observation of actin SFs and FAs during cell migration, the cells were cotransfected with pAcGFPI-actin (Clontech, USA) and pTagRFP-zyxin (Evrogen, Russia) using FuGENE HD transfection reagents (Promega, USA) according to the manufacturer's instructions. The cells were then seeded on silicone gel substrates. Both glass-bottom dishes and silicone gel substrates were precoated with 50 µg/mL fibronectin (BD Biosciences, USA) for 30 minutes at room temperature. After plating, the cells were incubated for at least 3 h in a 5% CO<sub>2</sub> incubator at 37°C, allowing the cells to adhere to and spread over the substrate.

**2.2. Silicone Gel Substrates.** A thin silicone gel substrate embedded with fluorescent microspheres was prepared, as described in detail elsewhere [35] with some modifications. Briefly, a pair of liquid silicones (CY52-276A and B; Dow Corning Toray, Japan) were mixed at a weight ratio of 6:5 and degassed. The mixture was spread on a 22 × 22 mm coverslip (Matsunami) using a spin coater (LH-D7; MIKASA, Japan). The thickness of the silicone layer was less than 50 µm. A 35 mm plastic dish with a hole (14 mm in diameter) at the bottom (Matsunami) was assembled with the silicone-coated coverslip by curing the silicone at 70°C for 30 minutes. Assembled silicone substrate-bottom dishes were kept in a hermetically sealed case with a 100 µL aliquot of liquid silane (3-aminopropyl triethoxysilane; Sigma-Aldrich Japan, Japan) for 1 h to attach the silane to the surface of the silicone substrate by vapor deposition. A 250 µL aliquot of a solution containing dark red fluorescent microspheres (0.2 µm in diameter, with peak excitation and emission wavelengths of 660 and 680 nm, resp., F-8807; Invitrogen, USA) diluted 400 times with distilled water was added to the solidified silicone. After approximately 10 minutes, the substrate was washed with distilled water. Young's modulus of the silicone substrate was typically 1.0 kPa [35].

**2.3. Live Cell Imaging and Image Processing for Long-Term Observation of Cell Migration.** Long-term observations of Swiss 3T3 fibroblast migration were performed at 37°C 5% CO<sub>2</sub> by phase contrast microscopy using an inverted microscope (ECLIPSE Ti-E; Nikon, Tokyo, Japan) equipped with the Perfect Focus System, a digital camera (Retiga-4000R CCD camera; QImaging, Canada), and a Plan Fluor 10x objective (NA 0.30; Nikon). Phase contrast images were captured every 10 minutes for up to 24 h controlled with NIS-Elements AR software (Nikon). The images were 1024 × 1024 pixels with a resolution of 1.48 µm/pixel. On the basis of the phase contrast images, cell edges were determined manually.

**2.4. Live Cell Imaging and Image Processing for Observation of Actin and Zyxin.** Swiss 3T3 fibroblasts expressing pAcGFP-actin and pTagRFP-zyxin plated on the silicone substrate embedded with fluorescent dark red microspheres (Figure 1(a)) were observed at 37°C 5% CO<sub>2</sub> using laser scanning confocal microscopy (AIR; Nikon) with a Plan Apo 60x oil immersion objective (NA 1.40; Nikon). Fluorescent images together with differential interference contrast (DIC) images were acquired every 3 minutes for up to 60 minutes. Here, the duration was limited to be 60 minutes that was shorter than the duration of images with phase contrast microscopy, which was due to the color shading especially in RFP-zyxin images. At each cycle of image capturing, *z*-stack fluorescent imaging was performed on 0.2 μm sections for a total thickness of 2.0 μm, the *z*-range of which included the top surface of the substrate and the bottom of the cell. Due to the difference in existing height positions among GFP-actin, RFP-zyxin, and dark red microspheres, a maximum intensity projection (MIP) image was configured from 5 series of slices from a total of 11 series of slices for each fluorescent image. One example is shown in Figure 1(b): MIP images of GFP-actin and RFP-zyxin were created from the 7th slice (*z* = 1.2 μm) to the 11th slice (*z* = 2.0 μm) from the bottom whereas the MIP images of fluorescent dark red microspheres were created from the 1st (*z* = 0 μm) to the 5th slice (*z* = 0.8 μm). From this imaging, we collected 3 sets of 512 × 512 pixels fluorescent images together with DIC images for a maximum of 21 cycles. Image resolution ranged from 0.14 to 0.21 μm/pixel.

All image processing was performed using the configured MIP images, which were saved as 12 bit gray scale images (Figure 1(c), left). The gray scale GFP-actin images were binarized using Otsu's method [36] and subsequently eroded, opened, and dilated (Figure 1(c), middle). Cell edges were found using the outline detection algorithm with the "bwperim" function in MATLAB. The obtained cell outline and area centroid are shown in Figure 1(c) (right). The area centroid  $\vec{C} = (C_x, C_y)$  was calculated from the binarized image by  $\vec{C} = \sum_i m_i \vec{r}_i / M$ , where  $\vec{r}_i = (r_{xi}, r_{yi})$  and  $m_i$  are the coordinates and pixel value of each pixel, respectively.  $m_i$  should be 1 (white) or 0 (black) for binarized images, and  $M$  is determined to be  $\sum_i m_i$ .

In each sequential MIP image of RFP-zyxin, an FA can be classified either to be born, to continue into the next time step, or to die. Firstly, individual FAs were identified manually from the gray scale RFP-zyxin images, and the duration of each FA was obtained from the time the FA was born to the time it died. Secondly, in order to calculate the area and area centroid for each FA, gray scale RFP-zyxin images were cropped locally around each FA and they were binarized using Otsu's method [36] (Figure 1(d), left). We determined individual FA areas as the number of pixels in the locally binarized image for each FA. In addition, an area centroid for each FA was also calculated using the same equation as for the whole cell, mentioned above. Finally, relocation distance was obtained from the distance between the area centroid of an FA to be born and that of the same FA to die (Figure 1(d), right).

**2.5. Classification of SFs.** We defined ventral SFs to be those SFs connecting to FAs at both ends and dorsal SFs to be those

connecting to only one end, with an FA close to the leading edge and the other end free or connecting to arc SFs. Strictly, ventral SFs commonly extend from an FA near the cell edge to another FA. Arc SFs, which are not anchored at FAs, can be observed on the dorsal surface of migrating cells. Lastly, dorsal SFs associate at an end with an FA close to the leading edge and rise into the dorsal part of the cell, often connecting to arc SFs [34]. In our analysis, whether SFs were ventral or dorsal was determined based on the MIP images according to the number of connection between the SFs and FAs.

**2.6. Displacement Field Analysis Using Image-Based Template Matching.** In order to measure the displacement field of the silicone substrate between images in time, sequential MIP images of the fluorescent dark red microspheres embedded in the silicone substrate were analyzed by template matching [37], which we implemented in MATLAB. In order to estimate the displacement field of the substrate between time phase *t* and *t* + *dt*, we calculated the normalized cross-correlation (NCC) function. The NCC function was calculated for each pixel in sample image *I* with size *M* × *N* at time *t* + *dt* according to the template *T* with size *U* × *V* at time *t*:

$$\begin{aligned} \text{NCC}(x, y) &= \frac{\sum_{u,v} (I(x+u, y+v) - \bar{I})(T(u, v) - \bar{T})}{\sqrt{\sum_{u,v} \sum_{u,v} (I(x+u, y+v) - \bar{I})^2 \times (T(u, v) - \bar{T})^2}}, \quad (1) \end{aligned}$$

where  $x = 0, 1, 2, \dots, M-1$ ,  $y = 0, 1, 2, \dots, N-1$ ,  $u = 0, 1, 2, \dots, U-1$  and  $v = 0, 1, 2, \dots, V-1$ .  $\bar{T}$  represents the mean of *T* and  $\bar{I}$  is the mean of *I*.

### 3. Results

**3.1. Cell Turning during Long-Term Migration.** Long-term observations of Swiss 3T3 fibroblast migration were performed on a glass substrate by phase contrast microscopy. A total of 19 cells were observed: 2 cells showed directed migration; 7 cells lost their polarity and remained at the same position; and 10 cells showed more than 90° turning with large deformation during slow migration. Four of these 10 cells in particular showed unusual turning behavior, a representative example of which is shown in Figure 2. As seen in Figure 2, the cell turned with the collapse of the initial leading edge, followed by the formation of new lamellipodia, orthogonal to the original direction of migration.

To focus on intracellular self-assembling actin cytoskeletal structure coupling with the dynamics of FAs in turning cells, we acquired time-lapse fluorescent images of migrating Swiss 3T3 fibroblasts expressing GFP-actin and RFP-zyxin with laser confocal microscopy and DIC microscopy. As shown in Figure 3(a), this setup enabled us to detect bundled filament-like actin SFs and spot-like FAs in cells establishing front-back polarity on the basis of direction of migration. Figure 3(b) represents the direction of the protrusion and retraction by red and blue arrows, respectively. The cell protruded largely to the upper region (red arrow 1) and also had a small protrusive region to the upper left (red arrow 2).

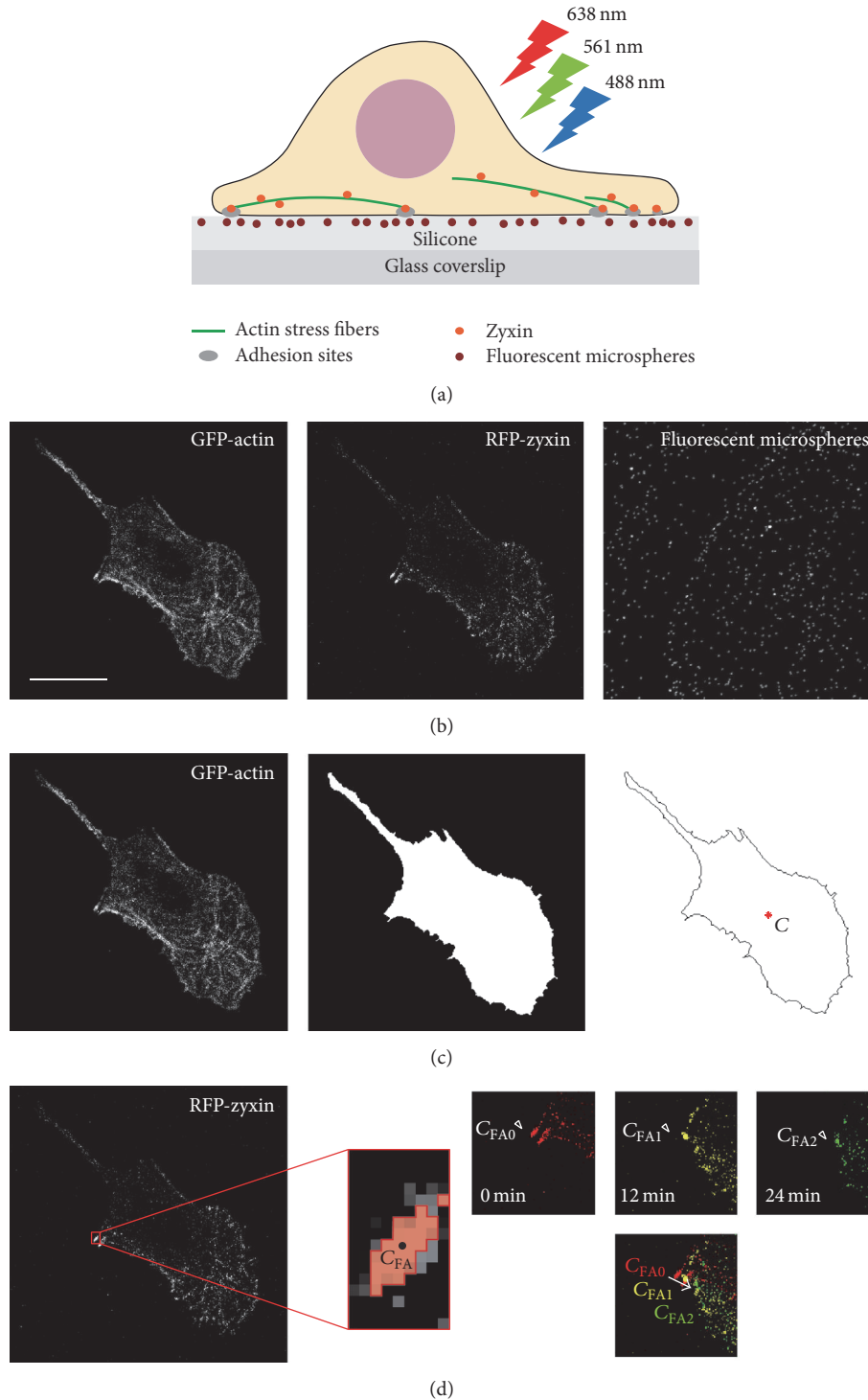
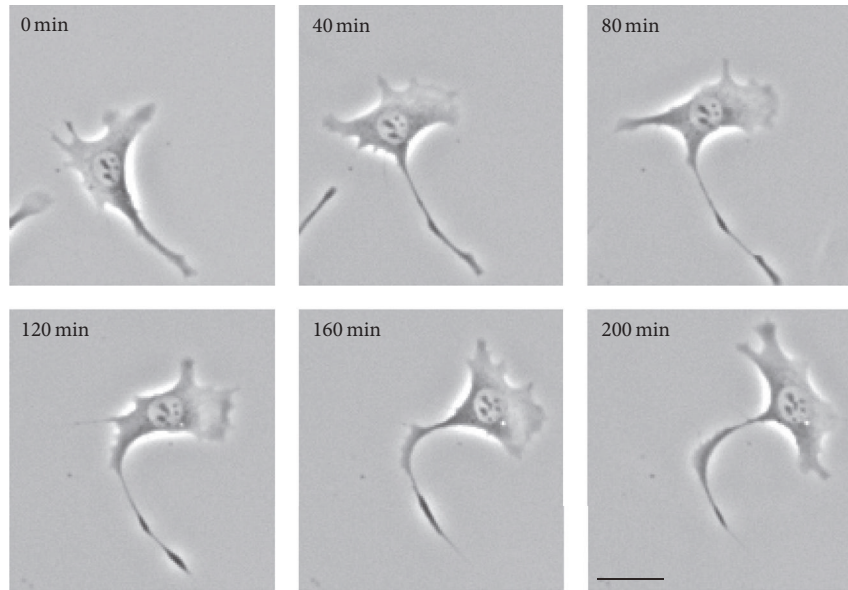
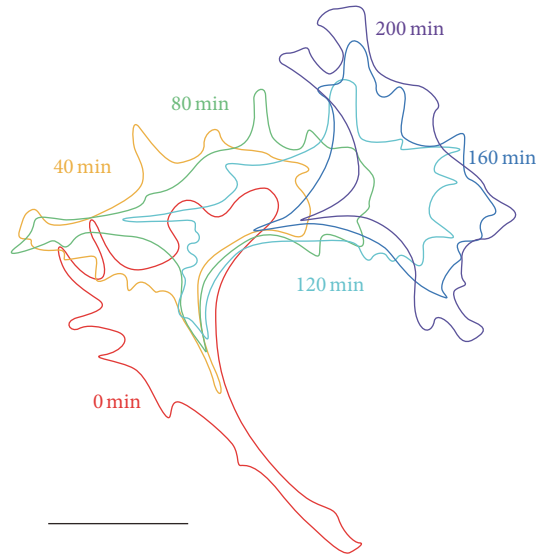


FIGURE 1: Schematics of image acquisition and processing. (a) Swiss 3T3 fibroblasts expressing GFP-actin and RFP-zyxin were plated on a silicone substrate in which fluorescent dark red microspheres were embedded. GFP, RFP, and dark red microspheres were excited by lasers at 488, 561, and 638 nm, respectively. (b) Examples of maximum intensity projection (MIP) images of GFP-actin, RFP-zyxin, and fluorescent dark red microspheres at time  $t = 0$  minutes. In this case, the MIP images of GFP-actin and RFP-zyxin were created from images #7 ( $z = 1.2 \mu\text{m}$ ) to #11 ( $z = 2.0 \mu\text{m}$ ), whereas the MIP image of fluorescent microspheres was created from the images #1 ( $z = 0 \mu\text{m}$ ) to #5 ( $z = 0.8 \mu\text{m}$ ). Scale bars:  $20 \mu\text{m}$ . (c) Image processing to identify the cell edge from an MIP image of GFP-actin. The position of the area centroid  $C$  is represented by a red asterisk. (d) Image processing for the identification of FAs from an MIP image of RFP-zyxin. Enlarged image around an FA cropped from the MIP image of RFP-zyxin is shown. The image is binarized locally, and the FA area with the area centroid  $C_{FA}$  is shown in red with a black dot. Relocation of the FA is shown on the right. In this example, from 0 to 24 minutes, the position of the area centroid of the FA changed from  $C_{FA0}$  to  $C_{FA2}$ .



(a)



(b)

FIGURE 2: A typical example of an image sequence of a Swiss 3T3 fibroblast exhibiting turning behavior. (a) Sequential phase contrast images of the cell every 40 minutes for up to 200 minutes. The cell turned with the collapse of the initial leading edge, followed by the formation of new lamellipodia, orthogonal to the original direction of migration. In this study, a total of 19 cells were observed and 10 cells showed more than 90° turning with large deformation during slow migration. Four of these 10 cells in particular showed such turning behavior. (b) Time sequence of the manually extracted outline of the cell in (a), with color denoting time elapsed. Scale bars: 20 μm.

At the cell rear, the lower right (blue arrow 1) and lower left (blue arrow 2) regions retracted. Here, the direction of red arrow 1 was almost the same as that of blue arrows 1 and 2, whereas the direction of red arrow 2 was perpendicular to that of the blue arrows. This suggests that the cell was turning from the direction of red arrow 1 to the direction of red arrow 2.

*3.2. Local FA Dynamics: Different Characteristics in the Front, Intermediate Lateral, and Rear Regions.* To analyze FA dynamics, we first quantitatively characterized FA dynamics

in a single cell. We extracted FAs from the cell shown in Figure 3(a), and then duration, maximum area, and relocation distance of each FA were obtained by image processing according to the method explained in Figure 1(d). As shown in Figures 4(a), 4(b), and 4(c), 21 FAs were extracted. On the basis of *k*-mean clustering [38], these 21 FAs were classified into 3 groups: one with a short duration, small maximum area, and short relocation distance (green circles); one with a long duration, large maximum area, and long relocation distance (red circles); and one with a long duration, large

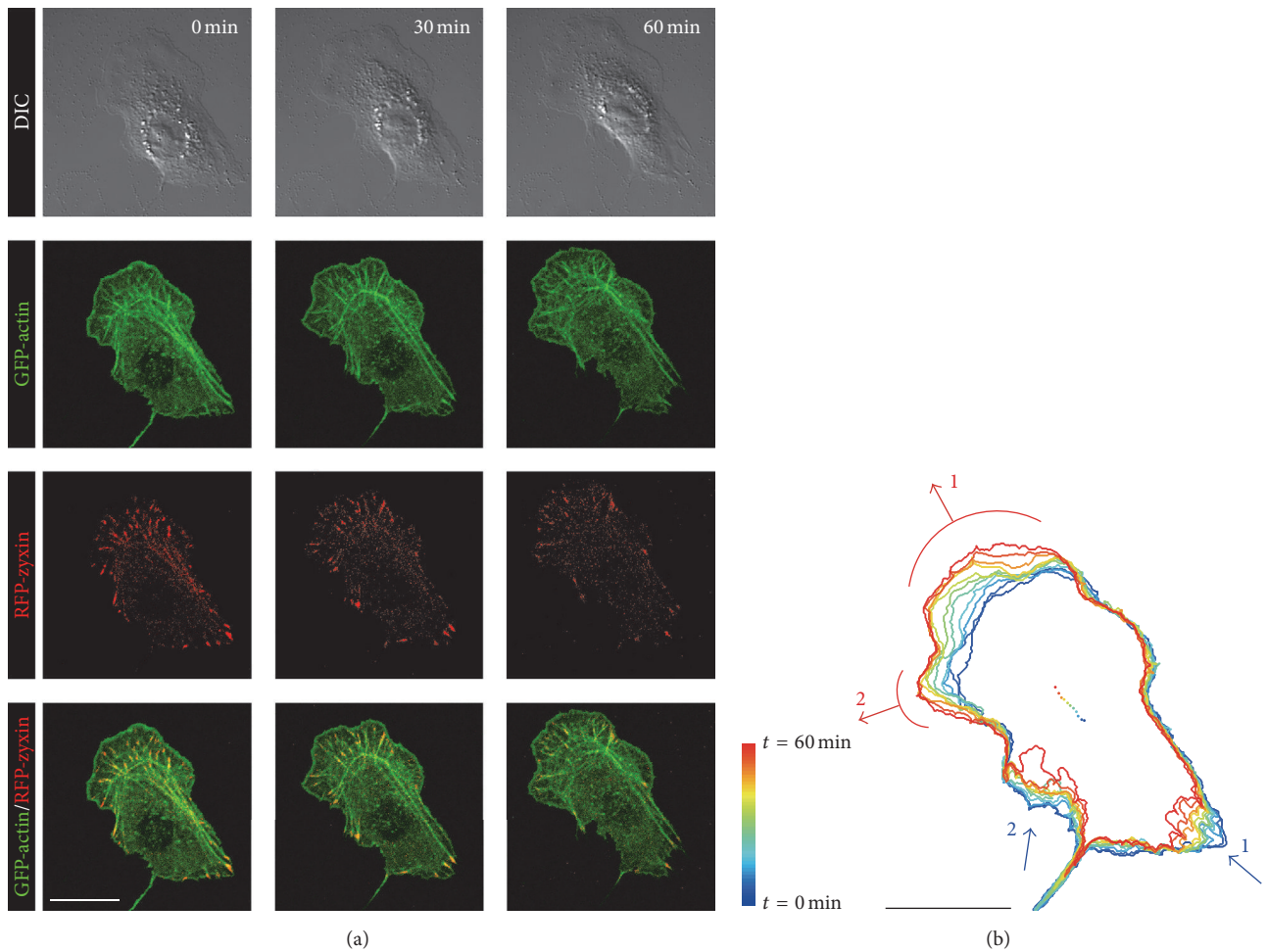


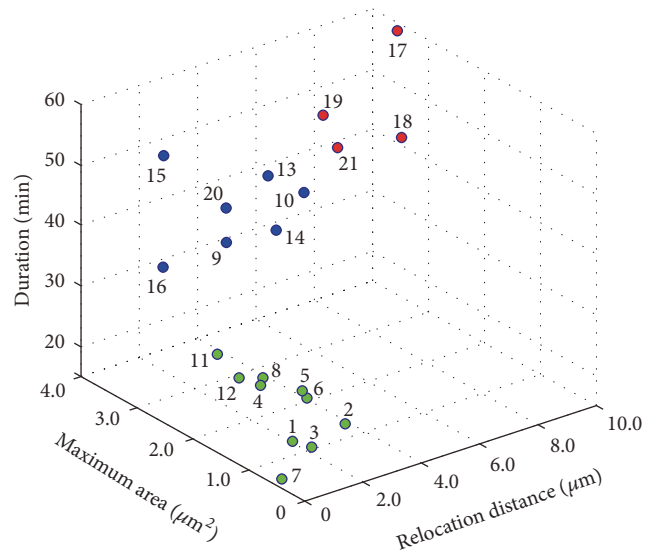
FIGURE 3: Protrusion and retraction during migration of a Swiss 3T3 fibroblast. (a) Time-lapse images of DIC, GFP-actin, and RFP-zyxin of cells expressing GFP-actin and RFP-zyxin at  $t = 0, 30,$  and  $60$  minutes. (b) Sequential images of outlines of the cell in (a) are depicted together with the centroid of the cell marked by dots every  $6$  minutes. The positions of protrusion and retraction are represented by red and blue arrows, respectively. Scale bars:  $20 \mu\text{m}$ .

maximum area, and short relocation distance (blue circles). The spatial distribution of the 21 FAs shown in Figure 4(d) demonstrated that the FAs indicated by the green circles were located at the front protrusive region, whereas the FAs indicated by the red circles were in the cell rear region where the cell retracted. The FAs indicated by the blue circles were rather scattered but were approximately in the lateral region between the cell front and rear. On the basis of these characteristics of the FAs, the migrating cell seemed to be divided into 3 regions: front, intermediate lateral, and rear regions.

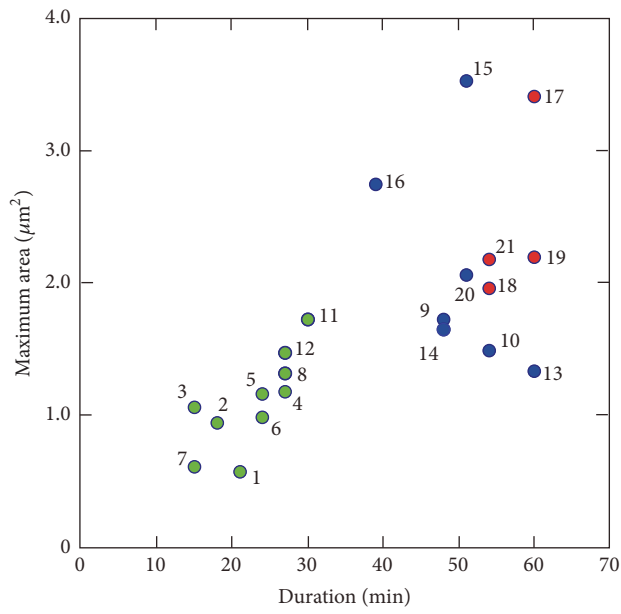
To confirm statistically whether this division of the cell into 3 regions based on the characteristics of the FAs was typical, a total of 70 FAs extracted from 10 cells were again analyzed by  $k$ -mean clustering and the FAs were classified by the region they were located in. The results found that the FAs were indeed classified into 3 groups: green group mainly existing in the front region (region F), blue group mainly existing in the intermediate lateral region (region L), and red group mainly existing in the rear region (region R).

The averages and standard deviations of the maximum area, duration, and relocation distance of the FAs in each region are shown in Figures 4(e), 4(f), and 4(g), respectively. One-way analysis of variance demonstrated significant difference in maximum area between FAs in region F, region L, and region R in Figure 4(e) ( $F = 16.8; n = 70; df = 2; p < 0.001$ ). The same analyses were performed, and both the difference in duration between FAs in three regions in Figure 4(f) ( $F = 99.4; n = 70; df = 2; p < 0.001$ ) and the difference in relocation distance between FAs in three regions in Figure 4(g) ( $F = 101.8; n = 70; df = 2; p < 0.001$ ) were found to be significant.

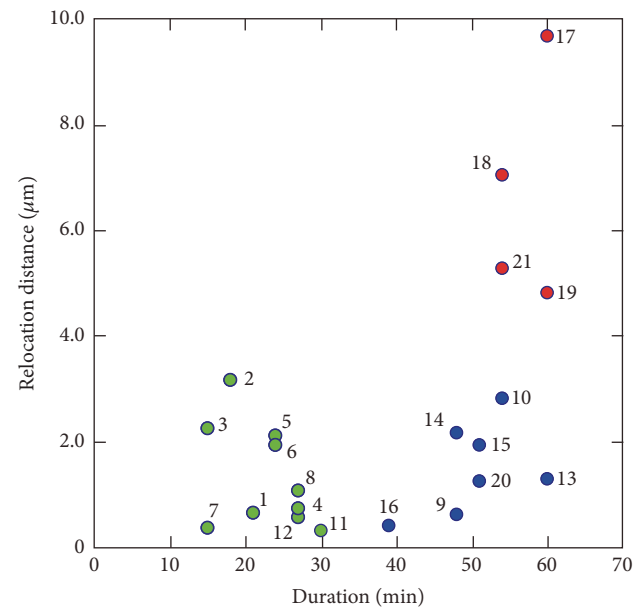
These results demonstrated that the cell could be divided clearly into 3 regions: (1) front region, where FAs had a small maximum area, short duration, and short relocation distance; (2) intermediate lateral region between the cell front and cell rear, where FAs had a large maximum area, long duration, and short relocation distance; and (3) rear region, where FAs had a large maximum area, long duration, and long relocation distance.



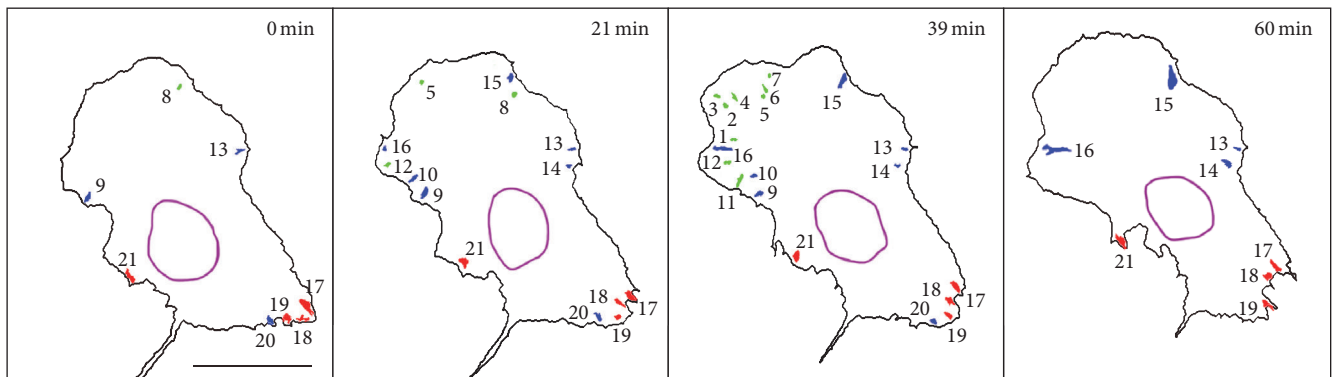
(a)



(b)



(c)



(d)

FIGURE 4: Continued.

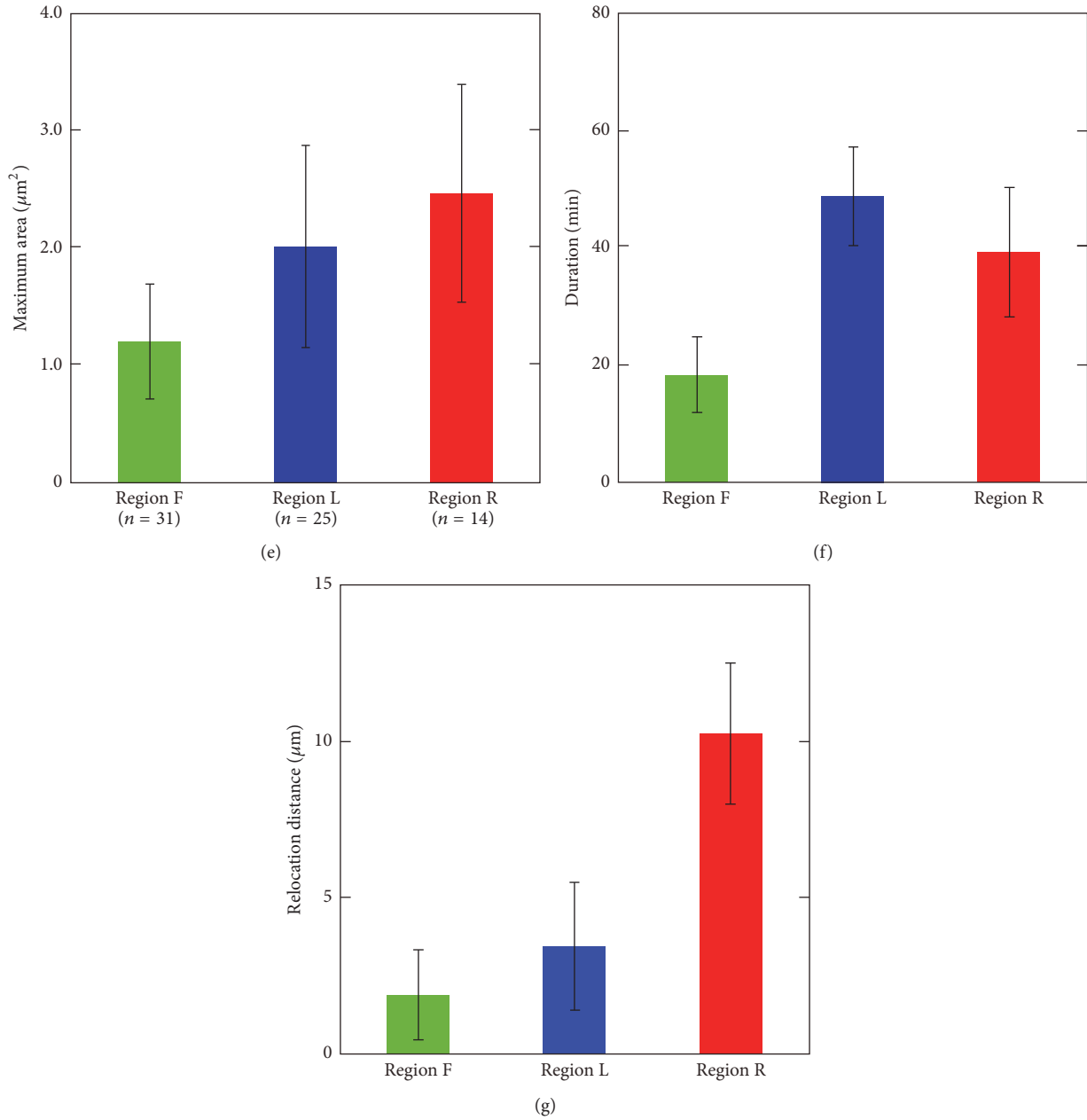


FIGURE 4: Classification of FAs on the basis of  $k$ -mean clustering. (a) The relationship among duration, maximum area, and relocation distance of 21 FAs extracted from the cell in Figure 3. Duration versus maximum area of the FAs and duration versus relocation distance of the FAs are also depicted in (b) and (c), respectively. On the basis of  $k$ -mean clustering, these FAs were classified into three groups: green, blue, and red circles. (d) Spatial distribution of these FAs at  $t = 0, 21, 39,$  and  $60$  minutes is shown. The FAs indicated by the green circles were located at the front protrusive region (region F), whereas the FAs indicated by the red circles were in the cell rear (region R). The FAs indicated by the blue circles were approximately in the lateral region between the cell front and the cell rear regions (region L). Scale bar:  $20 \mu\text{m}$ . (e, f, g) Average and standard deviations of the maximum area, duration, and relocation distance of FAs are shown in (e), (f), and (g), respectively. For statistical analysis, a total of 70 FAs were extracted from 10 cells. One-way analysis of variance demonstrated significant difference between FAs in region F, region L, and region R.

**3.3. Local FA Dynamics: Relationship between FA Relocation and Extracellular Matrix Deformation.** The substrate under the front region of the cell was displaced several micrometers, whereas the substrate under the rear region was displaced much less than that shown in Figure 5. The displacement field

of the silicone substrate under the other 9 cells also showed the same results.

According to Figure 4(g), the relocation distance of the FAs in the front region was several micrometers, whereas that in the rear region was approximately  $10 \mu\text{m}$ . When

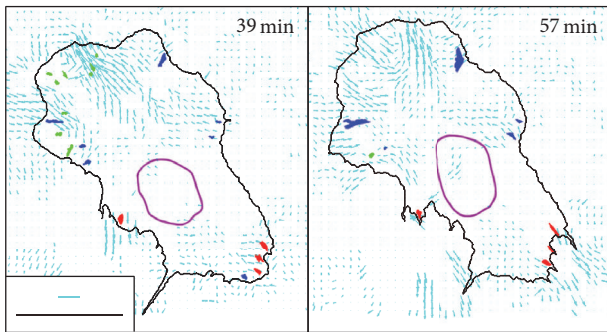


FIGURE 5: Displacement field of the substrate. Displacement vectors of the substrate analyzed by image-based template matching are shown by the cyan arrows. The length of the displacement vectors is enlarged from the original size and its scale is shown by the cyan scale bar ( $3\ \mu\text{m}$ ). The positions of the FAs in the front, intermediate lateral, and rear regions are shown in green, blue, and red, respectively. Black scale bar:  $20\ \mu\text{m}$ . The analysis here is based on the same data presented in Figures 3 and 4(a)–4(d).

compared with the displacement of the substrate under the front and the rear regions, this indicates that the FAs in the front region were firmly linked to the substrate and moved together with it. The FAs in the rear region were less strongly linked to the substrate and instead slipped on it. These results are consistent with a previous report that motile fibroblasts have a front-towing mechanism, where the cells exert strong propulsive forces within a discrete zone near the leading edge, resulting in the cell body being towed forward during migration [39], with sliding trailing adhesion at the cell rear [30].

**3.4. Local FA Dynamics: Quantitative Characterization of Growth and Decay in the Front, Intermediate Lateral, and Rear Regions.** For a more detailed understanding of the difference in the dynamics of the FAs in each region, time courses of the area of the FAs in the front, intermediate lateral, and rear regions were analyzed quantitatively (Figure 6).

In the front region of the cell, FA dynamics were classified further into 2 patterns. The first one was, as shown in Figure 6(a), the area of the FAs which was approximately  $1.0\ \mu\text{m}^2$  or less and their area fluctuated between small and big repeatedly, indicating that the FAs were unstable and not maturing. Their lifetime was less than 30 minutes, which was short compared to the FAs in the other regions. The second one is shown in Figure 6(b); the area of FAs was increased initially and then it decreased. This might correspond to the assembly and disassembly phases of FAs [40]. The lifetime of both patterns of FA dynamics (Figures 6(a) and 6(b)) was approximately 30 minutes.

In the intermediate lateral region, as shown in Figures 6(c) and 6(d), the FAs showed 2 patterns of dynamics. The first typical pattern is shown in Figure 6(c), in which the area increased over time. The other pattern is shown in Figure 6(d), in which the area of the FAs was almost constant for up to 60 minutes. The duration of the FAs in Figures 6(c) and 6(d) was more than 39 minutes, which was longer than that for the FAs in the front region (Figures 6(a) and 6(b)).

The change in area of the FAs in the rear region is shown in Figures 6(e) and 6(f). The FAs in this region showed 2 patterns of the dynamics. In Figure 6(e), the area decreased over time. Conversely, as shown in Figure 6(f), the area of the other FAs remained almost constant for up to 60 minutes.

**3.5. Local Dynamics of SFs Coupled with the FAs in the Front, Intermediate Lateral, and Rear Regions.** Next, the local dynamics of actin SFs and FAs in the front, intermediate lateral, and rear regions were investigated (Figure 7). Time-lapse montages of GFP-actin and RFP-zyxin were built for the front region (region F, boxed area B in Figure 7(a)), intermediate lateral region (region L, boxed area C), and rear region (region R, boxed area D).

In the front region, as shown in the montage of GFP-actin in Figure 7(b), the edge of the cell moved gradually in the upper direction, which indicated that the cell protruded. The montage of RFP-zyxin demonstrated that new FAs (orange, yellow, green, light blue, and blue arrowheads) were formed one after another at an anterior position to the preexisting FAs (red arrowheads), which is consistent with previous reports [41, 42]. As shown in the montage of RFP-zyxin in Figure 7(b), some FAs (indicated by yellow and light blue arrowheads) showed a short duration, whereas some FAs (indicated by orange and blue arrowheads) existed for nearly 30 minutes. From the comparison of the montages of GFP-actin and RFP-zyxin, both types of FAs formed simultaneously with SFs (thick bundled-like filaments) and disappeared simultaneously with the disappearance of the SFs.

The intermediate lateral region of the cell did not protrude (Figure 7(c)). The montage of RFP-zyxin showed that a small FA appeared close to the cell edge and its area became gradually larger (yellow arrowheads). In this case, as for the case in Figure 7(b), an SF was observed vertically from the position of the FA. However, as shown at 27 minutes in Figure 7(c), the vertical SF connected to the other SF that was aligned parallel to the leading edge (red arrowhead), which was a different behavior to the SFs in the front region in Figure 7(b). The same intersecting SF connection was observed again at 39 minutes in Figure 7(c) (red arrowhead) and in 8 of the 10 cells. This observation in Figure 7(c) together with the image of SFs in the whole cell in Figure 7(a) indicated that these connecting SFs were part of an arc SF that existed parallel to the leading edge. The interaction of vertical SFs with arc SF was consistent with a previous report [43].

The local SF and FA dynamics in the rear region are shown in Figure 7(d). The time-lapse montage of RFP-zyxin shows that a large FA existed initially and it relocated toward the upper direction, indicating that the FA in the rear region relocated toward the nucleus. The time-lapse montage of GFP-actin in Figure 7(d) shows that the relocating FA connected to a bundle-like SF with a contractile movement. This result is consistent with earlier studies that described sliding trailing adhesions with SFs [30, 44].

**3.6. Globally Coordinated SF Dynamics Coupled with FAs.** In Figure 8, how SFs connect globally is shown together with the change in stability of FAs. At 30 minutes, there were 2 FAs in the intermediate lateral region, which are shown by white

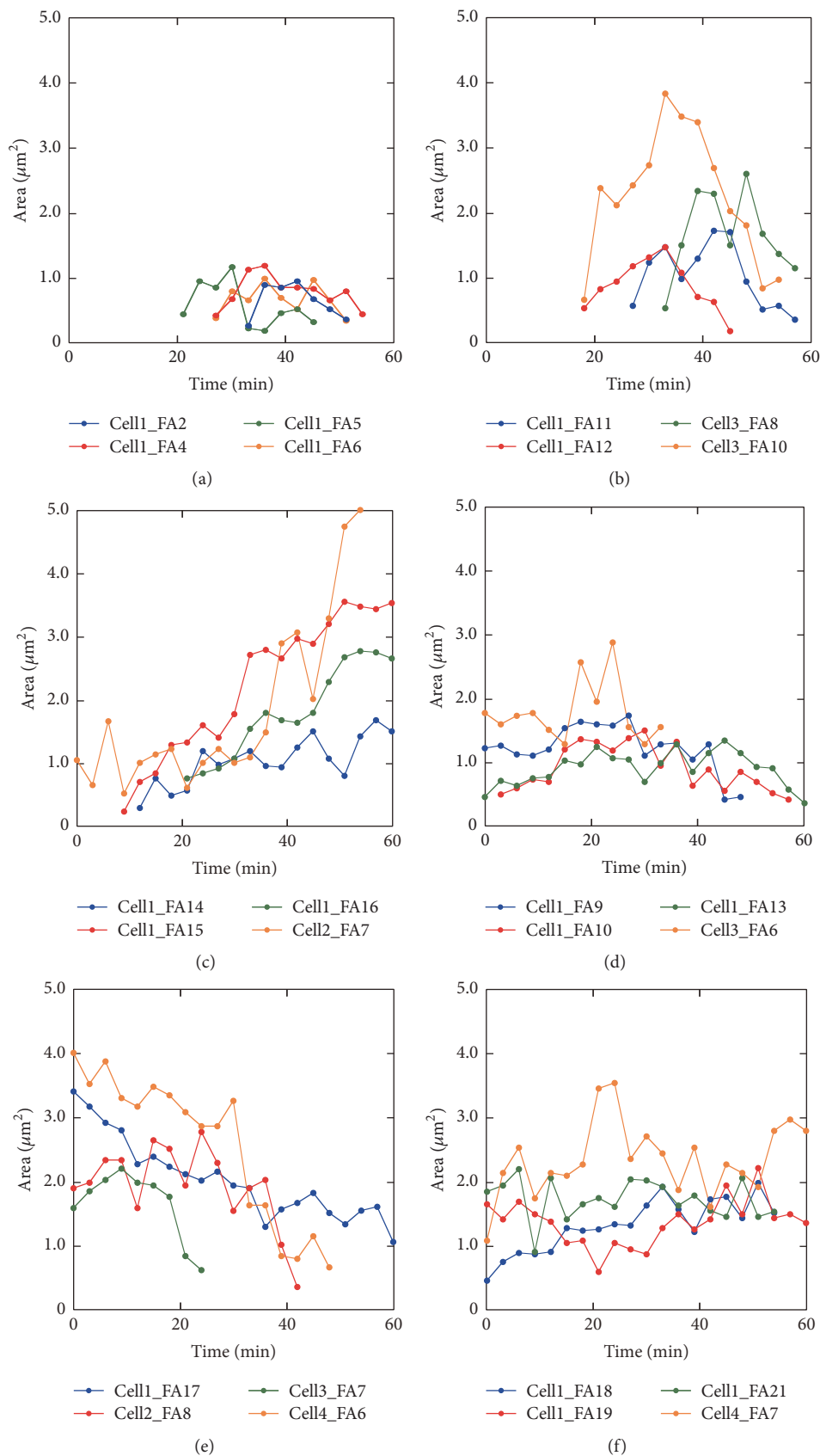


FIGURE 6: Growth and decay of FAs in the front, intermediate lateral, and rear regions. Time courses of FA area in the front (a, b), intermediate lateral (c, d), and rear regions (e, f) are shown. Representative 24 FAs from 4 cells, including the cell in Figure 3 (Cell 1) are used for the analysis. FAs were further classified into 2 patterns in each region. The FA number for Cell 1 corresponds to that shown in Figure 4(d).

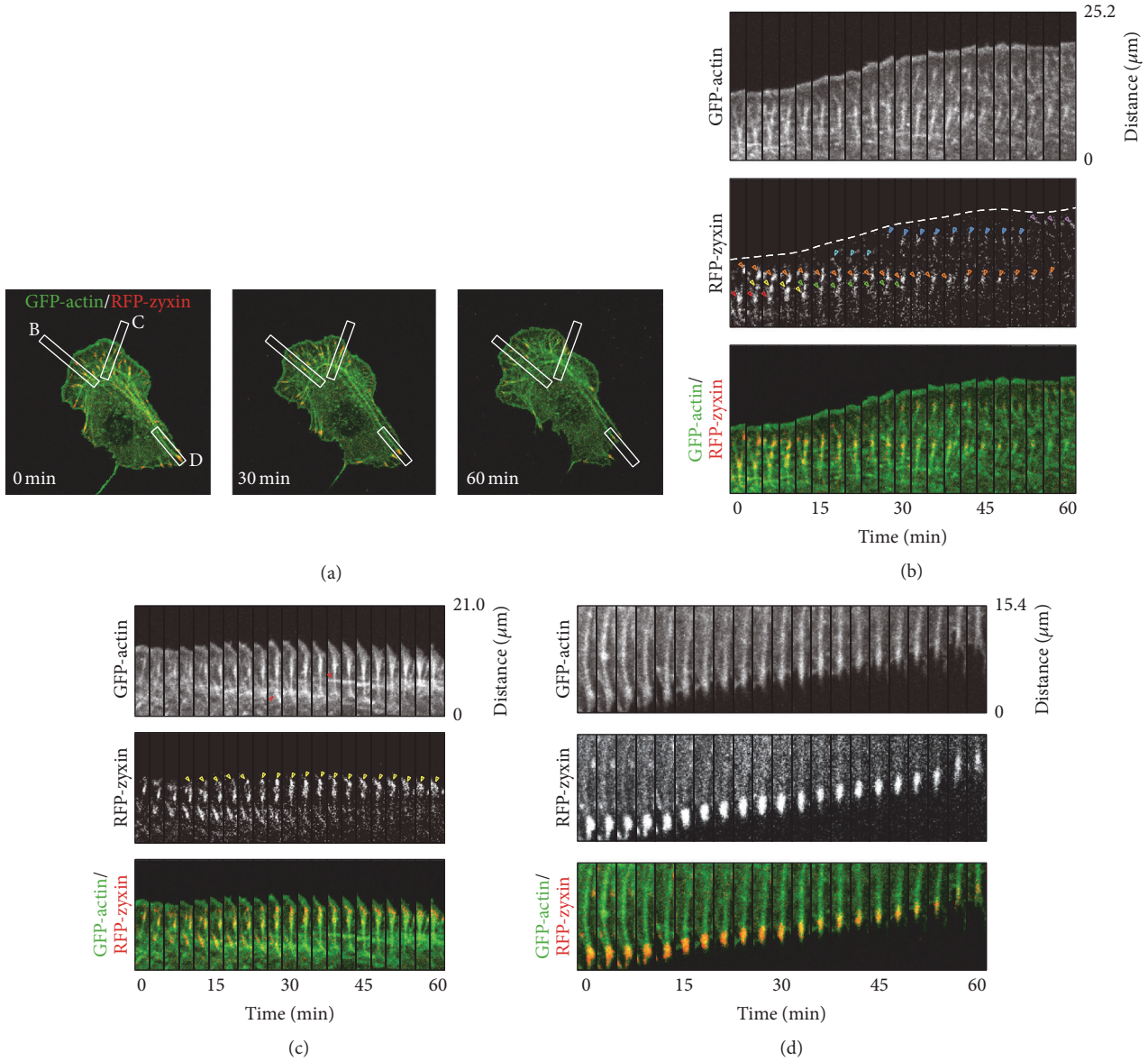


FIGURE 7: Dynamics of actin SFs together with FAs. The analysis here is based on the same data presented in Figures 3, 4(a)–4(d) and 5. (a) Merged images of GFP-actin and RFP-zyxin. (b) The time-lapse montages of GFP-actin and RFP-zyxin were built from the boxed area B in panel (a) (region F). The cell edge extracted from the montage of GFP-actin is indicated by a dotted line in the montage of RFP-zyxin. The edge of the cell moved gradually in the upper direction, which indicated that the cell protruded. The montage of RFP-zyxin demonstrated that new FAs (orange, yellow, green, light blue, and blue arrowheads) were formed one after another at an anterior position to the preexisting FAs (red arrowheads). The FAs in the region F formed simultaneously with SFs (thick bundled-like filaments in the montage of GFP-actin) and disappeared simultaneously with the disappearance of the SFs. (c) Time-lapse montages were built from the boxed area C in panel (a) (region L). From the montage of GFP-actin, the cell did not protrude. Yellow arrowheads in the montage of RFP-zyxin showed that a small FA appeared close to the cell edge and its area became gradually larger. As for the case in (c), an SF was observed vertically from the position of the FA and intersecting SF connections were also observed (red arrowheads in the montage of GFP-actin). (d) Time-lapse montages were built from the boxed area D in panel (a) (region R). From the montages of GFP-actin and RFP-zyxin, we could recognize the relocating FA connected to a bundle-like SF with a contractile movement.

triangles A and B (Figure 8(a)). Short SFs (red lines in Figure 8(b)) were assembled from both FAs toward the inside of the cell, which are dorsal SFs, and they seemed to connect to the other long SFs parallel to the leading edge, that is, arc SFs (yellow lines in Figure 8(b)). At this moment, the dorsal SF from the FA (indicated by B in Figure 8(a)) connected to

2 arc SFs. Then, at 39 minutes, both arc SFs parallel to the leading edge started to fuse into a single arc SF. At this time point, 2 dorsal SFs and the arc SF still seemed to be distinct; that is, there were 3 SFs between the FA-A and the FA-B. At 45 minutes, these 3 SFs became a single SF linked to the FAs, which is a ventral SF (green line in the intermediate region

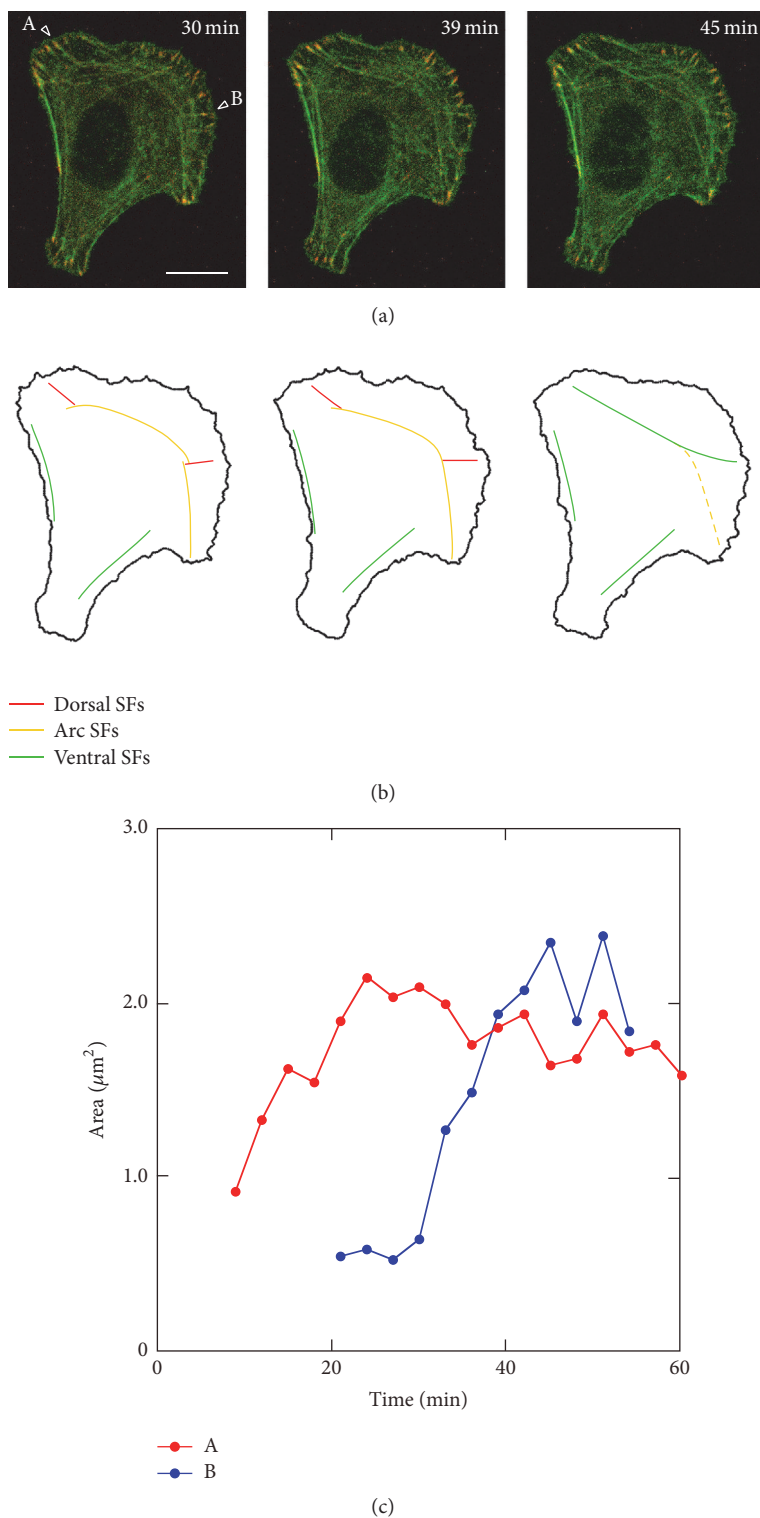


FIGURE 8: Change in alignment of SFs together with the change in FA stability in the front and intermediate regions. (a) Merged images of GFP-actin and RFP-zyxin. The time after the start of observation is denoted in minutes. (b) SFs of interest extracted from (a). Each image in (b) corresponds to that in (a). (c) Temporal change in FA area indicated as “A” and “B” in (a). At 30 minutes, there were 2 FAs in the intermediate lateral region (“A” and “B” in (a)). Short dorsal SFs (red lines in (b)) were assembled from both FAs toward the inside of the cell and they seemed to connect to the other two long arc SFs (yellow lines in (b)). Then, at 39 minutes, both arc SFs started to fuse into a single arc SF. At this time point, 2 dorsal SFs and the arc SF still seemed to be distinct. At 45 minutes, these 3 SFs became a single SF linked to the FAs, which is ventral SF (green line in the intermediate region in (b)).

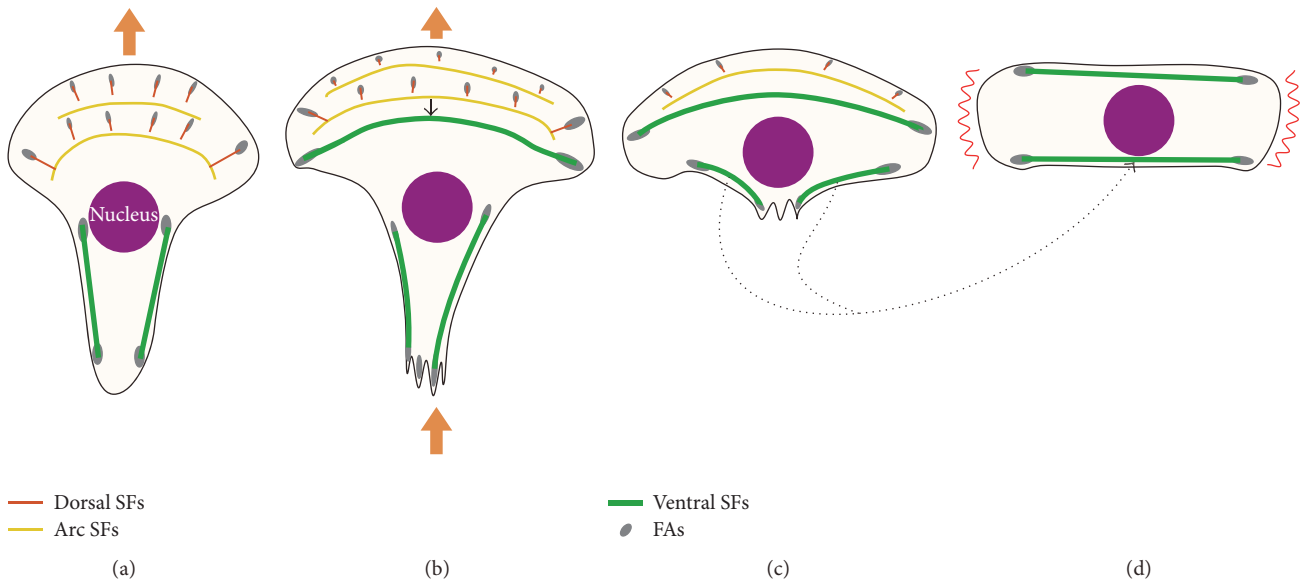


FIGURE 9: Hypothesized mechanism of spontaneous polarity change resulting in cell turning behavior. (a) Protrusion at the cell front. (b) Protrusion at the cell front together with retraction at the cell rear. A single ventral SF could be connected or fused from dorsal SFs and arc SFs in the intermediate region of the cell (green line). (c) End of retraction at the cell rear. The upper single ventral SF is the SF formed in (b), whereas the lower 2 ventral SFs are those in the rear region in (b), which could become a single ventral SF subsequently (dotted arrow). (d) End of the cyclic process of cell migration. Possible protrusion site of the cell is shown by the red winding lines, which is perpendicular to that in the initial direction of protrusion. This means that the cell could change its polarity, resulting in cell turning behavior.

in Figure 8(b)). A similar change in alignment of SFs with FA in the front and intermediate regions of the cell could be also observed in 3 migrating cells.

From 30 minutes to 45 minutes, the area of FA-A was almost constant, indicating that the rate of FA assembly was balanced by FA disassembly. This will result in the apparent stability of the FA. The area of FA-B increased during the period, which indicated that FA-B matured gradually. The result indicated that there were FAs at the intermediate lateral regions of both sides of the cell that were connected by several dorsal SFs, and these SFs fused gradually with arc SFs and finally became a single ventral SF with maturing and apparently stable FAs at both ends (green line in the intermediate region in Figure 8(b)). This SF assembly with FAs was also reported previously [43]. Conversely in the cell rear, from 30 minutes to 45 minutes, there were several thick and long SFs, which are ventral SFs (green lines in the rear region in Figure 8(b)), aligned close to the lateral side of the cell with FAs at both ends. A similar transition in the alignment of SFs with FAs in the intermediate region of the cell was observed in three other migrating cells.

#### 4. Discussion

In this study, we focused on the dynamics of FAs and SFs during the cycle of cell migration steps in Swiss 3T3 fibroblasts: leading edge protrusion at the cell front, contractile force generation against adhesions and release of rear adhesions, and retraction of the cell rear. Our precise observations and quantitative analyses of FA assembly-disassembly demonstrated

that the cycle of cell migration steps consisted of 3 distinct FA dynamics, and FAs with different dynamics were distributed in different cell regions: front, intermediate lateral, and rear regions (Figures 4, 6, and 7). Furthermore, analysis of the spatiotemporal changes in SFs in relation to the assembly-disassembly of FAs clarified SF dynamics locally (Figure 7) and globally (Figure 8) coupled with FA dynamics. On the basis of the results, Figure 9 summarizes the hypothesized mechanism of spontaneous polarity change that leads to cell turning behavior.

The first step of the migration cycle is protrusion of the cell front (Figure 9(a)). Some FAs newly assembled at the cell front were unstable (Figure 6(a)), while the others were assembled and disassembled quickly (Figure 6(b)). In the cell front, as illustrated by the red line in Figure 9(a), dorsal SFs extended perpendicular to the leading edge from the newly formed FAs toward the inside of the cell and then disappeared simultaneously with disassembly of the FAs (Figure 7(b)). Conversely, in the intermediate lateral region of the cell, some dorsal SFs connected or fused to long arc SFs parallel to the leading edge (Figure 7(c)), which is depicted by the yellow lines in Figure 8(a). These SFs finally became a single ventral SF (Figure 8), which is depicted by the green line in the intermediate region of the cell in Figure 9(b), with intermediate lateral FAs at both ends. In the cell rear, retraction occurred. Cell retraction might be due to the contraction of ventral SFs, which is depicted by the green lines in the cell rear in Figures 9(a), 9(b), and 9(c), accompanied by translocation of the FAs at the end of those SFs (Figure 7(d)).

After retraction in the cell rear, as shown in Figures 9(c) and 9(d), ventral SFs with FAs at both ends would align in the horizontal direction. Here in Figure 9(d), one of the SFs will come from the newly formed ventral SF with FAs at both ends in the intermediate region in Figure 9(b) (green line) [28]. The other one could possibly be formed by the annealing of 2 or more ventral SFs [45] at the cell rear during the process shown in Figures 9(c) and 9(d) (dotted arrows). In Figure 9(d), the possible protrusion site of the cell is assumed to be in the peripheral region (the red winding lines), along which there are no SFs. This assumption is supported by previous findings that localized tension transfer across integrins in FAs could locally activate Rac and Cdc42, which leads to the formation of lamellipodia [46], whereas mechanical stresses in FAs suppress lamellipodial protrusion through inhibition of Rac activation [47]. Therefore, the regions indicated by the red winding lines in Figure 9(d) could protrude with the formation of new FAs together with SFs. It should be noted that the direction of the new protrusion site is perpendicular to that in the initial state of the cell in Figure 9(a), which leads the cell to spontaneous polarity change and resulting turning behavior.

Cytoskeletal rearrangements where ventral SFs are assembled from dorsal SFs and arc SFs have been reported from the molecular point of view [43] and recently reviewed [48, 49]. However, to our knowledge, the relationship between such cytoskeletal rearrangements and cell migration has not been reported. In the present study, we show that the SF assembly, coupled with growing and apparently stable FA dynamics, occurred at the end of dorsal SFs in the intermediate lateral region of the cell. From this observation, we proposed the model in Figure 9, showing that such globally coordinated SF dynamics with FAs would lead to cell turning behavior during migration. Continuous protrusion in the direction of the cell might be the simplest description for cell turning behavior, which could be explained by the well-known key steps for migration: protrusion at the leading edge, adhesion to the extracellular matrix via FAs, and subsequent detachment. Our model could provide further novel insights into the mechanism of polarity change driven by self-assembling actin cytoskeletal structures. In order to establish the mechanism of polarity change mentioned here, further observation would be needed to confirm the process after Figure 9(d).

## 5. Conclusions

In this study, we proposed a hypothesis for cell turning focusing on the coupling dynamics of actin SFs and FAs in Swiss 3T3 fibroblasts. In the intermediate lateral region of the cell, we observed the FAs maturing and becoming stable. In addition, our analysis demonstrated that 2 dorsal SFs assembled from FAs close to the leading edge and then connected into arc SFs, fused gradually into a single ventral SF. This change in SF organization with cell retraction in the first cycle of migration followed by a newly formed protrusion in the next cycle will lead to cell turning during migration in Swiss 3T3 fibroblasts.

## Competing Interests

The authors declare that there is no conflict of interests regarding the publication of this paper.

## Authors' Contributions

Michiko Sugawara and Hiromi Miyoshi contributed equally to this work.

## Acknowledgments

The authors thank Dr. Yoshiaki Iwadate (Yamaguchi University, Yamaguchi, Japan) for their technical advice and help in making the silicone substrate embedded with microspheres. The authors also thank Mr. Daishi Inoue (RIKEN, Wako, Japan) and Dr. Michio Murakoshi (Kagoshima University, Japan) for their technical help in observing the surface topology of the silicone substrate embedded with microspheres using scanning electron microscopy and atomic force microscopy, respectively. This study was supported in part by Japan Society for the Promotion of Science KAKENHI Grant nos. 24700448, 25630046, and 16K01350.

## References

- [1] H. W. Detrich III, M. W. Kieran, F. Y. Chan et al., "Intraembryonic hematopoietic cell migration during vertebrate development," *Proceedings of the National Academy of Sciences of the United States of America*, vol. 92, no. 23, pp. 10713–10717, 1995.
- [2] M. P. Lutolf and J. A. Hubbell, "Synthetic biomaterials as instructive extracellular microenvironments for morphogenesis in tissue engineering," *Nature Biotechnology*, vol. 23, no. 1, pp. 47–55, 2005.
- [3] S. V. Puram and A. Bonni, "Cell-intrinsic drivers of dendrite morphogenesis," *Development*, vol. 140, no. 23, pp. 4657–4671, 2013.
- [4] W. S. Krawczyk, "A pattern of epidermal cell migration during wound healing," *The Journal of Cell Biology*, vol. 49, no. 2, pp. 247–263, 1971.
- [5] P. Martin, "Wound healing—aiming for perfect skin regeneration," *Science*, vol. 276, no. 5309, pp. 75–81, 1997.
- [6] H. Miyoshi and T. Adachi, "Topography design concept of a tissue engineering scaffold for controlling cell function and fate through actin cytoskeletal modulation," *Tissue Engineering Part B: Reviews*, vol. 20, no. 6, pp. 609–627, 2014.
- [7] V. Lecaudey and D. Gilmour, "Organizing moving groups during morphogenesis," *Current Opinion in Cell Biology*, vol. 18, no. 1, pp. 102–107, 2006.
- [8] S. Yumura, G. Itoh, Y. Kikuta, T. Kikuchi, T. Kitanishi-Yumura, and M. Tsujioka, "Cell-scale dynamic recycling and cortical flow of the actin-myosin cytoskeleton for rapid cell migration," *Biology Open*, vol. 2, no. 2, pp. 200–209, 2013.
- [9] R. Wedlich-Soldner and R. Li, "Spontaneous cell polarization: undermining determinism," *Nature Cell Biology*, vol. 5, no. 4, pp. 267–270, 2003.
- [10] C. Y. Chung, S. Funamoto, and R. A. Firtel, "Signaling pathways controlling cell polarity and chemotaxis," *Trends in Biochemical Sciences*, vol. 26, no. 9, pp. 557–566, 2001.

- [11] J. Zhang, W.-H. Guo, and Y.-L. Wang, "Microtubules stabilize cell polarity by localizing rear signals," *Proceedings of the National Academy of Sciences of the United States of America*, vol. 111, no. 46, pp. 16383–16388, 2014.
- [12] K. Oyama, V. Zeeb, Y. Kawamura et al., "Triggering of high-speed neurite outgrowth using an optical microheater," *Scientific Reports*, vol. 5, article 16611, 2015.
- [13] R. J. Pelham Jr. and Y.-L. Wang, "Cell locomotion and focal adhesions are regulated by substrate flexibility," *Proceedings of the National Academy of Sciences of the United States of America*, vol. 94, no. 25, pp. 13661–13665, 1997.
- [14] C.-M. Lo, H.-B. Wang, M. Dembo, and Y.-L. Wang, "Cell movement is guided by the rigidity of the substrate," *Biophysical Journal*, vol. 79, no. 1, pp. 144–152, 2000.
- [15] T. Kawano and S. Kidoaki, "Elasticity boundary conditions required for cell mechanotaxis on microelastically-patterned gels," *Biomaterials*, vol. 32, no. 11, pp. 2725–2733, 2011.
- [16] H. Miyoshi, J. Ju, S. M. Lee et al., "Control of highly migratory cells by microstructured surface based on transient change in cell behavior," *Biomaterials*, vol. 31, no. 33, pp. 8539–8545, 2010.
- [17] M. Ghibaud, L. Trichet, J. Le Digabel, A. Richert, P. Hersen, and B. Ladoux, "Substrate topography induces a crossover from 2D to 3D behavior in fibroblast migration," *Biophysical Journal*, vol. 97, no. 1, pp. 357–368, 2009.
- [18] H. Miyoshi, T. Adachi, J. Ju et al., "Characteristics of motility-based filtering of adherent cells on microgrooved surfaces," *Biomaterials*, vol. 33, no. 2, pp. 395–401, 2012.
- [19] G. Mahmud, C. J. Campbell, K. J. M. Bishop et al., "Directing cell motions on micropatterned ratchets," *Nature Physics*, vol. 5, no. 8, pp. 606–612, 2009.
- [20] M. Chrzanowska-Wodnicka and K. Burridge, "Rho-stimulated contractility drives the formation of stress fibers and focal adhesions," *Journal of Cell Biology*, vol. 133, no. 6, pp. 1403–1415, 1996.
- [21] K. Burridge and K. Wennerberg, "Rho and rac take center stage," *Cell*, vol. 116, no. 2, pp. 167–179, 2004.
- [22] R. D. Mullins, J. A. Heuser, and T. D. Pollard, "The interaction of Arp2/3 complex with actin: nucleation, high affinity pointed end capping, and formation of branching networks of filaments," *Proceedings of the National Academy of Sciences of the United States of America*, vol. 95, no. 11, pp. 6181–6186, 1998.
- [23] K. J. Amann and T. D. Pollard, "The Arp2/3 complex nucleates actin filament branches from the sides of pre-existing filaments," *Nature Cell Biology*, vol. 3, no. 3, pp. 306–310, 2001.
- [24] T. D. Pollard and G. G. Borisy, "Cellular motility driven by assembly and disassembly of actin filaments," *Cell*, vol. 112, no. 4, pp. 453–465, 2003.
- [25] M. Ghosh, X. Song, G. Mouneimne, M. Sidani, D. S. Lawrence, and J. S. Condeelis, "Cofilin promotes actin polymerization and defines the direction of cell motility," *Science*, vol. 304, no. 5671, pp. 743–746, 2004.
- [26] J. V. Small and G. P. Resch, "The comings and goings of actin: coupling protrusion and retraction in cell motility," *Current Opinion in Cell Biology*, vol. 17, no. 5, pp. 517–523, 2005.
- [27] K. O. Okeyo, T. Adachi, J. Sunaga, and M. Hojo, "Actomyosin contractility spatiotemporally regulates actin network dynamics in migrating cells," *Journal of Biomechanics*, vol. 42, no. 15, pp. 2540–2548, 2009.
- [28] D. T. Burnette, S. Manley, P. Sengupta et al., "A role for actin arcs in the leading-edge advance of migrating cells," *Nature Cell Biology*, vol. 13, no. 4, pp. 371–382, 2011.
- [29] M. Nemethova, S. Auinger, and J. V. Small, "Building the actin cytoskeleton: filopodia contribute to the construction of contractile bundles in the lamella," *Journal of Cell Biology*, vol. 180, no. 6, pp. 1233–1244, 2008.
- [30] R. Rid, N. Schiefermeier, I. Grigoriev, J. V. Small, and I. Kaverina, "The last but not the least: the origin and significance of trailing adhesions in fibroblastic cells," *Cell Motility and the Cytoskeleton*, vol. 61, no. 3, pp. 161–171, 2005.
- [31] C. Möhl, N. Kirchgessner, C. Schäfer, B. Hoffmann, and R. Merkel, "Quantitative mapping of averaged focal adhesion dynamics in migrating cells by shape normalization," *Journal of Cell Science*, vol. 125, no. 1, pp. 155–165, 2012.
- [32] A. B. Verkhovskiy, T. M. Svitkina, and G. G. Borisy, "Self-polarization and directional motility of cytoplasm," *Current Biology*, vol. 9, no. 1, pp. 11–20, 1999.
- [33] P. T. Yam, C. A. Wilson, L. Ji et al., "Actin-myosin network reorganization breaks symmetry at the cell rear to spontaneously initiate polarized cell motility," *Journal of Cell Biology*, vol. 178, no. 7, pp. 1207–1221, 2007.
- [34] J. V. Small, K. Rottner, I. Kaverina, and K. I. Anderson, "Assembling an actin cytoskeleton for cell attachment and movement," *Biochimica et Biophysica Acta (BBA)—Molecular Cell Research*, vol. 1404, no. 3, pp. 271–281, 1998.
- [35] Y. Iwate and S. Yumura, "Molecular dynamics and forces of a motile cell simultaneously visualized by TIRF and force microscopies," *BioTechniques*, vol. 44, no. 6, pp. 739–750, 2008.
- [36] N. Otsu, "A threshold selection method from gray-level histograms," *IEEE Transactions Systems Man Cybernetics*, vol. 9, no. 1, pp. 62–66, 1979.
- [37] J. P. Lewis, "Fast normalized cross-correlation," *Vision Interface*, vol. 10, pp. 120–123, 1995.
- [38] C. M. Bishop, *Neural Networks for Pattern Recognition*, Oxford University Press, 1995.
- [39] S. Munevar, Y.-L. Wang, and M. Dembo, "Traction force microscopy of migrating normal and H-ras transformed 3T3 fibroblasts," *Biophysical Journal*, vol. 80, no. 4, pp. 1744–1757, 2001.
- [40] M. E. Berginski, E. A. Vitriol, K. M. Hahn, and S. M. Gomez, "High-resolution quantification of focal adhesion spatiotemporal dynamics in living cells," *PLoS ONE*, vol. 6, no. 7, Article ID e22025, 2011.
- [41] D. J. Webb, J. T. Parsons, and A. F. Horwitz, "Adhesion assembly, disassembly and turnover in migrating cells—over and over and over again," *Nature Cell Biology*, vol. 4, no. 4, pp. E97–E100, 2002.
- [42] A. Y. Alexandrova, K. Arnold, S. Schaub et al., "Comparative dynamics of retrograde actin flow and focal adhesions: formation of nascent adhesions triggers transition from fast to slow flow," *PLoS ONE*, vol. 3, no. 9, Article ID e3234, 2008.
- [43] P. Hotulainen and P. Lappalainen, "Stress fibers are generated by two distinct actin assembly mechanisms in motile cells," *Journal of Cell Biology*, vol. 173, no. 3, pp. 383–394, 2006.
- [44] C. Ballestrem, B. Hinz, B. A. Imhof, and B. Wehrle-Haller, "Marching at the front and dragging behind: differential  $\alpha V\beta 3$ -integrin turnover regulates focal adhesion behavior," *Journal of Cell Biology*, vol. 155, no. 7, pp. 1319–1332, 2001.
- [45] D. B. Murphy, R. O. Gray, W. A. Grasser, and T. D. Pollard, "Direct demonstration of actin filament annealing in vitro," *Journal of Cell Biology*, vol. 106, no. 6, pp. 1947–1954, 1988.
- [46] K. I. T. Kevin Parker, A. M. Y. Lepre Brock, C. Brangwynne et al., "Directional control of lamellipodia extension by constraining cell shape and orienting cell tractional forces," *FASEB Journal*, vol. 16, no. 10, pp. 1195–1204, 2002.

- [47] A. Katsumi, J. Milanini, W. B. Kiosses et al., “Effects of cell tension on the small GTPase Rac,” *The Journal of Cell Biology*, vol. 158, no. 1, pp. 153–164, 2002.
- [48] P. Naumanen, P. Lappalainen, and P. Hotulainen, “Mechanisms of actin stress fibre assembly,” *Journal of Microscopy*, vol. 231, no. 3, pp. 446–454, 2008.
- [49] T. Vallenius, “Actin stress fibre subtypes in mesenchymal-migrating cells,” *Open Biology*, vol. 3, no. 6, Article ID 130001, 2013.

## Research Article

# A Two-Dimensional Numerical Investigation of Transport of Malaria-Infected Red Blood Cells in Stenotic Microchannels

Tong Wang,<sup>1</sup> Yong Tao,<sup>1</sup> Uwitije Rongin,<sup>1</sup> and Zhongwen Xing<sup>2</sup>

<sup>1</sup>Department of Mathematics, Nanjing University of Aeronautics and Astronautics, Nanjing 210016, China

<sup>2</sup>School of Electronic Science and Engineering, Nanjing University, Nanjing 210093, China

Correspondence should be addressed to Tong Wang; [twang@nuaa.edu.cn](mailto:twang@nuaa.edu.cn)

Received 28 August 2016; Revised 12 November 2016; Accepted 23 November 2016

Academic Editor: Hiroaki Hirata

Copyright © 2016 Tong Wang et al. This is an open access article distributed under the Creative Commons Attribution License, which permits unrestricted use, distribution, and reproduction in any medium, provided the original work is properly cited.

The malaria-infected red blood cells experience a significant decrease in cell deformability and increase in cell membrane adhesion. Blood hemodynamics in microvessels is significantly affected by the alteration of the mechanical property as well as the aggregation of parasitized red blood cells. In this study, we aim to numerically study the connection between cell-level mechanobiological properties of human red blood cells and related malaria disease state by investigating the transport of multiple red blood cell aggregates passing through microchannels with symmetric stenosis. Effects of stenosis magnitude, aggregation strength, and cell deformability on cell rheology and flow characteristics were studied by a two-dimensional model using the fictitious domain-immersed boundary method. The results indicated that the motion and dissociation of red blood cell aggregates were influenced by these factors and the flow resistance increases with the increase of aggregating strength and cell stiffness. Further, the roughness of the velocity profile was enhanced by cell aggregation, which considerably affected the blood flow characteristics. The study may assist us in understanding cellular-level mechanisms in disease development.

## 1. Introduction

Malaria infects 350–500 million people and kills more than two millions every year, mostly in Africa and other underdeveloped countries. In most of the malaria cases, red blood cells (RBCs) are parasitized by *Plasmodium falciparum* (*P-falciparum*), a protozoan parasite transmitted by mosquitos. When the RBCs are parasitized by *P-falciparum*, two critical effects have been observed in the infected cells, namely, the reduced deformability of the cell and increased adhesion of the RBCs to vessel endothelium and other blood cells [1]. Thus, the parasitized RBCs become stiffer (could be tenfold harder than healthy RBCs [2]) and tend to form aggregates in blood. Blood flow may be substantially affected by the change of structural and mechanical properties of the malaria-infected RBCs.

Under healthy physiological conditions, red blood cells move individually with blood plasma or form temporal

aggregates and they can undergo severe, reversible, large elastic deformation in blood flow. Although the formation of red blood cell aggregates could be due to other factors such as the decrease of the shear rate, increase of the hematocrit, and variation of the viscosity of the suspending plasma in the blood vessel, the malaria-infected RBCs tend to form firm and irreversible aggregates. Severe aggregation of RBCs may decrease the surface area of cells contacting with the blood plasma. It also causes pressure and shear stress change in the region of the aggregation. These aggregates get stuck in the small blood vessels, blocking individual RBC from passing, thus decreasing the amount of oxygen and the nutrition transferred in human body.

Experimental measurements have been done on dynamic or rheological properties and behaviors of parasitized RBCs [3–10]. In the experiments, microfluidic channels have been employed to probe the deformability of healthy and

malaria-infected red blood cells. The hardening of the cell and the blockage of the channel can be qualitatively studied. However, a major difficulty in carrying out experimental investigations on malaria-infected RBCs is the complexity of the microvessels. Moreover, experimental techniques are in general not fully capable of illustrating cellular-level rheological behaviors of RBC aggregates. Because of the relatively large number of red blood cells, cell-to-cell interactions and local rheological properties were unable to identify. Therefore, numerical simulations have been utilized as an alternative tool to study the rheology of parasitized RBCs in blood flow [11–15]. Numerical models that have been used for interpretation and prediction of mechanical properties and dynamic behavior of RBCs in malaria include dissipative particle dynamics (DPD) [13, 15], smoothed particle hydrodynamics (SPH) [14], lattice Boltzmann method (LBM) [16], and others [17]. Two or multiple RBCs are considered by numerical simulations to probe their interactions, for example, their aggregation and disaggregation in blood flow [18–22].

However, very few investigations on malaria-infected RBCs have been conducted in stenotic vessels and their impact on hemodynamics in stenotic vessels is not well understood. In particular, there is a lack of studies considering cell-to-cell interactions at microscopic scale. This paper aims to provide a qualitative analysis on the dynamics of malaria-infected RBCs in stenotic microvessels. Since the malaria-infected RBC gradually loses its deformability and develops adhesiveness through the three stages of infection ring, trophozoite (early trophozoite, late trophozoite), and schizont, this study considers the ring and trophozoite stages in which the cells become stiffer and more adhesive while the shape of the RBCs is not significantly modified. The RBC was simulated by a spring model and the hardening of the parasitized cell was mimicked by varying the membrane constants. The malaria-infected RBCs were assumed existing as aggregates with firm or loose adhesion. By using fictitious domain-immersed boundary formalism in two dimensions, we simulated the transit of RBC aggregates through a prototypical channel with a contraction. By studying the motion and dissociation of RBC aggregates and flow characteristics, we delineated the contribution to hemodynamics from each of the three factors, hardening of the membrane, aggregation strength, and stenosis magnitude.

## 2. Methods

We considered a two-dimensional microvessel with a symmetric stenosis and employed numerical simulations to study the rheological behavior of RBC aggregates in the blood flow. In this study, blood was assumed to be a suspension of RBCs in an incompressible, Newtonian fluid with constant density and viscosity. In order to simulate the blood flow and fluid-cell interactions in this irregular-shaped domain, the fictitious domain method was combined with the immersed boundary method and the RBCs have been modeled by the spring model.

**2.1. Red Blood Cell Model.** Two types of RBC model are widely used currently, namely, elastic membrane models [19, 23] and spring models [20, 24–27]. In this paper, we adopted the spring model introduced in [24, 28] and modeled individual RBC as cytoplasm enclosed by a membrane represented by a finite number of membrane particles connected by springs. The springs of stretch/compression and bending modulus change its length and the bending angle between two neighboring springs under external force. The elastic moduli are affected in disease conditions [29, 30]. Evidence shows that malaria-infected RBC has increased stiffness, which is closely related to the cell bending modulus. In this paper, we modeled malaria-infected RBC with different deformability by varying the bending constant of the spring. The shape of the RBCs was chosen with the reduced area  $s^* = 0.481$ .

**2.2. Aggregation Kinetics.** The hardening of the RBCs is due to the parasite of the *P-falciparum*. However, the stickiness of the cell surface and the mechanism of the aggregation still remain disputable. Two different theoretical models, namely, the bridging model [18, 31] and the depletion model [32], coexist nowadays. Although they are distinct in the cause of the aggregating force, both of them predict the force being attractive at far and repulsive at near distance. Because the investigation of the mechanism of aggregation is not within the scope of this research, we chose a simple model [20] in which aggregation of RBCs was achieved by introducing an aggregating force existing in a neighborhood of membrane particles and the aggregating force was derived from  $F = -\partial E/\partial r$  with the Morse-type potential  $E$  as

$$E = D_e \left( e^{2\beta(r_0-r)} - 2e^{\beta(r_0-r)} \right), \quad (1)$$

where  $D_e$  is the energy constant corresponding to the density of the aggregating particles;  $\beta$  is the scaling factor which relates to the thickness of the depletion layer or interactive distance;  $r_0$  is the reference distance or zero-force distance.

The scaling aggregation force ( $F/D_e$ ) as a function of separation distance for different parameters is shown in Figure 1. When the value of the scaling factor is negative, the force is attractive; when the value of the force is positive, the force is repulsive. The force decreases almost to zero at far enough distance. Aggregation could be increased either by increasing  $D_e$  or by decreasing  $\beta$ . On the other hand, decreasing in  $\beta$  and increasing in  $r_0$  may raise the depletion thickness and the equilibrium distance of the RBCs in aggregates.

**2.3. The Fictitious Domain-Immersed Boundary Scheme.** The flow region we studied was a stenotic microchannel for which the regular structured mesh was not applicable at the boundary of the region. Thus, we adopted the fictitious domain method because in this method the irregular-shaped domain is extended to regular shape so that simple structured mesh instead of unstructured mesh can be used, which substantially reduces computational complexity of the algorithm. The fictitious domain method and its applications to fluid flow problems have been extensively described [33, 34]. To employ the fictitious domain method, the flow region  $\Omega_f$  was

TABLE 1: Parameters used for the simulations.

Parameter	Symbol	Value
Blood plasma density	$\rho$	1.0 g/cm <sup>3</sup>
Blood plasma viscosity	$\mu$	1.2 cp
Aggregating energy constant	$D_e$	0.01, 0.1, 1.0 $\mu$ /m <sup>2</sup>
Scaling factor	$\beta$	80 $\mu$ m <sup>-1</sup>
Reference length	$r_0$	0.49 $\mu$ m
Spring constants for red blood cell membrane	$k_b$	$3.0 \times 10^{-13}$ , $3.0 \times 10^{-12}$ Nm
Length of the channel	$L$	140 $\mu$ m
Radius of inlet (outlet)	$R$	30 $\mu$ m
Grid size	$h$	1/64 $\mu$ m
Time step	$\Delta t$	$1 \times 10^{-5}$ ms <sup>-1</sup>

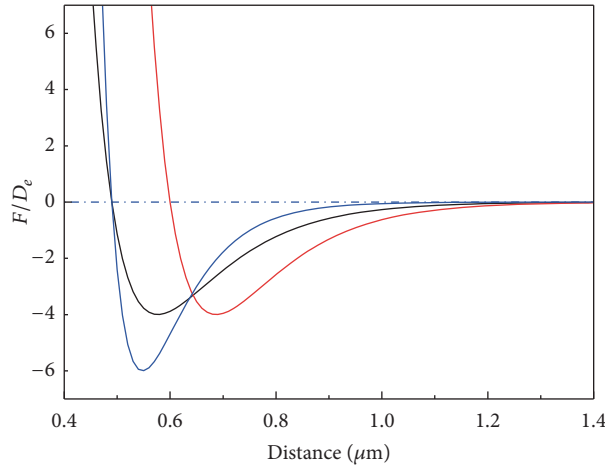


FIGURE 1: Dependence of aggregation force on distance for various parameters: black line:  $\beta = 80 \mu\text{m}^{-1}$  and  $r_0 = 0.49 \mu\text{m}$ ; red line:  $\beta = 80 \mu\text{m}^{-1}$  and  $r_0 = 0.6 \mu\text{m}$ ; blue line:  $\beta = 120 \mu\text{m}^{-1}$  and  $r_0 = 0.49 \mu\text{m}$ .

embedded in a rectangular domain denoted by  $\Omega$ . Then the fluid flow containing RBCs was solved in the bigger domain  $\Omega$ , and the no-flow condition in the solid region was treated as constraints. Therefore, the governing equations for the modeled problem were the following extended Navier-Stokes equations:

$$\begin{aligned} \rho \left[ \frac{\partial \mathbf{u}}{\partial t} + \mathbf{u} \cdot \nabla \mathbf{u} \right] &= -\nabla p + \mu \Delta \mathbf{u} + \mathbf{f}, \quad \text{in } \Omega_f, \\ \nabla \cdot \mathbf{u} &= 0, \quad \text{in } \Omega_f, \\ \mathbf{u} &= \mathbf{0}, \quad \text{in } \Omega \setminus \Omega_f, \end{aligned} \quad (2)$$

where  $\mathbf{u}(\mathbf{x}, t)$  and  $p$  are the fluid velocity and pressure anywhere in the flow;  $\rho$  is the fluid density;  $\mu$  is the fluid viscosity. The boundary conditions were such that, on  $\partial\Omega_f$ , a no-slip condition was applied and, at the inlet and outlet of the channel, a periodic flow condition was enforced. A detailed description of the solution method of (2) can be found elsewhere [33, 34]. In this study, the fluid-cell interaction was dealt with by the immersed boundary method developed by Peskin et al. [20, 35].

### 3. Results and Discussion

We studied the hydrodynamic behavior of multiple red blood cell aggregates in a horizontal channel filled with Newtonian fluid with a symmetric stenosis at the central part of the vessel. The blood plasma density and plasma viscosity were presumed fixed values. We performed a series of simulations to study RBC deformation, flow field, and cell-cell interactions as the aggregates traversed the stenotic vessel. The fluid flow was generated from left to right by a constant pressure drop. A stream of flow approaching the stenosis contracted to a high speed flow at the throat of the stenosis. Afterwards, the flow was allowed to develop fully along the straight rectangular channel. At the meantime, prelocated multiple RBC aggregates flowed with the fluid in the channel. The parameters used are given in Table 1. For the parameter used in this study, larger spring constant for RBC membrane and higher aggregation energy constant correspond to malaria-infected RBCs at more severe infection stages.

**3.1. Aggregation of Red Blood Cells.** Aggregates of four cells used in the simulations were formed in static plasma before putting them in the flow channels. The red blood cells were

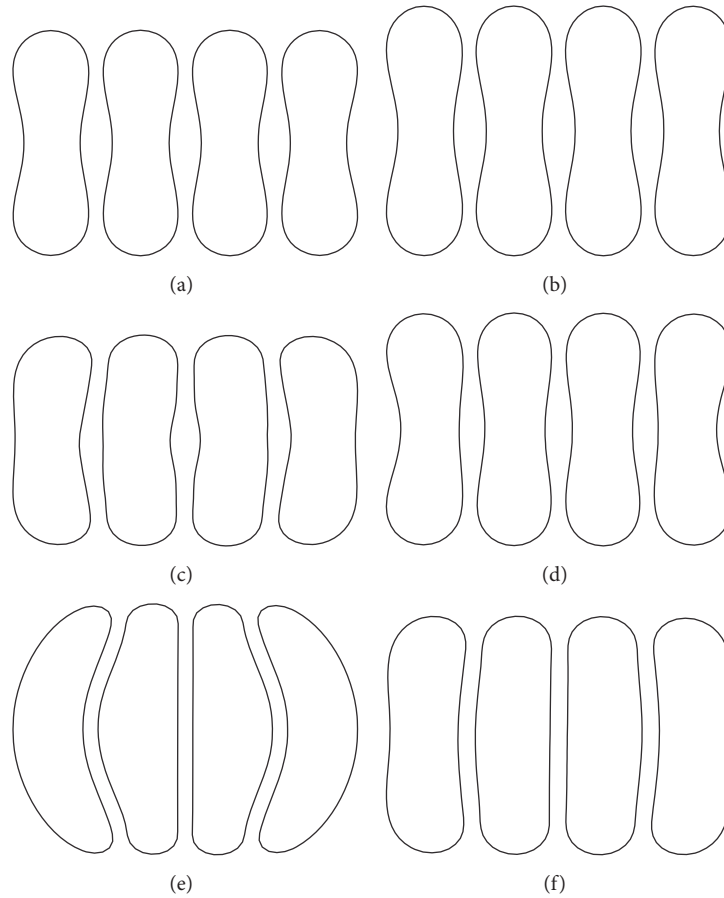


FIGURE 2: Equilibrium configuration of RBC aggregates for different simulation parameters: (a)  $D_e = 0.01 \mu\text{J}/\text{m}^2$  and  $k_b = 3.0 \times 10^{-13} \text{ Nm}$ ; (b)  $D_e = 0.01 \mu\text{J}/\text{m}^2$  and  $k_b = 3.0 \times 10^{-12} \text{ Nm}$ ; (c)  $D_e = 0.1 \mu\text{J}/\text{m}^2$  and  $k_b = 3.0 \times 10^{-13} \text{ Nm}$ ; (d)  $D_e = 0.1 \mu\text{J}/\text{m}^2$  and  $k_b = 3.0 \times 10^{-12} \text{ Nm}$ ; (e)  $D_e = 1.0 \mu\text{J}/\text{m}^2$  and  $k_b = 3.0 \times 10^{-13} \text{ Nm}$ ; and (f)  $D_e = 1.0 \mu\text{J}/\text{m}^2$  and  $k_b = 3.0 \times 10^{-12} \text{ Nm}$ .

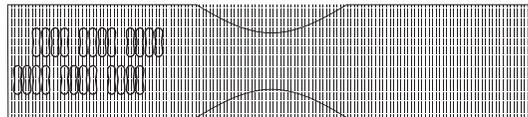


FIGURE 3: Schematic illustration of initial configuration of RBC aggregates in the blood vessel at the beginning of the simulations.

placed face-to-face in static plasma initially. The center-to-center distance was close enough in order for the aggregation force to take effect. When the simulation starts, red blood cells approached each other and reached an equilibrium configuration. The red blood cells were modeled by two membrane constants for two different stiffness and three aggregation strengths for different adhesiveness. Therefore, six different configurations were obtained and they are shown in Figure 2. The configuration in Figure 2(a) corresponds to healthy RBC. The configurations in Figures 2(b)–2(d) may correspond to the ring stage and early trophozoite stage infection, while Figures 2(e) and 2(f) are assumed to correspond to the late stage of trophozoite in which both the stiffness and stickiness of the cell membrane increase considerably.

**3.2. Motion and Dissociation of Aggregates.** The microvessel in this study is a  $140 \mu\text{m}$  long,  $30 \mu\text{m}$  wide two-dimensional channel with symmetric stenosis formed at the central location. The geometry of the fluid domain and the initial placement of the RBC aggregates are illustrated in Figure 3. Blood flow in the stenotic vessel was driven by a constant pressure gradient imposed at the inlet and the outlet. The pressure gradient was determined such that the maximum flow velocity was about  $20 \text{ cm/s}$  (a typical value in arterioles [36]).

**3.2.1. In the Channel with 40% Stenosis.** The motion and dissociation of 6 RBC aggregates in a 40% stenosis microvessel have been simulated. The results for two membrane bending

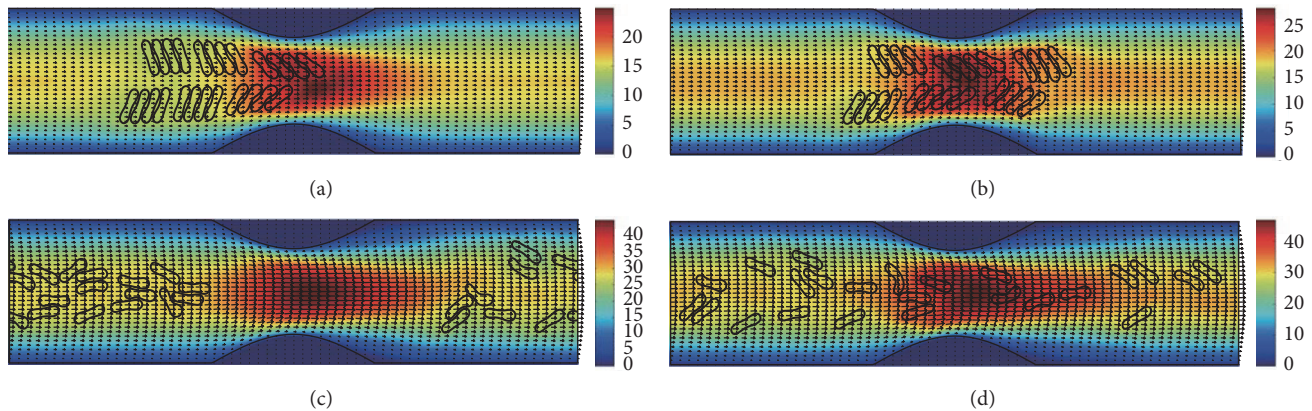


FIGURE 4: Motion of red blood cell aggregates (configuration in Figure 2(a)) in the microchannel with 40% stenosis at time instants (a)  $t = 0.35$  ms; (b)  $t = 0.45$  ms; (c)  $t = 1.34$  ms; (d)  $t = 4.80$  ms.

constants and three aggregating strengths are shown in Figures 4–9 for the initial configurations in Figure 2. The snapshots are for four time instants with the second subfigure showing the instant when the mean location of all cells was at the throat of the stenosis. When the RBCs are softer (Figures 4, 6, and 8), they experienced more deformation in the flow even after the dissociation. The aggregates with weak aggregating strength (Figures 4 and 5) were dissociated easily by the hydrodynamic force and the RBCs existed as dispersed individual cells after long enough elapsed time. The aggregates with mild aggregating strength (Figures 6 and 7) were partially disaggregated from their initial configurations. Smaller aggregates of two to three cells were observed in the simulation. However, when the aggregating strength was strong (Figures 8 and 9), the hydrodynamic force was unable to disaggregate the RBC aggregates. Aggregates underwent some deformation but however kept their initial configuration even at the stenosis. Because the velocity of the flow at the throat of the stenosis increased significantly due to the contraction, the aggregates lag behind which caught up the upstream ones. Eventually, agglomeration and rouleaux of RBCs of bigger size were formed by the aggregating force. In addition, more disturbance of the flow field around the aggregates or the cells has been noted.

**3.2.2. In the Channel with 50% Stenosis.** Figures 10–15 show the motion of 6 RBC aggregates in the microvessel with 50% stenosis. The parameters and the initial configuration of the aggregates were the same as in the last section. It has been shown in the simulations that the velocity of the blood flow at the throat of the stenosis increased comparing to the 40% stenosis vessel. The disassociation of the aggregates and the deformation of the RBCs were similar to the results for the 40% stenosis when the aggregating strength was weak or mild. However, when the aggregating strength became strong, the larger agglomeration or rouleaux of RBCs were formed. The reason for this phenomenon is because that the increase of stenosis severity increased blood velocity at the stenosis. Thus, the downstream cells easily caught up the

upstream cells which were slowed down by the friction of the vessel wall.

**3.2.3. In the Channel with 60% Stenosis.** Simulation also has been done in the microchannel with 60% stenosis and the results are shown in Figures 16–21. As the stenosis severity increased to 60%, the microvessel was blocked more than the last two cases. Unlike the cases of 40% and 50% stenosis, the aggregates with mild aggregating strength did not dissociate completely even when the elapsed time was long enough. On the other hand, they almost kept their original configuration for a long time (Figures 18(c) and 19(c)) before some of them disassociating into smaller aggregates or individual cells. Furthermore, aggregates formed by RBCs with strong aggregating strength attracted together and more compact aggregates were observed than in 50% stenosis case. It is reasonable to conclude that the increase of stenosis severity facilitated aggregation of malaria-infected RBCs. More disturbance of the flow at the throat of the stenosis was also observed.

In general, for all three stenosis levels, healthy RBCs and aggregates with ring stage or early trophozoite-stage infection (configurations in Figures 2(b)–2(d)) passed through the stenosis easily and dissociate into individual cells or smaller aggregates. They also recovered their normal biconcave shape quickly after passage through the constriction. However, configurations in Figures 2(e) and 2(f) maintained and even formed larger aggregates in the stenotic vessel. They tended to block the flow at the mouth of the stenosis and this can be seen from the decrease of the flow velocities in the straight section of the channel. Thus, the delivery of nutrients and removal of toxins by RBCs will be severely decreased and the phenomena show the behavior of late-stage trophozoite. These results are qualitatively consistent with the *in vivo* experimental findings [3].

### 3.3. Flow Characteristics

**3.3.1. Effect of Stenosis Magnitude.** In Figures 22(a)–22(f), velocity at the stenosis verses radial location for three

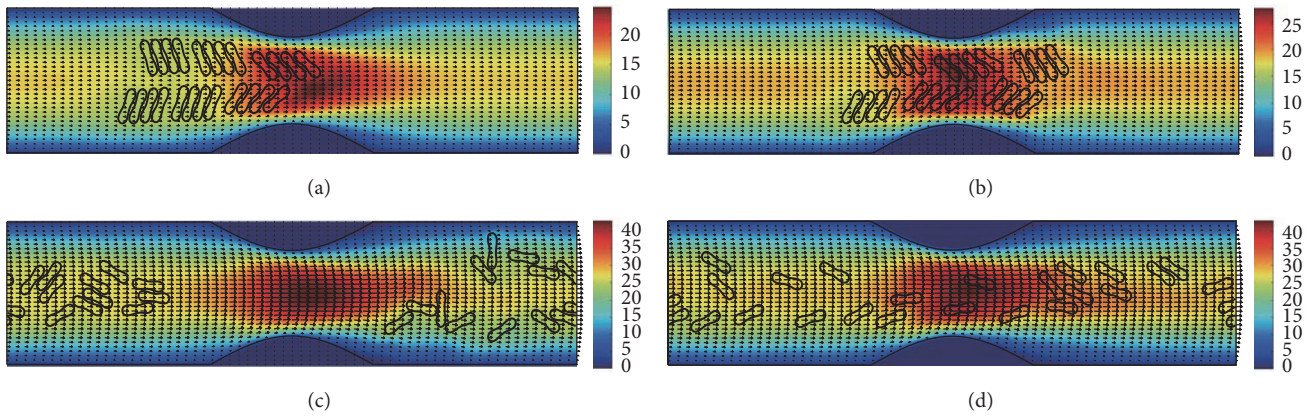


FIGURE 5: Motion of red blood cell aggregates (configuration in Figure 2(b)) in the microchannel with 40% stenosis at time instants (a)  $t = 0.35$  ms; (b)  $t = 0.46$  ms; (c)  $t = 1.35$  ms; (d)  $t = 4.80$  ms.

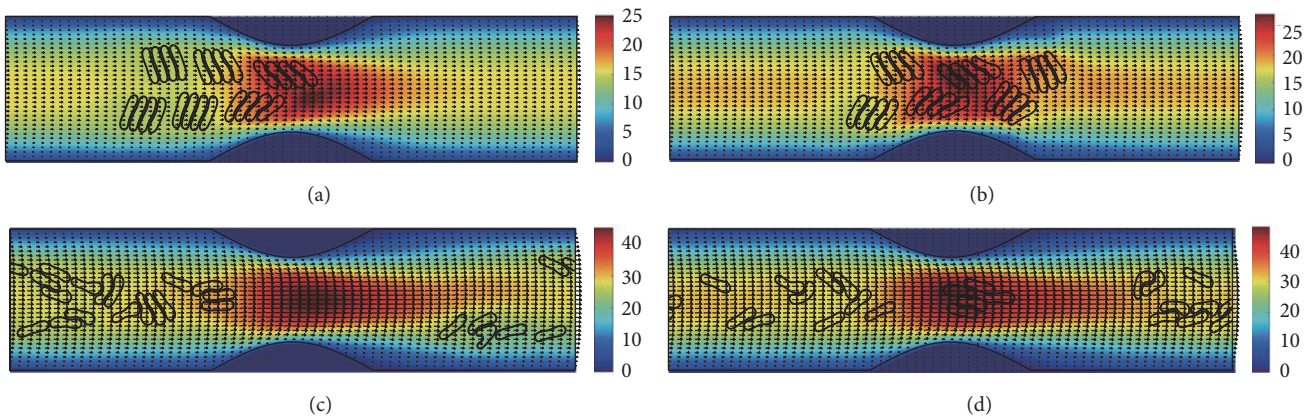


FIGURE 6: Motion of red blood cell aggregates (configuration in Figure 2(c)) in the microchannel with 40% stenosis at time instants (a)  $t = 0.35$  ms; (b)  $t = 0.46$  ms; (c)  $t = 1.37$  ms; (d)  $t = 4.80$  ms.

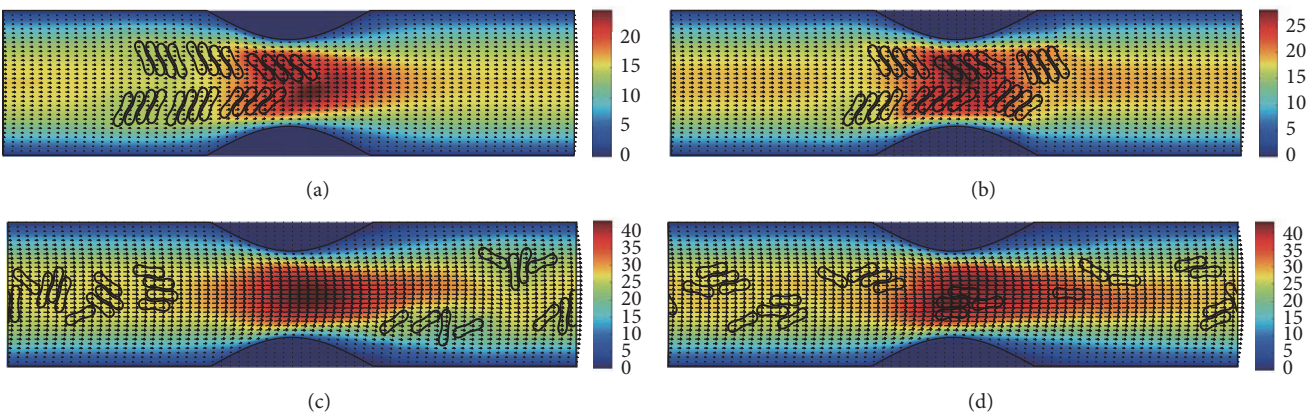


FIGURE 7: Motion of red blood cell aggregates (configuration in Figure 2(d)) in the microchannel with 40% stenosis at time instants (a)  $t = 0.35$  ms; (b)  $t = 0.46$  ms; (c)  $t = 1.36$  ms; (d)  $t = 4.80$  ms.

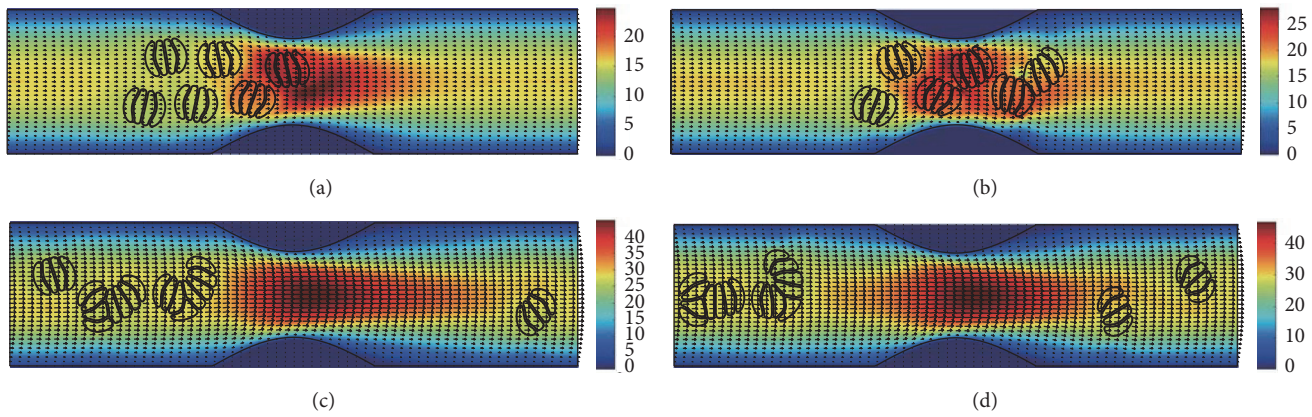


FIGURE 8: Motion of red blood cell aggregates (configuration in Figure 2(e)) in the microchannel with 40% stenosis at time instants (a)  $t = 0.35$  ms; (b)  $t = 0.46$  ms; (c)  $t = 1.39$  ms; (d)  $t = 4.80$  ms.

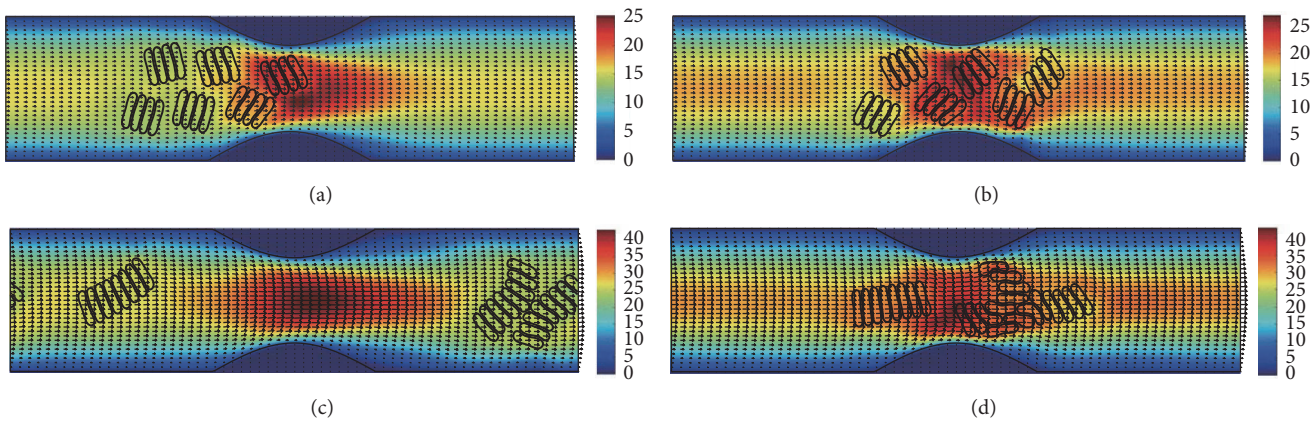


FIGURE 9: Motion of red blood cell aggregates (configuration in Figure 2(f)) in the microchannel with 40% stenosis at time instants (a)  $t = 0.35$  ms; (b)  $t = 0.46$  ms; (c)  $t = 1.37$  ms; (d)  $t = 4.80$  ms.

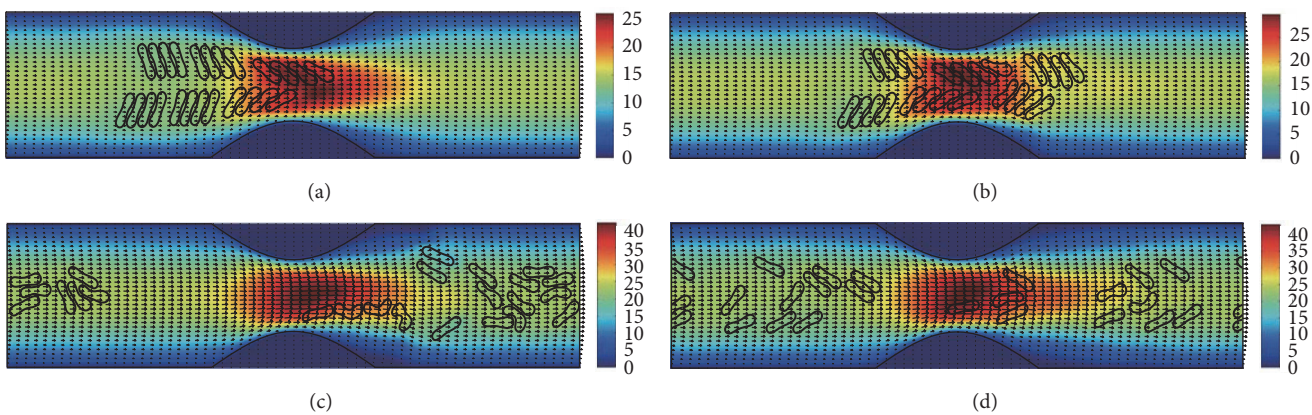


FIGURE 10: Motion of red blood cell aggregates (configuration in Figure 2(a)) in the microchannel with 50% stenosis at time instants (a)  $t = 0.37$  ms; (b)  $t = 0.47$  ms; (c)  $t = 1.38$  ms; (d)  $t = 4.80$  ms.

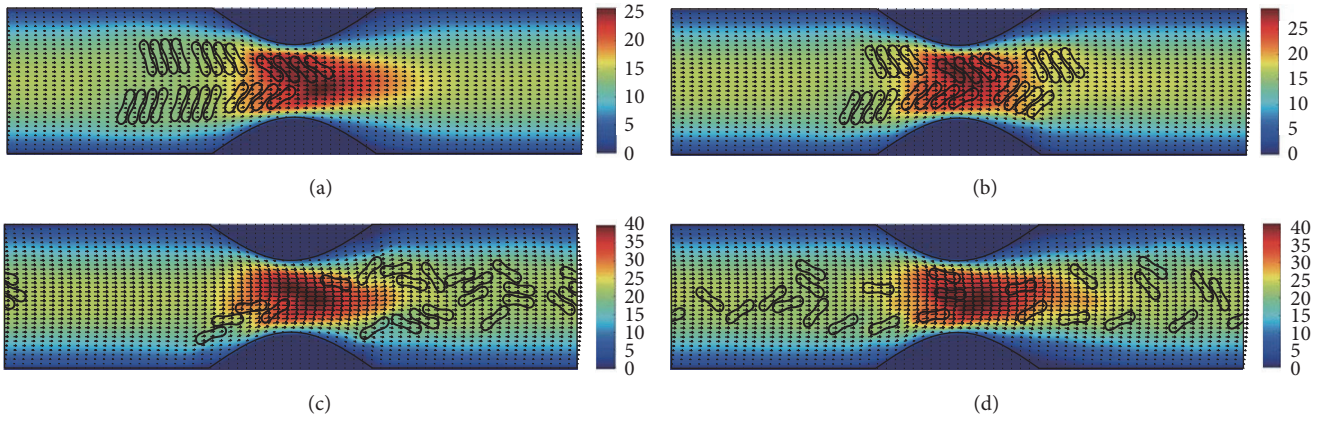


FIGURE 11: Motion of red blood cell aggregates (configuration in Figure 2(b)) in the microchannel with 50% stenosis at time instants (a)  $t = 0.37$  ms; (b)  $t = 0.48$  ms; (c)  $t = 1.34$  ms; (d)  $t = 4.80$  ms.

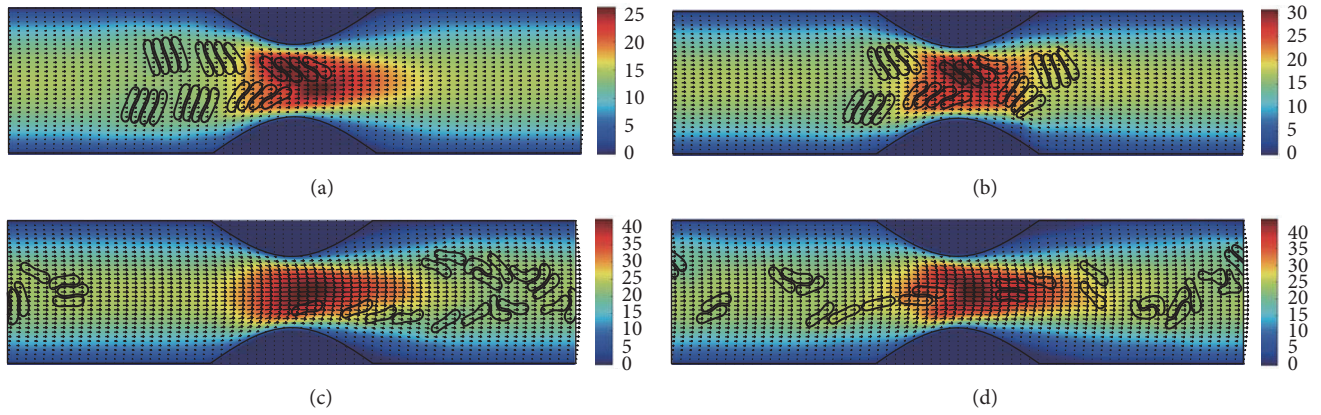


FIGURE 12: Motion of red blood cell aggregates (configuration in Figure 2(c)) in the microchannel with 50% stenosis at time instants (a)  $t = 0.37$  ms; (b)  $t = 0.47$  ms; (c)  $t = 1.37$  ms; (d)  $t = 4.80$  ms.

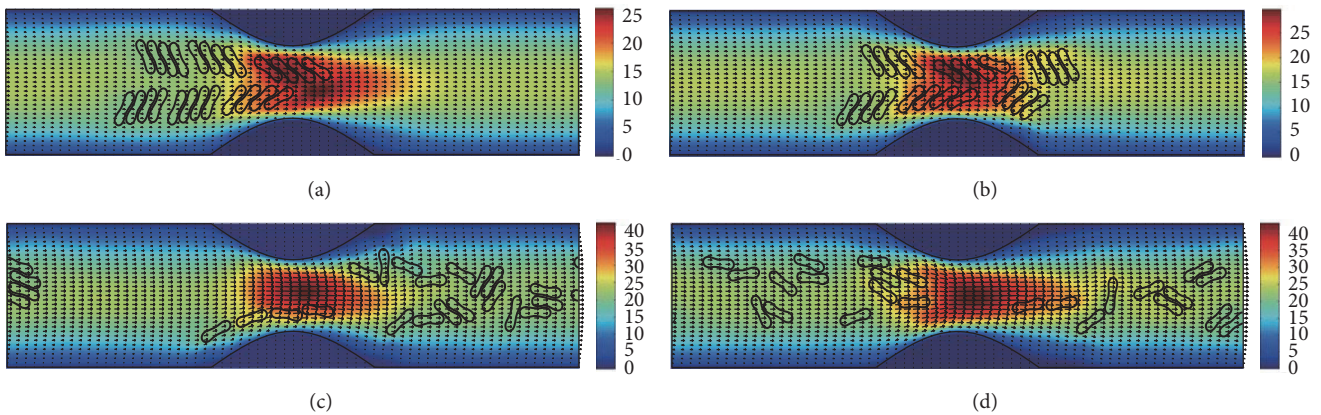


FIGURE 13: Motion of red blood cell aggregates (configuration in Figure 2(d)) in the microchannel with 50% stenosis at time instants (a)  $t = 0.37$  ms; (b)  $t = 0.48$  ms; (c)  $t = 1.37$  ms; (d)  $t = 4.80$  ms.

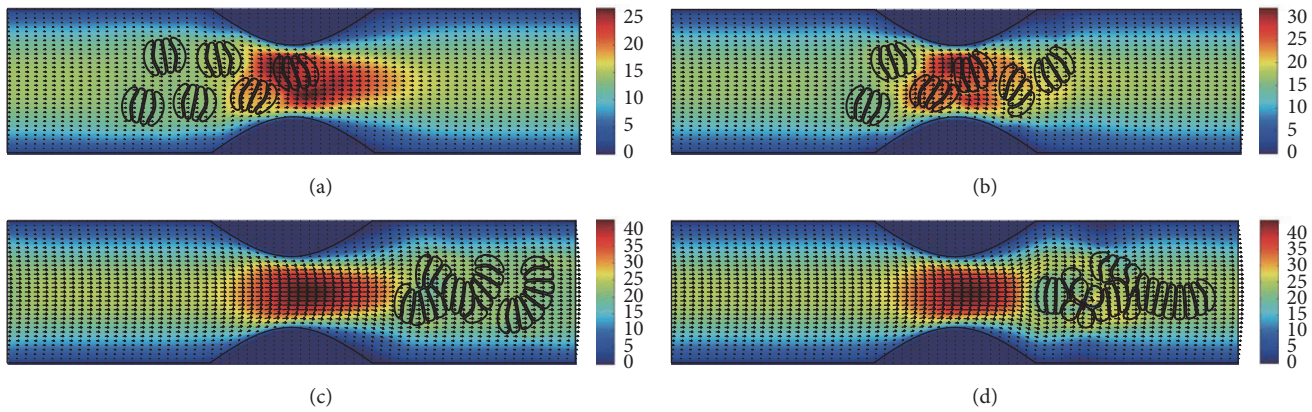


FIGURE 14: Motion of red blood cell aggregates (configuration in Figure 2(e)) in the microchannel with 50% stenosis at time instants (a)  $t = 0.37$  ms; (b)  $t = 0.48$  ms; (c)  $t = 1.36$  ms; (d)  $t = 4.80$  ms.

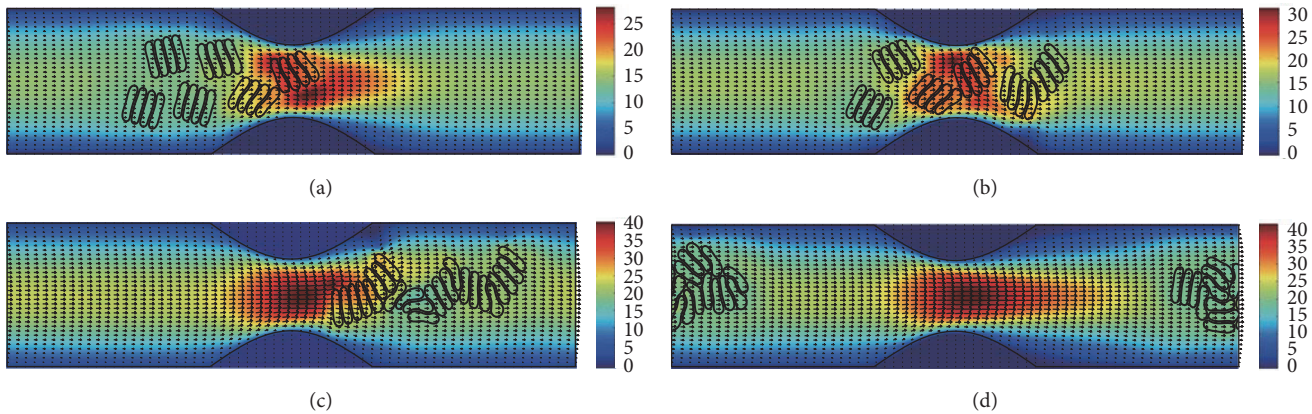


FIGURE 15: Motion of red blood cell aggregates (configuration in Figure 2(f)) in the microchannel with 50% stenosis at time instants (a)  $t = 0.37$  ms; (b)  $t = 0.49$  ms; (c)  $t = 1.35$  ms; (d)  $t = 4.80$  ms.

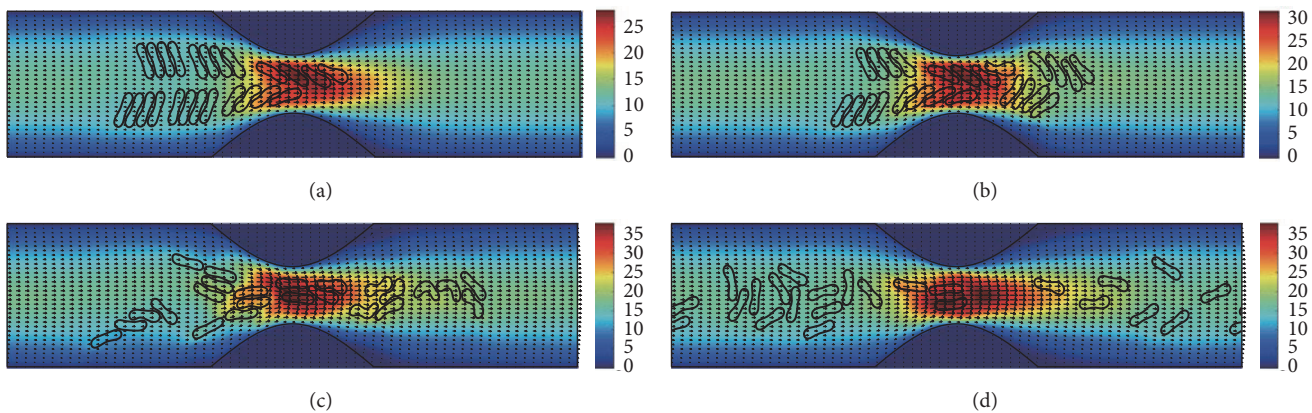


FIGURE 16: Motion of red blood cell aggregates (configuration in Figure 2(a)) in the microchannel with 60% stenosis at time instants (a)  $t = 0.39$  ms; (b)  $t = 0.51$  ms; (c)  $t = 1.37$  ms; (d)  $t = 4.80$  ms.

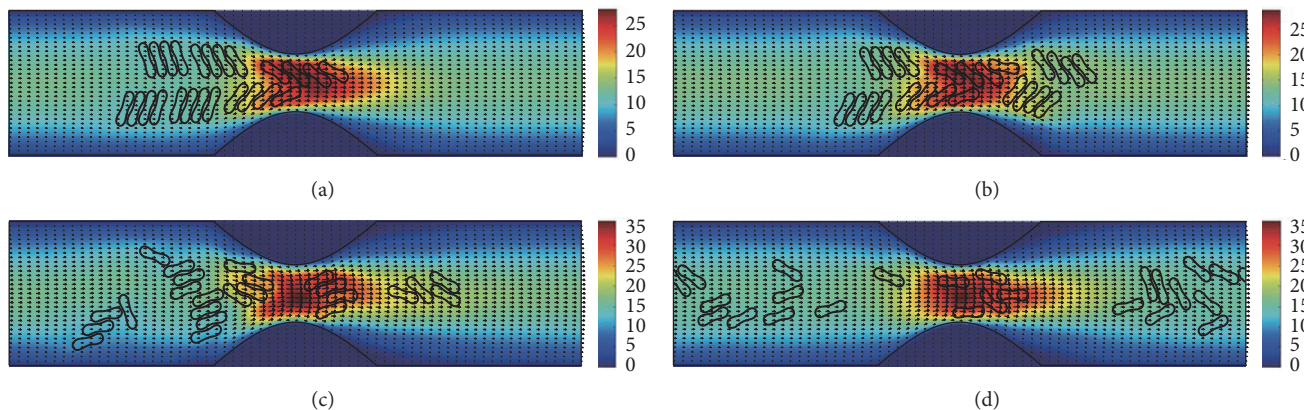


FIGURE 17: Motion of red blood cell aggregates (configuration in Figure 2(b)) in the microchannel with 50% stenosis at time instants (a)  $t = 0.39$  ms; (b)  $t = 0.52$  ms; (c)  $t = 1.37$  ms; (d)  $t = 4.80$  ms.

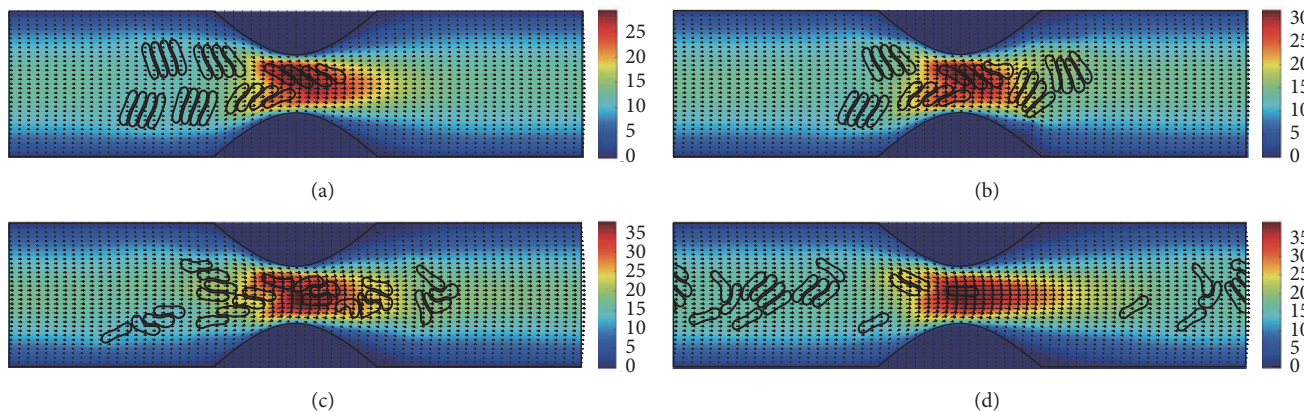


FIGURE 18: Motion of red blood cell aggregates (configuration in Figure 2(c)) in the microchannel with 50% stenosis at time instants (a)  $t = 0.39$  ms; (b)  $t = 0.51$  ms; (c)  $t = 1.35$  ms; (d)  $t = 4.80$  ms.

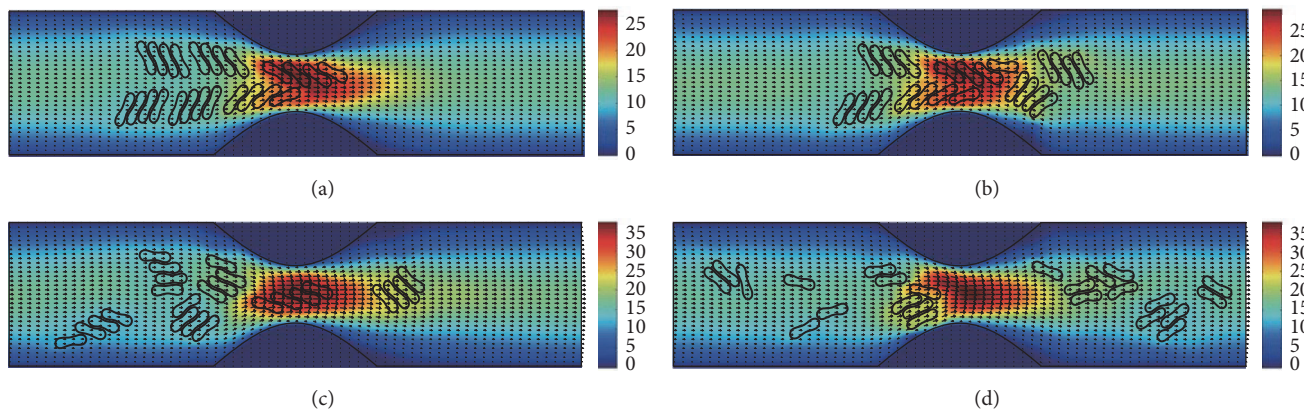


FIGURE 19: Motion of red blood cell aggregates (configuration in Figure 2(d)) in the microchannel with 50% stenosis at time instants (a)  $t = 0.39$  ms; (b)  $t = 0.52$  ms; (c)  $t = 1.34$  ms; (d)  $t = 4.80$  ms.

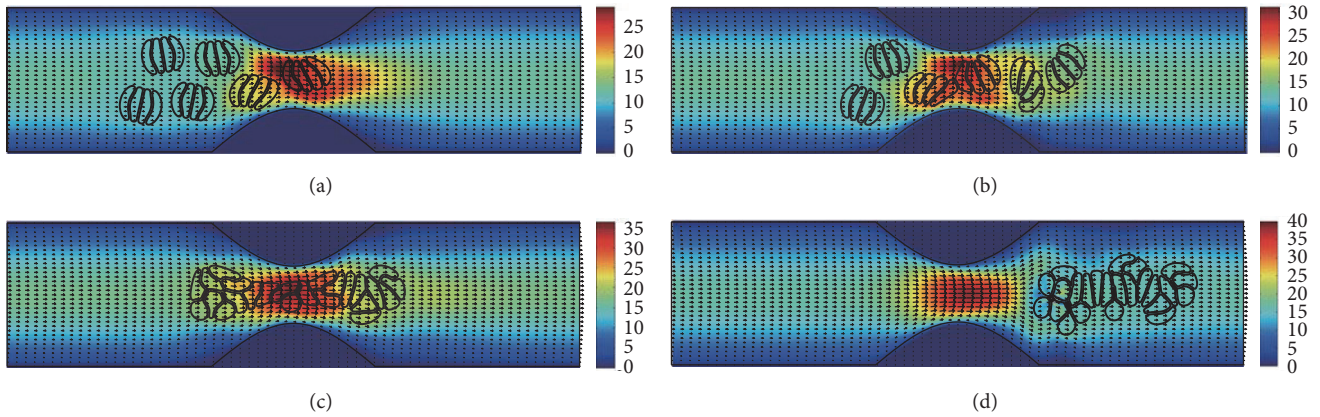


FIGURE 20: Motion of red blood cell aggregates (configuration in Figure 2(e)) in the microchannel with 50% stenosis at time instants (a)  $t = 0.39$  ms; (b)  $t = 0.52$  ms; (c)  $t = 1.38$  ms; (d)  $t = 4.80$  ms.

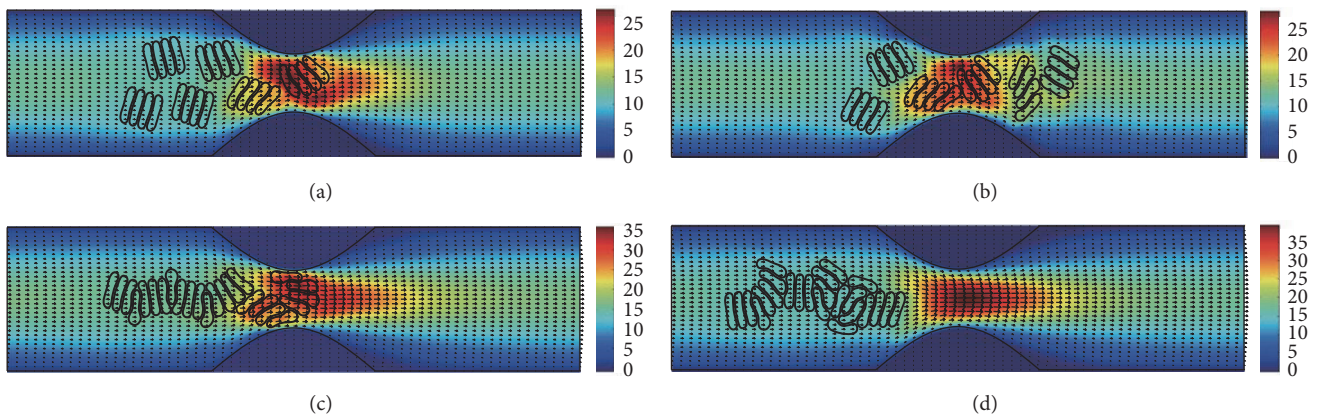


FIGURE 21: Motion of red blood cell aggregates (configuration in Figure 2(f)) in the microchannel with 50% stenosis at time instants (a)  $t = 0.40$  ms; (b)  $t = 0.53$  ms; (c)  $t = 1.36$  ms; (d)  $t = 4.80$  ms.

aggregation forces and two cell membrane constants are shown in the same panel for three stenosis magnitudes. The comparison shows that the velocity increased as the stenosis increased. This trend was more profound for the soft cells with mild and strong aggregating strength. It can also be seen from Figure 22 that velocity profiles were more distorted when the aggregating strength was strong. The asymmetry of the velocity profiles was mainly due to the initial asymmetric location of the aggregates.

**3.3.2. Effect of Aggregation Force.** Next we investigated the effect of aggregation force on the velocity profile at the throat of stenosis (Figure 23). It is noted that the flow velocity at the throat of the stenosis decreased as the aggregation force increased. This trend was found for all the stenosis magnitudes and both the soft and the rigid red blood cells. However, it is also observed that the decrease of the velocity was not linear. When the aggregation force increased from weak (blue lines) to mild (red lines), the results showed little to no effect on the velocity. While when the aggregation force

became strong (black lines), the effect was significant. The results indicated that increasing of aggregation strength up to a certain level led to increase of flow resistance in the stenotic vessels.

**3.3.3. Effect of Cell Deformability.** The cell membrane deformability also had an effect on the velocity of blood flow at the stenosis and the results are revealed in Figures 24(a)–24(i). Two membrane constant values have been used in the simulations and two types of RBCs were modeled with these constants, namely, soft cells and rigid cells. In Figure 24, black lines represented the velocity profile at the throat of the stenosis of the blood flow with soft RBCs, and red lines are for the blood flow with rigid cells. Overall, the flow velocity decreased with the increase in stiffness of the cell. In particular, the effect was more profound when the stenosis was more severe or when the aggregation force was stronger. Figure 24(a) shows the velocity profile for the case of 40% stenosis and the weak aggregation force. The velocity profile was relatively smooth and less disturbance was observed on

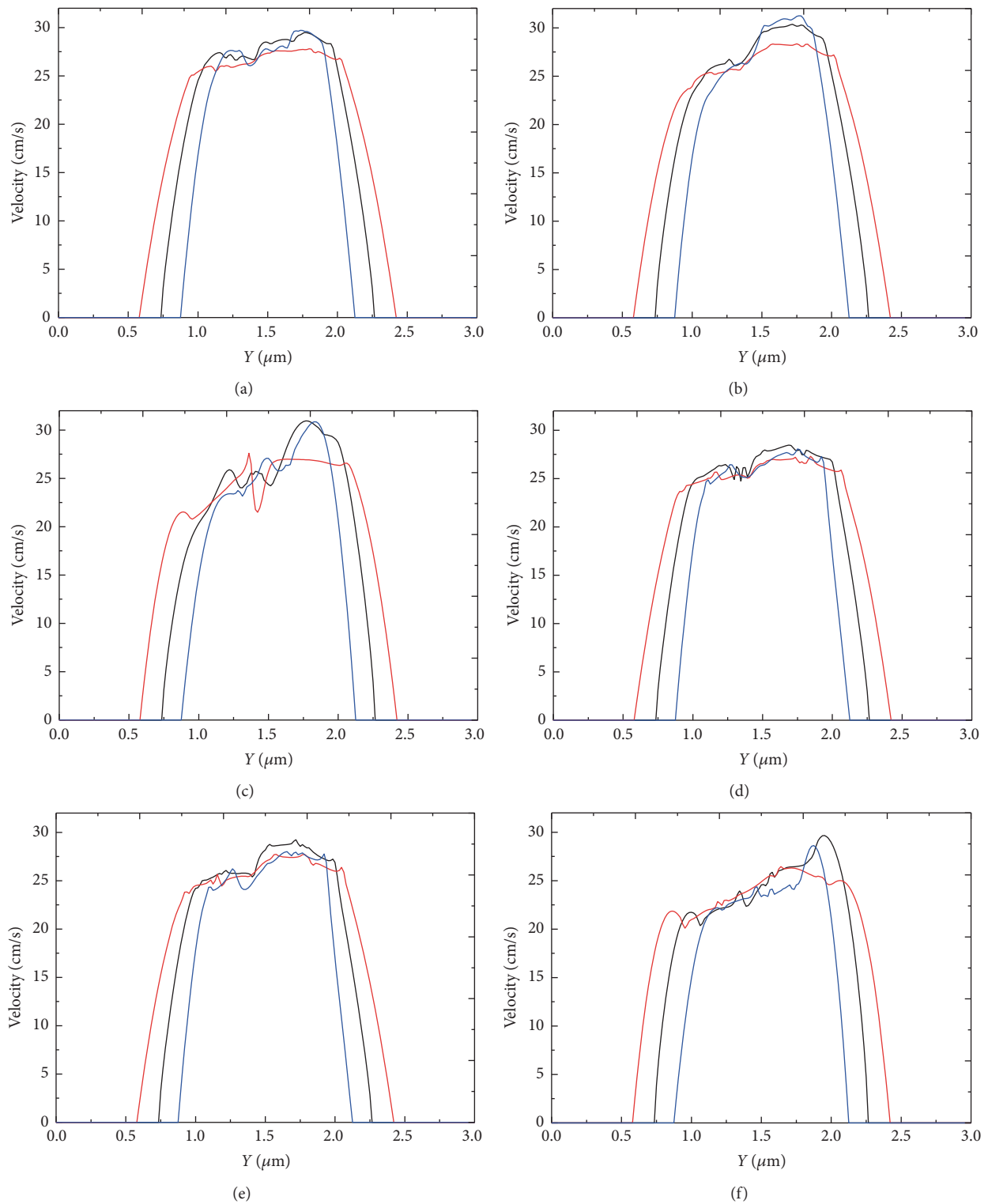


FIGURE 22: Blood velocity profile at the throat of the stenosis for three stenosis magnitudes: 40% stenosis (red lines); 50% stenosis (black lines); 60% stenosis (blue lines). (a)  $D_e = 0.01 \mu\text{J}/\text{m}^2$  and  $k_b = 3.0 \times 10^{-13} \text{ Nm}$ ; (b)  $D_e = 0.1 \mu\text{J}/\text{m}^2$  and  $k_b = 3.0 \times 10^{-13} \text{ Nm}$ ; (c)  $D_e = 1.0 \mu\text{J}/\text{m}^2$  and  $k_b = 3.0 \times 10^{-13} \text{ Nm}$ ; (d)  $D_e = 0.01 \mu\text{J}/\text{m}^2$  and  $k_b = 3.0 \times 10^{-12} \text{ Nm}$ ; (e)  $D_e = 0.1 \mu\text{J}/\text{m}^2$  and  $k_b = 3.0 \times 10^{-12} \text{ Nm}$ ; and (f)  $D_e = 1.0 \mu\text{J}/\text{m}^2$  and  $k_b = 3.0 \times 10^{-12} \text{ Nm}$ .

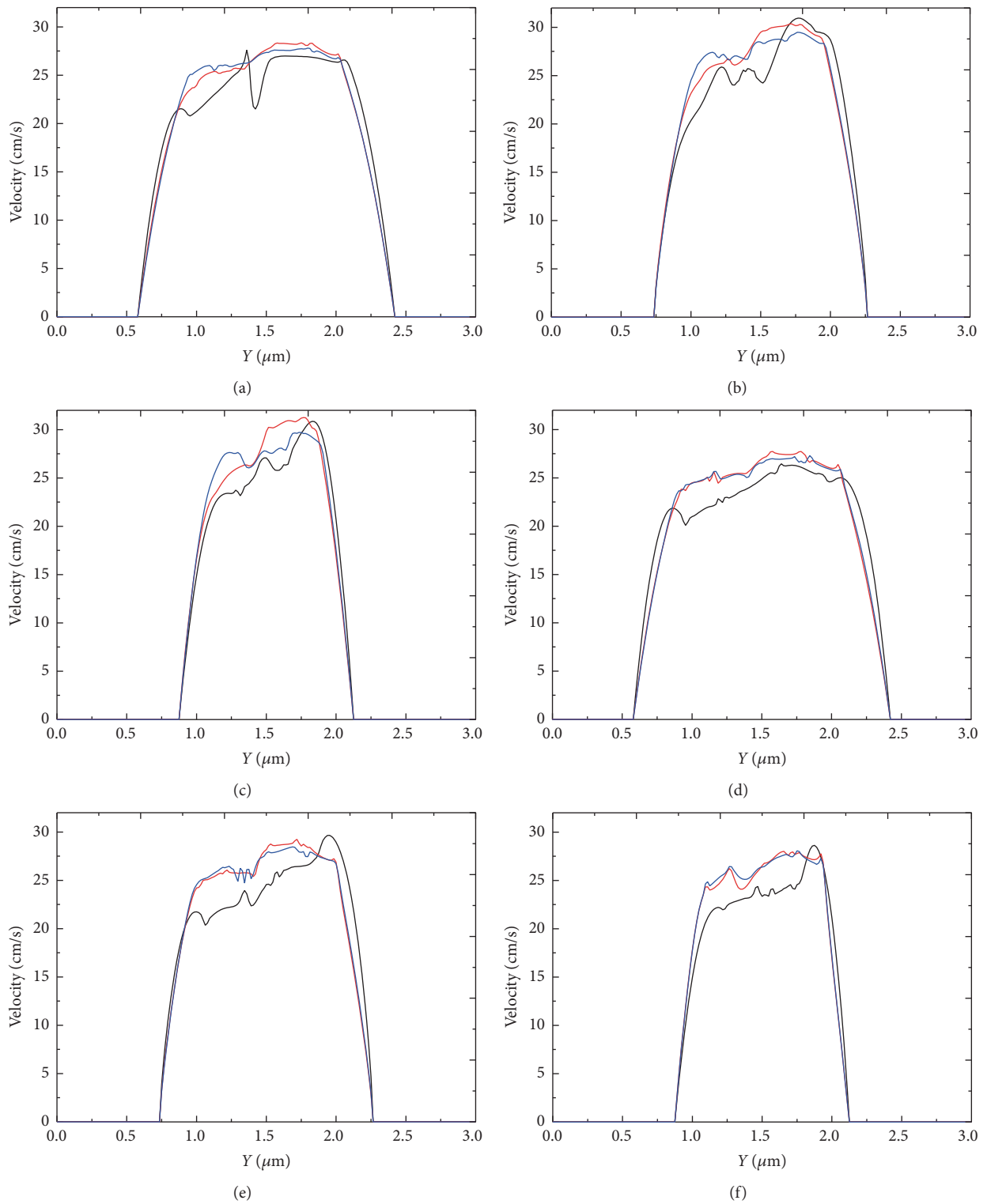


FIGURE 23: Blood velocity profile at the throat of the stenosis for three aggregating strengths:  $D_e = 0.01 \mu\text{J}/\text{m}^2$  (red lines);  $D_e = 0.1 \mu\text{J}/\text{m}^2$  (blue lines);  $D_e = 1.0 \mu\text{J}/\text{m}^2$  (black lines). (a)  $k_b = 3.0 \times 10^{-13} \text{ Nm}$ , 40% stenosis; (b)  $k_b = 3.0 \times 10^{-13} \text{ Nm}$ , 50% stenosis; (c)  $k_b = 3.0 \times 10^{-13} \text{ Nm}$ , 60% stenosis; (d)  $k_b = 3.0 \times 10^{-12} \text{ Nm}$ , 40% stenosis; (e)  $k_b = 3.0 \times 10^{-12} \text{ Nm}$ , 50% stenosis; and (f)  $k_b = 3.0 \times 10^{-12} \text{ Nm}$ , 60% stenosis.

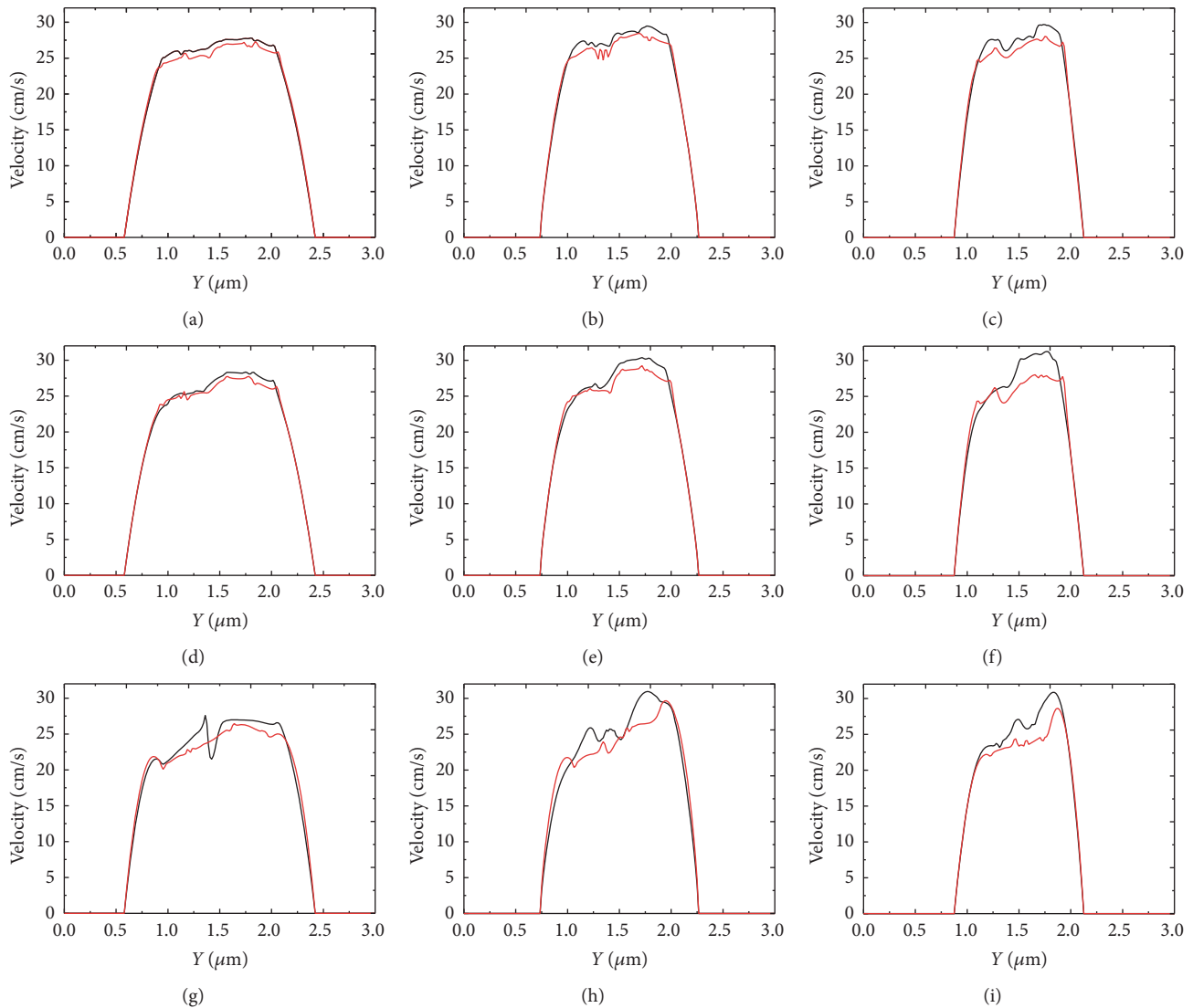


FIGURE 24: Blood velocity profile at the throat of the stenosis for two values of RBC deformability:  $k_b = 3.0 \times 10^{-13}$  Nm (red lines);  $k_b = 3.0 \times 10^{-12}$  Nm (black lines). (a)  $D_e = 0.01 \mu\text{J}/\text{m}^2$ , 40% stenosis; (b)  $D_e = 0.01 \mu\text{J}/\text{m}^2$ , 50% stenosis; (c)  $D_e = 0.01 \mu\text{J}/\text{m}^2$ , 60% stenosis; (d)  $D_e = 0.1 \mu\text{J}/\text{m}^2$ , 40% stenosis; (e)  $D_e = 0.1 \mu\text{J}/\text{m}^2$ , 50% stenosis; (f)  $D_e = 0.1 \mu\text{J}/\text{m}^2$ , 60% stenosis; (g)  $D_e = 1.0 \mu\text{J}/\text{m}^2$ , 40% stenosis; (h)  $D_e = 1.0 \mu\text{J}/\text{m}^2$ , 50% stenosis; and (i)  $D_e = 1.0 \mu\text{J}/\text{m}^2$ , 60% stenosis.

the curve. On the contrary, the velocity profiles were rougher in narrower stenotic vessels or when the aggregation of the RBCs was more severe.

#### 4. Conclusions

The main objective of this work is to probe how changes in the cell membrane rigidity, the aggregating strength, and the magnitude of the stenosis affect the transit of the malaria-infected RBC aggregates through stenotic microchannels. Two types of RBCs, namely, soft and rigid, have been studied under three different levels of aggregating strength. The simulations were performed over a range of stenosis magnitudes: 40%, 50%, and 60%.

It has been found in this study that soft RBCs with strong aggregating force formed the most compact aggregates. In

the aggregates, the RBCs experienced large deformation. Rigid ones with weak aggregating force formed the loosest aggregates. In these aggregates, the RBCs maintained their normal biconcave shape. In blood flow, the aggregates of weak aggregating strength were more likely to dissociate to individual cells, while the aggregates with strong aggregating strength would form even larger aggregates or rouleaux. The rigidity of the cell membrane hindered passage of the cell through microchannels and this result is qualitatively in agreement with experimental findings on the rheological behaviors of malaria-infected RBCs through a narrow constriction in a microchannel. The flow velocity at the throat of the stenosis decreased with increasing membrane modulus and more deviation from the parabolic profile was observed, especially for the narrower stenosis and stronger aggregating force.

The present study used a two-dimensional model to qualitatively simulate malaria-infected RBCs in stenotic microvessels. It is important to extend this algorithm to the physiologically relevant hematocrit contents in three-dimensional situation and compare the results with experimental observations quantitatively. It is also quite interesting to adapt the model for the more thorough investigation of RBC rheology at various stages of malaria infection as well as its impact on leukocyte migration. In addition, it provides a potential approach to investigate drug delivery at cellular level in microvessels involving infected RBCs.

## Competing Interests

The authors declare that they have no competing interests.

## Acknowledgments

The authors acknowledge the support of the National Natural Science Foundation of China (11671203) and the Foundation for Graduate Student Innovation at Nanjing University of Aeronautics and Astronautics, China.

## References

- [1] L. H. Miller, D. I. Baruch, K. Marsh, and O. K. Doumbo, "The pathogenic basis of malaria," *Nature*, vol. 415, no. 6872, pp. 673–679, 2002.
- [2] C. T. Lim, "Single cell mechanics study of the human disease malaria," *Journal of Biomechanical Science and Engineering*, vol. 1, no. 1, pp. 82–92, 2006.
- [3] J. P. Shelby, J. White, K. Ganesan, P. K. Rathod, and D. T. Chiu, "A microfluidic model for single-cell capillary obstruction by *Plasmodium falciparum*-infected erythrocytes," *Proceedings of the National Academy of Sciences of the United States of America*, vol. 100, no. 25, pp. 14618–14622, 2003.
- [4] S. Kim, A. S. Popel, M. Intaglietta, and P. C. Johnson, "Aggregate formation of erythrocytes in postcapillary venules," *American Journal of Physiology - Heart and Circulatory Physiology*, vol. 288, no. 2, pp. H584–H590, 2005.
- [5] M. Abkarian, M. Faivre, and H. Stone, "Red blood cell dynamics, deformation and separation in microfluidic devices," *Journal of Biomechanics*, vol. 39, no. 1, p. S332, 2006.
- [6] S. S. Lee, Y. Yim, K. H. Ahn, and S. J. Lee, "Extensional flow-based assessment of red blood cell deformability using hyperbolic converging microchannel," *Biomedical Microdevices*, vol. 11, no. 5, pp. 1021–1027, 2009.
- [7] H. Bow, I. V. Pivkin, M. Diez-Silva et al., "A microfabricated deformability-based flow cytometer with application to malaria," *Lab on a Chip*, vol. 11, no. 6, pp. 1065–1073, 2011.
- [8] V. Leble, R. Lima, R. Dias et al., "Asymmetry of red blood cell motions in a microchannel with a diverging and converging bifurcation," *Biomicrofluidics*, vol. 5, no. 4, Article ID 044120, 2011.
- [9] G. Tomaiuolo, M. Barra, V. Preziosi, A. Cassinese, B. Rotoli, and S. Guido, "Microfluidics analysis of red blood cell membrane viscoelasticity," *Lab on a Chip—Miniaturisation for Chemistry and Biology*, vol. 11, no. 3, pp. 449–454, 2011.
- [10] Q. Guo, S. J. Reiling, P. Rohrbach, and H. Ma, "Microfluidic biomechanical assay for red blood cells parasitized by *Plasmodium falciparum*," *Lab on a Chip—Miniaturisation for Chemistry and Biology*, vol. 12, no. 6, pp. 1143–1150, 2012.
- [11] Y. Imai, H. Kondo, T. Ishikawa, C. Teck Lim, and T. Yamaguchi, "Modeling of hemodynamics arising from malaria infection," *Journal of Biomechanics*, vol. 43, no. 7, pp. 1386–1393, 2010.
- [12] Y. Imai, K. Nakaaki, H. Kondo, T. Ishikawa, C. Teck Lim, and T. Yamaguchi, "Margination of red blood cells infected by *Plasmodium falciparum* in a microvessel," *Journal of Biomechanics*, vol. 44, no. 8, pp. 1553–1558, 2011.
- [13] D. A. Fedosov, B. Caswell, S. Suresh, and G. E. Karniadakis, "Quantifying the biophysical characteristics of *Plasmodium falciparum*-parasitized red blood cells in microcirculation," *Proceedings of the National Academy of Sciences of the United States of America*, vol. 108, no. 1, pp. 35–39, 2011.
- [14] T. Wu and J. J. Feng, "Simulation of malaria-infected red blood cells in microfluidic channels: passage and blockage," *Biomicrofluidics*, vol. 7, no. 4, Article ID 044115, 2013.
- [15] T. Ye, N. Phan-Thien, B. Cheong Khoo, and C. Teck Lim, "Numerical modelling of a healthy/malaria-infected erythrocyte in shear flow using dissipative particle dynamics method," *Journal of Applied Physics*, vol. 115, no. 22, Article ID 224701, 2014.
- [16] M. Navidbakhsh and M. Rezazadeh, "An immersed boundary-lattice Boltzmann model for simulation of malaria-infected red blood cell in micro-channel," *Scientia Iranica*, vol. 19, no. 5, pp. 1329–1336, 2012.
- [17] M. Aingaran, R. Zhang, S. K. Law et al., "Host cell deformability is linked to transmission in the human malaria parasite *Plasmodium falciparum*," *Cellular Microbiology*, vol. 14, no. 7, pp. 983–993, 2012.
- [18] P. Bagchi, P. C. Johnson, and A. S. Popel, "Computational fluid dynamic simulation of aggregation of deformable cells in a shear flow," *Journal of Biomechanical Engineering*, vol. 127, no. 7, pp. 1070–1080, 2005.
- [19] Y. Liu and W. K. Liu, "Rheology of red blood cell aggregation by computer simulation," *Journal of Computational Physics*, vol. 220, no. 1, pp. 139–154, 2006.
- [20] T. Wang, T.-W. Pan, Z. W. Xing, and R. Glowinski, "Numerical simulation of rheology of red blood cell rouleaux in microchannels," *Physical Review E—Statistical, Nonlinear, and Soft Matter Physics*, vol. 79, no. 4, Article ID 041916, 2009.
- [21] T. Wang, Z. Xing, and D. Xing, "Structure-induced dynamics of erythrocyte aggregates by microscale simulation," *Journal of Applied Mathematics*, vol. 2013, Article ID 409387, 13 pages, 2013.
- [22] H. Li, T. Ye, and K. Y. Lam, "Computational analysis of dynamic interaction of two red blood cells in a capillary," *Cell Biochemistry and Biophysics*, vol. 69, no. 3, pp. 673–680, 2014.
- [23] P. Bagchi, "Mesoscale simulation of blood flow in small vessels," *Biophysical Journal*, vol. 92, no. 6, pp. 1858–1877, 2007.
- [24] K. I. Tsubota, S. Wada, and T. Yamaguchi, "Simulation study on effects of hematocrit on blood flow properties using particle method," *Journal of Biomechanical Science and Engineering*, vol. 1, no. 1, pp. 159–170, 2006.
- [25] H. Noguchi and G. Gompper, "Shape transitions of fluid vesicles and red blood cells in capillary flows," *Proceedings of the National Academy of Sciences of the United States of America*, vol. 102, no. 40, pp. 14159–14164, 2005.

- [26] D. A. Fedosov, B. Caswell, and G. E. Karniadakis, "A multiscale red blood cell model with accurate mechanics, rheology, and dynamics," *Biophysical Journal*, vol. 98, no. 10, pp. 2215–2225, 2010.
- [27] D. A. Fedosov, B. Caswell, and G. E. Karniadakis, "Systematic coarse-graining of spectrin-level red blood cell models," *Computer Methods in Applied Mechanics and Engineering*, vol. 199, no. 29-32, pp. 1937–1948, 2010.
- [28] T. Wang, U. Rongin, and Z. Xing, "A micro-scale simulation of red blood cell passage through symmetric and asymmetric bifurcated vessels," *Scientific Reports*, vol. 6, Article ID 20262, 2016.
- [29] K. Tsukada, E. Sekizuka, C. Oshio, and H. Minamitani, "Direct measurement of erythrocyte deformability in diabetes mellitus with a transparent microchannel capillary model and high-speed video camera system," *Microvascular Research*, vol. 61, no. 3, pp. 231–239, 2001.
- [30] J. M. Higgins, D. T. Eddington, S. N. Bhatia, and L. Mahadevan, "Sickle cell vasoocclusion and rescue in a microfluidic device," *Proceedings of the National Academy of Sciences of the United States of America*, vol. 104, no. 51, pp. 20496–20500, 2007.
- [31] S. Chien and K.-M. Jan, "Ultrastructural basis of the mechanism of rouleaux formation," *Microvascular Research*, vol. 5, no. 2, pp. 155–166, 1973.
- [32] B. Neu and H. J. Meiselman, "Depletion-mediated red blood cell aggregation in polymer solutions," *Biophysical Journal*, vol. 83, no. 5, pp. 2482–2490, 2002.
- [33] R. Glowinski, T.-W. Pan, and J. Periaux, "A fictitious domain method for Dirichlet problem and applications," *Computer Methods in Applied Mechanics and Engineering*, vol. 111, no. 3-4, pp. 283–303, 1994.
- [34] R. Glowinski, T.-W. Pan, and J. Periaux, "A fictitious domain method for external incompressible viscous flow modeled by Navier-Stokes equations," *Computer Methods in Applied Mechanics and Engineering*, vol. 112, no. 1-4, pp. 133–148, 1994.
- [35] C. S. Peskin, "Numerical analysis of blood flow in the heart," *Journal of Computational Physics*, vol. 25, no. 3, pp. 220–252, 1977.
- [36] A. Quarteroni, "Cardiovascular mathematics," in *Proceedings of the International Congress of Mathematicians*, Madrid, Spain, August 2006.

## Review Article

# The Hedgehog Signaling Networks in Lung Cancer: The Mechanisms and Roles in Tumor Progression and Implications for Cancer Therapy

**Yoshinori Abe and Nobuyuki Tanaka**

*Department of Molecular Oncology, Institute for Advanced Medical Sciences, Nippon Medical School, 1-396 Kosugi-cho, Nakahara-ku, Kawasaki 211-8533, Japan*

Correspondence should be addressed to Nobuyuki Tanaka; [nobuta@nms.ac.jp](mailto:nobuta@nms.ac.jp)

Received 7 September 2016; Accepted 23 November 2016

Academic Editor: Daisuke Miyoshi

Copyright © 2016 Y. Abe and N. Tanaka. This is an open access article distributed under the Creative Commons Attribution License, which permits unrestricted use, distribution, and reproduction in any medium, provided the original work is properly cited.

Lung cancer is the most common cause of cancer-related death worldwide and is classified into small cell lung cancer (SCLC) and non-small-cell lung cancer (NSCLC). Several gene mutations that contribute to aberrant cell proliferation have been identified in lung adenocarcinoma, a part of NSCLC. Various anticancer drugs that target these mutated molecules have been developed for NSCLC treatment. However, although molecularly targeted drugs are initially effective for patients, the 5-year survival rate remains low because of tumor relapse. Therefore, more effective drugs for lung cancer treatment should be developed. The hedgehog (HH) signaling pathway contributes to organ development and stem cell maintenance, and aberrant activation of this signaling pathway is observed in various cancers including lung cancer. In lung cancer, HH signaling pathway upregulates cancer cell proliferation and maintains cancer stem cells as well as cancer-associated fibroblasts (CAFs). Furthermore, physical contact between CAFs and NSCLC cells induces HH signaling pathway activation in NSCLC cells to enhance their metastatic potential. Therefore, HH signaling pathway inhibitors could be a useful option for lung cancer therapy.

## 1. Introduction

Lung cancer is a leading cause of cancer-related death worldwide [1]. Lung cancer is classified into two major types: small cell lung cancer (SCLC) and non-small-cell lung cancer (NSCLC) (Figure 1). SCLC arises in the midlevel airway and is a very aggressive, highly metastasizing and lethal cancer type that comprises 15% of all lung cancers. NSCLC is the major type of lung cancer and comprises 85% of all lung cancers. NSCLC includes lung adenocarcinoma, lung squamous cell carcinoma (LSCC), and lung large cell carcinoma. Adenocarcinoma arises in the distal airway and its incidence is not related to smoking. LSCC arises in the proximal airway and is more aggressively and strongly associated with smoking than adenocarcinoma. Large cell carcinoma arises in the distal airway and the cancer cell mass is larger than the other two types of NSCLC. Large cell carcinoma is also an aggressive tumor [2]. Despite our current understanding of lung cancer,

the precise molecular mechanisms underlying tumorigenesis in the lung have still not been completely determined.

Several signaling pathways are aberrantly activated in lung cancer cells. Key oncogenic mutations, so-called driver mutations, in components of these signaling pathways have been identified in lung adenocarcinoma. These include epidermal growth factor receptor (*EGFR*), the Kirsten rat sarcoma viral oncogene homolog GTPase (*KRAS*), a member of the rapidly accelerated fibrosarcoma (RAF) family, B-RAF (*BRAF*), and the fusion oncogene echinoderm microtubule-associated protein-like 4-anaplastic lymphoma receptor tyrosine kinase (*EML4-ALK*) [3, 4]. Furthermore, gene amplifications of avian erythroblastic leukemia viral oncogene homolog 2 (*ERBB2*), *MET*, *ROSI*, Neuregulin 1 (*NRG1*), neurotrophic tyrosine kinase receptor 1 (*NTRK1*), and *RET* have also been found in lung adenocarcinoma [5–8]. In LSCC, discoidin domain-containing receptor 2 (*DDR2*), fibroblast growth factor receptor 1 (*FGFR1*), *FGFR2*, and *FGFR3* and

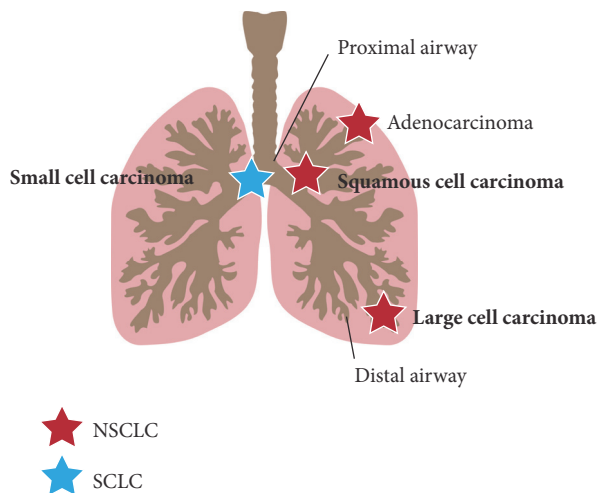


**FIGURE 1:** Lung cancer. Lung cancer is mainly classified into small cell lung cancer (SCLC) and non-small-cell lung cancer (NSCLC). NSCLC is further classified into adenocarcinoma, squamous cell carcinoma, and large cell carcinoma. Adenocarcinoma is the most common lung cancer and arises in the distal airway. Squamous cell carcinoma and SCLC arise in the proximal airway. Large cell carcinoma also arises in the distal airway.

genes in the phosphatidylinositol 3-kinase (PI3K) pathway seem to be more commonly mutated [9]. These gene mutations and gene amplifications induce activation of signaling pathways related to cell proliferation, such as the Ras-extracellular signal-regulated kinase (ERK) pathway and the signal transducer and activator of transcription 3 (STAT3) pathway. NSCLCs harboring *EGFR* mutations or *ALK* gene rearrangements have been successfully targeted with tyrosine kinase inhibitors (TKIs) [10, 11]. However, these TKIs have not yet been shown to improve the overall survival in patients because of tumor recurrence [12]. Moreover, there are no effective drugs for SCLC, LSCC, and large cell carcinoma. Therefore, the 5-year survival rate of lung cancer is only 16% at present [1].

A number of morphogenic signaling pathways that regulate developmental processes and organ homeostasis play critical roles in lung tumorigenesis. Studies of cancer stem cells (CSCs) support the idea that tumors harbor hallmarks of early development in their gene expression repertoire [13]. Recently, remarkable findings from an early stage clinical trial of an inhibitor for the hedgehog (HH) signaling pathway have renewed hope that disruption of developmental signaling in tumors can be of therapeutic benefit [14, 15]. HH pathway inhibitors block both intrinsic signaling in cancer cells and extrinsic signaling to stromal cells to reduce tumor growth [16]. These two strategies exploit distinct oncogenic functions of the pathway. As the HH signaling pathway is activated in SCLC as well as NSCLC, HH pathway inhibitors are expected to become a useful tool for treatment of lung cancer.

In this review, we discuss the roles of the HH signaling pathway in tumor development in SCLC and NSCLC and components of the HH signaling pathway that represent viable lung cancer therapy targets.

## 2. The HH Signaling Pathway

The HH signaling pathway regulates morphogenesis of various organs during embryogenesis [17]. The HH signaling pathway also regulates stem cell renewal and organ homeostasis in the adult [18]. The molecular mechanisms of the HH pathway are complex, and several comprehensive reviews have been published describing the detailed mechanisms [19–21]. In the canonical HH signaling pathway, three HH ligands have been identified: Sonic Hedgehog (SHH), Indian Hedgehog (IHH), and Desert Hedgehog (DHH). Each HH ligand has distinct spatial and temporal expression patterns and activates HH signaling by binding to Patched (PTCH), a 12-pass transmembrane-spanning receptor. In the absence of HH ligand, PTCH is localized to primary cilia and constitutively suppresses the activity of Smoothened (SMO), a 7-pass transmembrane-spanning protein, which is a member of the G-protein-coupled receptor superfamily [22] (Figure 2). In addition to PTCH, additional HH ligands binding cell surface proteins, such as CAM-related/downregulated by oncogenes (CDO), brother of Cdo (BOC), and growth-arrest-specific 1 (GAS1), have been identified, and these molecules function as HH ligand coreceptors to facilitate HH signal reception [23, 24]. Following binding of one of the three HH ligands to PTCH, SMO accumulates in the primary cilia and facilitates the activation of GLI transcriptional activators and their translocation into the nucleus to activate expression of HH target genes, including *GLI1* and *PTCH* genes (Figure 2) [25, 26]. Suppressor of fused (SUFU) is a key negative regulator of the HH signaling pathway [27]. In the absence of HH ligands, SUFU inhibits HH signaling by sequestration of GLI proteins in the cytoplasm and by promoting the formation of the GLI3 repressor (GLI3R). A nuclear function for SUFU in chromatin has also been suggested.

In vertebrates, the GLI family consists of three proteins, GLI1, GLI2, and GLI3 [21]. All GLI proteins contain an activator domain (GLI-A) at their C-terminus; GLI2 and GLI3 also have an N-terminal repressor domain (GLI-R) [28]. Studies in mutant mice suggest that GLI2 is the major activator of HH signaling pathway [29], whereas GLI3 is the major repressor [30, 31]. GLI1 most likely serves as a signal amplifier downstream of GLI2 [29, 32]. *Gli2* knockout (KO) mice die at birth, whereas *Gli1* KO mice show normal development, unless one copy of *Gli2* is also defective [33]. Interestingly, experiments in mutant mice further suggest that GLI2 can rescue GLI1 protein function, whereas *Gli1* knock-in into the *Gli2* allele can rescue the *Gli2* null phenotype [34]. Upon binding of the HH ligand to the receptor PTCH, followed by SMO activation, SUFU-GLI2 and SUFU-GLI3 complexes dissociate and GLI2 and GLI3 translocate into the nucleus, where they activate expression of HH target genes, including *GLI1* and *PTCH* [35]. The balance between the activating and repressive forms of the GLI family transcription factors results in the expression of target genes [21].

The HH signaling pathway has critical roles during embryonic lung development as well as postnatal lung development [36]. During embryonic lung development, HH signaling pathway molecules dramatically change expression patterns and expression levels. The SHH expression pattern

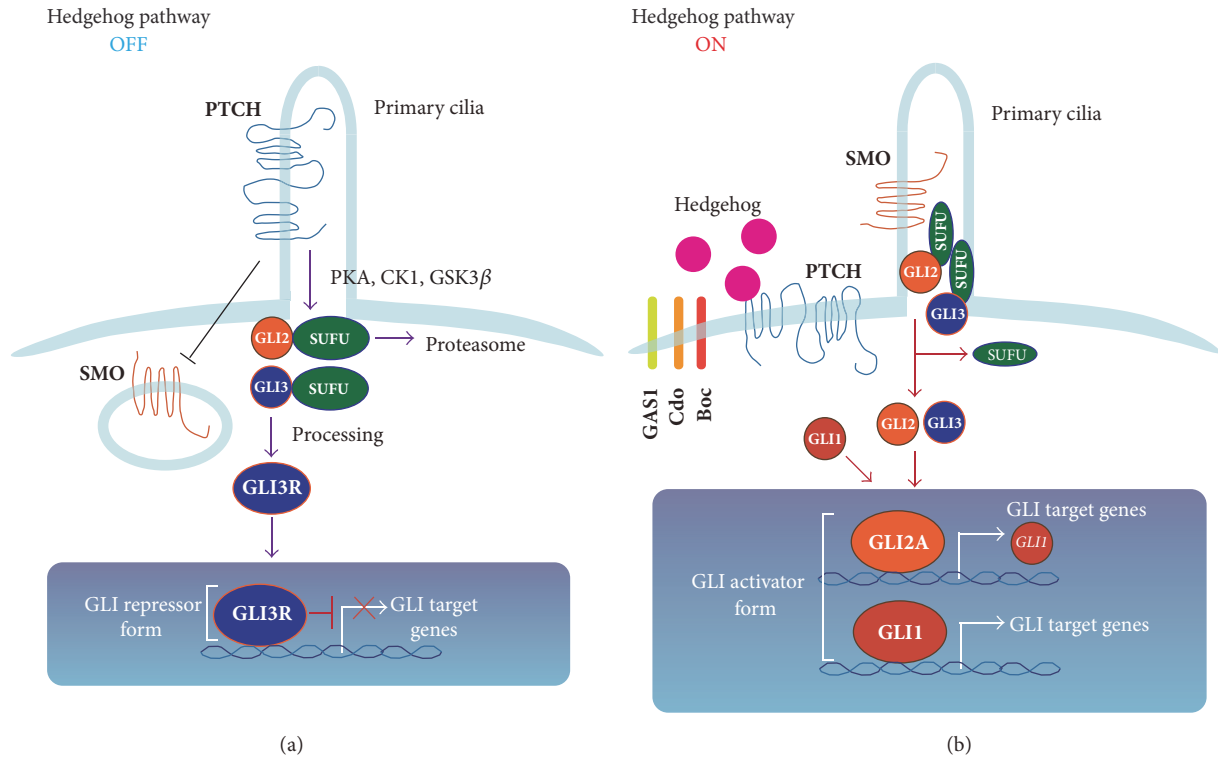


FIGURE 2: HH signaling pathway during development. (a) In the absence of HH ligands, PTCH blocks ciliary localization of SMO and the GLI repressor form (mainly GLI3 repressor form [GLI3R]) suppresses induction of GLI target gene expression. (b) In the presence of HH ligands, the HH pathway is activated. Binding of HH ligand to PTCH prevents PTCH inhibition of SMO, and SMO is free to translocate into primary cilia and is fully activated. SMO then activates the GLI family, mainly GLI2. GLI2 upregulates expression of *GLI1* as well as GLI target genes. GLI1 is also activated downstream of SMO. Activated GLI2 (GLI2A) and GLI1 further upregulate expression of various GLI target genes.

from embryonic day (E) 10 to 16.5 is important for branching and growing bronchi [37]. After E16.5, SHH expression is restricted to a subset of the epithelial cells [37]. PTCH expression pattern in growing bronchi mirrors the expression pattern of SHH [38]. PTCH is also expressed in mesenchyme around E11.5 [39]. Smo is reportedly expressed in epithelium and mesenchyme between E12.5 and E16.5 (pseudoglandular stage) [40]. GLI1, GLI2, and GLI3 are expressed in the mesenchyme during the pseudoglandular stage, and their levels decrease near birth [41]. Although SHH and PTCH expression levels are decreased at birth, they are still observed in epithelial cells [38]. Reduction of the HH signaling pathway in the postnatal lung induces abnormal lung maturation. Therefore, the HH signaling pathway is also involved in postnatal lung maturation [42, 43]. In the healthy adult lung, HH signaling maintains adult lung quiescence and regulates repair [44]. However, it is still currently unclear how HH signaling can promote quiescence on the one hand and tumorigenesis on the other.

Constitutive activation of HH signaling has been observed in many cancers (e.g., skin, lung, stomach, and colon) [45] and promotes cancer cell proliferation, metastasis, and CSC maintenance. Multiple mechanisms of HH signaling pathway activation in cancer have been proposed. Somatic mutations in HH pathway components and overproduction of HH ligands cause aberrant HH signaling pathway

activation. Somatic mutations of *PTCH1* and *SMO* were identified in patients with basal cell carcinoma and medulloblastoma [46–49]. Other mutations in genes encoding HH pathway components have been reported, including *SUFU* in medulloblastoma [50] and *GLI1* and *GLI3* in pancreatic adenocarcinoma [51]. Moreover, *GLI1* amplification was observed in glioblastoma [52]. HH ligand overproduction was observed in upper gastrointestinal tract, pancreas, colon, and metastatic prostate cancers, as well as SCLC, glioblastomas, and melanomas [53–58]. Overproduction of HH ligands constitutively activates the HH pathway in HH ligand-producing cancer cells by autocrine signaling [53, 54] and in stroma cells such as cancer-associated fibroblasts (CAFs) surrounding HH ligand-producing cancer cells by paracrine signaling [16, 59] (Figure 3). In addition, noncanonical HH signaling has been defined as ligand-dependent activation of SMO but independent of GLI activation [60] or as GLI activation independent of SMO. The noncanonical GLI activation pathway includes transforming growth factor  $\beta$  (TGF- $\beta$ ) [61], EGFR [62], Ras-Erk [63, 64], and PI3K-Akt-mechanistic target of rapamycin (mTOR) [65] signaling pathways.

### 3. HH Signaling Pathway in SCLC

Although mutation or amplification of genes involved in the HH pathway has not been found in SCLC, the HH signaling

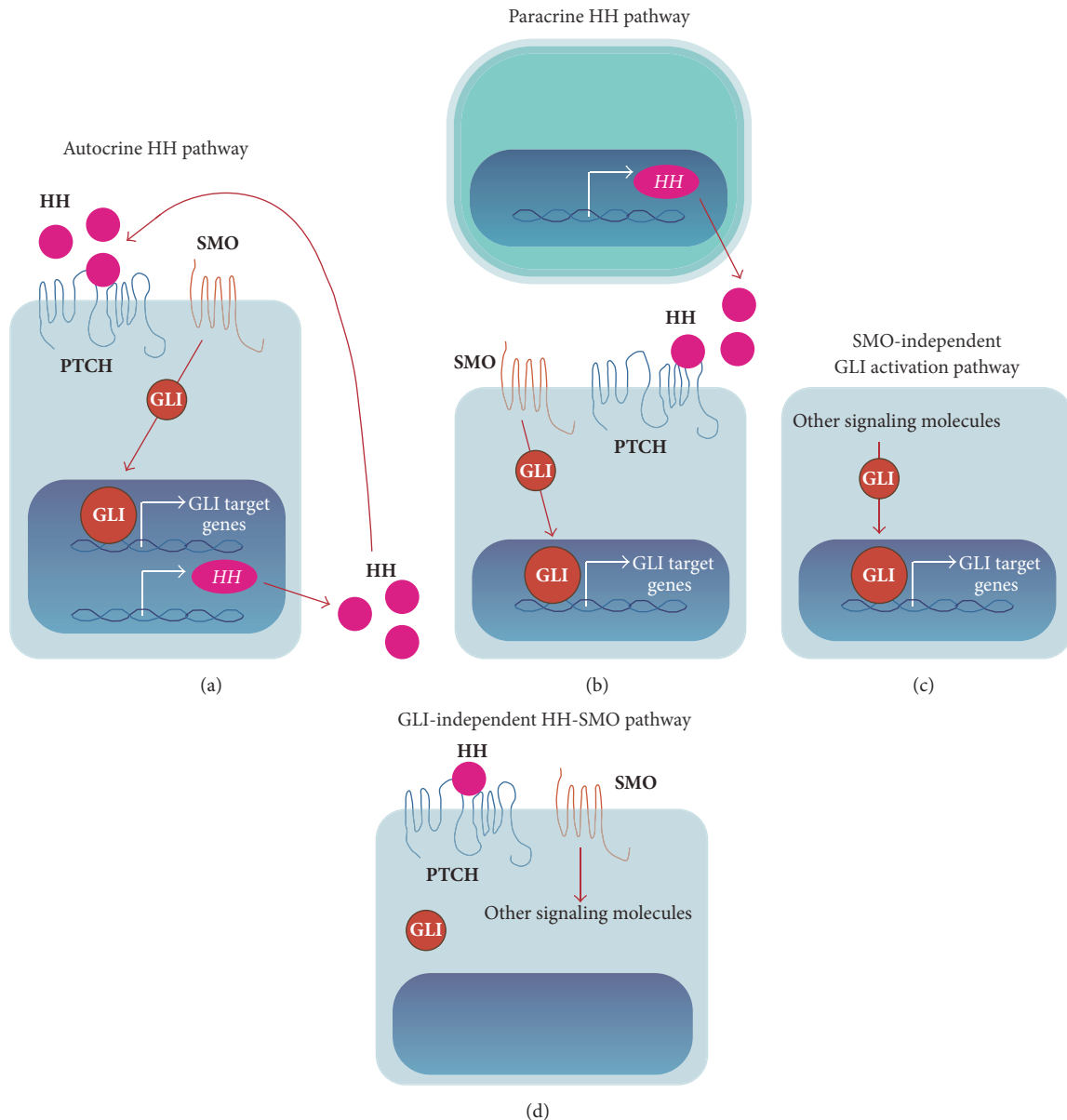


FIGURE 3: Modes of HH-GLI signaling pathway activation in cancer. (a) HH ligands constitutively activate the HH pathway in HH ligand-producing cancer cells by autocrine signaling. Cancer cells produce HH ligand, and secreted HH ligands activate the HH signaling pathway in these cancer cells. (b) Cancer cell-mediated production of HH ligands also activates the HH pathway in stroma cells (e.g., CAFs) to maintain cancer cells by paracrine signaling. (c) GLI family transcription factors are activated in a SMO-independent manner, called the noncanonical pathway. (d) SMO can also activate other signaling molecules in cancer cells.

pathway was activated in many SCLC cases [66]. Watkins et al. found HH pathway activation in neuroendocrine cells in later lung development (E16.5) and the airway epithelium during repair of acute airway injury [53]. Neuroendocrine cells are considered candidates for the origin of SCLC. HH pathway activation was also observed in SCLC tissue and this observation was confirmed by analysis of SCLC cell lines. Moreover, a SCLC cell xenograft model using nude mice demonstrated that the HH pathway was activated in SHH-producing SCLC cells but not in surrounding non-SHH-producing cancer cells, suggesting that HH pathway

activation was an autocrine and/or juxtacrine loop in SCLC. Analysis using a SCLC model mouse also revealed that HH pathway activation initiated and progressed mouse SCLC independent of the tumor microenvironment. Furthermore, suppression of SMO in a SCLC mouse model strongly suppressed initiation and progression of SCLC [67]. In addition, immunohistochemistry analysis revealed upregulation of HH pathway components in SCLC patients, suggesting that the HH signaling pathway is also activated in SCLC patients [68].

A recent study reported a novel crosstalk between the HH pathway and bombesin- (BBS-) like neuropeptide-mediated

signaling in SCLC [69]. SCLC cells secrete BBS, which acts as an autocrine growth factor. Expression of both SHH and gastrin-releasing peptide receptor (GRPR), a BBS-cognate receptor, was observed in 56% of SCLC. Analysis of SCLC cell lines revealed that BBS signaling activates GLII activity and that BBS-mediated GLII activation is suppressed by cyclopamine, a SMO inhibitor. Furthermore, GLII activation was mediated by BBS signaling-nuclear factor- $\kappa$ B- (NF- $\kappa$ B-) mediated production of SHH ligand in SCLC cells.

#### 4. HH Signaling Pathway in NSCLC

Various studies have also demonstrated that the HH pathway is activated in NSCLC. The expressions of GLII target genes, such as Forkhead Box M1 (*FOXM1*), B cell-specific Moloney murine leukemia virus integration site 1 (*BMI1*), and *NANOG*, were elevated in NSCLC patients [70, 71]. Another study showed that 40 S ribosomal protein S6 kinase 2 (p70S6K2) regulates GLII activity in NSCLC cells. siRNA-mediated p70S6K2 knockdown suppressed cell viability and GLII activity, and p70S6K2 knockdown promoted GLII degradation through inhibition of glycogen synthase kinase 3 $\beta$ - (GSK3 $\beta$ -) mediated GLII phosphorylation. However, a SMO inhibitor, 3-keto-N-aminoethylaminocaproyldihydrocinnamoyl- (KAAD-) cyclopamine [72], did not affect GLII activity, and PI3K inhibitor treatment suppressed GLII activity [73].

CAFs are widely defined as all fibroblast cells within the tumor stroma and key players in the process of tumorigenesis through modulation of tumor microenvironment, CSC maintenance, and regulation of tumor metabolism [74]. CAF proliferation is maintained by various factors such as growth factors (e.g., TGF- $\beta$  and platelet-derived growth factor [PDGF]) and cytokines (e.g., interleukin 1 [IL-1] and IL-6) [75]. Bermudez et al. showed that NSCLC cells can secrete SHH ligand, and secreted SHH ligand activates the HH signaling pathway in CAFs. This pathway activation induces CAF proliferation [76]. Huang et al. showed that PTCH, SMO, and GLI2 expressions were upregulated in LSCC-derived cell lines. However, SMO inhibitor treatment or SMO knockdown demonstrated only a minor inhibitory effect on cell proliferation, whereas GLI2 suppression significantly suppressed cell proliferation and induced extensive apoptosis. Therefore, GLI transcriptional activity would be regulated by a noncanonical (SMO-independent) pathway [77]. These reports suggest that the HH pathway is activated by the paracrine mechanism and GLI activation in NSCLC cells is regulated by the noncanonical (SMO-independent) pathway.

On the other hand, several studies have reported that HH signaling is activated by the autocrine pathway in NSCLC cells. The aggressiveness of NSCLC has been shown to be associated with the acquisition of epithelial-to-mesenchymal transition (EMT) [78]. A549 lung adenocarcinoma cells that obtain mesenchymal phenotype (A549-M cells) show upregulated SHH ligand and GLII expression compared with A549 cells. In A549-M cells, the HH pathway was activated by autocrine signaling, and suppression of the HH pathway contributed to suppression of TGF- $\beta$  signaling-induced cancer cell migration and metastatic characteristics [79].

CAFs can secrete various growth factors and cytokines. Secreted proteins induce extracellular matrix (ECM) remodeling. Furthermore, CAFs interact with cancer cells and CAF-secreted proteins activate various signaling pathways by paracrine signaling. ECM remodeling and CAF-mediated paracrine signaling pathway activation could induce metastatic properties of cancer cells [75]. Choe et al. [80] showed that EMT-related gene expression and the HH signaling pathway was upregulated in adenocarcinoma cells by means of direct coculture of NSCLC cells and lung CAFs. The authors proposed that metastatic properties might be acquired by direct interaction of adenocarcinoma cells and CAFs and CAF-mediated paracrine HH signaling pathway activation in adenocarcinoma cells.

CSCs exhibit a self-renewing capacity and are responsible for tumor maintenance and relapse [81]. CSC maintenance in adenocarcinoma and LSCC are regulated by the autocrine HH signaling pathway. Several molecules and enzymatic activities such as CD44, CD133, and high aldehyde dehydrogenase (ALDH) activity have been identified as CSC markers of NSCLC [82–85]. The HH signaling pathway was activated in CD44<sup>high</sup>/ALDH<sup>high</sup> cancer cells harboring CSC properties [86]. Furthermore, CD133<sup>+</sup> NSCLC cells also exhibit CSC properties and secrete SHH ligand, and HH pathway inhibition in CD133<sup>+</sup> cells attenuated sphere formation, suggesting that the autocrine HH pathway is involved in CD133<sup>+</sup> CSC maintenance [87]. Although CD133<sup>+</sup> SCLC cells are identified as a CSC phenotype [88], there is no evidence that the HH pathway is involved in SCLC stem cell maintenance. Moreover, a previous report showed that GLII upregulated expression of the embryonic stem cell transcription factor SRY- (sex determining region Y-) box 2 (SOX2) by cooperation with EGF signaling in lung adenocarcinoma-derived cell lines [89]. As described above, the interaction of CAFs and NSCLC cells induces metastatic properties of NSCLC cells via CAF-mediated HH signaling pathway activation in NSCLC cells. Chen et al. showed that an interaction of CAFs and NSCLC cells and CAF-mediated HH signaling pathway activation in NSCLC cells are also involved in CSC maintenance [90]. We independently observed that GLII inhibition but not SMO inhibition attenuated sphere formation, suggesting that GLII activity was regulated by other signaling pathways for NSCLC stem cell maintenance (unpublished data).

SOX2 expression is upregulated in LSCC [91], and therefore SOX2 is used as one of the tumor markers for LSCC. Although SOX2 has critical roles in CSC maintenance, the precise mechanism of SOX2-mediated CSC maintenance is largely unknown. Justilien et al. reported that the SOX2-HH pathway has important roles for CSC maintenance in LSCC. Protein kinase C iota (PRKCI) phosphorylated Ser394 in SOX2, resulting in upregulated expression of hedgehog acyltransferase (*HHAT*). The SHH ligand is changed to its active form by HHAT, resulting in HH signaling pathway activation. The PRKCI-SOX2-HH signaling pathway plays important roles in CSC maintenance [92].

TABLE 1: The HH signaling pathway inhibitors.

Inhibitor Name	Organization	Clinical Trial
(1) SMO inhibitors		
Cyclopamine, KAAD-cyclopamine	—	No
GDC-0449 (Vismodegib/Erivedge)	Roche/Genentech/Curis	Yes (phases 0, I, and II)
LDE225 (Erismodegib/Sonidegib/Odomzo)	Novartis	Yes (phases 0, I, and II)
BMS-833923/XL139	Bristol Myers Squibb/Exelixis	Yes (phases I and II)
PF-04449913 (Glasdegib)	Pfizer	Yes (Phase II)
PF-527857	Pfizer	No
LY2940680 (Taladegib)	Ignyta	Yes (phases I and II)
IPI-926 (Sadegib)	Infinity	Yes (phase I)
TAK-441	—	No
MRT-92	—	No
(2) GLI inhibitors		
GANT-58, GANT-61	—	No
Arsenic trioxide (ATO)	—	Yes (phases I, II, III, and IV)
HPI-1	—	No
Glabrescione B (GlaB)	—	No

See [14] for description of the clinical trials of HH signaling pathway inhibitors.

As described above, SMO inhibitor treatment suppressed EMT properties through remodeling of the actin cytoskeleton and motility of NSCLC cells [79]. Although SMO inhibition downregulated EMT-associated gene expression, expressions of GLI1 target genes were not affected [93]. These results suggest that SMO might activate other signaling molecules as well as GLI transcription factors in NSCLC cells harboring mesenchymal properties.

Many studies on the roles of the HH signaling pathway in NSCLC suggested that GLI1 and GLI2 play central roles in tumor progression, tumor metastasis, and CSC maintenance. The mechanisms of GLI activation are diverse in cancer cell types and the tumor microenvironment surrounding cancer cells, since GLI is activated by various pathways including the autocrine and paracrine HH pathways as well as canonical and noncanonical GLI activation pathway.

## 5. HH Signaling Pathway-Targeted Cancer Therapy in Lung Cancer

Previous studies have revealed that subsets of lung cancer patients harbor mutations in the key oncogenic drivers upon which tumor survival and progression are dependent. These include mutations in EGFR and the EML4-ALK fusion protein [3]. Therefore, various TKIs targeting EGFR and EML4-ALK have been developed. However, the clinical efficacy of TKIs differs among patients, and acquired resistance for chronic treatment often develops in most patients who are treated with TKIs [5, 94, 95]. Furthermore, there are no effective anticancer drugs for SCLC, LSCC, and large cell carcinoma.

Previous studies reported that tumor volume and tumor recurrence were suppressed by HH pathway inhibitor treatment or combination treatment of HH pathway inhibitors

and other types of chemotherapeutic agents such as TKIs and platinum-containing drugs. Park et al. [67] demonstrated that combination treatment of etoposide and a SMO inhibitor (LDE225: Sonidegib) [96] attenuated tumor recurrence of SCLC using a mouse xenograft model. Moreover, LDE225 treatment attenuated the TKI-resistant NSCLC cell line HCC827-GR (gefitinib resistant) derived tumor growth. In addition, cotreatment of SMO inhibitor and MET inhibitor to HCC827-GR xenografted tumors further suppressed tumor volume, since constitutive MET activation was observed in HCC827-GR cells [97]. Moreover, RNAi-mediated GLI1 knockdown suppressed tumor formation and tumor sphere formation. Several SMO inhibitors and GLI inhibitors have been developed [14]. GDC-0449 (Vismodegib) [98] is approved for basal cell carcinoma therapy, and several SMO inhibitors including GDC-0449 are used in clinical investigations for SCLC. GLI inhibitors such as GLI-antagonist- (GANT-) 58, GANT-61, HH pathway inhibitor- (HPI-) 1, Genistein, and Glabrescione B (GlaB) have also been developed [43, 99–101]. In addition, arsenic trioxide (ATO), which suppresses GLI1 transcriptional activity [102, 103], is used in clinical investigations as a GLI inhibitor (Table 1) [14]. However, other GLI inhibitors have not yet progressed to clinical trials. Since the HH pathway and GLI activity have important roles in lung cancer formation and lung CSC maintenance, these chemical compounds may be useful for lung cancer therapy.

## 6. Conclusion

We have discussed the relationship between the HH signaling pathway and lung cancer and the mechanism of HH signaling pathway activation in lung cancer. As summarized in Figure 4, the GLI activation machinery and the role of the HH pathway in lung cancer are different in NSCLC and SCLC

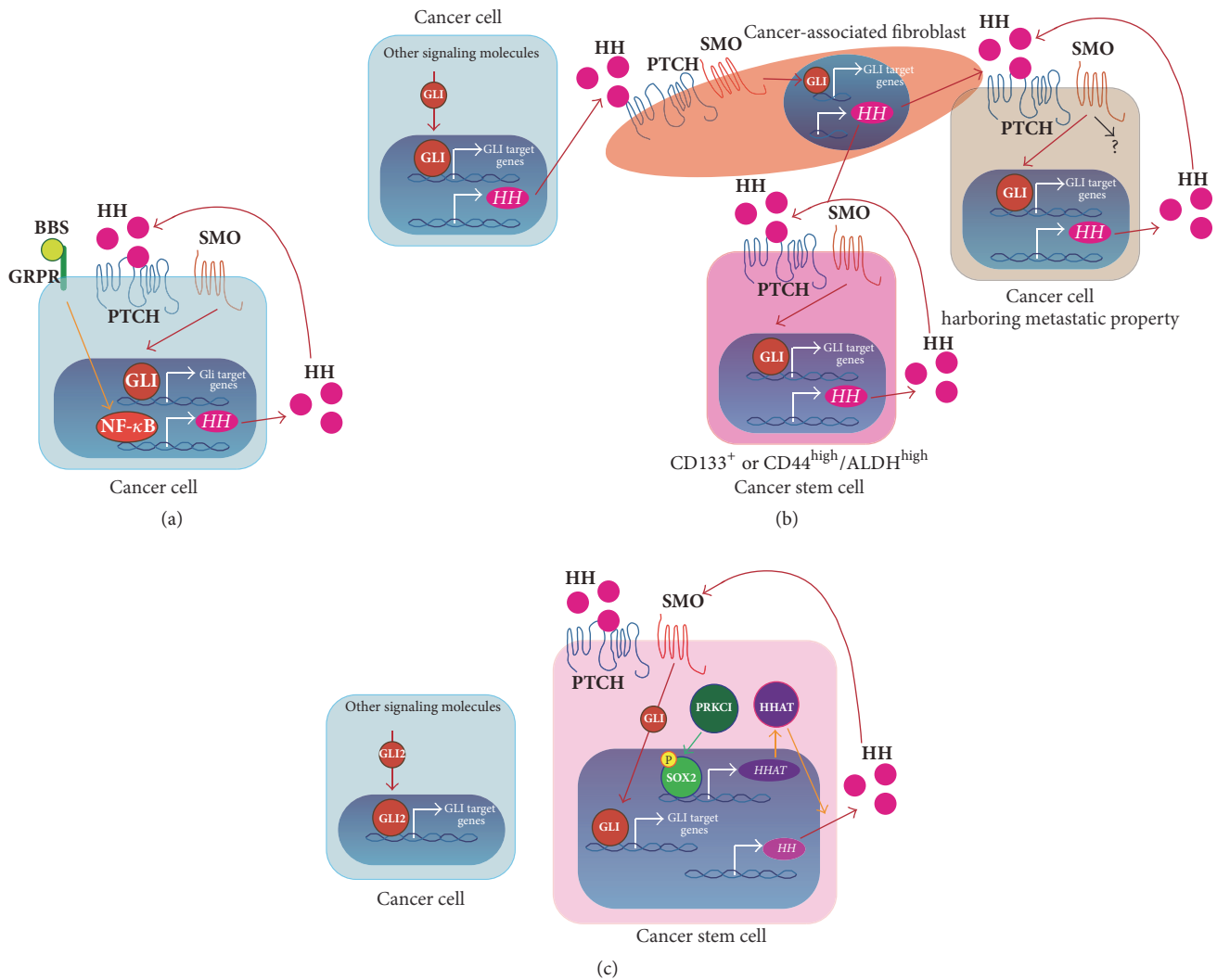


FIGURE 4: The role of the HH signaling pathway in lung cancer. (a) The HH signaling pathway in SCLC. The autocrine HH signaling pathway promotes cancer cell proliferation. (b) The HH signaling pathway in adenocarcinoma. The noncanonical GLI activation pathway would maintain cancer cell proliferation. CAF maintenance would be regulated by paracrine HH signaling pathway activation. CAF-secreted HH ligands would activate the HH signaling pathway in cancer cells and CSCs. CAFs-mediated paracrine HH pathway activation in cancer cells has important roles in acquisition of metastatic properties. Moreover, CAF-mediated HH signaling pathway activation might be involved in CSC maintenance. Cancer cells harboring metastatic properties and CSCs would be also maintained by autocrine HH signaling pathway activation. In addition, SMO might activate other signaling molecules in cancer cells harboring metastatic properties. (c) The HH signaling pathway in LSCC. Cancer cells would be maintained by the noncanonical GLI2 activation pathway. PRKCI-SOX2-HH signaling pathway has important roles in CSC maintenance.

as well as among the types of NSCLC. Furthermore, the HH signaling pathway is involved in the interaction of cancer cells and CAFs for tumor maintenance. Various SMO inhibitors are used in clinical investigations for lung cancer. Results from *in vitro* and *in vivo* experiments have demonstrated that SMO inhibitor treatment is effective for lung tumor suppression. In fact, SMO inhibitors are used in clinical trials for SCLC. The HH signaling pathway is involved in CSC maintenance, tumor progression, and metastasis in NSCLC. Therefore, SMO inhibitors may be a better option for lung cancer therapy in the future. However, previous studies suggest that

GLI transcription factors are activated by various mechanisms, including the SMO-independent pathway. In particular, dysregulated SMO-independent GLI activation pathway may cause SMO inhibitor resistance. Several GLI inhibitors have also been recently developed. Therefore, a HH-pathway-activated lung cancer therapy using GLI inhibitors would be an effective option. To develop the most effective HH pathway inhibitor for treatment of lung cancer, the current challenge is not only to accelerate HH inhibitor development but also to more deeply understand the regulatory mechanism of GLI-mediated transcription.

## Competing Interests

The authors have no competing interests to review.

## Authors' Contributions

Yoshinori Abe and Nobuyuki Tanaka contributed equally to this work.

## References

- [1] R. Siegel, D. Naishadham, and A. Jemal, "Cancer statistics, 2013," *CA Cancer Journal for Clinicians*, vol. 63, no. 1, pp. 11–30, 2013.
- [2] M. R. Davidson, A. F. Gazdar, and B. E. Clarke, "The pivotal role of pathology in the management of lung cancer," *Journal of Thoracic Disease*, vol. 5, no. 5, pp. S463–S478, 2013.
- [3] C. J. Langer, B. Besse, A. Gualberto, E. Brambilla, and J.-C. Soria, "The evolving role of histology in the management of advanced non-small-cell lung cancer," *Journal of Clinical Oncology*, vol. 28, no. 36, pp. 5311–5320, 2010.
- [4] M. Soda, Y. L. Choi, M. Enomoto et al., "Identification of the transforming EML4-ALK fusion gene in non-small-cell lung cancer," *Nature*, vol. 448, no. 7153, pp. 561–566, 2007.
- [5] J. A. Engelman, K. Zejnullahu, T. Mitsudomi et al., "MET amplification leads to gefitinib resistance in lung cancer by activating ERBB3 signaling," *Science*, vol. 316, no. 5827, pp. 1039–1043, 2007.
- [6] K. Rikova, A. Guo, Q. Zeng et al., "Global survey of phosphotyrosine signaling identifies oncogenic kinases in lung cancer," *Cell*, vol. 131, no. 6, pp. 1190–1203, 2007.
- [7] P. Stephens, C. Hunter, G. Bignell et al., "Lung cancer: intragenic ERBB2 kinase mutations in tumours," *Nature*, vol. 431, no. 7008, pp. 525–526, 2004.
- [8] A. Vaishnavi, M. Capelletti, A. T. Le et al., "Oncogenic and drug-sensitive NTRK1 rearrangements in lung cancer," *Nature Medicine*, vol. 19, no. 11, pp. 1469–1472, 2013.
- [9] T. C. G. A. R. Network, "Comprehensive genomic characterization of squamous cell lung cancers," *Nature*, vol. 489, no. 7417, pp. 519–525, 2012.
- [10] B. Hallberg and R. H. Palmer, "Mechanistic insight into ALK receptor tyrosine kinase in human cancer biology," *Nature Reviews Cancer*, vol. 13, no. 10, pp. 685–700, 2013.
- [11] W. Pao and J. Chmielecki, "Rational, biologically based treatment of EGFR-mutant non-small-cell lung cancer," *Nature Reviews Cancer*, vol. 10, no. 11, pp. 760–774, 2010.
- [12] J. N. Spaans and G. D. Goss, "Epidermal growth factor receptor tyrosine kinase inhibitors in early-stage nonsmall cell lung cancer," *Current Opinion in Oncology*, vol. 27, no. 2, pp. 102–107, 2015.
- [13] L. Strizzi, K. M. Hardy, E. A. Seftor et al., "Development and cancer: at the crossroads of Nodal and Notch signaling," *Cancer Research*, vol. 69, no. 18, pp. 7131–7134, 2009.
- [14] T. K. Rimkus, R. L. Carpenter, S. Qasem, M. Chan, and H.-W. Lo, "Targeting the sonic hedgehog signaling pathway: review of smoothened and GLI inhibitors," *Cancers*, vol. 8, no. 2, article 22, 2016.
- [15] A. A. Merchant and W. Matsui, "Targeting Hedgehog—a cancer stem cell pathway," *Clinical Cancer Research*, vol. 16, no. 12, pp. 3130–3140, 2010.
- [16] R. L. Yauch, S. E. Gould, S. J. Scales et al., "A paracrine requirement for hedgehog signalling in cancer," *Nature*, vol. 455, no. 7211, pp. 406–410, 2008.
- [17] P. W. Ingham and A. P. McMahon, "Hedgehog signaling in animal development: paradigms and principles," *Genes & Development*, vol. 15, no. 23, pp. 3059–3087, 2001.
- [18] P. A. Beachy, S. S. Karhadkar, and D. M. Berman, "Tissue repair and stem cell renewal in carcinogenesis," *Nature*, vol. 432, no. 7015, pp. 324–331, 2004.
- [19] J. M. Y. Ng and T. Curran, "The Hedgehog's tale: developing strategies for targeting cancer," *Nature Reviews Cancer*, vol. 11, no. 7, pp. 493–501, 2011.
- [20] J. Brechbiel, K. Miller-Moslin, and A. A. Adjei, "Crosstalk between hedgehog and other signaling pathways as a basis for combination therapies in cancer," *Cancer Treatment Reviews*, vol. 40, no. 6, pp. 750–759, 2014.
- [21] F. Aberger and A. Ruiz i Altaba, "Context-dependent signal integration by the GLI code: the oncogenic load, pathways, modifiers and implications for cancer therapy," *Seminars in Cell & Developmental Biology*, vol. 33, pp. 93–104, 2014.
- [22] R. Rohatgi, L. Milenkovic, and M. P. Scott, "Patched1 regulates hedgehog signaling at the primary cilium," *Science*, vol. 317, no. 5836, pp. 372–376, 2007.
- [23] B. L. Allen, T. Tenzen, and A. P. McMahon, "The Hedgehog-binding proteins Gas1 and Cdo cooperate to positively regulate Shh signaling during mouse development," *Genes and Development*, vol. 21, no. 10, pp. 1244–1257, 2007.
- [24] A. Okada, F. Charron, S. Morin et al., "Boc is a receptor for sonic hedgehog in the guidance of commissural axons," *Nature*, vol. 444, no. 7117, pp. 369–373, 2006.
- [25] K. C. Corbit, P. Aanstad, V. Singla, A. R. Norman, D. Y. R. Stainier, and J. F. Reiter, "Vertebrate Smoothened functions at the primary cilium," *Nature*, vol. 437, no. 7061, pp. 1018–1021, 2005.
- [26] C. J. Haycraft, B. Banizs, Y. Aydin-Son, Q. Zhang, E. J. Michaud, and B. K. Yoder, "Gli2 and Gli3 localize to cilia and require the intraflagellar transport protein polaris for processing and function," *PLoS Genetics*, vol. 1, no. 4, article no. e53, 2005.
- [27] Y. Lee, R. Kawagoe, K. Sasai et al., "Loss of suppressor-of-fused function promotes tumorigenesis," *Oncogene*, vol. 26, no. 44, pp. 6442–6447, 2007.
- [28] H. Sasaki, Y. Nishizaki, C.-C. Hui, M. Nakafuku, and H. Kondo, "Regulation of Gli2 and Gli3 activities by an amino-terminal repression domain: implication of Gli2 and Gli3 as primary mediators of Shh signaling," *Development*, vol. 126, no. 17, pp. 3915–3924, 1999.
- [29] C. B. Bai, W. Auerbach, J. S. Lee, D. Stephen, and A. L. Joyner, "Gli2, but not Gli1, is required for initial Shh signaling and ectopic activation of the Shh pathway," *Development*, vol. 129, no. 20, pp. 4753–4761, 2002.
- [30] H. Masuya, T. Sagai, K. Moriwaki, and T. Shiroishi, "Multigenic control of the localization of the zone of polarizing activity in limb morphogenesis in the mouse," *Developmental Biology*, vol. 182, no. 1, pp. 42–51, 1997.
- [31] D. Büscher, B. Bosse, J. Heymer, and U. Rütter, "Evidence for genetic control of Sonic hedgehog by Gli3 in mouse limb development," *Mechanisms of Development*, vol. 62, no. 2, pp. 175–182, 1997.
- [32] Q. Ding, J. Motoyama, S. Gasca et al., "Diminished Sonic hedgehog signaling and lack of floor plate differentiation in Gli2 mutant mice," *Development*, vol. 125, no. 14, pp. 2533–2543, 1998.

- [33] H. L. Park, C. Bai, K. A. Platt et al., "Mouse Gli1 mutants are viable but have defects in SHH signaling in combination with a Gli2 mutation," *Development*, vol. 127, no. 8, pp. 1593–1605, 2000.
- [34] C. B. Bai and A. L. Joyner, "Gli1 can rescue the in vivo function of Gli2," *Development*, vol. 128, no. 24, pp. 5161–5172, 2001.
- [35] H. Tukachinsky, L. V. Lopez, and A. Salic, "A mechanism for vertebrate Hedgehog signaling: recruitment to cilia and dissociation of SuFu-Gli protein complexes," *Journal of Cell Biology*, vol. 191, no. 2, pp. 415–428, 2010.
- [36] M. C. Kugler, A. L. Joyner, C. A. Loomis, and J. S. Munger, "Sonic hedgehog signaling in the lung: from development to disease," *American Journal of Respiratory Cell and Molecular Biology*, vol. 52, no. 1, pp. 1–13, 2015.
- [37] L.-A. D. Miller, S. E. Wert, and J. A. Whitsett, "Immunolocalization of sonic hedgehog (Shh) in developing mouse lung," *Journal of Histochemistry and Cytochemistry*, vol. 49, no. 12, pp. 1593–1603, 2001.
- [38] S. Bellusci, Y. Furuta, M. G. Rush, R. Henderson, G. Winnier, and B. L. M. Hogan, "Involvement of Sonic hedgehog (Shh) in mouse embryonic lung growth and morphogenesis," *Development*, vol. 124, no. 1, pp. 53–63, 1997.
- [39] M. Weaver, L. Batts, and B. L. M. Hogan, "Tissue interactions pattern the mesenchyme of the embryonic mouse lung," *Developmental Biology*, vol. 258, no. 1, pp. 169–184, 2003.
- [40] M. Zhang, H. Wang, H. Teng, J. Shi, and Y. Zhang, "Expression of SHH signaling pathway components in the developing human lung," *Histochemistry and Cell Biology*, vol. 134, no. 4, pp. 327–335, 2010.
- [41] J. C. Grindley, S. Bellusci, D. Perkins, and B. L. M. Hogan, "Evidence for the involvement of the Gli gene family in embryonic mouse lung development," *Developmental Biology*, vol. 188, no. 2, pp. 337–348, 1997.
- [42] L. Liu, M. C. Kugler, C. A. Loomis et al., "Hedgehog signaling in neonatal and adult lung," *American Journal of Respiratory Cell and Molecular Biology*, vol. 48, no. 6, pp. 703–710, 2013.
- [43] J. M. Hyman, A. J. Firestone, V. M. Heine et al., "Small-molecule inhibitors reveal multiple strategies for Hedgehog pathway blockade," *Proceedings of the National Academy of Sciences of the United States of America*, vol. 106, no. 33, pp. 14132–14137, 2009.
- [44] T. Peng, D. B. Frank, R. S. Kadzik et al., "Hedgehog actively maintains adult lung quiescence and regulates repair and regeneration," *Nature*, vol. 526, no. 7574, pp. 578–582, 2015.
- [45] L. L. Rubin and F. J. de Sauvage, "Targeting the Hedgehog pathway in cancer," *Nature Reviews Drug Discovery*, vol. 5, no. 12, pp. 1026–1033, 2006.
- [46] C. Raffel, R. B. Jenkins, L. Frederick et al., "Sporadic medulloblastomas contain PTCH mutations," *Cancer Research*, vol. 57, no. 5, pp. 842–845, 1997.
- [47] M. Wolter, J. Reifenberger, C. Sommer, T. Ruzicka, and G. Reifenberger, "Mutations in the human homologue of the *Drosophila* segment polarity gene patched (PTCH) in sporadic basal cell carcinomas of the skin and primitive neuroectodermal tumors of the central nervous system," *Cancer Research*, vol. 57, no. 13, pp. 2581–2585, 1997.
- [48] J. Reifenberger, M. Wolter, R. G. Weber et al., "Missense mutations in SMOH in sporadic basal cell carcinomas of the skin and primitive neuroectodermal tumors of the central nervous system," *Cancer Research*, vol. 58, no. 9, pp. 1798–1803, 1998.
- [49] J. Xie, M. Murone, S.-M. Luoh et al., "Activating Smoothed mutations in sporadic basal-cell carcinoma," *Nature*, vol. 391, no. 6662, pp. 90–92, 1998.
- [50] M. D. Taylor, L. Liu, C. Raffel et al., "Mutations in SUFU predispose to medulloblastoma," *Nature Genetics*, vol. 31, no. 3, pp. 306–310, 2002.
- [51] S. Jones, X. Zhang, D. W. Parsons et al., "Core signaling pathways in human pancreatic cancers revealed by global genomic analyses," *Science*, vol. 321, no. 5897, pp. 1801–1806, 2008.
- [52] A. J. Wong, S. H. Bigner, D. D. Bigner, K. W. Kinzler, S. R. Hamilton, and B. Vogelstein, "Increased expression of the epidermal growth factor receptor gene in malignant gliomas is invariably associated with gene amplification," *Proceedings of the National Academy of Sciences of the United States of America*, vol. 84, no. 19, pp. 6899–6903, 1987.
- [53] D. N. Watkins, D. M. Berman, S. G. Burkholder, B. Wang, P. A. Beachy, and S. B. Baylin, "Hedgehog signalling within airway epithelial progenitors and in small-cell lung cancer," *Nature*, vol. 422, no. 6929, pp. 313–317, 2003.
- [54] D. M. Berman, S. S. Karhadkar, A. Maitra et al., "Widespread requirement for Hedgehog ligand stimulation in growth of digestive tract tumours," *Nature*, vol. 425, no. 6960, pp. 846–851, 2003.
- [55] F. Varnat, A. Duquet, M. Malerba et al., "Human colon cancer epithelial cells harbour active HEDGEHOG–GLI signalling that is essential for tumour growth, recurrence, metastasis and stem cell survival and expansion," *EMBO Molecular Medicine*, vol. 1, no. 6–7, pp. 338–351, 2009.
- [56] S. S. Karhadkar, G. S. Bova, N. Abdallah et al., "Hedgehog signalling in prostate regeneration, neoplasia and metastasis," *Nature*, vol. 431, no. 7009, pp. 707–712, 2004.
- [57] E. E. Bar, A. Chaudhry, A. Lin et al., "Cyclopamine-mediated Hedgehog pathway inhibition depletes stem-like cancer cells in glioblastoma," *STEM CELLS*, vol. 25, no. 10, pp. 2524–2533, 2007.
- [58] B. Stecca, C. Mas, V. Clement et al., "Melanomas require HEDGEHOG–GLI signaling regulated by interactions between GLI1 and the RAS–MEK/AKT pathways," *Proceedings of the National Academy of Sciences of the United States of America*, vol. 104, no. 14, pp. 5895–5900, 2007.
- [59] J.-W. Theunissen and F. J. De Sauvage, "Paracrine hedgehog signaling in cancer," *Cancer Research*, vol. 69, no. 15, pp. 6007–6010, 2009.
- [60] D. Jenkins, "Hedgehog signalling: emerging evidence for non-canonical pathways," *Cellular Signalling*, vol. 21, no. 7, pp. 1023–1034, 2009.
- [61] D. Javelaud, M.-J. Pierrat, and A. Mauviel, "Crosstalk between TGF- $\beta$  and hedgehog signaling in cancer," *FEBS Letters*, vol. 586, no. 14, pp. 2016–2025, 2012.
- [62] M. Eberl, S. Klingler, D. Mangelberger et al., "Hedgehog-EGFR cooperation response genes determine the oncogenic phenotype of basal cell carcinoma and tumour-initiating pancreatic cancer cells," *EMBO Molecular Medicine*, vol. 4, no. 3, pp. 218–233, 2012.
- [63] O. Nolan-Stevaux, J. Lau, M. L. Truitt et al., "GLI1 is regulated through Smoothed-independent mechanisms in neoplastic pancreatic ducts and mediates PDAC cell survival and transformation," *Genes & Development*, vol. 23, no. 1, pp. 24–36, 2009.
- [64] T. Mazumdar, J. DeVecchio, A. Agyeman, T. Shi, and J. A. Houghton, "The GLI genes as the molecular switch in disrupting Hedgehog signaling in colon cancer," *Oncotarget*, vol. 2, no. 8, pp. 638–645, 2011.
- [65] Y. Wang, Q. Ding, C.-J. Yen et al., "The crosstalk of mTOR/S6K1 and Hedgehog pathways," *Cancer Cell*, vol. 21, no. 3, pp. 374–387, 2012.

- [66] J. Voortman, J.-H. Lee, J. K. Killian et al., "Array comparative genomic hybridization-based characterization of genetic alterations in pulmonary neuroendocrine tumors," *Proceedings of the National Academy of Sciences of the United States of America*, vol. 107, no. 29, pp. 13040–13045, 2010.
- [67] K.-S. Park, L. G. Martelotto, M. Peifer et al., "A crucial requirement for Hedgehog signaling in small cell lung cancer," *Nature Medicine*, vol. 17, no. 11, pp. 1504–1508, 2011.
- [68] J. Vestergaard, M. W. Pedersen, N. Pedersen et al., "Hedgehog signaling in small-cell lung cancer: frequent in vivo but a rare event in vitro," *Lung Cancer*, vol. 52, no. 3, pp. 281–290, 2006.
- [69] M. D. Castellone, M. O. Laukkanen, H. Teramoto et al., "Cross talk between the bombesin neuropeptide receptor and Sonic hedgehog pathways in small cell lung carcinoma," *Oncogene*, vol. 34, no. 13, pp. 1679–1687, 2015.
- [70] I. P. Gialmanidis, V. Bravou, I. Petrou et al., "Expression of bmi1, FoxF1, nanog, and  $\gamma$ -catenin in relation to hedgehog signaling pathway in human non-small-cell lung cancer," *Lung*, vol. 191, no. 5, pp. 511–521, 2013.
- [71] I. P. Gialmanidis, V. Bravou, S. G. Amanetopoulou, J. Varakis, H. Kourea, and H. Papadaki, "Overexpression of hedgehog pathway molecules and FOXM1 in non-small cell lung carcinomas," *Lung Cancer*, vol. 66, no. 1, pp. 64–74, 2009.
- [72] J. Talpale, J. K. Chen, M. K. Cooper et al., "Effects of oncogenic mutations in Smoothened and Patched can be reversed by cyclopamine," *Nature*, vol. 406, no. 6799, pp. 1005–1009, 2000.
- [73] S. Mizuarai, A. Kawagishi, and H. Kotani, "Inhibition of p70S6K2 down-regulates Hedgehog/GLI pathway in non-small cell lung cancer cell lines," *Molecular Cancer*, vol. 8, article no. 44, 2009.
- [74] D. Hanahan and R. A. Weinberg, "Hallmarks of cancer: the next generation," *Cell*, vol. 144, no. 5, pp. 646–674, 2011.
- [75] D. Öhlund, E. Elyada, and D. Tuveson, "Fibroblast heterogeneity in the cancer wound," *Journal of Experimental Medicine*, vol. 211, no. 8, pp. 1503–1523, 2014.
- [76] O. Bermudez, E. Hennen, I. Koch, M. Lindner, and O. Eickelberg, "Gli1 mediates lung cancer cell proliferation and sonic hedgehog-dependent mesenchymal cell activation," *PLoS ONE*, vol. 8, no. 5, Article ID e63226, 2013.
- [77] L. Huang, V. Walter, D. N. Hayes, and M. Onaitis, "Hedgehog-Gli1 signaling inhibition suppresses tumor growth in squamous lung cancer," *Clinical Cancer Research*, vol. 20, no. 6, pp. 1566–1575, 2014.
- [78] S. Thomson, E. Buck, F. Petti et al., "Epithelial to mesenchymal transition is a determinant of sensitivity of non-small-cell lung carcinoma cell lines and xenografts to epidermal growth factor receptor inhibition," *Cancer Research*, vol. 65, no. 20, pp. 9455–9462, 2005.
- [79] M. Y. Maitah, S. Ali, A. Ahmad, S. Gadgeel, and F. H. Sarkar, "Up-regulation of sonic hedgehog contributes to TGF- $\beta$ 1-induced epithelial to mesenchymal transition in NSCLC cells," *PLoS ONE*, vol. 6, no. 1, Article ID e16068, 2011.
- [80] C. Choe, Y.-S. Shin, S.-H. Kim et al., "Tumor-stromal interactions with direct cell contacts enhance motility of non-small cell lung cancer cells through the hedgehog signaling pathway," *Anticancer Research*, vol. 33, no. 9, pp. 3715–3724, 2013.
- [81] P. Valent, D. Bonnet, R. De Maria et al., "Cancer stem cell definitions and terminology: the devil is in the details," *Nature Reviews Cancer*, vol. 12, no. 11, pp. 767–775, 2012.
- [82] Y.-C. Chen, H.-S. Hsu, Y.-W. Chen et al., "Oct-4 expression maintained cancer stem-like properties in lung cancer-derived CD133-positive cells," *PLoS ONE*, vol. 3, no. 7, Article ID e2637, 2008.
- [83] V. Tirino, R. Camerlingo, R. Franco et al., "The role of CD133 in the identification and characterisation of tumour-initiating cells in non-small-cell lung cancer," *European Journal of Cardiothoracic Surgery*, vol. 36, no. 3, pp. 446–453, 2009.
- [84] E. L.-H. Leung, R. R. Fiscus, J. W. Tung et al., "Non-small cell lung cancer cells expressing CD44 are enriched for stem cell-like properties," *PLoS ONE*, vol. 5, no. 11, Article ID e14062, 2010.
- [85] M. Alamgeer, C. D. Peacock, W. Matsui, V. Ganju, and D. N. Watkins, "Cancer stem cells in lung cancer: evidence and controversies," *Respirology*, vol. 18, no. 5, pp. 757–764, 2013.
- [86] J. Liu, Z. Xiao, S. K.-M. Wong et al., "Lung cancer tumorigenicity and drug resistance are maintained through ALDH(hi)CD44(hi) tumor initiating cells," *Oncotarget*, vol. 4, no. 10, pp. 1698–1711, 2013.
- [87] S. O. Lee, X. Yang, S. Duan et al., "IL-6 promotes growth and epithelial-mesenchymal transition of CD133+ cells of non-small cell lung cancer," *Oncotarget*, vol. 7, no. 6, pp. 6626–6638, 2015.
- [88] S. Sarvi, A. C. Mackinnon, N. Avlonitis et al., "CD133+ cancer stem-like cells in small cell lung cancer are highly tumorigenic and chemoresistant but sensitive to a novel neuropeptide antagonist," *Cancer Research*, vol. 74, no. 5, pp. 1554–1565, 2014.
- [89] N. Bora-Singhal, D. Perumal, J. Nguyen, and S. Chellappan, "Gli1-mediated regulation of Sox2 facilitates self-renewal of stem-like cells and confers resistance to EGFR inhibitors in non-small cell lung cancer," *Neoplasia*, vol. 17, no. 7, pp. 538–551, 2015.
- [90] W.-J. Chen, C.-C. Ho, Y.-L. Chang et al., "Cancer-associated fibroblasts regulate the plasticity of lung cancer stemness via paracrine signalling," *Nature Communications*, vol. 5, article 3472, 2014.
- [91] P. Yuan, H. Kadara, C. Behrens et al., "Sex determining region Y-box 2 (SOX2) is a potential cell-lineage gene highly expressed in the pathogenesis of squamous cell carcinomas of the lung," *PLoS ONE*, vol. 5, no. 2, Article ID e9112, 2010.
- [92] V. Justilien, M. P. Walsh, S. A. Ali, E. A. Thompson, N. R. Murray, and A. P. Fields, "The PRKCI and SOX2 Oncogenes are coamplified and cooperate to activate hedgehog signaling in lung squamous cell carcinoma," *Cancer Cell*, vol. 25, no. 2, pp. 139–151, 2014.
- [93] C. Choe, Y.-S. Shin, C. Kim et al., "Crosstalk with cancer-associated fibroblasts induces resistance of non-small cell lung cancer cells to epidermal growth factor receptor tyrosine kinase inhibition," *OncoTargets and Therapy*, vol. 8, pp. 3665–3678, 2015.
- [94] R. Katayama, A. T. Shaw, T. M. Khan et al., "Mechanisms of acquired crizotinib resistance in ALK-rearranged lung cancers," *Science translational medicine*, vol. 4, no. 120, Article ID 120ra17, 2012.
- [95] S. Kobayashi, T. J. Boggon, T. Dayaram et al., "EGFR mutation and resistance of non-small-cell lung cancer to gefitinib," *The New England Journal of Medicine*, vol. 352, no. 8, pp. 786–792, 2005.
- [96] S. Pan, X. Wu, J. Jiang et al., "Discovery of NVP-LDE225, a potent and selective smoothened antagonist," *ACS Medicinal Chemistry Letters*, vol. 1, no. 3, pp. 130–134, 2010.
- [97] C. M. Della Corte, C. Bellevisine, G. Vicidomini et al., "SMO gene amplification and activation of the hedgehog pathway as novel mechanisms of resistance to anti-epidermal growth factor receptor drugs in human lung cancer," *Clinical Cancer Research*, vol. 21, no. 20, pp. 4686–4697, 2015.

- [98] K. D. Robarge, S. A. Brunton, G. M. Castanedo et al., "GDC-0449-A potent inhibitor of the hedgehog pathway," *Bioorganic and Medicinal Chemistry Letters*, vol. 19, no. 19, pp. 5576–5581, 2009.
- [99] M. Lauth, Å. Bergström, T. Shimokawa, and R. Toftgård, "Inhibition of GLI-mediated transcription and tumor cell growth by small-molecule antagonists," *Proceedings of the National Academy of Sciences of the United States of America*, vol. 104, no. 20, pp. 8455–8460, 2007.
- [100] P. Infante, M. Mori, R. Alfonsi et al., "Gli1/DNA interaction is a druggable target for Hedgehog-dependent tumors," *The EMBO Journal*, vol. 34, no. 2, pp. 200–217, 2015.
- [101] L. Zhang, L. Li, M. Jiao et al., "Genistein inhibits the stemness properties of prostate cancer cells through targeting Hedgehog-Gli1 pathway," *Cancer Letters*, vol. 323, no. 1, pp. 48–57, 2012.
- [102] J. Kim, J. J. Lee, J. Kim, D. Gardner, and P. A. Beachy, "Arsenic antagonizes the Hedgehog pathway by preventing ciliary accumulation and reducing stability of the Gli2 transcriptional effector," *Proceedings of the National Academy of Sciences of the United States of America*, vol. 107, no. 30, pp. 13432–13437, 2010.
- [103] K. Chang, M. Yang, J. Zheng et al., "Arsenic trioxide inhibits cancer stem-like cells via down-regulation of Gli1 in lung cancer," *American Journal of Translational Research*, vol. 8, no. 2, pp. 1133–1143, 2016.

## Research Article

# Voltage-Dependent Inactivation of MscS Occurs Independently of the Positively Charged Residues in the Transmembrane Domain

Takeshi Nomura,<sup>1,2</sup> Masahiro Sokabe,<sup>1,3</sup> and Kenjiro Yoshimura<sup>1,4</sup>

<sup>1</sup>International Cooperative Research Project (ICORP)/Solution Oriented Research for Science and Technology (SORST), Cell-Mechanosensing Project, Japan Science and Technology Agency, Nagoya 466-8550, Japan

<sup>2</sup>Department of Rehabilitation, Kyushu Nutrition Welfare University, Kitakyushu 800-029, Japan

<sup>3</sup>Mechanobiology Laboratory, Nagoya University Graduate School of Medicine, Nagoya 466-8550, Japan

<sup>4</sup>Department of Machinery and Control Systems, Shibaura Institute of Technology, Saitama 337-8570, Japan

Correspondence should be addressed to Takeshi Nomura; [tnomura@knwu.ac.jp](mailto:tnomura@knwu.ac.jp)

Received 5 September 2016; Accepted 23 November 2016

Academic Editor: Daisuke Miyoshi

Copyright © 2016 Takeshi Nomura et al. This is an open access article distributed under the Creative Commons Attribution License, which permits unrestricted use, distribution, and reproduction in any medium, provided the original work is properly cited.

MscS (mechanosensitive channel of small conductance) is ubiquitously found among bacteria and plays a major role in avoiding cell lysis upon rapid osmotic downshock. The gating of MscS is modulated by voltage, but little is known about how MscS senses membrane potential. Three arginine residues (Arg-46, Arg-54, and Arg-74) in the transmembrane (TM) domain are possible to respond to voltage judging from the MscS structure. To examine whether these residues are involved in the voltage dependence of MscS, we neutralized the charge of each residue by substituting with asparagine (R46N, R54N, and R74N). Mechanical threshold for the opening of the expressed wild-type MscS and asparagine mutants did not change with voltage in the range from  $-40$  to  $+100$  mV. By contrast, inactivation process of wild-type MscS was strongly affected by voltage. The wild-type MscS inactivated at  $+60$  to  $+80$  mV but not at  $-60$  to  $+40$  mV. The voltage dependence of the inactivation rate of all mutants tested, that is, R46N, R54N, R74N, and R46N/R74N MscS, was almost indistinguishable from that of the wild-type MscS. These findings indicate that the voltage dependence of the inactivation occurs independently of the positive charges of R46, R54, and R74.

## 1. Introduction

Various types of mechanosensitive (MS) channels are present in virtually all living organisms and detect forces due to mechanical stimulus such as touch, hearing, turgor, and osmotic change [1–6]. The bacterial MS channels of small (MscS) and large (MscL) conductance are considered to act as a “safety valve” to protect cells from lysis upon osmotic downshock by releasing osmolytes [7–9].

MscS is directly activated by membrane stretch [10] and the gating is modulated by membrane voltage [11–13]. The MscS crystal structure resolved at  $3.9$  Å shows that MscS is a homoheptamer of a subunit with three TM helices (TM1, TM2, and TM3). A large cytoplasmic vestibule with seven side portals and a distal entrance possibly acts as a molecular

prefilter for ion permeation [14–18]. MscS has a conductance of  $\sim 1$  nS and has a slight preference to anions as the permeable ions [10, 11].

MscS shows marked voltage-dependent inactivation under depolarizing conditions [13, 19–22]. Inactivation is facilitated when an electrostatic interaction between TM and cytoplasmic domains is disrupted [21]. The arginine residues at positions 46 and 74 in TM1 and TM2, respectively, of MscS have been predicted as the candidates for voltage sensor taking into account that the voltage-gated  $\text{Na}^+$ ,  $\text{K}^+$ , and  $\text{Ca}^{2+}$  channels have an array of arginine residues especially in the fourth TM segment (S4) that carries most of the gating charge as the voltage sensor [23–27] (Figure 1). Arg-54 in TM1 may also be susceptible to membrane voltage since it is embedded in lipid bilayer in the modeled structure [28]. However, these

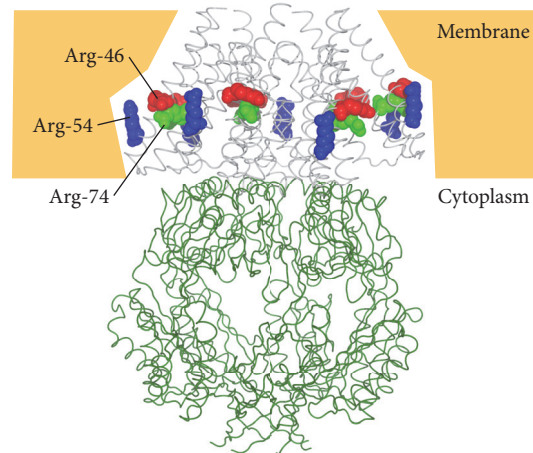


FIGURE 1: Homoheptameric structure of MscS (2OAU, [30]). The residues 46 (red), 54 (Blue), and 74 (green) are shown in space fill representation. The transmembrane (white) and cytoplasmic (green) domains are shown in ribbon representation.

arginine residues have not been examined in the context of voltage-dependent inactivation [13, 19–21, 29].

In the present study, we investigated whether or not the three charged residues (R46, R54, and R74) in the TM1 and TM2 domains of MscS are involved in the voltage-dependent inactivation by using patch-clamp technique and hypoosmotic shock experiment. Our results suggest that voltage-dependent inactivation occurs independently of the positively charged residues in the TM domains of MscS.

## 2. Materials and Methods

The *Escherichia coli* strain PB111 ( $\Delta mscS$ ) and MJF455 ( $\Delta mscL\Delta mscS$ ) were used to host MscS expression in patch-clamp and hypoosmotic shock experiments [21, 31]. Site-directed mutagenesis was performed on the *mscS* gene in a pB10b vector by mega-primer PCR method [32]. Successful mutagenesis was verified by DNA sequencing. Mutants were expressed in PB111 or MJF455.

Giant spheroplasts were prepared as described [33]. Briefly, PB111 cells were grown in a modified LB (Luria Bertani) medium containing 0.5% NaCl instead of 1% NaCl [11] in the presence of cephalexin (final concentration: 0.06 mg/mL). After incubation for 1.5 h, IPTG (isopropyl- $\beta$ -D-thiogalactoside) was added (final concentration: 1 mM) to induce MscS expression. The induction time was 10 min. The cells were harvested, digested by lysozyme (0.2 mg/mL), and collected by centrifugation.

The channel activities of MscS were recorded in the inside-out membrane patch mode of the patch-clamp technique as described previously [32]. The pipette solution contained 200 mM KCl, 90 mM MgCl<sub>2</sub>, 10 mM CaCl<sub>2</sub>, and 5 mM HEPES (pH 6.0), whereas the bath solution additionally contained 300 mM sucrose. Negative pressure was applied by using a syringe at various voltages (intracellular potential against extracellular one) ranging from -100 to +40 mV to obtain the gating threshold of MscS and MscL. For the

evaluation of the inactivation process, pressure was controlled using High-Speed Pressure-Clamp apparatus (HSPC-1; ALA Scientific Inst. Inc., Westbury, NY) [34], following the protocol by Akitake et al. [13]. Currents were amplified with an AXOPATCH 200B amplifier (Axon Instruments, Foster City, CA), and data were acquired at a sampling rate of 5 kHz with 2 kHz low-pass filtration. The pCLAMP 9 software (Axon Instruments, Foster City, CA) was used for data acquisition and analysis. The MscS/MscL gating threshold ratios were determined by the pressure (proportional to membrane tension) applied through patch pipettes required for the first channel opening of MscS and MscL [32].

Cell viability after hypoosmotic shock was determined by the method described previously [9, 31, 35]. When cell density reached  $OD_{600} = \sim 0.15$  in the minimal medium, IPTG (1 mM) was added to induce expression. After 1 h of growth, the cells were diluted 1:20 in the prewarmed minimal medium with or without 0.5 M NaCl. A downshock into 0 M NaCl medium was applied to the cells for 5 min. After the downshock, each sample was spread on LB agar plates containing 1 mM IPTG and incubated overnight at 37°C before counting the ratio of colony forming units. The downshock experiment was performed three times for each MscS mutant.

## 3. Results

Candidate arginine residues (R46, R54, and R74) that are possibly involved in voltage sensing were substituted with asparagine to examine the effects of charge neutralization. Thus, we generated three single mutants (R46N, R54N, and R74N) and one double mutant (R46N/R74N). To examine the effect of these mutations on the gating threshold of MscS, the channel activities were measured while applying negative pressure through a patch pipette to the inside-out membrane patch of the giant spheroplasts expressing the wild-type or mutant MscS. Figure 2(a) shows typical channel activities of the wild-type MscS at membrane voltage of +20 mV.

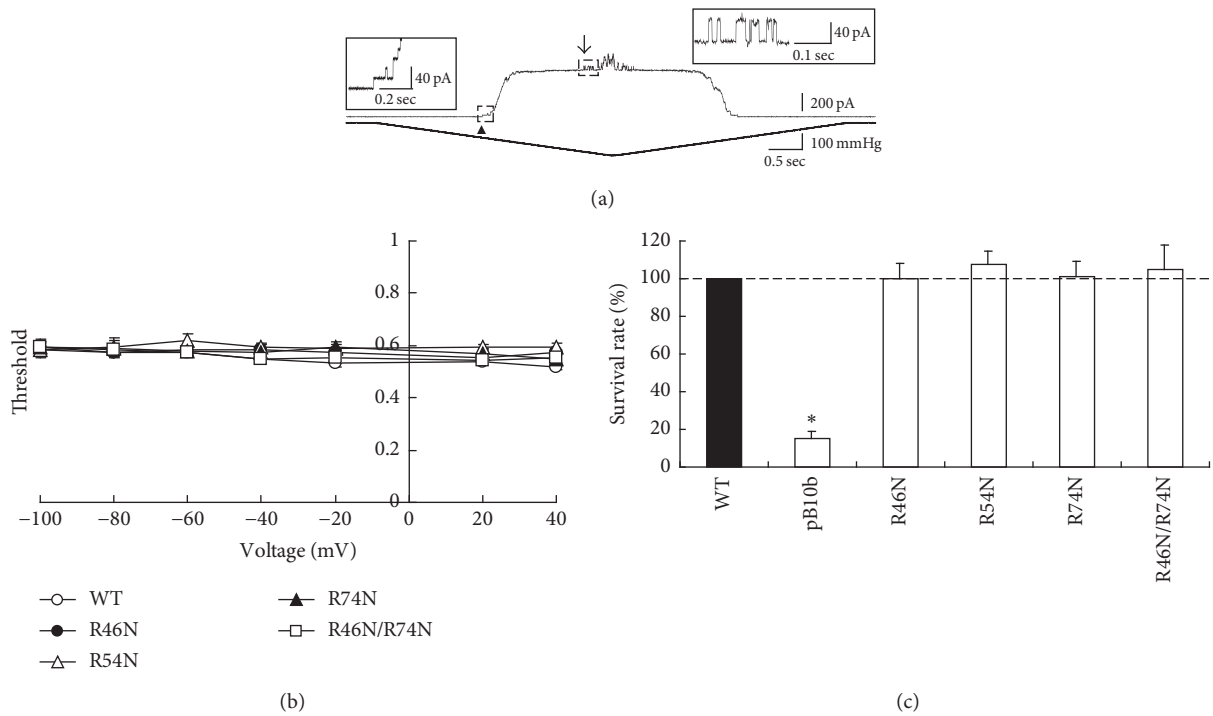


FIGURE 2: Characteristics of the wild-type and mutant MscS expressed in PB111 ( $\Delta mscS$ ) cells. (a) PB111 cells expressing the wild-type MscS. Channel current (*upper*) and pressure applied through a pipette (*bottom*) are shown. The insets show the magnification of the MscS and MscL traces indicated by *arrowhead* and *arrow*, respectively. Membrane voltage: +20 mV. (b) The gating threshold ratio (MscS/MscL) of the wild-type and mutant MscS at various voltages (−100 to +40 mV). Values are expressed as mean  $\pm$  SEM (standard error of the mean) ( $n = 5-7$ ). (c) Effects of hypoosmotic shock on MJF455 ( $\Delta mscS\Delta mscL$ ) cells expressing MscS or harboring an empty vector (pB10b) (mean  $\pm$  SEM,  $n = 9$ ). No significant difference was observed between the wild-type and mutant MscS. The asterisks indicate significant difference from the wild-type ( $p < 0.05$  by *t*-test).

Upon increasing the negative pressure, MscS appeared first (*arrowhead*). The channel conductance was  $\sim 1$  nS. Further increase in the negative pressure opened MscL, which has a conductance of  $\sim 2.5$  nS (*arrow*). MscS and MscL were assigned based on the conductance and threshold. Using MscL as an internal standard, the threshold of MscS was expressed as the ratio to that of MscL (MscS/MscL). The threshold of the wild-type MscS was constantly  $\sim 0.6$  when the membrane (cytoplasmic) potential was scanned between  $-100$  and  $+40$  mV (Figure 2(b)). The gating threshold of each MscS mutant (R46N, R54N, R74N, and R46N/R74N) was also constant at  $\sim 0.6$  in this voltage range.

When *E. coli* cells are exposed to hypoosmotic condition, they avoid cell lysis by opening MscS and MscL. Consistently, most of MJF455 double-knockout ( $\Delta mscL\Delta mscS$ ) cells harboring an empty vector (pB10b) did not survive upon hypoosmotic shock from 0.5 M to 0 M NaCl (Figure 2(c)). Hypotonic shock experiments are advantageous to patch-clamp experiments in that the MscS activity can be assessed under native conditions. When the cells expressing MscS mutants were challenged with hypoosmotic shock, the threshold did not differ statistically from that of wild-type MscS (R46N;  $100 \pm 8\%$ , R54N;  $108 \pm 7\%$ , R74N;  $101 \pm 8\%$  and R46N/R74N;  $105 \pm 13\%$ ; Figure 2(c)), suggesting that the charge neutralization does not alter the MscS activity to a degree at which cell survival is affected.

MscS exhibits prominent voltage-dependent inactivation under depolarizing conditions [13, 19–21]. To test whether the neutralization of the positively charged residues in TM segments modifies the inactivation, we recorded the inactivation at cytoplasmic potentials ranging from  $-60$  to  $+80$  mV. Figure 3(a) illustrates the current traces of channel activities of the wild-type MscS (*upper trace*). A rapid decrease in channel current was observed at  $+60$  and  $+80$  mV, whereas the decay in current was significantly slow at negative potentials. R46N MscS also inactivated at  $+60$  and  $+80$  mV but not at negative potentials (Figure 3(a), *lower trace*). Furthermore, R54N MscS, R74N MscS, and R46N/R74N MscS showed rapid inactivation at positive potentials of  $+60$  and  $+80$  mV (Figure S1) (see Supplementary Material available online at <http://dx.doi.org/10.1155/2016/2401657>). Figure 3(b) depicts the relationship between voltage and time constant of inactivation when an exponential function is fitted. All MscS mutants showed rapid current decrease at  $+60$  and  $+80$  mV at rates similar to the wild-type MscS.

In the above experiment, the initial phase of inactivation was not resolved because it overlapped with the activation phase. To separate the inactivation process from the activation process, we activated MscS at  $-20$  mV by applying negative pressure and then switched the membrane potential to  $+60$  mV (Figure 4(a)). The transition from the full open to closed state fitted best to two exponential functions at  $+60$  mV

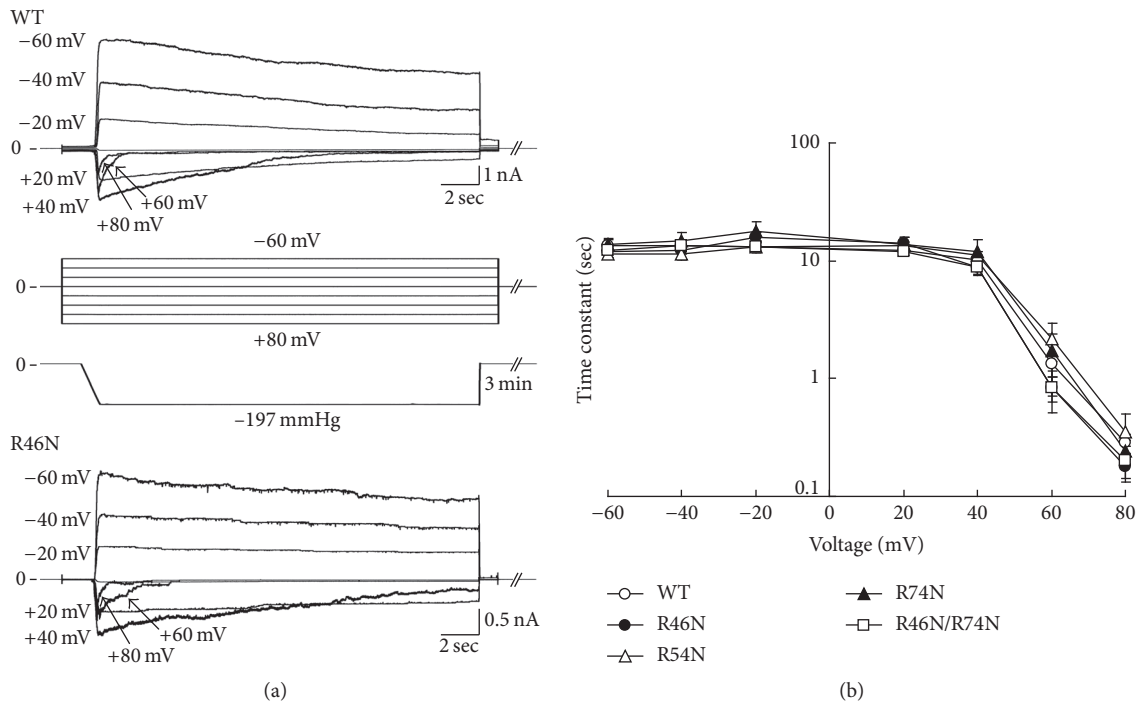


FIGURE 3: Inactivation of the wild-type and mutant MscS expressed in MJF455 ( $\Delta mscS\Delta mscL$ ) cells. (a) Channel currents (*upper*) of the wild-type and R46N MscS at different voltages ranging from  $-60$  to  $+80$  mV (*middle*). Subsaturating negative pressure (*bottom*) was applied after the change in voltage. (b) The time constant of inactivation at each voltage. Time constant was faster at depolarizing voltages of  $+60$  and  $+80$  mV (mean  $\pm$  SEM,  $n = 5-9$ ).

in the wild-type MscS: the fast and slow time constants were  $\tau = 0.28 \pm 0.03$  sec and  $\tau = 0.88 \pm 0.27$  sec, respectively. This observation indicates that voltage-dependent inactivation process has multiple processes. When the same protocol was applied to the R46N MscS (Figure 4(a) *lower trace*), R54N MscS, R74N MscS, and R46N/R74N MscS (Fig. S2), the current decayed at rates roughly similar to the wild-type MscS.

Figure 4(b) summarizes the fast and slow time constants of the wild-type and mutant MscS. Either component did not differ significantly between the wild-type and mutant MscS. The above observations indicate that charged residues at TM domains are not involved in the voltage-dependent inactivation process.

#### 4. Discussion

An array of positively charged residues in the S4 segment of voltage-gated ion channels is responsible for voltage-dependent channel activities [23, 24]. Voltage dependence of MscS may also be attributed to the positively charged residues in TM1 and TM2 [27]. In the present study, we investigated the role of arginine residues in TM1 and TM2 in the voltage-dependent inactivation of MscS. The channel properties of MscS mutants were examined using patch-clamp technique and cell viability test. Against our prediction, we found that the neutralization of positive charges in TM1 and TM2 has little impact on the voltage dependence of MscS inactivation.

The voltage sensor in voltage-gated sodium, potassium, and calcium channels contains a conserved pattern of 6-7

positively charged residues (Arg or Lys) in their S4 segment [36]. These charges move on a change in the electric potential gradient across the TM domain, resulting in the channel gating. The gating charge of Kv channels has been estimated to be about 12-13 per channel [37]. On the other hand, the opening of MscS is only weakly voltage-dependent and thus the gating charge of MscS is estimated to be as small as about 0.8 per channel [13]. By contrast, the inactivation of MscS is more dependent on voltage and two positive charges are proposed to be transferred [13].

The movement of gating charges is of crucial importance for understanding the mechanism of voltage-dependent inactivation of MscS. The positively charged residues R46, R54, and R74 are predicted to be close to the cytoplasmic surface of the lipid bilayer in the closed resting state. Generally, when a membrane potential shifts from hyperpolarizing to depolarizing condition, TM helices with positive charges move toward the extracellular side [36]. On the other hand, TM1 and TM2 of MscS interact with membrane lipid and the hydrophobic residues at both ends of TM1 and TM2 provide lipid-protein interaction important for mechanosensitivity [31]. Therefore, even if the electrical field is changed, TM1 and TM2 may move little in the direction perpendicular to membrane because of the tight lipid-protein interactions at both ends of the TM helices. This speculation argues against the idea that TM1 and TM2 move on depolarization but is consistent with the present result.

In a molecular dynamics simulation (MD) study, neutralization of R46 and R74 reduces the hydration of the pore and

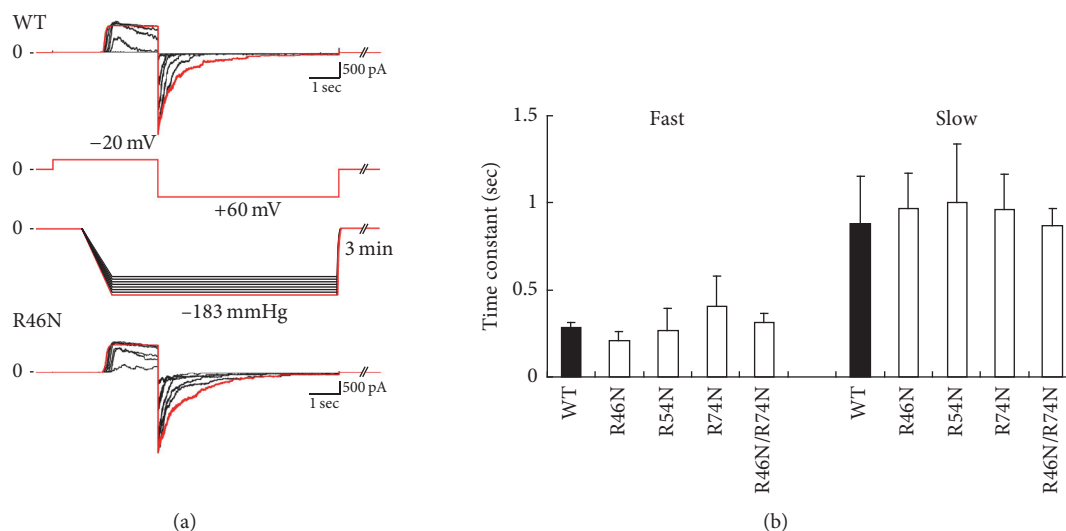


FIGURE 4: Rate of inactivation in the wild-type and mutant MscS expressed in MJF455 ( $\Delta mscS\Delta mscL$ ) cells. (a) Macroscopic currents of wild-type (upper) and R46N MscS (bottom). Voltage was changed from  $-20$  to  $+60$  mV (upper middle) in the presence of pressure (lower middle). Red traces show the traces at the pressure where MscS was activated fully ( $-183$  mmHg in wild-type and  $-203$  mmHg in R46N MscS). (b) Time constant of fast and slow components of the wild-type and mutant MscS (mean  $\pm$  SE,  $n = 5-7$ ) as determined by fitting current traces to two-exponential functions.

results in loss of conductivity, although they are distant from the pore [38]. However, our results show that neutralizing these positively charged residues does not influence the conductance of MscS. The MD study detected movement of TM1 and TM2 at  $\pm 100$  mV but not at smaller voltage; the movement was reduced greatly in R46 mutants. This finding also does not fit well our data that inactivation occurs at  $+60$  and  $+80$  mV and that R46N MscS inactivates like the wild-type MscS. These discrepancies may be because the crystal structure used in the MD study is different from the structure in the lipid bilayer or under membrane stretch.

A variety of models of MscS inactivation process have been proposed: (1) shrinking of the cytoplasmic vestibule [39], (2) kink formation between the pore-lining helix TM3a and TM3b, which connects the gate and the cytoplasmic vestibule [29], and (3) electrostatic interaction between the upper surface of the cytoplasmic vestibule and the loop that connects the TM1-TM2 helices [21]. However, none of these models incorporate the charged residues in TM1 and TM2. Thus, we speculate that potential gradient is present not only in TM domain but also in the cytoplasmic vestibule and that the cytoplasmic vestibule is responsible for the voltage dependence of the inactivation process of MscS.

In conclusion, we have shown that the neutralization of the arginine residues in TM1 and TM2 does not influence the stretch activation and voltage-dependent inactivation of MscS. We also found that voltage-dependent inactivation process has two (fast and slow) components. The structural bases of these components are yet to be determined.

## Competing Interests

The authors declare no conflict of interests.

## Acknowledgments

This work was supported by a Grant-in-Aid from the Ministry of Education, Culture, Sports, Science, and Technology, Japan (26460300 to Takeshi Nomura).

## References

- [1] A. Anishkin and C. Kung, "Microbial mechanosensation," *Current Opinion in Neurobiology*, vol. 15, no. 4, pp. 397-405, 2005.
- [2] J. H. Naismith and I. R. Booth, "Bacterial mechanosensitive channels-MscS: evolution's solution to creating sensitivity in function," *Annual Review of Biophysics*, vol. 41, no. 1, pp. 157-177, 2012.
- [3] C. Kung, "A possible unifying principle for mechanosensation," *Nature*, vol. 436, no. 7051, pp. 647-654, 2005.
- [4] C. D. Cox, Y. Nakayama, T. Nomura, and B. Martinac, "The evolutionary 'tinkering' of MscS-like channels: generation of structural and functional diversity," *Pflügers Archiv European Journal of Physiology*, vol. 467, no. 1, pp. 3-13, 2014.
- [5] O. P. Hamill and B. Martinac, "Molecular basis of mechanotransduction in living cells," *Physiological Reviews*, vol. 81, no. 2, pp. 685-740, 2001.
- [6] E. Perozo, "Gating prokaryotic mechanosensitive channels," *Nature Reviews Molecular Cell Biology*, vol. 7, no. 2, pp. 109-119, 2006.
- [7] P. Blount, M. J. Schroeder, and C. Kung, "Mutations in a bacterial mechanosensitive channel change the cellular response to osmotic stress," *The Journal of Biological Chemistry*, vol. 272, no. 51, pp. 32150-32157, 1997.
- [8] B. Ajouz, C. Berrier, A. Garrigues, M. Besnard, and A. Ghazi, "Release of thioredoxin via the mechanosensitive channel MscL during osmotic downshock of *Escherichia coli* cells," *The Journal of Biological Chemistry*, vol. 273, no. 41, pp. 26670-26674, 1998.

- [9] N. Levina, S. Töttemeyer, N. R. Stokes, P. Louis, M. A. Jones, and I. R. Booth, "Protection of *Escherichia coli* cells against extreme turgor by activation of MscS and MscL mechanosensitive channels: identification of genes required for MscS activity," *The EMBO Journal*, vol. 18, no. 7, pp. 1730–1737, 1999.
- [10] S. Sukharev, "Purification of the small mechanosensitive channel of *Escherichia coli* (MscS): the subunit structure, conduction, and gating characteristics in liposomes," *Biophysical Journal*, vol. 83, no. 1, pp. 290–298, 2002.
- [11] B. Martinac, M. Buechner, A. H. Delcour, J. Adler, and C. Kung, "Pressure-sensitive ion channel in *Escherichia coli*," *Proceedings of the National Academy of Sciences of the United States of America*, vol. 84, no. 8, pp. 2297–2301, 1987.
- [12] P. Koprowski and A. Kubalski, "Voltage-independent adaptation of mechanosensitive channels in *Escherichia coli* protoplasts," *Journal of Membrane Biology*, vol. 164, no. 3, pp. 253–262, 1998.
- [13] B. Akitake, A. Anishkin, and S. Sukharev, "The 'dashpot' mechanism of stretch-dependent gating in MscS," *Journal of General Physiology*, vol. 125, no. 2, pp. 143–154, 2005.
- [14] R. B. Bass, P. Strop, M. Barclay, and D. C. Rees, "Crystal structure of *Escherichia coli* MscS, a voltage-modulated and mechanosensitive channel," *Science*, vol. 298, no. 5598, pp. 1582–1587, 2002.
- [15] P. Koprowski and A. Kubalski, "C termini of the *Escherichia coli* mechanosensitive ion channel (MscS) move apart upon the channel opening," *Journal of Biological Chemistry*, vol. 278, no. 13, pp. 11237–11245, 2003.
- [16] S. Miller, M. D. Edwards, C. Ozdemir, and I. R. Booth, "The closed structure of the MscS mechanosensitive channel. Cross-linking of single cysteine mutants," *Journal of Biological Chemistry*, vol. 278, no. 34, pp. 32246–32250, 2003.
- [17] S. Miller, W. Bartlett, S. Chandrasekaran, S. Simpson, M. Edwards, and I. R. Booth, "Domain organization of the MscS mechanosensitive channel of *Escherichia coli*," *The EMBO Journal*, vol. 22, no. 1, pp. 36–46, 2003.
- [18] C. D. Cox, T. Nomura, C. S. Ziegler, A. K. Campbell, K. T. Wann, and B. Martinac, "Selectivity mechanism of the mechanosensitive channel MscS revealed by probing channel subconducting states," *Nature Communications*, vol. 4, article no. 2137, 2013.
- [19] V. Vásquez and E. Perozo, "Voltage dependent gating in MscS," *Biophysical Journal*, vol. 86, p. 545A, 2004.
- [20] M. Sotomayor, V. Vásquez, E. Perozo, and K. Schulten, "Ion conduction through MscS as determined by electrophysiology and simulation," *Biophysical Journal*, vol. 92, no. 3, pp. 886–902, 2007.
- [21] T. Nomura, M. Sokabe, and K. Yoshimura, "Interaction between the cytoplasmic and transmembrane domains of the mechanosensitive channel MscS," *Biophysical Journal*, vol. 94, no. 5, pp. 1638–1645, 2008.
- [22] I. Rowe, A. Anishkin, K. Kamaraju, K. Yoshimura, and S. Sukharev, "The cytoplasmic cage domain of the mechanosensitive channel MscS is a sensor of macromolecular crowding," *The Journal of General Physiology*, vol. 143, no. 5, pp. 543–557, 2014.
- [23] L. M. Mannuzzu, M. M. Moronne, and E. Y. Isacoff, "Direct physical measure of conformational rearrangement underlying potassium channel gating," *Science*, vol. 271, no. 5246, pp. 213–216, 1996.
- [24] A. Cha and F. Bezanilla, "Characterizing voltage-dependent conformational changes in the Shaker K<sup>+</sup> channel with fluorescence," *Neuron*, vol. 19, no. 5, pp. 1127–1140, 1997.
- [25] S. K. Aggarwal and R. MacKinnon, "Contribution of the S4 segment to gating charge in the Shaker K<sup>+</sup> channel," *Neuron*, vol. 16, no. 6, pp. 1169–1177, 1996.
- [26] S.-A. Seoh, D. Sigg, D. M. Papazian, and F. Bezanilla, "Voltage-sensing residues in the S2 and S4 segments of the Shaker K<sup>+</sup> channel," *Neuron*, vol. 16, no. 6, pp. 1159–1167, 1996.
- [27] F. Bezanilla and E. Perozo, "Structural biology: force and voltage sensors in one structure," *Science*, vol. 298, no. 5598, pp. 1562–1563, 2002.
- [28] A. Anishkin, B. Akitake, and S. Sukharev, "Characterization of the resting MscS: modeling and analysis of the closed bacterial mechanosensitive channel of small conductance," *Biophysical Journal*, vol. 94, no. 4, pp. 1252–1266, 2008.
- [29] B. Akitake, A. Anishkin, N. Liu, and S. Sukharev, "Straightening and sequential buckling of the pore-lining helices define the gating cycle of MscS," *Nature Structural and Molecular Biology*, vol. 14, no. 12, pp. 1141–1149, 2007.
- [30] S. Steinbacher, R. Bass, P. Strop, and D. C. Rees, "Structures of the prokaryotic mechanosensitive channels MscL and MscS," *Current Topics in Membranes*, vol. 58, pp. 1–24, 2007.
- [31] T. Nomura, M. Sokabe, and K. Yoshimura, "Lipid-protein interaction of the MscS mechanosensitive channel examined by scanning mutagenesis," *Biophysical Journal*, vol. 91, no. 8, pp. 2874–2881, 2006.
- [32] K. Yoshimura, A. Batiza, M. Schroeder, P. Blount, and C. Kung, "Hydrophilicity of a single residue within MscL correlates with increased channel mechanosensitivity," *Biophysical Journal*, vol. 77, no. 4, pp. 1960–1972, 1999.
- [33] P. Blount, S. I. Sukharev, P. C. Moe, B. Martinac, and C. Kung, *Mechanosensitive Channels of Bacteria*, vol. 294 of *Methods in Enzymology*, 1999.
- [34] S. R. Besch, T. Suchyna, and F. Sachs, "High-speed pressure clamp," *Pflugers Archiv European Journal of Physiology*, vol. 445, no. 1, pp. 161–166, 2002.
- [35] K. Yoshimura, T. Nomura, and M. Sokabe, "Loss-of-function mutations at the rim of the funnel of mechanosensitive channel MscL," *Biophysical Journal*, vol. 86, no. 4, pp. 2113–2120, 2004.
- [36] F. Bezanilla, "The voltage sensor in voltage-dependent ion channels," *Physiological Reviews*, vol. 80, no. 2, pp. 555–592, 2000.
- [37] N. E. Schoppa, K. McCormack, M. A. Tanouye, and F. J. Sigworth, "The size of gating charge in wild-type and mutant Shaker potassium channels," *Science*, vol. 255, no. 5052, pp. 1712–1715, 1992.
- [38] S. A. Spronk, D. E. Elmore, and D. A. Dougherty, "Voltage-dependent hydration and conduction properties of the hydrophobic pore of the mechanosensitive channel of small conductance," *Biophysical Journal*, vol. 90, no. 10, pp. 3555–3569, 2006.
- [39] W. Grajkowski, A. Kubalski, and P. Koprowski, "Surface changes of the mechanosensitive channel MscS upon its activation, inactivation, and closing," *Biophysical Journal*, vol. 88, no. 4, pp. 3050–3059, 2005.

## Review Article

# Roles of pRB in the Regulation of Nucleosome and Chromatin Structures

**Chiharu Uchida**

*Advanced Research Facilities & Services, Preeminent Medical Photonics Education & Research Center,  
Hamamatsu University School of Medicine, 1-20-1 Handayama, Higashi-ku, Hamamatsu, Shizuoka 431-3192, Japan*

Correspondence should be addressed to Chiharu Uchida; [cuchida@hama-med.ac.jp](mailto:cuchida@hama-med.ac.jp)

Received 8 September 2016; Accepted 8 November 2016

Academic Editor: Keiko Kawauchi

Copyright © 2016 Chiharu Uchida. This is an open access article distributed under the Creative Commons Attribution License, which permits unrestricted use, distribution, and reproduction in any medium, provided the original work is properly cited.

Retinoblastoma protein (pRB) interacts with E2F and other protein factors to play a pivotal role in regulating the expression of target genes that induce cell cycle arrest, apoptosis, and differentiation. pRB controls the local promoter activity and has the ability to change the structure of nucleosomes and/or chromosomes via histone modification, epigenetic changes, chromatin remodeling, and chromosome organization. Functional inactivation of pRB perturbs these cellular events and causes dysregulated cell growth and chromosome instability, which are hallmarks of cancer cells. The role of pRB in regulation of nucleosome/chromatin structures has been shown to link to tumor suppression. This review focuses on the ability of pRB to control nucleosome/chromatin structures via physical interactions with histone modifiers and chromatin factors and describes cancer therapies based on targeting these protein factors.

## 1. Introduction

Retinoblastoma protein (pRB) was the first identified tumor suppressor that negatively regulates the G0/G1 to S phase transition of the cell cycle [1–4]. The most studied mechanism by which pRB negatively regulates the cell cycle progression involves the binding of pRB to E2F transcription factors (E2F1, E2F2, and E2F3a), which inhibits E2F-mediated expression of S phase-promoting genes, such as DNA polymerase, dihydrofolate reductase, and cdc2 [5–8]. pRB inhibits E2F transcriptional activity via a direct interaction with E2F; however, pRB also blocks cell cycle progression by repressing the target gene transcription through the recruitment of transcriptional corepressors and/or chromatin remodeling protein factors at promoter regions [9] (Figure 1). The repressors and protein factors that cooperatively participate in the pRB-mediated transient repression and silencing of the target genes include histone deacetylase (HDAC) [10, 11], replication factor C [12], ATPase subunit of the SWI/SNF complexes Brm and BRG1 (Brm-related gene 1) proteins [13, 14], DNA methyltransferase DNMT1 [11], and heterochromatin protein HP1 [15], which all belong to “LXCXE proteins” that possess the LXCXE-binding motif for pRB [16]. In addition to these

LXCXE proteins, pRB interacts with many nuclear proteins independently of the LXCXE motif, such as histone methyltransferase Suv39h1 [15, 17], histone demethylase LSD1 [18], and histone demethylase RBP2 (KDM5A) [19, 20]. Through the physical interaction with these protein factors, pRB is involved in not only local gene promoter inactivation but also global epigenetic control of cellular senescence [21] and differentiation [22]. Furthermore, pRB was recently shown to play a role in DNA replication during the S phase and G2/M phases via interactions with regulator proteins for DNA replication [12, 23], chromatin condensation [24–27], and mitotic spindle formation [28]. Understandably, cellular events, such as G0/G1 maintenance, DNA replication, and mitosis progression, require drastic nuclear structural changes and chromosomal rearrangement. In fact, pRB plays an important role in chromosome dynamics and modulation of chromatin structure. For example, pRB depletion alters chromatin structure due to changes in epigenetic histone modifications, such as methylation and acetylation, which controls the status in G0/G1 cells [9] or heterochromatin region in the interphase cells [29, 30]. pRB depletion can also cause incomplete chromosomal condensation and segregation in mitosis [24–27]. Importantly, it has been

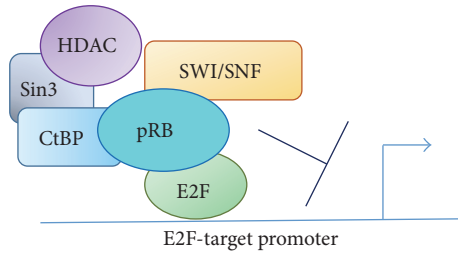


FIGURE 1: pRB blocks cell cycle progression by repressing the E2F-target gene transcription through the recruitment of transcriptional corepressors and/or chromatin remodeling protein factors, such as HDAC, Sin3, CtBP, and SWI/SNF, at promoter regions.

demonstrated that the aberrant chromatin structure and chromosome arrangement caused by pRB inactivation are associated with chromosomal instability [25, 27, 31], which is a hallmark of human cancer cells. The focus of this review is to highlight the active role of pRB in chromatin/chromosome structure and stability. Indeed, this appears to be the most crucial aspect in the tumor suppressor ability of pRB.

## 2. pRB-Mediated Repression of Gene Transcription via Chromatin Structure Modification

**2.1. Cooperative Function of Chromatin Remodeling Complex SWI/SNF with pRB.** The SWI/SNF is a chromatin remodeling protein complex that participates in ATP-dependent histone exchange or removal of histones from DNA, thereby altering nucleosome structure and mobilizing higher-order formation of chromatin [32]. SWI/SNF-mediated structural changes of nucleosomes are involved in both activation and repression of gene transcription depending on components of the SWI/SNF complex. As an example of transactivation ability, a SWI/SNF subunit, BRG1, is necessary for *MAX* gene transcription, *MAX*-dependent prodifferentiation gene expression, and the subsequent suppression of lung cancer development [33]. In this case, the BRG1-containing SWI/SNF complex may facilitate gene transcription by enhancing the accessibility of transcriptional activator proteins to the *MAX* enhancer/promoter regions. It is also known that some SWI/SNF complexes containing Brm and/or BRG1 bind to pRB and repress transcription. The ATPases of SWI/SNF/Brm/BRG1 are involved in chromatin remodeling and the pRB-mediated inhibition of cell proliferation. pRB was reported to recruit Brm or BRG1 through their LXCXE domains, thereby repressing gene expression and effectively inducing cell cycle arrest [13, 14]. Although the LXCXE-dependent interaction between endogenous pRB and Brm/BRG1 is not fully confirmed, their cooperative function was identified in transcriptional inactivation mechanisms [34]. The cell lines C33A and A437 are deficient in both Brm and BRG1 and are resistant to active pRB-mediated cell cycle arrest; however, ectopic expression of either Brm or BRG1 restored cell cycle arrest [35, 36]. Brm is required for nuclease resistance at cyclin

A promoter region [36]. Although it is not clear whether Brm and BRG1 can be included in the same SWI/SNF/pRB complex, pRB uses the ATPase activity of Brm or BRG1 to change nucleosome structures. This occurs in cooperation with histone deacetylases and/or histone demethylases (as described below) to produce compact and tight nucleosome structures and thus repression of target gene expression. Because Brm and BRG1 can interact with both pRB and E2F [37], these ATPase chromatin remodelers efficiently facilitate the formation of closed chromatin structures and the pRB-mediated repression of the E2F-target genes.

**2.2. Cooperative Function of Histone and DNA Modifiers with pRB.** Histone deacetylase 1 (HDAC1) is also an important pRB binding protein for the inhibition of gene expression. In addition to the direct inhibition of E2F-mediated transactivation, pRB also recruits HDAC1 to the DNA strands near the promoter region of the E2F-target gene [10]. A canonical LXCXE motif derived from a viral oncogene competed with the pRB-HDAC1 binding, which suggests that the interaction between pRB and HDAC1 is LXCXE motif dependent [16]. However, recent studies have indicated that pRB-HDAC1 interactions can be indirect because HDAC1 is found in Sin3 and CtBP/CtIP complexes, which are also pRB-interacting proteins [38, 39].

Histone acetylation opens the chromatin structure so that transcriptional activators can access the target promoter region and stimulate transcription. On the other hand, HDACs catalyze the removal of an acetyl group from lysine residues in histones and nonhistone target proteins. By reducing acetylation, HDACs facilitate the inactivation of gene expression, including pRB-mediated repression of E2F-target gene expression (Figure 1). A previous study showed that the levels of histone acetylation at the E2F-target, that is, the *cyclin E promoter*, are reduced when *cyclin E* is silenced; furthermore, the HDAC inhibitor trichostatin A inhibited the pRB-mediated inactivation of cyclin E expression [40].

These studies suggest that pRB regulates the local chromatin structure by recruiting HDAC1 to modulate the balance of histone acetylation levels, and HDAC inhibitors may compromise the tumor suppressive pRB-E2F axis. However, a number of studies showed that HDACs are overexpressed in many human cancer cells [41, 42]. Indeed, many HDAC inhibitors have been characterized as anticancer drugs that show great efficacy for cancer cell death [43, 44]. This may reflect the pRB-E2F-independent effect of HDACs on cell viability, or the inhibitors may exert a stronger effect on HDAC-suppressed E2F-dependent apoptotic signaling compared to E2F-dependent cell proliferation.

Histone methylation and demethylation are important modifications of nucleosome/chromatin modifications induced by pRB. pRB interacts with the histone methyltransferase, Suv39h1, which is mainly responsible for trimethylation of H3K9 (H3K9me3), although it can also catalyze dimethylation of H3K9 (H3K9me2) [45, 46]. H3K9me2/3 is recognized by heterochromatin protein HP1 through its N-terminal chromodomain. This interaction changes the

neighboring nucleosome structure into a packed form that is transcriptionally inactive. Accordingly, H3K9me3 is known as a “repressive histone mark” [47–50]. Notably, both of H3K9 methylation and HDAC-mediated deacetylation are induced on nucleosome histones near cyclin E promoter region after pRB-mediated E2F inactivation [15], suggesting that pRB has the ability to alter local chromatin structure via Suv39h1, HP1, and HDAC. HP1 is a family of three subtypes (HP1 $\alpha$ , HP1 $\beta$ , and HP1 $\gamma$ ) and each HP1 subtype plays common and also distinct roles in human cells. HP1 $\alpha$  is mainly located in heterochromatin, while HP1 $\beta$  and HP1 $\gamma$  are associated with both heterochromatin and euchromatin [51, 52]. HP1 binds to the N-terminus of Suv39h1 through its chromoshadow domain [53, 54]. In this context, HP1 $\beta$ - or HP1 $\gamma$ -bound pRB may repress the euchromatic local promoter region of *cyclin E* by recruiting Suv39h1. This induces heterochromatin formation by recruiting additional Suv39h1 molecules to methylate the neighboring nucleosomes and produce a tightly packed and inactivated promoter region. Consistently, HP1 $\beta$  was found at E2F-responsive promoter regions when pRB was activated to repress these promoters [55]. Furthermore, pRB-HP1 $\gamma$  interaction mediates silencing of E2F-target gene expression and heterochromatin formation during senescence [56]. pRB-HP1 $\gamma$ -H3K9me3 is also involved in gene silencing in adult cardiac myocytes, which permanently exit the cell cycle [57]. However, it is not clear whether pRB directly interacts with HP1 $\alpha$  to repress the expression of E2F-target genes because HP1 $\alpha$  was found to be preferentially phosphorylated in the G2/M phase and to bind to histone H3 modified with both K9me3 and phosphorylated serine 10 in mitotic chromosomes [58]. HDAC-mediated deacetylation could effectively induce methylation in target regions, because HDAC interacts with Suv39h1 [59] and Suv39h1 binds to HP1 [47–50, 53, 54]. Although Suv39h1 does not have the LXCXE motif, in contrast to HP1, excess LXCXE peptides compete with pRB to bind to these proteins [15, 60]. Thus, many LXCXE-dependent interactions between pRB and pRB binding proteins are important for the regulation of chromatin structure dynamics.

LSD1 [18, 61] and RBP2 [20, 62] are pRB-interacting histone demethylases that catalyze the removal of methyl groups from H3K4me1/2 and H3K4me3, respectively. Methylated H3K4 is an “active histone mark” because it is enriched at the actively transcribing promoter region. pRB binds to these demethylases in a LXCXE-independent manner and represses transcription by recruiting them to demethylate H3K4me1/2 and H3K4me3 on the pRB-target promoter region. pRB recruits LSD1 on the same promoter for E2F binding; however, pRB-E2F immunoprecipitates did not contain LSD1 even though E2F was precipitated with LSD1 [18]. Although the functional significance of LSD1 on pRB-dependent E2F inhibition of cell cycle progression is not clear, recent studies showed that LSD1 is a member of different subsets of repressor complexes, such as CoREST families [63]. Importantly, these repressor complexes include several chromatin remodeling proteins and positively contribute to cell differentiation and somatic cell reprogramming. It is likely that the pRB-LSD1-E2F interaction functions in these cellular events.

At the onset of cell differentiation, cell cycle-driving gene expression is silenced for the exit from the cell cycle. The active histone marks are removed, while the repressive marks are introduced in target nucleosomes near the cell cycle-driving genes. The H3K4me3 demethylase activity of RBP2 has also been demonstrated to contribute to regulating cell differentiation [20]. Studies using RBP2 RNAi in pRB-null cells showed that RBP2 inhibits pRB-mediated differentiation under certain conditions; however, RBP2 also shares common roles with pRB at the initial step of differentiation by repressing transcription of cell cycle-driving genes [64]. These observations suggest that the pRB-mediated H3K4me3 demethylases modulate the histone modification with repressive marks on the pRB-target gene promoters and alter the chromatin structure to induce differentiation.

In addition to histone methyltransferase and demethylases, pRB binds to DNA methyl transferase 1 (DNMT1), which associates with HDAC *in vivo* [11]. pRB forms a complex with E2F, DNMT1, and HDAC through the LXCXE motif to repress E2F-mediated transactivation [11, 65]. Based on a previous report, the methylation of pRB-E2F's target promoter DNA may enhance and spread the histone modulation near the promoter. Many studies have demonstrated that methylated DNA recruits HDAC to deacetylate histones, thus resulting in an efficient repression of transcription [11, 66–68]. Although E2F-bound reporter DNA was not methylated under experimental conditions, the E2F-binding domain within a CpG-rich region of the endogenous *RB* promoter is highly methylated in many types of human cancer cells [17, 69, 70]. Taken together, these pRB binding histone modifiers, DNA methyltransferases, and chromatin modifiers can promote the pRB-dependent regulation of gene expression by changing the chromatin structure to a repressive form near the pRB-E2F-target promoter.

### 3. pRB-Mediated Regulation of Higher-Order Chromatin Structures and Chromosomes

In addition to the regulation of local nucleosome structures at the pRB-E2F-target promoter region, pRB plays a pivotal role in maintaining whole chromosome dynamics, such as heterochromatin formation and mitotic chromosome segregation. Cells expressing mutant pRB that lacks the LXCXE-interacting domain show abnormal chromatin structures, including decondensed chromatin and display butterfly chromosomes [71]. These aberrant chromosomes fail to properly separate during anaphase. This role of pRB is closely linked to terminal differentiation, senescence, and chromosome stability. In this section, the protein factors that directly/indirectly bind to pRB are discussed with a focus on regulation of higher-order of chromatin/chromosome structures.

**3.1. The Role of pRB in Heterochromatin Formation.** pRB participates in the formation and maintenance of heterochromatin structure [9, 72]. As described above, pRB binds

to Suv39h and members of HP1 family, and the Suv39h-H3K9me3-HP1 axis is a key axis of regulator of heterochromatin formation [15, 45–60, 71]. In addition to H3K9m3, pRB binds to Suv4-20h1 and h2, which are methyltransferases that trimethylate histone H4K20 [71].

The H4K20me3 is enriched at pericentromeric heterochromatin, whereas pRB-deficient mouse fibroblasts show reduced levels of H4K20me3 at pericentromeric heterochromatin [73]. Similarly, cells that expressed a mutant pRB lacking the LXCXE-interacting domain (RB1<sup>ΔL/ΔL</sup>) showed diminished methylation of H4K20 at pericentromeric DNA [74]. Furthermore, loss of all of RB families caused a reduction in H4K20m3 levels at telomere DNA [75]. Interestingly, HP1 recruitment by the Suv39h-H3K9me3 axis is essential for Suv4-20h1/h2-mediated H4K20 trimethylation [76]. Notably, BRG1 depletion resulted in an aberrant chromatin organization caused by a dispersion of H3K9me3 and H4K20me3 and an increased mitotic failure caused by lagging anaphase chromosomes [77]. These effects are similar to the results found after pRB depletion in fibroblast cells. Taken together, these data strongly suggest that the regulation of type-specific histone methylation/demethylation by pRB leads to proper chromatin organization via several chromatin modulators, including HP1 and BRG1.

Polycomb group (PcG) proteins were originally identified as repressor complexes for *Hox* genes. PcG proteins regulate the *Hox* expression pattern required for development [78, 79]. Recent studies showed that PcG proteins are essential for the regulation of normal gene expression during cell differentiation and embryonic development [80, 81]. Two major PcG protein complexes, PRC1 and PRC2, are recruited to target sites in the genome [82] to modulate the chromatin structure and repress gene expression. Early studies revealed that HPC2, a PcG protein, coimmunoprecipitated with pRB, E2F, and CtBP and colocalized with pRB in a nuclear PcG complex in cultured cells [83]. In addition, pRB showed HPC2-dependent and HDAC-independent repressor activity for E2F-target cyclin A gene expression [83]. pRB is required for the binding of PRC2 and its target gene to establish H3K27me3 at the gene site [84]. A recent study showed that RBR, a pRB ortholog in plants, directly interacts with PRC2 and inactivates the late embryonic genes through facilitating PRC2-mediated H3K27 trimethylation [85]. Thus, pRB promotes global gene silencing via interactions with PRC1 and PRC2, which contribute to cell differentiation and embryonic development.

**3.2. The Role of pRB in Chromatin Structure and Dynamics for Differentiation and Senescence.** pRB facilitates cell cycle arrest and thus influences differentiation and senescence [21, 86] (Figure 2). Since differentiation requires multiple steps, including exit from the cell cycle and drastic changes in gene expression/silencing via both local and global nucleosome remodeling, notably, pRB binding epigenetic/chromatin modifiers are actively involved in differentiation. As described above, epigenetic or chromatin modifiers, such as histone demethylase RBP2 and the PcG protein complexes PRCs, are closely associated with pRB-mediated

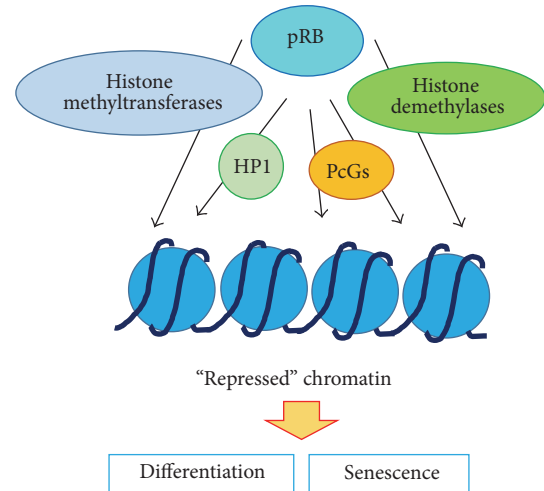


FIGURE 2: pRB facilitates cell cycle arrest and thus influences differentiation and senescence via interactions with histone modifiers and chromatin associating factors including histone methyltransferases, histone demethylases, HP1, and PcGs.

cell differentiation. One example is the role of these proteins in the pRB-mediated onset of myogenic differentiation [87, 88]. RBP2 appears to possess two opposing activities in pRB-mediated myogenic differentiation: inhibiting E2F-targeted cell cycle genes and the other is antagonizing differentiation by repressing the mitochondrial genes necessary for myogenic differentiation [89]. Apart from RBP2, Suv39h depletion in myoblasts leads to a reduction in H3K9 methylation, repression of S phase genes, and expression of myogenic marker genes under differentiating conditions [90].

Cellular senescence can be triggered by repetitive replication (replicative senescence), activation of oncogenic genes (oncogenic senescence), telomere shortening, and genotoxic stresses [91]. Senescence requires permanent cell cycle arrest and maintenance of a “repressed” nucleosome/chromatin structure. Here, the pRB-dependent packed nucleosome/chromatin structure appears to be a key event for the initiation and maintenance of senescence (Figure 2). Acute loss of pRB in senescent fibroblasts shows cell cycle reentry and recovery of cell proliferation [92], while reintroduction and overexpression of pRB in cancer cells induce senescence [93]. Furthermore, pRB is enriched on the E2F-target promoter region when cells are senescent [21, 56]. These observations prompt us to predict an active role of pRB in establishing senescence by forming a “repressed” chromatin structure. However, a previous study suggested that pRB plays a crucial role in the later stages of establishing or maintaining senescence, since cells lacking pRB or expressing a mutant pRB retain abilities to exhibit cell cycle arrest but definitively reenter to cell cycle and restart proliferation [94]. Thus, pRB-dependent epigenetic modification, that is, a repressive histone methylation mark, appears to be important for the establishment and maintenance of senescence. Indeed, pRB is necessary for the enrichment of H3K9me3 and demethylation of H3K4me3 on E2F-target promoters in senescent cells [56, 94, 95]. In addition, H3K9me3 levels are reduced

in mutant pRB-expressing  $RBI^{\Delta L/\Delta L}$  MEFs, which are unable to maintain senescence [94]. The study on  $RBI^{\Delta L/\Delta L}$  MEFs also showed that the pRB binds to promyelocytic leukemia (PML) protein, and the LXCXE-interacting domain in pRB was important for PML-pRB binding to establish constitutive heterochromatin H3K9me3 at E2F-target genes [96–98]. Importantly, recent findings revealed that pRB was involved in the formation of senescent-associated heterochromatin foci (SAHF) [56]. This result furthers our understanding of the role of pRB in the establishment of senescence. SAHF is involved in the compaction of entire individual chromosomes and contain enriched H3K9me3, H3K27me3, and high mobility group A (HMGA) proteins that are known chromatin architectural factors. Active hypophosphorylated pRB is required for SAHF formation, and the knockdown of pRB inhibited SAHF formation [99–101]. Similarly, an experiment using E7-driven inactivation of pRB showed that pRB is crucial for HMGA2-induced SAHF formation [102]. pRB associates with PML to enrich H3K9me3 at the target genes, and PML can be a component of SAHF [96]. Taken together, pRB can control the structural changes in heterochromatin that are dependent on senescence induction, including SAHF formation; however, the precise mechanism by which pRB contributes to SAHF assembly remains unclear.

**3.3. The Role of pRB in Chromatin Condensation and Chromosome Segregation.** Early studies demonstrated that pRB is a component of nuclear matrix, which consists of highly compartmentalized and insoluble nonchromatin structures [103]. The nuclear matrix is composed of fibrogranular-like networks that associate with particular DNA regions and corresponding proteins. Thus, the matrix is considered as a platform where “DNA events” occur efficiently, such as transcription, replication, or heterochromatin formation, chromatin condensation, and chromatin remodeling. This indicates a crucial and primordial role for pRB as a nuclear matrix protein that actively participates in the repression of transcription and chromatin organization. A number of nuclear matrix proteins have been identified, including nuclear restricted protein/brain NRP/B, which binds to pRB and regulates neuronal differentiation [104]. This study suggests that an adequate composition of nuclear matrix proteins is important for cell function and pRB-dependent.

Recently, pRB was discovered to bind to nuclear matrix apparatus protein NuMA [28], a mitotic spindle organizer and essential protein for mitotic progression [105]. Mitotic progression requires highly dynamic chromosome changes. Knockdown of pRB results in the aberrant distribution of NuMA in M phase cells and misalignment of spindle poles and spindle microtubules. Cells overexpressing mutant NuMA, which are deficient in pRB binding, showed similar defects. Notably, these M phase defects were associated with an uncondensed and dispersed chromosome structure, which can trigger chromosomal/genomic instability. Chromosomal instability is a hallmark of cancer cells accompanied with aneuploidy and an abnormal number of chromosomes, mainly caused by chromosome missegregation [106]. Importantly, a number of studies showed that pRB inactivation

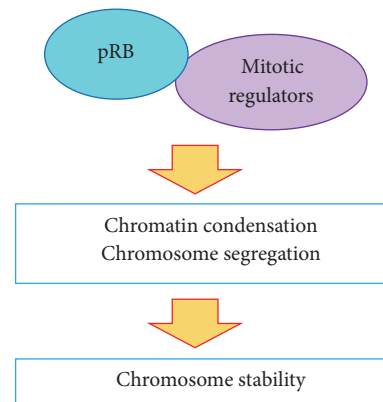


FIGURE 3: pRB is involved in proper chromatin condensation and chromosome segregation via interactions with mitotic regulators, such as condensin II and NuMA, which is important for chromosome stability.

increased chromosomal instability [25–27, 107]. Consistently, the mutant NuMA-expressing cells showed low survival rates, and the surviving mutant cells showed multiple micronuclei after a long culture period [28]. These data indicate that the pRB-NuMA interaction is required for proper mitotic progression and chromosome organization (Figure 3).

Condensin II complex is another important factor that highlights the role of pRB in mitotic chromosome dynamics and stability (Figure 3). An initial study reported that Rbf, the fruit fly ortholog of pRB, interacted with drosophila condensin II subunit Cap-D3, which requires Rbf for the correct localization on chromosomes; furthermore, *Rbf* mutant showed abnormal and dispersed chromatin during prophase and prometaphase [24]. Additionally, human CAP-D3 (hCAP-D3) binds to pRB in an LXCXE-dependent manner, and  $RBI^{\Delta L/\Delta L}$  cells displayed an inefficient localization of condensin II on chromosomes, delayed progression to metaphase, and lagging chromosomes in anaphase [26]. Moreover, a recent study showed that pRB, E2F, and hCAP-D3 form a complex at pericentromeric heterochromatin, and disruption of the complex in  $RBI^{-/-}$  cells and  $RBI^{\Delta L/\Delta L}$  cells correlated with an increase in aberrant replication, mitotic errors, and aneuploidy [27]. Surprisingly, the loss of even one copy of *RBI* can produce the same phenotype, suggesting that pRB plays a pivotal role in the maintenance of the chromosome structure and stability via physical interactions with chromatin-related proteins.

#### 4. Maintenance of Nucleosome/Chromosome Structures by pRB and Cancer

pRB acts as a central tumor suppressor mainly by inhibiting the cell cycle progression driven by E2F-target genes. In this context, the involvement of pRB directs antitumorigenesis via a conformational change in the local promoter region with or without epigenetic marks. In many types of human cancer cells, the levels of pRB and pRB binding

nucleosome/chromatin-related proteins that act cooperatively with pRB, such as HDACs [42], PML [98], and BRG1 [108], are decreased. Furthermore, loss of Suv4-20h1 in breast cancer cells was reported [109]. On the other hand, the binding proteins that are largely inactivated by pRB appear to be overexpressed in cancer cells. One example is that the expression of the H3K4me3 demethylase RBP2 was increased in lung cancer [110]. Interestingly, the H3K4me3 demethylase LSD1 is also overexpressed in many human cancers, including lung, breast, prostate, and blood cancers [63], which seems incomprehensible since LSD1 is a member of the pRB repressor complex. Some reports have proposed the tumor suppressor role of LSD1; however, the majority of studies demonstrated the tumor-promoting activity of LSD1 [111]. Although this controversial function needs to be fully investigated, it is possible that LSD1 plays two opposing roles that are dependent on the formation of distinct complexes. In support of this notion, LSD1 is able to act as a transcriptional activator and a repressor [112, 113]. A possible explanation is that LSD1 binds to the tumor suppressor, p53, to repress p53-mediated transcriptional activation and inhibit p53-induced apoptosis by removing monomethylation (K370me1) at K370 [114]. This indicates a tumor-promoting function of LSD1.

The increase in chromosomal instability due to dysfunctional pRB binding may be related to cancer development in the light of the normal pRB role in maintaining the global nucleosome structure and chromosome organization. Indeed, NuMA is overexpressed in colorectal and breast cancer [105, 115–118], suggesting that overexpressed NuMA, which can overcome sequestering by pRB, induces mitotic defects leading to chromosomal instability, which is similar to the results of pRB depletion. In addition,  $Rb1^{\Delta L/\Delta L}$ , a mutant pRB lacking the LXCXE-binding cleft, enhances tumorigenesis and genomic instability in mouse tumor models [26]. All of these findings support a central role for pRB and its nuclear binding proteins in the regulation and maintenance of the global nucleosome/chromosome structure, which is crucial for tumor suppression.

## 5. Cancer Treatments and Perspectives

Overall, this review focuses on the physical contribution of pRB, which controls local nucleosome structure and whole chromosome organization. pRB inactivation results in dysregulated cell proliferation, apoptosis, differentiation, and senescence, and all those defects can lead to tumorigenesis and cancer progression [31]. Phosphorylation is a well-known mechanism to inactivate pRB; in addition, pRB inactivation by oncogenic proteins is induced with viral infection, and *Rb1* gene expression is repressed via promoter DNA methylation. The proteasome-dependent degradation of pRB promoted by ubiquitin ligase Mdm2, which was the first identified ubiquitin ligase for p53 [119, 120], is another pathway for pRB inactivation [121–126]. Therefore, inhibiting pRB inactivation is a relevant strategy to suppress cancer progression. Some efficacious compounds and small molecules have been investigated, such as CDK4/6 inhibitors to suppress pRB phosphorylation [127] and Nutlin-3, a small molecule

inhibitor of Mdm2, to regulate Mdm2-mediated regulation of pRB expression [128–130]. The CDK4/6 inhibitor palbociclib is currently in phase II development, and ribociclib and abemaciclib are in phase I development. These inhibitors are being tested in breast cancer, lung cancer, liposarcoma, and neuroblastoma [131]. A recent study showed that Nutlin-3 caused p53 and p21 accumulation and hypophosphorylation of pRB, which lead to cell cycle arrest in some cell lines; however, in other cell lines, Nutlin-3 downregulated pRB and resulted in E2F-independent apoptosis [129]. These results are Mdm2-dependent, as evidenced by Mdm2 knockdown experiments that abolished the effects. Thus, Nutlin-3 is a potential therapeutic agent that can suppress and/or kill cancer cells. However, the mechanism by which Nutlin-3 induces degradation of hypophosphorylated pRB in some cells is not clear.

Targeting enzyme activities related to nucleosome histone modification may be a potent strategy for cancer therapy. Despite its repression of E2F-target gene expression, HDAC is overexpressed in many human cancers, and a number of HDAC inhibitors, including trichostatin A and vorinostat (also known as SAHA (suberoylanilide hydroxamic acid)), are antitumor agents [43]. SAHA was the first clinically approved HDAC inhibitor for the treatment of cutaneous T-cell lymphoma (CTCL). Belinostat (PXD101, Beleodaq) is used for the treatment of refractory peripheral T-cell lymphoma (PTCL), and panobinostat (LBH589) is used for the treatment of multiple myeloma. These drugs were approved by the FDA in 2014 and in 2015, respectively. In addition to these compounds, other HDAC inhibitors, including givinostat (ITF2357), abexinostat (PCI-24781), quisinostat (JNJ-26481585), resminostat (4SC-201), pracinostat (SB939), CUDC-101, CHR-2845, and CHR-2847, are currently in various clinical phases [43].

Chaetocin was the first discovered inhibitor for drosophila histone methyltransferase Su(var)3-9, and it selectively inhibits human Suv39h1 [111]. BIX01294 shows good *in vitro* inhibitory potency against Suv39h. LSD1 inhibitors, including the small molecules GSK2879552 and ORY1001, have been developed [63]. A screening of a panel of 165 cancer cell lines revealed that the SCLC and AML cell lines were sensitive to GSK2879552 [63]. Studies on the molecular mechanism of action suggested that GSK2879552 inhibits the demethylation of H3K4me1/2 by LSD1, leading to alterations in neuroendocrine gene expression and the suppression of SCLC cell growth. GSK2879552 is currently in a phase I clinical trial for AML and SCLC [132]. Compound 4SC-202 inhibits both HDAC1/2/3 and LSD1 and its phase I trial for the treatment of hematological tumors was recently completed [133].

Thus, the continued development of inhibitors of CDK4/6 and histone modifiers aims to eradicate cancer cells. Several agents showed sufficient potency in clinical trials. However, selective inhibitors or activators that target the interaction between pRB and its binding proteins during nucleosome/chromatin organization have not been identified. It is understandable that development of such agents, such as LXCXE-binding inhibitors, is difficult because pRB and its LXCXE-dependent interactions have central and diverse

functions in living cells. To increase antitumor effectiveness, treatment with a combination of CDK4/6 inhibitors and inhibitors of histone modifiers could inhibit cell cycle progression and induce apoptosis via structural changes in the nucleosome/chromosome. A greater understanding of the direct role of pRB role in chromatin remodeling or chromosome organization will facilitate the development of antitumor agents and therapeutics for pRB-inactivated human cancers.

## Competing Interests

The author declares that there is no conflict of interests regarding the publication of this paper.

## Acknowledgments

The author thanks colleagues for discussion and helpful suggestions.

## References

- [1] A. G. Knudson Jr., "Mutation and cancer: statistical study of retinoblastoma," *Proceedings of the National Academy of Sciences of the United States of America*, vol. 68, no. 4, pp. 820–823, 1971.
- [2] W. K. Cavenee, T. P. Dryja, R. A. Phillips et al., "Expression of recessive alleles by chromosomal mechanisms in retinoblastoma," *Nature*, vol. 305, no. 5937, pp. 779–784, 1983.
- [3] W. K. Cavenee, M. F. Hansen, M. Nordenskjold et al., "Genetic origin of mutations predisposing to retinoblastoma," *Science*, vol. 228, no. 4698, pp. 501–503, 1985.
- [4] S. H. Friend, R. Bernards, S. Rogelj et al., "A human DNA segment with properties of the gene that predisposes to retinoblastoma and osteosarcoma," *Nature*, vol. 323, no. 6089, pp. 643–646, 1986.
- [5] R. A. Weinberg, "The retinoblastoma protein and cell cycle control," *Cell*, vol. 81, no. 3, pp. 323–330, 1995.
- [6] R. J. White, "Regulation of RNA polymerases I and III by the retinoblastoma protein: a mechanism for growth control?" *Trends in Biochemical Sciences*, vol. 22, no. 3, pp. 77–80, 1997.
- [7] N. Dyson, "The regulation of E2F by pRB-family proteins," *Genes & Development*, vol. 12, no. 15, pp. 2245–2262, 1998.
- [8] Y. Takahashi, J. B. Rayman, and B. D. Dynlacht, "Analysis of promoter binding by the E2F and pRB families in vivo: distinct E2F proteins mediate activation and repression," *Genes & Development*, vol. 14, no. 7, pp. 804–816, 2000.
- [9] R. Ferreira, I. Naguibneva, L. L. Pritchard, S. Ait-Si-Ali, and A. Harel-Bellan, "The Rb/chromatin connection and epigenetic control: opinion," *Oncogene*, vol. 20, no. 24, pp. 3128–3133, 2001.
- [10] A. Brehm, E. A. Miska, D. J. McCance, J. L. Reid, A. J. Bannister, and T. Kouzarides, "Retinoblastoma protein recruits histone deacetylase to repress transcription," *Nature*, vol. 391, no. 6667, pp. 597–601, 1998.
- [11] K. D. Robertson, S. Ait-Si-Ali, T. Yokochi, P. A. Wade, P. L. Jones, and A. P. Wolffe, "DNMT1 forms a complex with RB, E2F1 and HDAC1 and represses transcription from E2F-responsive promoters," *Nature Genetics*, vol. 25, no. 3, pp. 338–342, 2000.
- [12] V. Pennaneach, I. Salles-Passador, A. Munshi et al., "The large subunit of replication factor C promotes cell survival after DNA damage in an LXCXE motif- and Rb-dependent manner," *Molecular Cell*, vol. 7, no. 4, pp. 715–727, 2001.
- [13] J. L. Dunaief, B. E. Strober, S. Guha et al., "The retinoblastoma protein and BRG1 form a complex and cooperate to induce cell cycle arrest," *Cell*, vol. 79, no. 1, pp. 119–130, 1994.
- [14] B. E. Strober, J. L. Dunaief, Guha, and S. P. Goff, "Functional interactions between the hBRM/hBRG1 transcriptional activators and the pRB family of proteins," *Molecular and Cellular Biology*, vol. 16, no. 4, pp. 1576–1583, 1996.
- [15] S. J. Nielsen, R. Schneider, U.-M. Bauer et al., "Rb targets histone H3 methylation and HP1 to promoters," *Nature*, vol. 412, no. 6846, pp. 561–565, 2001.
- [16] A. Dahiya, M. R. Gavin, R. X. Luo, and D. C. Dean, "Role of the LXCXE binding site in Rb function," *Molecular and Cellular Biology*, vol. 20, no. 18, pp. 6799–6805, 2000.
- [17] C. Giacinti and A. Giordano, "RB and cell cycle progression," *Oncogene*, vol. 25, no. 38, pp. 5220–5227, 2006.
- [18] C. M. Chau, Z. Deng, H. Kang, and P. M. Lieberman, "Cell cycle association of the retinoblastoma protein Rb and the histone demethylase LSD1 with the Epstein-Barr virus latency promoter Cp," *Journal of Virology*, vol. 82, no. 7, pp. 3428–3437, 2008.
- [19] A. R. Fattaey, K. Helin, M. S. Dembski et al., "Characterization of the retinoblastoma binding proteins RBP1 and RBP2," *Oncogene*, vol. 8, no. 11, pp. 3149–3156, 1993.
- [20] J. Christensen, K. Agger, P. A. C. Cloos et al., "RBP2 belongs to a family of demethylases, specific for tri- and dimethylated lysine 4 on histone 3," *Cell*, vol. 128, no. 6, pp. 1063–1076, 2007.
- [21] A. Chicas, X. Wang, C. Zhang et al., "Dissecting the unique role of the retinoblastoma tumor suppressor during cellular senescence," *Cancer Cell*, vol. 17, no. 4, pp. 376–387, 2010.
- [22] L. Khidr and P.-L. Chen, "RB, the conductor that orchestrates life, death and differentiation," *Oncogene*, vol. 25, no. 38, pp. 5210–5219, 2006.
- [23] N. E. Simon and A. Schwacha, "The Mcm2-7 replicative helicase: a promising chemotherapeutic target," *BioMed Research International*, vol. 2014, Article ID 549719, 14 pages, 2014.
- [24] M. S. Longworth, A. Herr, J.-Y. Ji, and N. J. Dyson, "RBF1 promotes chromatin condensation through a conserved interaction with the Condensin II protein dCAP-D3," *Genes & Development*, vol. 22, no. 8, pp. 1011–1024, 2008.
- [25] A. L. Manning, M. S. Longworth, and N. J. Dyson, "Loss of pRB causes centromere dysfunction and chromosomal instability," *Genes & Development*, vol. 24, no. 13, pp. 1364–1376, 2010.
- [26] C. H. Coschi, A. L. Martens, K. Ritchie et al., "Mitotic chromosome condensation mediated by the retinoblastoma protein is tumor-suppressive," *Genes & Development*, vol. 24, no. 13, pp. 1351–1363, 2010.
- [27] C. H. Coschi, C. A. Ishak, D. Gallo et al., "Haploinsufficiency of an RB-E2F1-condensin II complex leads to aberrant replication and aneuploidy," *Cancer Discovery*, vol. 4, no. 7, pp. 840–853, 2014.
- [28] C. Uchida, T. Hattori, H. Takahashi, N. Yamamoto, M. Kitagawa, and Y. Taya, "Interaction between RB protein and NuMA is required for proper alignment of spindle microtubules," *Genes to Cells*, vol. 19, no. 2, pp. 89–96, 2014.
- [29] F. P. Fiorentino, I. Marchesi, and A. Giordano, "On the role of retinoblastoma family proteins in the establishment and maintenance of the epigenetic landscape," *Journal of Cellular Physiology*, vol. 228, no. 2, pp. 276–284, 2013.

- [30] K. Meier and A. Brehm, "Chromatin regulation: how complex does it get?" *Epigenetics*, vol. 9, no. 11, pp. 1485–1495, 2014.
- [31] C. Uchida, "The retinoblastoma protein: functions beyond the GI-S regulator," *Current Drug Targets*, vol. 13, no. 13, pp. 1622–1632, 2012.
- [32] P. M. Brownlee, C. Meisenberg, and J. A. Downs, "The SWI/SNF chromatin remodelling complex: its role in maintaining genome stability and preventing tumorigenesis," *DNA Repair*, vol. 32, pp. 127–133, 2015.
- [33] O. A. Romero, M. Torres-Diz, E. Pros et al., "MAX inactivation in small cell lung cancer disrupts MYC-SWI/SNF programs and is synthetic lethal with BRG1," *Cancer discovery*, vol. 4, no. 3, pp. 292–303, 2014.
- [34] M. Singh, M. Krajewski, A. Mikolajka, and T. A. Holak, "Molecular determinants for the complex formation between the retinoblastoma protein and LXCXE sequences," *The Journal of Biological Chemistry*, vol. 280, no. 45, pp. 37868–37876, 2005.
- [35] M. W. Strobeck, D. N. Reisman, R. W. Gunawardena et al., "Compensation of BRG-1 function by Brm. Insight into the role of the core SWI-SNF subunits in retinoblastoma tumor suppressor signaling," *The Journal of Biological Chemistry*, vol. 277, no. 7, pp. 4782–4789, 2002.
- [36] M. Coisy-Quivy, O. Disson, V. Roure, C. Muchardt, J.-M. Blanchard, and J.-C. Dantonel, "Role for Brm in cell growth control," *Cancer Research*, vol. 66, no. 10, pp. 5069–5076, 2006.
- [37] D. Trouche, C. Le Chalony, C. Muchardt, M. Yaniv, and T. Kouzarides, "RB and hbrm cooperate to repress the activation functions of E2F1," *Proceedings of the National Academy of Sciences of the United States of America*, vol. 94, no. 21, pp. 11268–11273, 1997.
- [38] A. Lai, B. K. Kennedy, D. A. Barbie et al., "RBP1 recruits the mSIN3-histone deacetylase complex to the pocket of retinoblastoma tumor suppressor family proteins found in limited discrete regions of the nucleus at growth arrest," *Molecular and Cellular Biology*, vol. 21, no. 8, pp. 2918–2932, 2001.
- [39] A. R. Meloni, E. J. Smith, and J. R. Nevins, "A mechanism for Rb/p130-mediated transcription repression involving recruitment of the CtBP corepressor," *Proceedings of the National Academy of Sciences of the United States of America*, vol. 96, no. 17, pp. 9574–9579, 1999.
- [40] A. J. Morrison, C. Sardet, and R. E. Herrera, "Retinoblastoma protein transcriptional repression through histone deacetylation of a single nucleosome," *Molecular and Cellular Biology*, vol. 22, no. 3, pp. 856–865, 2002.
- [41] S. Roperio and M. Esteller, "The role of histone deacetylases (HDACs) in human cancer," *Molecular Oncology*, vol. 1, no. 1, pp. 19–25, 2007.
- [42] H. P. Chen, Y. T. Zhao, and T. C. Zhao, "Histone deacetylases and mechanisms of regulation of gene expression," *Critical Reviews in Oncogenesis*, vol. 20, no. 1–2, pp. 35–47, 2015.
- [43] M. Manal, M. J. N. Chandrasekar, J. Gomathi Priya, and M. J. Nanjan, "Inhibitors of histone deacetylase as antitumor agents: a critical review," *Bioorganic Chemistry*, vol. 67, pp. 18–42, 2016.
- [44] A. Newbold, K. J. Falkenberg, M. H. Prince, and R. W. Johnstone, "How do tumor cells respond to HDAC inhibition?" *FEBS Journal*, vol. 283, no. 22, pp. 4032–4046, 2016.
- [45] S. Rea, F. Eisenhaber, D. O'Carroll et al., "Regulation of chromatin structure by site-specific histone H3 methyltransferases," *Nature*, vol. 406, no. 6796, pp. 593–599, 2000.
- [46] M. M. Müller, B. Fierz, L. Bittova, G. Liszczak, and T. W. Muir, "A two-state activation mechanism controls the histone methyltransferase Suv39h1," *Nature Chemical Biology*, vol. 12, no. 3, pp. 188–193, 2016.
- [47] T. Zhang, S. Cooper, and N. Brockdorff, "The interplay of histone modifications —writers that read," *EMBO Reports*, vol. 16, no. 11, pp. 1467–1481, 2015.
- [48] A. J. Bannister, P. Zegerman, J. F. Partridge et al., "Selective recognition of methylated lysine 9 on histone H3 by the HP1 chromo domain," *Nature*, vol. 410, no. 6824, pp. 120–124, 2001.
- [49] D. Canzio, A. Larson, and G. J. Narlikar, "Mechanisms of functional promiscuity by HP1 proteins," *Trends in Cell Biology*, vol. 24, no. 6, pp. 377–386, 2014.
- [50] S. H. Kwon and J. L. Workman, "The heterochromatin protein 1 (HP1) family: put away a bias toward HP1," *Molecules and Cells*, vol. 26, no. 3, pp. 217–227, 2008.
- [51] E. Minc, Y. Allory, H. J. Worman, J.-C. Courvalin, and B. Buendia, "Localization and phosphorylation of HP1 proteins during the cell cycle in mammalian cells," *Chromosoma*, vol. 108, no. 4, pp. 220–234, 1999.
- [52] A. L. Nielsen, M. Oulad-Abdelghani, J. A. Ortiz, E. Rembout-sika, P. Chambon, and R. Losson, "Heterochromatin formation in mammalian cells: interaction between histones and HP1 Proteins," *Molecular Cell*, vol. 7, no. 4, pp. 729–739, 2001.
- [53] L. Aagaard, G. Laible, P. Selenko et al., "Functional mammalian homologues of the *Drosophila* PEV-modifier Su(var)3-9 encode centromere-associated proteins which complex with the heterochromatin component M31," *The EMBO Journal*, vol. 18, no. 7, pp. 1923–1938, 1999.
- [54] G. Schotta, A. Ebert, V. Krauss et al., "Central role of *Drosophila* SU(VAR)3-9 in histone H3-K9 methylation and heterochromatic gene silencing," *The EMBO Journal*, vol. 21, no. 5, pp. 1121–1131, 2002.
- [55] A. P. Young and G. D. Longmore, "Differences in stability of repressor complexes at promoters underlie distinct roles for Rb family members," *Oncogene*, vol. 23, no. 3, pp. 814–823, 2004.
- [56] M. Narita, S. Núñez, E. Heard et al., "Rb-mediated heterochromatin formation and silencing of E2F target genes during cellular senescence," *Cell*, vol. 113, no. 6, pp. 703–716, 2003.
- [57] P. Sdek, P. Zhao, Y. Wang et al., "Rb and p130 control cell cycle gene silencing to maintain the postmitotic phenotype in cardiac myocytes," *Journal of Cell Biology*, vol. 194, no. 3, pp. 407–423, 2011.
- [58] G. Nishibuchi and J.-I. Nakayama, "Biochemical and structural properties of heterochromatin protein 1: understanding its role in chromatin assembly," *Journal of Biochemistry*, vol. 156, no. 1, pp. 11–20, 2014.
- [59] O. Vaute, E. Nicolas, L. Vandel, and D. Trouche, "Functional and physical interaction between the histone methyl transferase Suv39H1 and histone deacetylases," *Nucleic Acids Research*, vol. 30, no. 2, pp. 475–481, 2002.
- [60] L. Vandel, E. Nicolas, O. Vaute, R. Ferreira, S. Ait-Si-Ali, and D. Trouche, "Transcriptional repression by the retinoblastoma protein through the recruitment of a histone methyltransferase," *Molecular and Cellular Biology*, vol. 21, no. 19, pp. 6484–6494, 2001.
- [61] Y.-J. Shi, C. Matson, F. Lan, S. Iwase, T. Baba, and Y. Shi, "Regulation of LSD1 histone demethylase activity by its associated factors," *Molecular Cell*, vol. 19, no. 6, pp. 857–864, 2005.

- [62] E. V. Benevolenskaya, H. L. Murray, P. Branton, R. A. Young, and W. G. Kaelin Jr., "Binding of pRB to the PHD protein RBP2 promotes cellular differentiation," *Molecular Cell*, vol. 18, no. 6, pp. 623–635, 2005.
- [63] A. Maiques-Diaz and T. C. Somervaille, "LSD1: biologic roles and therapeutic targeting," *Epigenomics*, vol. 8, no. 8, pp. 1103–1116, 2016.
- [64] N. Lopez-Bigas, T. A. Kisiel, D. C. DeWaal et al., "Genome-wide analysis of the H3K4 histone demethylase RBP2 reveals a transcriptional program controlling differentiation," *Molecular Cell*, vol. 31, no. 4, pp. 520–530, 2008.
- [65] F. A. Dick, "Structure-function analysis of the retinoblastoma tumor suppressor protein—is the whole a sum of its parts?" *Cell Division*, vol. 2, article 26, 2007.
- [66] F. Fuks, W. A. Burgers, A. Brehm, L. Hughes-Davies, and T. Kouzarides, "DNA methyltransferase Dnmt1 associates with histone deacetylase activity," *Nature Genetics*, vol. 24, no. 1, pp. 88–91, 2000.
- [67] M. R. Rountree, K. E. Bachman, and S. B. Baylin, "DNMT1 binds HDAC2 and a new co-repressor, DMAP1, to form a complex at replication foci," *Nature Genetics*, vol. 25, no. 3, pp. 269–277, 2000.
- [68] Y. Ling, U. T. Sankpal, A. K. Robertson, J. G. McNally, T. Karpova, and K. D. Robertson, "Modification of de novo DNA methyltransferase 3a (Dnmt3a) by SUMO-1 modulates its interaction with histone deacetylases (HDACs) and its capacity to repress transcription," *Nucleic Acids Research*, vol. 32, no. 2, pp. 598–610, 2004.
- [69] C. Stirzaker, D. S. Millar, C. L. Paul et al., "Extensive DNA methylation spanning the Rb promoter in retinoblastoma tumors," *Cancer Research*, vol. 57, no. 11, pp. 2229–2237, 1997.
- [70] J. R. Melki, P. C. Vincent, and S. J. Clark, "Concurrent DNA hypermethylation of multiple genes in acute myeloid leukemia," *Cancer Research*, vol. 59, no. 15, pp. 3730–3740, 1999.
- [71] S. Gonzalo, M. García-Cao, M. F. Fraga et al., "Role of the RB1 family in stabilizing histone methylation at constitutive heterochromatin," *Nature Cell Biology*, vol. 7, no. 4, pp. 420–428, 2005.
- [72] S. Talluri and F. A. Dick, "Regulation of transcription and chromatin structure by pRB: here, there and everywhere," *Cell Cycle*, vol. 11, no. 17, pp. 3189–3198, 2012.
- [73] H. Siddiqui, S. R. Fox, R. W. Gunawardena, and E. S. Knudsen, "Loss of RB compromises specific heterochromatin modifications and modulates HP1 $\alpha$  dynamics," *Journal of Cellular Physiology*, vol. 211, no. 1, pp. 131–137, 2007.
- [74] C. E. Isaac, S. M. Francis, A. L. Martens et al., "The retinoblastoma protein regulates pericentric heterochromatin," *Molecular and Cellular Biology*, vol. 26, no. 9, pp. 3659–3671, 2006.
- [75] M. García-Cao, S. Gonzalo, D. Dean, and M. A. Blasco, "A role for the Rb family of proteins in controlling telomere length," *Nature Genetics*, vol. 32, no. 3, pp. 415–419, 2002.
- [76] G. Schotta, M. Lachner, K. Sarma et al., "A silencing pathway to induce H3-K9 and H4-K20 trimethylation at constitutive heterochromatin," *Genes & Development*, vol. 18, no. 11, pp. 1251–1262, 2004.
- [77] R. J. Bourgo, H. Siddiqui, S. Fox et al., "SWI/SNF deficiency results in aberrant chromatin organization, mitotic failure, and diminished proliferative capacity," *Molecular Biology of the Cell*, vol. 20, no. 14, pp. 3192–3199, 2009.
- [78] A. Gould, "Functions of mammalian Polycomb group and trithorax group related genes," *Current Opinion in Genetics & Development*, vol. 7, no. 4, pp. 488–494, 1997.
- [79] A. Schumacher and T. Magnuson, "Murine Polycomb- and trithorax-group genes regulate homeotic pathways and beyond," *Trends in Genetics*, vol. 13, no. 5, pp. 167–170, 1997.
- [80] J. A. Kennison, "The polycomb and trithorax group proteins of *Drosophila*: trans-regulators of homeotic gene function," *Annual Review of Genetics*, vol. 29, no. 1, pp. 289–303, 1995.
- [81] V. Pirrotta, "Polycomb the genome: PcG, trxG, and chromatin silencing," *Cell*, vol. 93, no. 3, pp. 333–336, 1998.
- [82] N. P. Blackledge, N. R. Rose, and R. J. Klose, "Targeting Polycomb systems to regulate gene expression: modifications to a complex story," *Nature Reviews Molecular Cell Biology*, vol. 16, no. 11, pp. 643–649, 2015.
- [83] A. Dahiya, S. Wong, S. Gonzalo, M. Gavin, and D. C. Dean, "Linking the Rb and Polycomb pathways," *Molecular Cell*, vol. 8, no. 3, pp. 557–568, 2001.
- [84] Y. Kotake, T. Nakagawa, K. Kitagawa et al., "Long non-coding RNA ANRIL is required for the PRC2 recruitment to and silencing of p15(INK4B) tumor suppressor gene," *Oncogene*, vol. 30, no. 16, pp. 1956–1962, 2011.
- [85] A. Kuwabara and W. Gruissem, "*Arabidopsis* RETINOBLASTOMA-RELATED and Polycomb group proteins: cooperation during plant cell differentiation and development," *Journal of Experimental Botany*, vol. 65, no. 10, pp. 2667–2676, 2014.
- [86] A. J. Parry and M. Narita, "Old cells, new tricks: chromatin structure in senescence," *Mammalian Genome*, vol. 27, no. 7, pp. 320–331, 2016.
- [87] W. R. Sellers, B. G. Novitch, S. Miyake et al., "Stable binding to E2F is not required for the retinoblastoma protein to activate transcription, promote differentiation, and suppress tumor cell growth," *Genes & Development*, vol. 12, no. 1, pp. 95–106, 1998.
- [88] T.-T. Chen and J. Y. J. Wang, "Establishment of irreversible growth arrest in myogenic differentiation requires the RB LXCXE-binding function," *Molecular and Cellular Biology*, vol. 20, no. 15, pp. 5571–5580, 2000.
- [89] R. Váraljai, A. B. M. M. K. Islam, M. L. Beshiri, J. Rehman, N. Lopez-Bigas, and E. V. Benevolenskaya, "Increased mitochondrial function downstream from KDM5a histone demethylase rescues differentiation in pRB-deficient cells," *Genes & Development*, vol. 29, no. 17, pp. 1817–1834, 2015.
- [90] S. Ait-Si-Ali, V. Guasconi, L. Fritsch et al., "A Suv39h-dependent mechanism for silencing S-phase genes in differentiating but not in cycling cells," *The EMBO Journal*, vol. 23, no. 3, pp. 605–615, 2004.
- [91] G. P. Dimri, "What has senescence got to do with cancer?" *Cancer Cell*, vol. 7, no. 6, pp. 505–512, 2005.
- [92] J. Sage, A. L. Miller, P. A. Pérez-Mancera, J. M. Wysocki, and T. Jacks, "Acute mutation of retinoblastoma gene function is sufficient for cell cycle re-entry," *Nature*, vol. 424, no. 6945, pp. 223–228, 2003.
- [93] H.-J. Xu, Y. Zhou, W. Ji et al., "Reexpression of the retinoblastoma protein in tumor cells induces senescence and telomerase inhibition," *Oncogene*, vol. 15, no. 21, pp. 2589–2596, 1997.
- [94] S. Talluri, C. E. Isaac, M. Ahmad et al., "A G1 checkpoint mediated by the retinoblastoma protein that is dispensable in terminal differentiation but essential for senescence," *Molecular and Cellular Biology*, vol. 30, no. 4, pp. 948–960, 2010.

- [95] A. Chicas, A. Kapoor, X. Wang et al., "H3K4 demethylation by Jarid1a and Jarid1b contributes to retinoblastoma-mediated gene silencing during cellular senescence," *Proceedings of the National Academy of Sciences of the United States of America*, vol. 109, no. 23, pp. 8971–8976, 2012.
- [96] M. Vernier, V. Bourdeau, M.-F. Gaumont-Leclerc et al., "Regulation of E2Fs and senescence by PML nuclear bodies," *Genes & Development*, vol. 25, no. 1, pp. 41–50, 2011.
- [97] S. Talluri and F. A. Dick, "The retinoblastoma protein and PML collaborate to organize heterochromatin and silence E2F-responsive genes during senescence," *Cell Cycle*, vol. 13, no. 4, pp. 641–651, 2014.
- [98] M. Vernier and G. Ferbeyre, "Complete senescence: RB and PML share the task," *Cell Cycle*, vol. 13, no. 5, p. 696, 2014.
- [99] L. Schulz and J. Tyler, "Heterochromatin focuses on senescence," *Molecular Cell*, vol. 17, no. 2, pp. 168–170, 2005.
- [100] M. Collado and M. Serrano, "The power and the promise of oncogene-induced senescence markers," *Nature Reviews Cancer*, vol. 6, no. 6, pp. 472–476, 2006.
- [101] R. Funayama and F. Ishikawa, "Cellular senescence and chromatin structure," *Chromosoma*, vol. 116, no. 5, pp. 431–440, 2007.
- [102] X. Shi, B. Tian, L. Liu et al., "Rb protein is essential to the senescence-associated heterochromatic foci formation induced by HMGA2 in primary WI38 cells," *Journal of Genetics and Genomics*, vol. 40, no. 8, pp. 391–398, 2013.
- [103] M. A. Mancini, B. Shan, J. A. Nickerson, S. Penman, and W. H. Lee, "The retinoblastoma gene product is a cell cycle-dependent, nuclear matrix-associated protein," *Proceedings of the National Academy of Sciences of the United States of America*, vol. 91, no. 1, pp. 418–422, 1994.
- [104] T.-A. Kim, J. Lim, S. Ota et al., "NRP/B, a novel nuclear matrix protein, associates with p110(RB) and is involved in neuronal differentiation," *The Journal of Cell Biology*, vol. 141, no. 3, pp. 553–566, 1998.
- [105] A. E. Radulescu and D. W. Cleveland, "NuMA after 30 years: the matrix revisited," *Trends in Cell Biology*, vol. 20, no. 4, pp. 214–222, 2010.
- [106] K. Tanaka and T. Hirota, "Chromosomal instability: a common feature and a therapeutic target of cancer," *Biochimica et Biophysica Acta—Reviews on Cancer*, vol. 1866, no. 1, pp. 64–75, 2016.
- [107] F. A. Dick and S. M. Rubin, "Molecular mechanisms underlying RB protein function," *Nature Reviews Molecular Cell Biology*, vol. 14, no. 5, pp. 297–306, 2013.
- [108] S. B. Marquez-Vilendrer, K. Thompson, L. Lu, and D. Reisman, "Mechanism of BRG1 silencing in primary cancers," *Oncotarget*, vol. 7, no. 35, pp. 56153–56169, 2016.
- [109] Y. Yokoyama, A. Matsumoto, M. Hieda et al., "Loss of histone H4K20 trimethylation predicts poor prognosis in breast cancer and is associated with invasive activity," *Breast Cancer Research*, vol. 16, no. 3, article no. R66, 2014.
- [110] Y.-C. Teng, C.-F. Lee, Y.-S. Li et al., "Histone demethylase RBP2 promotes lung tumorigenesis and cancer metastasis," *Cancer Research*, vol. 73, no. 15, pp. 4711–4721, 2013.
- [111] Y. He, I. Korboukh, J. Jin, and J. Huang, "Targeting protein lysine methylation and demethylation in cancers," *Acta Biochimica et Biophysica Sinica*, vol. 44, no. 1, pp. 70–79, 2012.
- [112] Y. Shi, F. Lan, C. Matson et al., "Histone demethylation mediated by the nuclear amine oxidase homolog LSD1," *Cell*, vol. 119, no. 7, pp. 941–953, 2004.
- [113] E. Metzger, M. Wissmann, N. Yin et al., "LSD1 demethylates repressive histone marks to promote androgen-receptor-dependent transcription," *Nature*, vol. 437, no. 7057, pp. 436–439, 2005.
- [114] J. Huang, R. Sengupta, A. B. Espejo et al., "p53 is regulated by the lysine demethylase LSD1," *Nature*, vol. 449, no. 7158, pp. 105–108, 2007.
- [115] U. Hasholzner, P. Stieber, A. Zimmermann et al., "Nuclear mitotic apparatus protein (NuMA) in benign and malignant diseases," *Anticancer Research*, vol. 19, no. 4, pp. 2415–2420, 1999.
- [116] J. Briggman, R. Genduso, C. Camara et al., "NuMA: evaluation of a new biomarker for the detection of low stage colorectal cancer," *Anticancer Research*, vol. 19, no. 4, pp. 2411–2414, 1999.
- [117] S. Kammerer, R. B. Roth, C. R. Hoyal et al., "Association of the NuMA region on chromosome 11q13 with breast cancer susceptibility," *Proceedings of the National Academy of Sciences of the United States of America*, vol. 102, no. 6, pp. 2004–2009, 2005.
- [118] O. Kilpivaara, M. Rantanen, A. Tamminen, K. Aittomäki, C. Blomqvist, and H. Nevanlinna, "Comprehensive analysis of NuMA variation in breast cancer," *BMC Cancer*, vol. 8, no. 1, article 71, 2008.
- [119] R. Honda, H. Tanaka, and H. Yasuda, "Oncoprotein MDM2 is a ubiquitin ligase E3 for tumor suppressor p53," *FEBS Letters*, vol. 420, no. 1, pp. 25–27, 1997.
- [120] Y. Haupt, R. Maya, A. Kazaz, and M. Oren, "Mdm2 promotes the rapid degradation of p53," *Nature*, vol. 387, no. 6630, pp. 296–299, 1997.
- [121] C. Uchida, S. Miwa, K. Kitagawa et al., "Enhanced Mdm2 activity inhibits pRB function via ubiquitin-dependent degradation," *The EMBO Journal*, vol. 24, no. 1, pp. 160–169, 2005.
- [122] P. Sdek, H. Ying, D. L. F. Chang et al., "MDM2 promotes proteasome-dependent ubiquitin-independent degradation of retinoblastoma protein," *Molecular Cell*, vol. 20, no. 5, pp. 699–708, 2005.
- [123] S. Miwa, C. Uchida, K. Kitagawa et al., "Mdm2-mediated pRB downregulation is involved in carcinogenesis in a p53-independent manner," *Biochemical and Biophysical Research Communications*, vol. 340, no. 1, pp. 54–61, 2006.
- [124] C. Uchida, S. Miwa, T. Isobe et al., "Effects of MdmX on Mdm2-mediated downregulation of pRB," *FEBS Letters*, vol. 580, no. 7, pp. 1753–1758, 2006.
- [125] H. Zhang, L. Hu, W. Qiu et al., "MDMX exerts its oncogenic activity via suppression of retinoblastoma protein," *Oncogene*, vol. 34, no. 44, pp. 5560–5569, 2015.
- [126] L. Hu, H. Zhang, J. Bergholz, S. Sun, and Z.-X. J. Xiao, "MDM2/MDMX: master negative regulators for p53 and RB," *Molecular & Cellular Oncology*, vol. 3, no. 2, Article ID e1106635, 2016.
- [127] J. Johnson, B. Thijssen, U. McDermott, M. Garnett, L. F. A. Wessels, and R. Bernards, "Targeting the RB-E2F pathway in breast cancer," *Oncogene*, vol. 35, no. 37, pp. 4829–4835, 2016.
- [128] N. A. Laurie, S. L. Donovan, C.-S. Shih et al., "Inactivation of the p53 pathway in retinoblastoma," *Nature*, vol. 444, no. 7115, pp. 61–66, 2006.
- [129] W. Du, J. Wu, E. M. Walsh, Y. Zhang, C. Y. Chen, and Z.-X. J. Xiao, "Nutlin-3 affects expression and function of retinoblastoma protein: role of retinoblastoma protein in cellular response to nutlin-3," *The Journal of Biological Chemistry*, vol. 284, no. 39, pp. 26315–26321, 2009.

- [130] E. M. Walsh, M. Niu, J. Bergholz, and Z.-X. Jim Xiao, "Nutlin-3 down-regulates retinoblastoma protein expression and inhibits muscle cell differentiation," *Biochemical and Biophysical Research Communications*, vol. 461, no. 2, pp. 293–299, 2015.
- [131] E. Hamilton and J. R. Infante, "Targeting CDK4/6 in patients with cancer," *Cancer Treatment Reviews*, vol. 45, pp. 129–138, 2016.
- [132] H. P. Mohammad and R. G. Kruger, "Antitumor activity of LSD1 inhibitors in lung cancer," *Molecular & Cellular Oncology*, vol. 3, no. 2, Article ID e1117700, 2016.
- [133] L. Morera, M. Lübbert, and M. Jung, "Targeting histone methyltransferases and demethylases in clinical trials for cancer therapy," *Clinical Epigenetics*, vol. 8, no. 1, article 57, 2016.

## Review Article

# Functions of the Tumor Suppressors p53 and Rb in Actin Cytoskeleton Remodeling

Takahiro Ebata,<sup>1</sup> Hiroaki Hirata,<sup>2</sup> and Keiko Kawauchi<sup>1,3</sup>

<sup>1</sup>Frontiers of Innovative Research in Science and Technology, Konan University, 7-1-20 Minatojima-minamimachi, Chuo-ku, Kobe, Hyogo 650-0047, Japan

<sup>2</sup>Nagoya University Graduate School of Medicine, 65 Tsurumai, Showa-ku, Nagoya, Aichi 466-8550, Japan

<sup>3</sup>Department of Molecular Oncology, Institute for Advanced Medical Sciences, Nippon Medical School, 1-396 Kosugi-cho, Nakahara-ku, Kawasaki, Kanagawa 211-8533, Japan

Correspondence should be addressed to Keiko Kawauchi; [kawauchi@center.konan-u.ac.jp](mailto:kawauchi@center.konan-u.ac.jp)

Received 8 September 2016; Accepted 21 November 2016

Academic Editor: Wuyuan Lu

Copyright © 2016 Takahiro Ebata et al. This is an open access article distributed under the Creative Commons Attribution License, which permits unrestricted use, distribution, and reproduction in any medium, provided the original work is properly cited.

Mechanical microenvironments, such as extracellular matrix stiffness and strain, have crucial roles in cancer progression. Cells sense their microenvironments with mechanosensing biomolecules, which is accompanied by the modulation of actin cytoskeleton structures, and the signals are subsequently transduced downstream as biochemical signals. The tumor suppressors p53 and retinoblastoma protein (Rb) are known to prevent cancer progression. The p53 and Rb signaling pathways are disrupted in many types of cancers. Here, we review recent findings about the roles of these tumor suppressors in the regulation of mechanosensing biomolecules and the actin cytoskeleton. We further discuss how dysfunction in the p53- and/or Rb-mediated mechanosignaling pathways is potentially involved in cancer progression. These pathways might provide good targets for developing anticancer therapies.

## 1. Introduction

During cancer progression, cells acquire several abilities, including continual unregulated proliferation, resistance to cell death, invasiveness, and epithelial-mesenchymal transition (EMT) [1–3]. Remodeling of the actin cytoskeleton is also associated with cancer progression [4, 5]. Actin is one of the most abundant proteins in eukaryotic cells. Globular actin (G-actin) monomers polymerize into actin filaments (F-actin), which is then depolymerized, in a steady-state equilibrium. Actin polymerization is regulated by actin nucleators, including the formins, actin-related protein 2/3 (Arp2/3) complex, and spire [6–8]. The activation of these actin nucleators is regulated by Rho GTPases, including Rho, Rac, and Cdc42, which typically induce the formation of stress fibers, lamellipodia, and filopodia, respectively [9]. Actin depolymerization is enhanced by gelsolin and actin-depolymerizing factor (ADF)/cofilin, while spontaneous depolymerization is slow [10]. Gelsolin is activated by calcium

ions but inhibited by phosphatidylinositol 4,5-bisphosphate. Activation of ADF/cofilin is regulated by its phosphorylation. Kinases, including LIM kinase (LIMK), testicular protein kinase (TESK), and integrin-linked kinase (ILK), induce the activation of ADF/cofilin, while phosphatases, such as slingshot and chronophin, induce its inactivation [11–13].

The invasion of cancer cells is associated with the formation of several actin-mediated structures, including lamellipodia, filopodia, podosomes, and invadopodia [14, 15]. Podosomes and invadopodia degrade the extracellular matrix (ECM), which facilitates invasion into other tissues. Protrusions of lamellipodia and filopodia are likely to promote cancer cell invasion through the generation of traction forces that are required for mesenchymal-mode migration. Blebs are also formed during the migration of cancer cells and promote their invasion [16, 17]. The formation of blebs is initiated upon disruption of the actin cortex and driven by intracellular pressure generated in the cytoplasm. In association with reassembly of the actin cortex, the blebs are then retracted by

actomyosin contraction, generating traction forces that move the cells forward. While membrane blebbing is typically associated with apoptotic cell death [18], aggressive cancer cells appear to form and use blebs for invasion independently of cell death [16, 17]. In addition to invasion, the insensitivity of aggressive cancer cells to antitumor drug-induced apoptosis might also be affected by actin cytoskeletal structures. Stress fibers, lamellipodia, and filopodia are considered to promote the survival of cancer cells.

Actomyosin contraction is essential for sensing the mechanical environments surrounding cells [19]. At the sites of cell-ECM adhesion, the formation of focal adhesion complexes, including integrins, focal adhesion kinase (FAK), p130 Crk-associated substrate (p130Cas; also known as Bcr1), and paxillin, promotes actin polymerization and activates myosin [20–24]. Activated actomyosin generates a contractile force that induces conformational changes in several focal adhesion proteins to enhance downstream signaling [25]. Furthermore,  $\alpha$ -catenin has been identified as a mechanosensing protein in adherens junction (AJ) complexes at cell-cell junctions [26]. The homophilic interaction of cadherin ectodomains induces the assembly of AJ complexes and local actin polymerization. While actin filaments link to cadherins via  $\beta$ -catenin and  $\alpha$ -catenin, an actomyosin-generated force transmitted to this linkage causes conformational changes in  $\alpha$ -catenin, which promotes its binding to vinculin [27]. This results in the recruitment of various proteins, including zyxin and Arp2/3, to AJs and a further increase in actin polymerization [26, 28]. The expression and activity of proteins in focal adhesions and AJ complexes are often altered during cancer progression.

Actin dynamics influence cellular behavior not only by regulating cytoskeletal organization but also by controlling gene expression. For example, in skeletal muscle differentiation, disassembly of actin filaments is required for the muscle-specific gene expression induced by serum response factor (SRF) [29–32]. G-actin binds to megakaryocytic acute leukemia (MAL; also known as MKLI/MRTF-A), a cofactor of SRF, and sequesters it from the nucleus, therefore, causing alterations in the equilibrium between actin polymerization and depolymerization perturb differentiation [33].

Cancer progression is associated with the accumulation of gene mutations and cancer is generally considered to be a genomic disease. *TP53*, which encodes the p53 transcription factor, is mutated in more than 50% of human cancers [34]. This protein exerts its biological activities, such as cell cycle arrest and induction of apoptosis or senescence, by upregulating the expression of various target genes [35–37]. Stresses, such as DNA damage, induce the stabilization and activation of p53 by affecting its posttranscriptional modifications such as phosphorylation and acetylation [38, 39]. The expression level of p53 is low under low stress conditions. However, it still contributes to cellular homeostasis involving differentiation and cell cycle progression.

Germline mutations in the retinoblastoma (*Rb*) gene occur frequently in retinoblastoma, which is the most common cancer of the developing retina in early childhood [40]. Somatic mutations in *Rb* are also observed in several cancers, including small-cell lung cancer and bladder cancer [41].

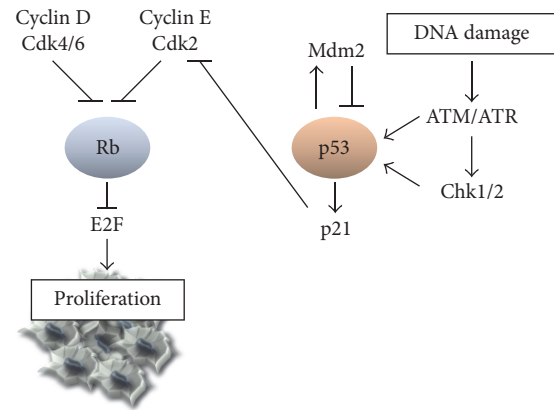


FIGURE 1: p53 suppresses the cell proliferation mediated by the Rb-E2F pathway. Phosphorylation of Rb by CDK4/6-cyclin D and CDK2-cyclin E causes the dissociation of Rb from E2F to promote cell cycle progression. In response to DNA damage, ataxia telangiectasia mutated (ATM) or ataxia telangiectasia and Rad3-related protein (ATR) are activated and phosphorylate p53 either directly or through Chk1/2. Phosphorylated p53 dissociates from Mdm2 and is thereby stabilized. Active p53 then induces the transcription of its target genes involving  $p21^{WAF1}$ , resulting in the inhibition of CDK2-cyclin E activity.

Furthermore, inactivation of Rb by hyperphosphorylation via the constitutive activation of its kinases has been implicated in tumor initiation and progression [40, 42, 43]. Phosphorylation of Rb by cell cycle kinase complexes, that is, cyclin-dependent kinase (CDK) 4/6-cyclin D and Cdk-2-cyclin E, releases the transcriptional repression of E2F, resulting in cell cycle progression. The activity of Cdk-2-cyclin E is inhibited by the CDK-inhibitor  $p21^{WAF1}$ , a transcriptional target of p53 (Figure 1) [44]. Rb also plays a critical role in the development of several tissues, including muscle and bone, by regulating other transcriptional factors such as MyoD and RUNX2 [43].

While various molecules that constitute the actin cytoskeleton, focal adhesions, and AJs are involved in sensing the mechanical microenvironments surrounding cells, little is known about the contribution of p53 and Rb to mechanosensing. In this review, we summarize the roles of p53 and Rb in the regulation of the actin cytoskeleton and mechanosensing proteins, which provides insights into the mechanisms of cancer progression.

## 2. p53 Regulates Integrin Expression and Activation

Integrins, which are heterodimers composed of  $\alpha$  and  $\beta$  subunits, form a connection between the ECM and actin cytoskeleton, and their downstream signaling molecules drive actin polymerization [45–47]. In humans, 18 types of  $\alpha$  subunits and 8 types of  $\beta$  subunits have been identified, and they assemble into 24 types of integrins that bind specifically to their ligands, including fibronectin, laminin, and collagen [48]. The binding of a ligand to the extracellular domain of integrin induces the recruitment of focal adhesion proteins, including FAK, p130Cas, and paxillin, at the cytoplasmic side,

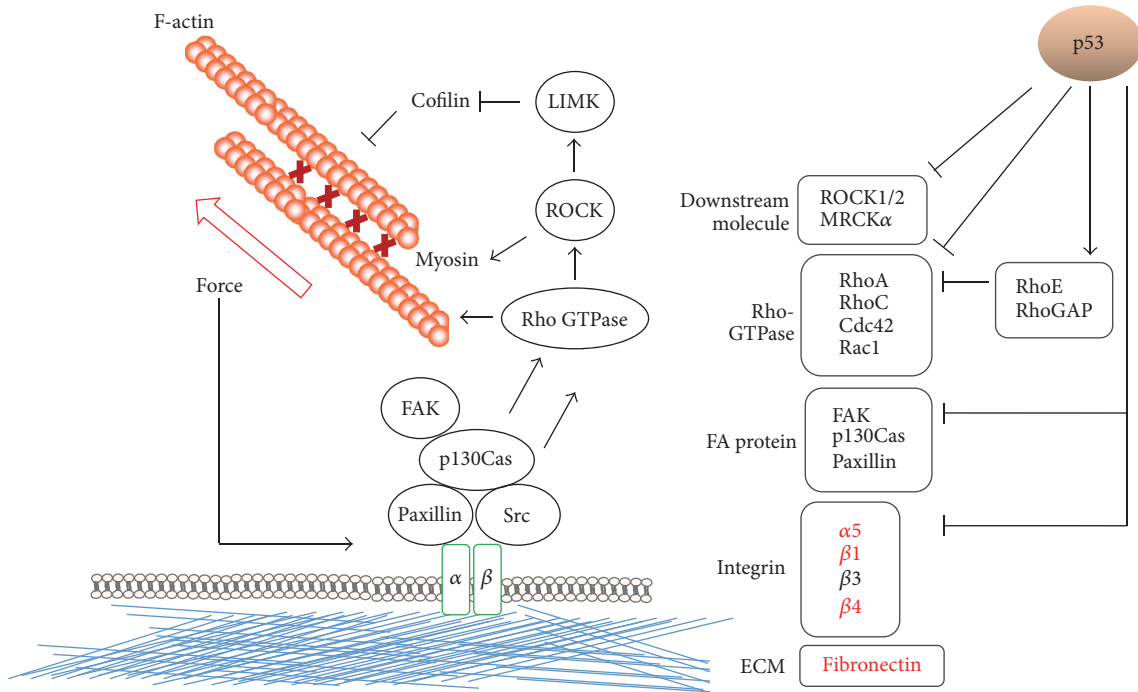


FIGURE 2: Effects of p53 on molecules in mechanosensing pathways. Cells sense ECM stiffness and modulate actin cytoskeleton structures through the integrin signaling pathways. p53 wild-type suppresses cancer progression through downregulation of the molecules in the integrin signaling pathways. Conversely, several p53 mutants exert gain-of-function effects on the upregulation of molecules in the integrin signaling pathways. The molecules indicated by red letters are upregulated by p53 GOF mutants.

leading to the activation of Rho GTPases and stimulation of actin polymerization [20–24]. The cytoplasmic domain of integrin links to actin filaments through several adaptor proteins. Actomyosin contraction potentially modulates the affinity of integrin to its ligands by changing the conformation of integrin.

Integrin signaling plays a fundamental role in tumor cell invasion and metastasis. The expression levels of several integrins, including  $\alpha 5\beta 1$ ,  $\alpha 6\beta 4$ ,  $\alpha 4\beta 1$ ,  $\alpha v\beta 3$ ,  $\alpha v\beta 5$ ,  $\alpha v\beta 6$ , and  $\alpha 2\beta 1$ , in cancer cells correlate with their aggressiveness [46, 49, 50]. It has been revealed that p53 regulates the expression of integrins  $\alpha 5$ ,  $\beta 1$ ,  $\beta 3$ , and  $\beta 4$  (Figure 2) [51–56]. Janouskova et al. showed that Nutlin-3a, an MDM2 antagonist that acts as a p53 activator, decreases the expression of integrin  $\alpha 5$  in glioma and colorectal cancer cells [51, 52]. Bon et al. reported that the expression of integrin  $\beta 4$  was decreased by either the ectopic expression of p53 or DNA damage in wild-type p53-expressing cells [56]. Conversely, the ectopic expression of transactivating p63 (TAp63) or transactivating p73 (TAp73), two p53 family members, increased the promoter activity of *ITGB4*, which encodes integrin  $\beta 4$ . Importantly, depletion of p53 enhanced the TAp63- or TAp73-dependent activation of the *ITGB4* promoter. Not only DNA damage triggered by genotoxic drugs or activation of oncogenes but also other forms of stress, such as chromosomal aberrations, hypoxia, and telomere shortening, are associated with cancer progression [36]. Repression of integrin  $\alpha 5$  and  $\beta 4$  expression

by p53 activated in response to these stresses is likely to prevent the progression of cancer stimulated by these stresses.

Vaillant et al. reported, using mammary tumors derived from p53-deficient mice lacking one allele (*p53*<sup>+/-</sup>), that loss of p53 function promotes cancer cell invasion by upregulating integrin  $\beta 3$  expression at the cell surface [54]. We also reported that the depletion of p53 increased the expression of integrin  $\beta 3$ , encoded by *ITGB3*, in a transcription factor NF- $\kappa$ B-dependent manner. This leads to an increase in integrin  $\alpha v\beta 3$  expression at the cell surface, which promotes the formation of lamellipodia. Lamellipodia formation mediated by integrin  $\alpha v\beta 3$  contributes to the constitutive activation of another transcription factor, STAT3, which plays an integral role in tumor cell invasion [55]. Conversely, Qui et al. showed that pifithrin- $\alpha$ , a p53 inhibitor, increases the expression of integrin  $\beta 1$  in endothelial cells when the expression of *ID1* (encoding inhibitor of DNA binding [ID] 1, which belongs to a family of basic helix-loop-helix transcription factors lacking DNA-binding domains and plays a critical role in angiogenesis) is depleted [53]. Pifithrin- $\alpha$  also enhances the formation of F-actin at the peripheral rim and promotes tubular formation. *ID1* expression is upregulated in angiogenic tumor vessels. These results suggest that the p53-dependent maintenance of the low expression levels of integrins  $\beta 1$  and  $\beta 3$  helps to attenuate both cancer cell invasion and angiogenesis, which would prevent cancer progression.

### 3. Regulation of Focal Adhesion-Rho Signaling Pathways by p53

FAK contains three distinct domains: a four-point-one, ezrin, radixin, moesin (FERM) domain; a kinase domain; and a focal adhesion targeting (FAT) domain [21]. The residues in the FERM domain are responsible for the autoinhibition of FAK by intramolecular interactions. External forces are believed to induce a conformational change of the FAT domain to disrupt these intramolecular interactions. However, since FAK does not bind directly to actin filaments, it is unclear whether FAK activity in cells is truly regulated by force such as actomyosin contraction.

Phosphorylation of p130Cas is also facilitated by external forces [57]. Src phosphorylates the substrate domain of p130Cas (CasSD), which is characterized by 15 YXXP motifs. Phosphorylated CasSD provides a binding site for the Crk-DOCK180 complex, a guanine nucleotide exchange factor (GEF) for Rac. External forces induce a conformational change of CasSD, which facilitates the phosphorylation of p130Cas. Like FAK, p130Cas does not bind directly to actin filaments [25]. Recently, we found that tensin 1 mediates the interaction of p130Cas with actin filaments [58]. However, given that the expression level of tensin 1 is generally low in metastatic cancers [59, 60], it may not be responsible for the enhanced phosphorylation of p130Cas and FAK in aggressive cancer cells.

Paxillin, an adaptor protein at focal adhesions, is known to be involved in the mechanical-cue-dependent regulation of Rho GTPases [22]. While the underlying mechanism remains unclear, the C-terminal LIM domains of paxillin are likely to be involved in the responses of paxillin against mechanical inputs [61]. Paxillin potentially promotes the invasion of cancer cells; however, its levels of expression and phosphorylation differ largely among cancer cell types [62].

It has been suggested that p53 regulates these mechanoreponsive proteins at focal adhesions (Figure 2). The ectopic expression of p53 suppresses the promoter activity of FAK either directly [63] or by inducing the expression of X-linked ectodermal dysplasia receptor (XEDAR), a member of the tumor necrosis factor receptor (TNFR) superfamily [64]. Recently, we reported that oncogenic Ras-induced transformation leads to the cleavage of  $\beta$ -actin and concomitant suppression of p130Cas phosphorylation in a p53-dependent manner [65]. We have further shown that both the oncogenic Ras-induced disruption of mitochondrial integrity and p53-mediated activation of the mitochondrial protease high temperature requirement A2 (HtrA2; also known as Omi) are involved in the cleavage of  $\beta$ -actin in Ras-transformed cells. The p130Cas-Rac1 axis is known to promote cell invasion by inducing lamellipodia formation [66]. Interestingly, the cytoplasmic localization of p53 was increased by Ras transformation, causing mitochondrial translocation of the mitogen-activated protein kinase p38. p38 translocated into mitochondria and then enhances activation of HtrA2/Omi [67]. While cytoplasmic p53 is known to have tumor suppressive functions via the suppression of centrosome duplication, induction of cell death, and inhibition of autophagy [68], our

results revealed a novel mechanism underlying the tumor suppressive function of cytoplasmic p53.

The constitutively active form of Src and oncogenic Ras induce cellular transformation and invasion. Mukhopadhyay et al. reported that loss of p53 function enhances Src-driven cell invasion by promoting the formation of actin-rich structures, such as podosomes and invadopodia [14, 69–71]. They showed that the level of caldesmon, an actin binding protein that can suppress both podosome and invadopodia formation [72], was decreased by inhibition of p53 [70]. Further, there is a possibility that p53 diminishes Src-driven cell invasion via inhibition of p130Cas-mediated podosome and invadopodia activity. As described above, a decrease in p130Cas phosphorylation by impairment of actin filaments following Ras-induced transformation was suppressed by p53 knockdown, while the activity of Src, a kinase of p130Cas, was not affected. Indeed, knockdown of p53 decreases p130Cas phosphorylation in Src-transformed cells (personal communication).

p53 regulates the activity of Rho GTPases (Figure 2) [73–75]. p53 mediates the oncogenic-Ras-induced activation of p190 Rho GTPase-activating protein (RhoGAP) [76]. A deficiency in p53 expression increases RhoA activity and stimulates the formation of blebs via the activation of Rho-associated protein kinase (ROCK) [77]. While RhoA typically promotes stress fiber formation [9], RhoA can increase cell-exerted contractile forces even in Ras-transformed cells in which stress fiber formation is largely diminished [76]. The generation of cell-exerted contractile forces plays a crucial role in the invasion and intravasation/extravasation of cancer cell tissue and blood vessels.

p53 regulates the expression of several genes that encode effector proteins of RhoA/RhoC and Cdc42. For example, depletion of p53 increases the expression of *ROCK1/2* and *MRCK $\alpha$* , which encodes myotonic dystrophy kinase-related Cdc42-binding kinase  $\alpha$  (MRCK $\alpha$ ). The ectopic expression of p53 in turn increases the expression of these genes [78]. Not only RhoA signaling but also Rac and Cdc42 signaling is affected by p53. Depletion of p53 increases phosphoinositide 3-kinase- (PI3-kinase-) mediated Rac activity [79]. Conversely, the ectopic expression of p53 decreases Cdc42 activity and concomitant filopodia formation [80].

F-actin formation is both negatively and positively regulated by p53 in response to DNA damage. Croft et al. reported that treatment with the antitumor drug doxorubicin reduces the activity of cofilin by increasing the expression of RhoC and LIM kinase 2 (LIMK2) in a p53-dependent manner [81]. While doxorubicin treatment promotes the formation of stress fibers, depletion of either RhoC or LIMK2 abrogates doxorubicin-induced stress fiber formation. Conversely, other antitumor drugs, including camptothecin and etoposide, attenuate the formation of stress fibers through the p53-dependent expression of RhoE [82]. Depletion of RhoE prevents the camptothecin-induced disassembly of stress fibers.

It has been suggested that, in response to DNA damage, p53 influences actin cytoskeleton remodeling by regulating the cytoskeleton adaptor protein ankyrin-1, which is encoded by *ANK1*. Hall et al. reported that the etoposide-induced activation of p53 increases the expression of *ANK1* [83]. Etoposide treatment promotes the formation of actin-rich long

protrusions, even though knockdown of ankyrin-1 attenuates this response. By contrast, stress fiber formation in etoposide-treated cells is enhanced by depleting ankyrin-1 expression. The ankyrin-1-mediated activation of cofilin may be involved in these actin remodeling processes. Furthermore, ankyrin-1 contributes to the association of the cortical spectrin-actin network with the plasma membrane by linking spectrin with membrane proteins including the anion exchanger and CD44 [84, 85]. Spectrin plays a crucial role in maintaining the structural integrity of the plasma membrane and has been suggested to be a potential mechanosensing protein [86]. Therefore, the p53-dependent regulation of ankyrin-1 may contribute not only to actin remodeling but also to mechanosensing/mechanoprotection of cells.

#### 4. Regulation of Cadherin Expression by p53

It is well established that EMT promotes cell invasion and metastasis. It is important to note that EMT is associated with a decrease in E-cadherin expression and an increase in N-cadherin expression, which are major components of cell-cell adhesion complexes. They form homophilic adhesion bonds. Since the interactions of N-cadherin are much weaker than those of E-cadherin, the shift from E-cadherin to N-cadherin during EMT weakens cell-cell adhesions, which promotes the scattering and migration of cancer cells. Like focal adhesions, AJs are reportedly involved in sensing the mechanical microenvironments of cells [26, 87–90].

In cells undergoing EMT, the expression of E-cadherin, encoded by *CDH1*, is suppressed by Snail, zinc finger E-box binding homeobox 1/2 (*ZEB1/2*), and Slug. These proteins in turn increase the expression of N-cadherin, which is encoded by *CDH2* [91]. It has been revealed that p53 prevents EMT by regulating the expression of E- and N-cadherins. Siemens et al. showed that activated p53 suppresses Snail expression by inducing the expression of microRNA- (miR-) 34a/b/c [92]. The expression of miR-200 and miR-192 is also p53-dependent, and their expression is negatively correlated with *ZEB1/2* expression [93, 94]. Both p53 itself and its transcriptional targets (*MDM2* and *p21<sup>WAF1</sup>*) regulate Slug expression [95]. The ectopic expression of p53 induces the proteasomal degradation of Slug, which is mediated by the E3 ligase *MDM2*. A further study by Kim et al. showed that complex formation of Slug with *p21<sup>WAF1</sup>* and p53 is involved in *MDM2*-mediated Slug degradation [96].

#### 5. p53 Gain-of-Function Mutants Regulate Cell Adhesion Molecules and Downstream Pathways

Mutations in *TP53* often result in a gain-of-function (GOF) of the protein [97]. Muller et al. showed that p53 GOF mutants increase the Rab-coupling protein- (RCP-) driven recycling of integrin  $\alpha5\beta1$  by inhibiting TAp63-mediated transcription [98]. This would induce the formation of filopodia-like protrusions and thereby promotes the invasion of cancer cells. Furthermore, p53 GOF mutants promote the translocation of integrin  $\beta1$  to the tips of filopodia by increasing the early

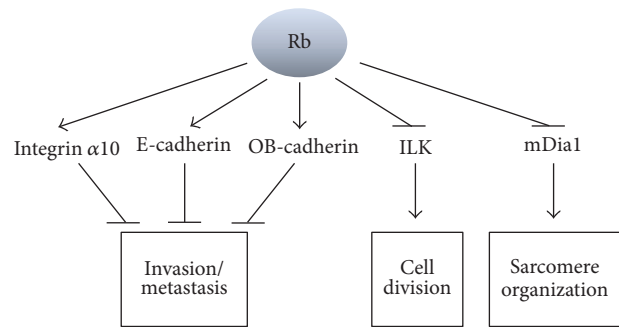


FIGURE 3: Rb-dependent regulation of the molecules involved in actin cytoskeleton remodeling. In cancer cells, Rb is inactivated either by Cdk4/6- and Cdk2-dependent hyperphosphorylation or by its mutation. Rb prevents cancer progression by suppressing both invasion and cell division via the alteration of actin cytoskeleton remodeling. Conversely, under inflammatory conditions, Rb is likely to have a promoting effect on cancer cachexia, which is associated with muscle atrophy characterized by disorganization of sarcomeres.  $\text{TNF}\alpha$  upregulates the Cdk4/6-dependent phosphorylation of Rb, which causes disorganization of sarcomeres by inhibiting mDia1-mediated actin polymerization.

growth response protein 1- (EGRI-) mediated expression of myosin-X (*Myo10*), an unconventional myosin [99]. The expression of integrin  $\alpha5\beta1$  and its ligand fibronectin is also increased by p53 GOF mutants [100], which contributes to the survival of suspended cells.

Recently, Lee et al. showed that p53 GOF mutants increase the transcription of *ITGB4*, which encodes integrin  $\beta4$  [101]. TAp63 and TAp73 also upregulate the expression of *ITGB4*, as described above [56]. Conversely, the transcriptional activity of TAp63 and TAp73 is reduced by their binding with a subset of p53 mutants [102]. Thus, additional studies are needed to reveal the actual relationship between p53 GOF mutants, p63, and p73 in terms of the regulation of *ITGB4* expression, which would provide a better understanding of the mechanisms underlying cancer progression.

p53 GOF mutants appear to contribute to cancer progression via the expression of the EMT-promoting factors Snail, Slug, and Twist [103, 104]. In addition, p53 GOF mutants upregulate the expression of paxillin and *ARHGDI*, which encodes Rho GDP-dissociation inhibitor alpha ( $\text{Rho-GDI}\alpha$ ) that typically downregulates Rho GTPases [105]. However, the role of paxillin and Rho-GDIs in metastasis is controversial, which may reflect the diversity of cancers.

#### 6. Rb Regulates Cell Adhesion Molecules and Downstream Pathways

Several studies have suggested a role for Rb in the regulation of the actin cytoskeleton and related pathways (Figure 3). Engel et al. showed, using Rb knockout cells and the ectopic expression of Rb mutants, that Rb promotes the expression of *ITGA10* (encoding integrin  $\alpha10$ ) in osteoblasts independently of the canonical Rb-E2F pathway [106]. They used bioinformatic analysis to show that the expression of integrin  $\alpha10$  is downregulated in several tumors compared with normal

tissues. Integrin  $\alpha 10$  heterodimerizes with the integrin  $\beta 1$  subunit [107]. While both loss-of-function and gain-of-function of p53 drive integrin  $\beta 1$ -mediated cancer cell progression as discussed above [53, 98–100], Rb might prevent cancer progression by increasing the heterodimerization of integrins  $\alpha 10$  and  $\beta 1$  and by suppressing the heterodimerization of integrins  $\alpha 4$  or  $\alpha 5$  with  $\beta 1$ .

It has been suggested that loss of Rb function causes the upregulation of ILK expression, which is required for cell division [108]. In retinoblastoma cells carrying mutations in the *Rb* gene, inhibition of ILK by the small molecule QLT-0267 induces the accumulation of multinucleated cells, which is associated with a decrease in cortical F-actin, alteration of mitotic spindle organization, and declustering of centrosomes. ILK upregulates actin polymerization by inactivating cofilin and by activating both Rac and Cdc42 [109]. Furthermore, ILK controls the complex formation of Aurora A kinase/chTOG/TACC3, which is essential for the assembly of mitotic spindles [110, 111]. Both microtubule-dependent forces and actin-dependent forces at the cell cortex contribute to centrosome clustering [112]. These findings suggest that loss of Rb function prevents mitotic defects, such as the arrest of and exit from mitosis, through upregulation of the ILK-mediated assembly of actin filaments and microtubules, which would ensure cell division.

We reported recently that Rb causes disruption of the sarcomeric structure of skeletal muscle myotubes via its interaction with the formin protein mDial [113], an effector of RhoA [114]. This pathway is stimulated by the inflammatory cytokine TNF $\alpha$ . TNF $\alpha$  increases the CDK4-dependent but CDK2-independent phosphorylation of Rb. Phosphorylated Rb subsequently translocates from the nucleus to the cytosol, where it binds to mDial. The sarcomere, which consists of a highly ordered array of actin thin filaments and myosin thick filaments, provides a contractile unit in muscle cells and confers muscle strength. Our findings suggest that inflammation hampers the homeostasis of skeletal muscle via inhibition of mDial-mediated actin polymerization by Rb. In advanced cancer patients, cachexia—the loss of body mass that is associated with muscle atrophy characterized by disorganization of sarcomeres—is often observed. Cytoplasmic Rb might contribute to cancer progression by promoting muscle atrophy. Indeed, cytoplasmic Rb was detected in atrophied tibialis anterior muscles, but not the normal muscles, of cancer patients [113].

Rb has also been implicated in the regulation of cadherin expression. Sosa-García et al. reported that, in Rb-deficient osteoblasts, the expression of E-cadherin and osteoblast-cadherin (OB-cadherin) is downregulated [115]. Associated with this, AJs are disrupted in these cells, which is mediated by the inactivation of merlin, a member of the ezrin, radixin, and moesin (ERM) family of proteins that links actin filaments to AJ complexes [116]. OB-cadherin (also known as cadherin-11), a cadherin isoform that is expressed in mesoderm-derived tissues, is known to be involved in cancer progression both positively and negatively. In prostate and brain cancers, OB-cadherin enhances the engagement between cancer cells and bone tissues by its hemophilic interactions, which promotes cancer metastasis [117–122].

By contrast, osteosarcoma formation is promoted by the disruption of OB-cadherin-mediated cell-cell interactions. These results imply that loss of Rb function might induce cancer progression preferentially in growing tissues.

## 7. Concluding Remarks

In this paper, we focused on the findings regarding the roles of the central tumor suppressors p53 and Rb in the regulation of the actin cytoskeleton and mechanoresponsive molecules. Intense studies have revealed that both these tumor suppressors and mechanical environments surrounding cells have significant effects on cancer progression. However, little is known about how these tumor suppressors influence the mechanical environment-dependent regulation of cancer progression.

Cancer cells sense various different mechanical environments during metastasis, leading to an alteration of cell behavior [123, 124]. The tumor stroma is composed of non-cancerous cells, including cancer-associated fibroblasts (CAFs), as well as noncellular components, such as the ECM. The excess production of the ECM mainly by CAFs stiffens solid tumors [125, 126], which promotes the growth of cancer cells [127, 128]. In addition, along with the growth of tumor mass, cancer cells suffer high pressure caused by tissue compression and/or an increase in interstitial pressure [129]. Similar to ECM stiffening, this high pressure also promotes the metastasis of cancer cells. Following intravasation, cancer cells in blood vessels are exposed to shear forces exerted by blood flow, which facilitates the interaction of cancer cells with endothelial cells to permit extravasation [130]. Cell growth and sensitivity against chemotherapy and radiotherapy treatments are also affected by mechanical environments [131]. Furthermore, mechanical environments appear to be crucial for maintaining the properties of cancer stem cells, such as self-renewal and tumor formation abilities. Thus, mechanical environments affect cancer progression at multiple stages.

We have proposed the possibility that cancer cachexia with muscle atrophy is caused by Rb-mediated disruption of sarcomeric organization [113]. Currently there is no effective treatment for muscle atrophy, which makes it difficult to improve the quality of life (QOL) of patients with advanced cancers. Since CDK4 is responsible for the TNF $\alpha$ -induced phosphorylation of Rb and resultant disorganization of sarcomeres, disrupting the function of CDK4 may prevent cachexia in advanced cancers, which would improve QOL. p53 is known to be required for the promotion of muscle atrophy induced by inflammatory cytokines, including TNF $\alpha$  [132]. p53 may be involved in Rb-promoted muscle atrophy. It is well known that the p53 and Rb pathways cooperatively regulate cell proliferation and senescence; however, the relationship between p53 and Rb in actin cytoskeleton remodeling is totally unknown. As described above, we have shown that Rb appears to inhibit mDial-mediated actin polymerization to disrupt sarcomeres. However, activation of RhoA, which promotes mDial-induced actin polymerization [114], is prevented by p53 [77]. These observations support the notion that p53 synergistically enhances Rb-promoted

muscle atrophy. In addition to CDK4 inhibition, development of a drug that targets the pathway for p53-mediated inactivation of RhoA may enable the suppression of cancer-associated cachexia.

While accumulating evidence reveals that mechanical environments significantly affect the aggressiveness of cancer cells, it remains unclear how mechanical environments regulate the activities of p53 and Rb. Further studies into the mechanotransduction mechanisms responsible for mechanical cue-dependent regulation of these tumor suppressors would aid the development a definitive treatment for cancers and a treatment that improves the QOL of advanced cancer patients.

## Competing Interests

The authors declare that there is no conflict of interests regarding the publication of this paper.

## Acknowledgments

The authors thank Drs. Steven J. Wolf and Keigo Araki for discussion. This work was supported by The Naito Foundation.

## References

- [1] G. I. Evan and K. H. Vousden, "Proliferation, cell cycle and apoptosis in cancer," *Nature*, vol. 411, no. 6835, pp. 342–348, 2001.
- [2] D. Hanahan and R. A. Weinberg, "Hallmarks of cancer: the next generation," *Cell*, vol. 144, no. 5, pp. 646–674, 2011.
- [3] S. Heerboth, G. Housman, M. Leary et al., "EMT and tumor metastasis," *Clinical and Translational Medicine*, vol. 4, no. 1, article 6, 2015.
- [4] S. H. Lee and R. Dominguez, "Regulation of actin cytoskeleton dynamics in cells," *Molecules and Cells*, vol. 29, no. 4, pp. 311–325, 2010.
- [5] A. Nürnberg, T. Kitzing, and R. Grosse, "Nucleating actin for invasion," *Nature Reviews Cancer*, vol. 11, no. 3, pp. 117–187, 2011.
- [6] M. D. Welch, J. Rosenblatt, J. Skoble, D. A. Portnoy, and T. J. Mitchison, "Interaction of human Arp2/3 complex and the *Listeria monocytogenes* ActA protein in actin filament nucleation," *Science*, vol. 281, no. 5373, pp. 105–108, 1998.
- [7] M. E. Quinlan, J. E. Heuser, E. Kerkhoff, and R. D. Mullins, "Drosophila Spire is an actin nucleation factor," *Nature*, vol. 433, no. 7024, pp. 382–388, 2005.
- [8] J. Faix and R. Grosse, "Staying in shape with formins," *Developmental Cell*, vol. 10, no. 6, pp. 693–706, 2006.
- [9] C. D. Nobes and A. Hall, "Rho, Rac, and Cdc42 GTPases regulate the assembly of multimolecular focal complexes associated with actin stress fibers, lamellipodia, and filopodia," *Cell*, vol. 81, no. 1, pp. 53–62, 1995.
- [10] F. S. Southwick, "Gelsolin and ADF/cofilin enhance the actin dynamics of motile cells," *Proceedings of the National Academy of Sciences of the United States of America*, vol. 97, no. 13, pp. 6936–6938, 2000.
- [11] B. W. Bernstein and J. R. Bamburg, "ADF/Cofilin: a functional node in cell biology," *Trends in Cell Biology*, vol. 20, no. 4, pp. 187–195, 2010.
- [12] J. Toshima, J. Y. Toshima, T. Amano, N. Yang, S. Narumiya, and K. Mizuno, "Cofilin phosphorylation by protein kinase testicular protein kinase 1 and its role in integrin-mediated actin reorganization and focal adhesion formation," *Molecular Biology of the Cell*, vol. 12, no. 4, pp. 1131–1145, 2001.
- [13] Y.-B. Kim, S. Choi, M.-C. Choi et al., "Cell adhesion-dependent cofilin serine 3 phosphorylation by the integrin-linked kinase-c-Src complex," *Journal of Biological Chemistry*, vol. 283, no. 15, pp. 10089–10096, 2008.
- [14] S. Linder, "The matrix corroded: podosomes and invadopodia in extracellular matrix degradation," *Trends in Cell Biology*, vol. 17, no. 3, pp. 107–117, 2007.
- [15] L. M. Machesky, "Lamellipodia and filopodia in metastasis and invasion," *FEBS Letters*, vol. 582, no. 14, pp. 2102–2111, 2008.
- [16] O. T. Fackler and R. Grosse, "Cell motility through plasma membrane blebbing," *The Journal of Cell Biology*, vol. 181, no. 6, pp. 879–884, 2008.
- [17] G. Charras and E. Paluch, "Blebs lead the way: how to migrate without lamellipodia," *Nature Reviews Molecular Cell Biology*, vol. 9, no. 9, pp. 730–736, 2008.
- [18] M. De Nicola, C. Cerella, M. D'Alessio et al., "The cleavage mode of apoptotic nuclear vesiculation is related to plasma membrane blebbing and depends on actin reorganization," *Annals of the New York Academy of Sciences*, vol. 1090, pp. 69–78, 2006.
- [19] B. Geiger, J. P. Spatz, and A. D. Bershadsky, "Environmental sensing through focal adhesions," *Nature Reviews Molecular Cell Biology*, vol. 10, no. 1, pp. 21–33, 2009.
- [20] J. Y.-J. Shyy and S. Chien, "Role of integrins in endothelial mechanosensing of shear stress," *Circulation Research*, vol. 91, no. 9, pp. 769–775, 2002.
- [21] S. K. Mitra, D. A. Hanson, and D. D. Schlaepfer, "Focal adhesion kinase: in command and control of cell motility," *Nature Reviews Molecular Cell Biology*, vol. 6, no. 1, pp. 56–68, 2005.
- [22] N. O. Deakin and C. E. Turner, "Paxillin comes of age," *Journal of Cell Science*, vol. 121, no. 15, pp. 2435–2444, 2008.
- [23] S. Huveneers and E. H. J. Danen, "Adhesion signaling—cross-talk between integrins, Src and Rho," *Journal of Cell Science*, vol. 122, no. 8, pp. 1059–1069, 2009.
- [24] S. V. Plotnikov, A. M. Pasapera, B. Sabass, and C. M. Waterman, "Force fluctuations within focal adhesions mediate ECM-rigidity sensing to guide directed cell migration," *Cell*, vol. 151, no. 7, pp. 1513–1527, 2012.
- [25] S. W. Moore, P. Roca-Cusachs, and M. P. Sheetz, "Stretchy proteins on stretchy substrates: the important elements of integrin-mediated rigidity sensing," *Developmental Cell*, vol. 19, no. 2, pp. 194–206, 2010.
- [26] S. Yonemura, Y. Wada, T. Watanabe, A. Nagafuchi, and M. Shibata, " $\alpha$ -Catenin as a tension transducer that induces adherens junction development," *Nature Cell Biology*, vol. 12, no. 6, pp. 533–542, 2010.
- [27] M. Yao, W. Qiu, R. Liu et al., "Force-dependent conformational switch of  $\alpha$ -catenin controls vinculin binding," *Nature Communications*, vol. 5, article no. 4525, 2014.
- [28] S. Huveneers and J. de Rooij, "Mechanosensitive systems at the cadherin-f-actin interface," *Journal of Cell Science*, vol. 126, no. 2, pp. 403–413, 2013.
- [29] L. Wei, W. Zhou, J. D. Croissant et al., "RhoA signaling via serum response factor plays an obligatory role in myogenic differentiation," *Journal of Biological Chemistry*, vol. 273, no. 46, pp. 30287–30294, 1998.
- [30] A. L'Honore, N. J. Lamb, M. Vandromme, P. Turowski, G. Carnac, and A. Fernandez, "MyoD distal regulatory region contains an SRF binding CArG element required for MyoD

- expression in skeletal myoblasts and during muscle regeneration," *Molecular Biology of the Cell*, vol. 14, no. 5, pp. 2151–2162, 2003.
- [31] G. C. T. Pipes, E. E. Creemers, and E. N. Olson, "The myocardin family of transcriptional coactivators: versatile regulators of cell growth, migration, and myogenesis," *Genes and Development*, vol. 20, no. 12, pp. 1545–1556, 2006.
- [32] J.-R. Kim, H. J. Kee, J.-Y. Kim et al., "Enhancer of polycomb1 acts on serum response factor to regulate skeletal muscle differentiation," *Journal of Biological Chemistry*, vol. 284, no. 24, pp. 16308–16316, 2009.
- [33] K. Kawauchi, W. W. Tan, K. Araki et al., "p130Cas-dependent actin remodelling regulates myogenic differentiation," *Biochemical Journal*, vol. 445, no. 3, pp. 323–332, 2012.
- [34] N. Rivlin, R. Brosh, M. Oren, and V. Rotter, "Mutations in the p53 tumor suppressor gene: important milestones at the various steps of tumorigenesis," *Genes and Cancer*, vol. 2, no. 4, pp. 466–474, 2011.
- [35] K. H. Vousden and X. Lu, "Live or let die: the cell's response to p53," *Nature Reviews Cancer*, vol. 2, no. 8, pp. 594–604, 2002.
- [36] M. Oren, "Decision making by p53: life, death and cancer," *Cell Death and Differentiation*, vol. 10, no. 4, pp. 431–442, 2003.
- [37] K. H. Vousden and D. P. Lane, "p53 in health and disease," *Nature Reviews Molecular Cell Biology*, vol. 8, no. 4, pp. 275–283, 2007.
- [38] E. Appella and C. W. Anderson, "Post-translational modifications and activation of p53 by genotoxic stresses," *European Journal of Biochemistry*, vol. 268, no. 10, pp. 2764–2772, 2001.
- [39] D. W. Meek, "Tumour suppression by p53: a role for the DNA damage response?" *Nature Reviews Cancer*, vol. 9, no. 10, pp. 714–723, 2009.
- [40] C. Giacinti and A. Giordano, "RB and cell cycle progression," *Oncogene*, vol. 25, no. 38, pp. 5220–5227, 2006.
- [41] R. A. Weinberg, "The retinoblastoma protein and cell cycle control," *Cell*, vol. 81, no. 3, pp. 323–330, 1995.
- [42] J. W. Harbour and D. C. Dean, "The Rb/E2F pathway: expanding roles and emerging paradigms," *Genes and Development*, vol. 14, no. 19, pp. 2393–2409, 2000.
- [43] P. Viatour and J. Sage, "Newly identified aspects of tumor suppression by RB," *Disease Models and Mechanisms*, vol. 4, no. 5, pp. 581–585, 2011.
- [44] K. Fukasawa, "Oncogenes and tumour suppressors take on centrosomes," *Nature Reviews Cancer*, vol. 7, no. 12, pp. 911–924, 2007.
- [45] C. Brakebusch and R. Fässler, "The integrin-actin connection, an eternal love affair," *The EMBO Journal*, vol. 22, no. 10, pp. 2324–2333, 2003.
- [46] J. S. Desgrosellier and D. A. Cheresh, "Integrins in cancer: biological implications and therapeutic opportunities," *Nature Reviews Cancer*, vol. 10, no. 1, pp. 9–22, 2010.
- [47] S. Cabodi, M. Del Pilar Camacho-Leal, P. Di Stefano, and P. Defilippi, "Integrin signalling adaptors: not only figurants in the cancer story," *Nature Reviews Cancer*, vol. 10, no. 12, pp. 858–870, 2010.
- [48] S. Johansson, G. Svineng, K. Wennerberg, A. Armulik, and L. Lohikangas, "Fibronectin-integrin interactions," *Frontiers in Bioscience*, vol. 2, pp. d126–d146, 1997.
- [49] M. M. Zutter, S. A. Santoro, W. D. Staatz, and Y. L. Tsung, "Re-expression of the  $\alpha 2 \beta 1$  integrin abrogates the malignant phenotype of breast carcinoma cells," *Proceedings of the National Academy of Sciences of the United States of America*, vol. 92, no. 16, pp. 7411–7415, 1995.
- [50] A. Kren, V. Baeriswyl, F. Lehembre et al., "Increased tumor cell dissemination and cellular senescence in the absence of  $\beta 1$ -integrin function," *The EMBO Journal*, vol. 26, no. 12, pp. 2832–2842, 2007.
- [51] H. Janouskova, A. Maglott, D. Y. Leger et al., "Integrin  $\alpha 5 \beta 1$  plays a critical role in resistance to temozolomide by interfering with the p53 pathway in high-grade glioma," *Cancer Research*, vol. 72, no. 14, pp. 3463–3470, 2012.
- [52] H. Janouskova, A.-M. Ray, F. Noulet et al., "Activation of p53 pathway by Nutlin-3a inhibits the expression of the therapeutic target  $\alpha 5$  integrin in colon cancer cells," *Cancer Letters*, vol. 336, no. 2, pp. 307–318, 2013.
- [53] J. Qiu, G. Wang, J. Hu, Q. Peng, and Y. Zheng, "Id1-induced inhibition of p53 facilitates endothelial cell migration and tube formation by regulating the expression of beta1-integrin," *Molecular and Cellular Biochemistry*, vol. 357, no. 1-2, pp. 125–133, 2011.
- [54] F. Vaillant, M.-L. Asselin-Labat, M. Shackleton, N. C. Forrest, G. J. Lindeman, and J. E. Visvader, "The mammary progenitor marker CD61/ $\beta 3$  integrin identifies cancer stem cells in mouse models of mammary tumorigenesis," *Cancer Research*, vol. 68, no. 19, pp. 7711–7717, 2008.
- [55] A. K. Guo, Y. Y. Hou, H. Hirata et al., "Loss of p53 enhances NF- $\kappa$ B-dependent lamellipodia formation," *Journal of Cellular Physiology*, vol. 229, no. 6, pp. 696–704, 2014.
- [56] G. Bon, S. E. Di Carlo, V. Folgiero et al., "Negative regulation of  $\beta 4$  integrin transcription by homeodomain-interacting protein kinase 2 and p53 impairs tumor progression," *Cancer Research*, vol. 69, no. 14, pp. 5978–5986, 2009.
- [57] Y. Sawada, M. Tamada, B. J. Dubin-Thaler et al., "Force Sensing by Mechanical Extension of the Src Family Kinase Substrate p130Cas," *Cell*, vol. 127, no. 5, pp. 1015–1026, 2006.
- [58] Z. Zhao, S. H. Tan, H. Machiyama et al., "Association between tensin 1 and p130Cas at focal adhesions links actin inward flux to cell migration," *Biology Open*, vol. 5, no. 4, pp. 499–506, 2016.
- [59] H. Chen, A. Ishii, W.-K. Wong, L. B. Chen, and S. H. Lo, "Molecular characterization of human tensin," *Biochemical Journal*, vol. 351, no. 2, pp. 403–411, 2000.
- [60] D. R. Rhodes, J. Yu, K. Shanker et al., "ONCOMINE: a cancer microarray database and integrated data-mining platform," *Neoplasia*, vol. 6, no. 1, pp. 1–6, 2004.
- [61] T. Watanabe-Nakayama, M. Saito, S. Machida, K. Kishimoto, R. Afrin, and A. Ikai, "Requirement of LIM domains for the transient accumulation of paxillin at damaged stress fibres," *Biology Open*, vol. 2, no. 7, pp. 667–674, 2013.
- [62] M. C. Brown and C. E. Turner, "Paxillin: adapting to change," *Physiological Reviews*, vol. 84, no. 4, pp. 1315–1339, 2004.
- [63] V. Golubovskaya, A. Kaur, and W. Cance, "Cloning and characterization of the promoter region of human focal adhesion kinase gene: nuclear factor kappa B and p53 binding sites," *Biochimica et Biophysica Acta (BBA)—Gene Structure and Expression*, vol. 1678, no. 2-3, pp. 111–125, 2004.
- [64] C. Tanikawa, Y. Furukawa, N. Yoshida, H. Arakawa, Y. Nakamura, and K. Matsuda, "XEDAR as a putative colorectal tumor suppressor that mediates p53-regulated anoikis pathway," *Oncogene*, vol. 28, no. 34, pp. 3081–3092, 2009.
- [65] S. Yamauchi, Y. Y. Hou, A. K. Guo et al., "p53-mediated activation of the mitochondrial protease HtrA2/Omi prevents cell invasion," *Journal of Cell Biology*, vol. 204, no. 7, pp. 1191–1207, 2014.

- [66] A. Sharma and B. J. Mayer, "Phosphorylation of p130Cas initiates Rac activation and membrane ruffling," *BMC Cell Biology*, vol. 9, article 50, 2008.
- [67] H. Plun-Favreau, K. Klupsch, N. Moisoï et al., "The mitochondrial protease HtrA2 is regulated by Parkinson's disease-associated kinase PINK1," *Nature Cell Biology*, vol. 9, no. 11, pp. 1243–1252, 2007.
- [68] D. R. Green and G. Kroemer, "Cytoplasmic functions of the tumour suppressor p53," *Nature*, vol. 458, no. 7242, pp. 1127–1130, 2009.
- [69] M. Aga, J. M. Bradley, K. E. Keller, M. J. Kelley, and T. S. Acott, "Specialized podosome-or invadopodia-like structures (PILS) for focal trabecular meshwork extracellular matrix turnover," *Investigative Ophthalmology and Visual Science*, vol. 49, no. 12, pp. 5353–5365, 2008.
- [70] U. K. Mukhopadhyay, R. Eves, L. Jia, P. Mooney, and A. S. Mak, "p53 suppresses Src-induced podosome and rosette formation and cellular invasiveness through the upregulation of caldesmon," *Molecular and Cellular Biology*, vol. 29, no. 11, pp. 3088–3098, 2009.
- [71] U. K. Mukhopadhyay, P. Mooney, L. Jia, R. Eves, L. Raptis, and A. S. Mak, "Doubles game: Src-Stat3 versus p53-PTEN in cellular migration and invasion," *Molecular and Cellular Biology*, vol. 30, no. 21, pp. 4980–4995, 2010.
- [72] T. Yoshio, T. Morita, Y. Kimura, M. Tsujii, N. Hayashi, and K. Sobue, "Caldesmon suppresses cancer cell invasion by regulating podosome/invadopodium formation," *FEBS Letters*, vol. 581, no. 20, pp. 3777–3782, 2007.
- [73] P. A. J. Muller, K. H. Vousden, and J. C. Norman, "p53 and its mutants in tumor cell migration and invasion," *Journal of Cell Biology*, vol. 192, no. 2, pp. 209–218, 2011.
- [74] E. Powell, D. Piwnica-Worms, and H. Piwnica-Worms, "Contribution of p53 to metastasis," *Cancer Discovery*, vol. 4, no. 4, pp. 405–414, 2014.
- [75] K. Araki, T. Ebata, A. K. Guo, K. Tobiume, S. J. Wolf, and K. Kawachi, "P53 regulates cytoskeleton remodeling to suppress tumor progression," *Cellular and Molecular Life Sciences*, vol. 72, no. 21, pp. 4077–4094, 2015.
- [76] M. Xia and H. Land, "Tumor suppressor p53 restricts Ras stimulation of RhoA and cancer cell motility," *Nature Structural and Molecular Biology*, vol. 14, no. 3, pp. 215–223, 2007.
- [77] G. Gadea, M. de Toledo, C. Anguille, and P. Roux, "Loss of p53 promotes RhoA-ROCK-dependent cell migration and invasion in 3D matrices," *The Journal of Cell Biology*, vol. 178, no. 1, pp. 23–30, 2007.
- [78] K. Lefort, A. Mandinova, P. Ostano et al., "Notch1 is a p53 target gene involved in human keratinocyte tumor suppression through negative regulation of ROCK1/2 and MRCK $\alpha$  kinases," *Genes and Development*, vol. 21, no. 5, pp. 562–577, 2007.
- [79] F. Guo, Y. Gao, L. Wang, and Y. Zheng, "p19<sup>Arf</sup>-p53 tumor suppressor pathway regulates cell motility by suppression of phosphoinositide 3-kinase and Rac1 GTPase activities," *Journal of Biological Chemistry*, vol. 278, no. 16, pp. 14414–14419, 2003.
- [80] G. Gadéa, L. Lapasset, C. Gauthier-Rouvière, and P. Roux, "Regulation of Cdc42-mediated morphological effects: a novel function for p53," *EMBO Journal*, vol. 21, no. 10, pp. 2373–2382, 2002.
- [81] D. R. Croft, D. Crighton, M. S. Samuel et al., "p53-mediated transcriptional regulation and activation of the actin cytoskeleton regulatory RhoC to LIMK2 signaling pathway promotes cell survival," *Cell Research*, vol. 21, no. 4, pp. 666–682, 2011.
- [82] P. P. Ongusaha, H.-G. Kim, S. A. Boswell et al., "RhoE is a pro-survival p53 target gene that inhibits ROCK 1-mediated apoptosis in response to genotoxic stress," *Current Biology*, vol. 16, no. 24, pp. 2466–2472, 2006.
- [83] A. E. Hall, W. Lu, J. D. Godfrey et al., "The cytoskeleton adaptor protein ankyrin-1 is upregulated by p53 following DNA damage and alters cell migration," *Cell Death and Disease*, vol. 7, no. 4, Article ID e2184, 2016.
- [84] V. Bennett and A. J. Baines, "Spectrin and ankyrin-based pathways: metazoan inventions for integrating cells into tissues," *Physiological Reviews*, vol. 81, no. 3, pp. 1353–1392, 2001.
- [85] V. Bennett and J. Healy, "Membrane domains based on ankyrin and spectrin associated with cell-cell interactions," *Cold Spring Harbor Perspectives in Biology*, vol. 1, no. 6, Article ID a003012, 2009.
- [86] P. R. Stabach, I. Simonović, M. A. Ranieri et al., "The structure of the ankyrin-binding site of  $\beta$ -spectrin reveals how tandem spectrin-repeats generate unique ligand-binding properties," *Blood*, vol. 113, no. 22, pp. 5377–5384, 2009.
- [87] A. Nagafuchi, "Molecular architecture of adherens junctions," *Current Opinion in Cell Biology*, vol. 13, no. 5, pp. 600–603, 2001.
- [88] A. R. Harris, A. Daeden, and G. T. Charras, "Formation of adherens junctions leads to the emergence of a tissue-level tension in epithelial monolayers," *Journal of Cell Science*, vol. 127, no. 11, pp. 2507–2517, 2014.
- [89] T. Lecuit and A. S. Yap, "E-cadherin junctions as active mechanical integrators in tissue dynamics," *Nature Cell Biology*, vol. 17, no. 5, pp. 533–539, 2015.
- [90] B. Ladoux, W. J. Nelson, J. Yan, and R. M. Mège, "The mechanotransduction machinery at work at adherens junctions," *Integrative Biology*, vol. 7, no. 10, pp. 1109–1119, 2015.
- [91] G. Berx and F. van Roy, "Involvement of members of the cadherin superfamily in cancer," *Cold Spring Harbor Perspectives in Biology*, vol. 1, no. 6, Article ID a003129, 2009.
- [92] H. Siemens, R. Jackstadt, S. Hünten et al., "miR-34 and SNAIL form a double-negative feedback loop to regulate epithelial-mesenchymal transitions," *Cell Cycle*, vol. 10, no. 24, pp. 4256–4271, 2011.
- [93] C.-J. Chang, C.-H. Chao, W. Xia et al., "P53 regulates epithelial-mesenchymal transition and stem cell properties through modulating miRNAs," *Nature Cell Biology*, vol. 13, no. 3, pp. 317–323, 2011.
- [94] T. Kim, A. Veronese, F. Pichiorri et al., "p53 regulates epithelial-mesenchymal transition through microRNAs targeting ZEB1 and ZEB2," *Journal of Experimental Medicine*, vol. 208, no. 5, pp. 875–883, 2011.
- [95] S.-P. Wang, W.-L. Wang, Y.-L. Chang et al., "p53 controls cancer cell invasion by inducing the MDM2-mediated degradation of Slug," *Nature Cell Biology*, vol. 11, no. 6, pp. 694–704, 2009.
- [96] J. Kim, S. Bae, S. An et al., "Cooperative actions of p21WAF1 and p53 induce Slug protein degradation and suppress cell invasion," *EMBO Reports*, vol. 15, no. 10, pp. 1062–1068, 2014.
- [97] P. A. J. Muller and K. H. Vousden, "P53 mutations in cancer," *Nature Cell Biology*, vol. 15, no. 1, pp. 2–8, 2013.
- [98] P. A. J. Muller, P. T. Caswell, B. Doyle et al., "Mutant p53 drives invasion by promoting integrin recycling," *Cell*, vol. 139, no. 7, pp. 1327–1341, 2009.
- [99] A. Arjonen, R. Kaukonen, E. Mattila et al., "Mutant p53-associated myosin-X upregulation promotes breast cancer invasion and metastasis," *Journal of Clinical Investigation*, vol. 124, no. 3, pp. 1069–1082, 2014.

- [100] M. P. Iwanicki, H. Y. Chen, C. Iavarone et al., "Mutant p53 regulates ovarian cancer transformed phenotypes through autocrine matrix deposition," *JCI Insight*, vol. 1, no. 10, 2016.
- [101] J.-G. Lee, J.-H. Ahn, T. J. Kim, J. H. Lee, and J.-H. Choi, "Mutant p53 promotes ovarian cancer cell adhesion to mesothelial cells via integrin  $\beta 4$  and Akt signals," *Scientific Reports*, vol. 5, Article ID 12642, 2015.
- [102] Y. Li and C. Prives, "Are interactions with p63 and p73 involved in mutant p53 gain of oncogenic function?" *Oncogene*, vol. 26, no. 15, pp. 2220–2225, 2007.
- [103] Y. Zhang, W. Yan, and X. Chen, "Mutant p53 disrupts MCF-10A cell polarity in three-dimensional culture via epithelial-to-mesenchymal transitions," *Journal of Biological Chemistry*, vol. 286, no. 18, pp. 16218–16228, 2011.
- [104] I. Kogan-Sakin, Y. Tabach, Y. Buganim et al., "Mutant p53(R175H) upregulates Twist1 expression and promotes epithelial-mesenchymal transition in immortalized prostate cells," *Cell Death & Differentiation*, vol. 18, no. 2, pp. 271–281, 2011.
- [105] G. Bossi, F. Marampon, R. Maor-Aloni et al., "Conditional RNA interference in vivo to study mutant p53 oncogenic gain of function on tumor malignancy," *Cell Cycle*, vol. 7, no. 12, pp. 1870–1879, 2008.
- [106] B. E. Engel, E. Welsh, M. F. Emmons, P. G. Santiago-Cardona, and W. D. Cress, "Expression of integrin alpha 10 is transcriptionally activated by pRb in mouse osteoblasts and is downregulated in multiple solid tumors," *Cell Death and Disease*, vol. 4, no. 11, article e938, 2013.
- [107] M. Barczyk, S. Carracedo, and D. Gullberg, "Integrins," *Cell and Tissue Research*, vol. 339, no. 1, pp. 269–280, 2010.
- [108] W. K. A. Sikkema, A. Strikwerda, M. Sharma et al., "Regulation of mitotic cytoskeleton dynamics and cytokinesis by integrin-linked kinase in retinoblastoma cells," *PLoS ONE*, vol. 9, no. 6, Article ID e98838, 2014.
- [109] N. R. Filipenko, S. Attwell, C. Roskelley, and S. Dedhar, "Integrin-linked kinase activity regulates Rac- and Cdc42-mediated actin cytoskeleton reorganization via  $\alpha$ -PIX," *Oncogene*, vol. 24, no. 38, pp. 5837–5849, 2005.
- [110] A. B. Fielding, I. Dobрева, and S. Dedhar, "Beyond focal adhesions: integrin-linked kinase associates with tubulin and regulates mitotic spindle organization," *Cell Cycle*, vol. 7, no. 13, pp. 1899–1906, 2008.
- [111] A. B. Fielding, S. Lim, K. Montgomery, I. Dobрева, and S. Dedhar, "A critical role of integrin-linked kinase, ch-TOG and TACC3 in centrosome clustering in cancer cells," *Oncogene*, vol. 30, no. 5, pp. 521–534, 2011.
- [112] M. Kwon, S. A. Godinho, N. S. Chandhok et al., "Mechanisms to suppress multipolar divisions in cancer cells with extra centrosomes," *Genes and Development*, vol. 22, no. 16, pp. 2189–2203, 2008.
- [113] K. Araki, K. Kawachi, H. Hirata, M. Yamamoto, and Y. Taya, "Cytoplasmic translocation of the retinoblastoma protein disrupts sarcomeric organization," *eLife*, vol. 2, Article ID e01228, 2013.
- [114] A. Mammoto, S. Huang, K. Moore, P. Oh, and D. E. Ingber, "Role of RhoA, mDia, and ROCK in cell shape-dependent control of the Skp2-p27kip-1 pathway and the G1/S transition," *Journal of Biological Chemistry*, vol. 279, no. 25, pp. 26323–26330, 2004.
- [115] B. Sosa-García, V. Gunduz, V. Vazquez-Rivera et al., "A role for the retinoblastoma protein as a regulator of mouse osteoblast cell adhesion: implications for osteogenesis and osteosarcoma formation," *PLOS ONE*, vol. 5, no. 11, Article ID e13954, 2010.
- [116] R. G. Fehon, A. I. McClatchey, and A. Bretscher, "Organizing the cell cortex: the role of ERM proteins," *Nature Reviews Molecular Cell Biology*, vol. 11, no. 4, pp. 276–287, 2010.
- [117] K. Tomita, A. Van Bokhoven, G. J. L. H. Van Leenders et al., "Cadherin switching in human prostate cancer progression," *Cancer Research*, vol. 60, no. 13, pp. 3650–3654, 2000.
- [118] G. Nakajima, A. Patino-Garcia, S. Bruheim et al., "CDH11 expression is associated with survival in patients with osteosarcoma," *Cancer Genomics and Proteomics*, vol. 5, no. 1, pp. 37–42, 2008.
- [119] D. Tamura, T. Hiraga, A. Myoui, H. Yoshikawa, and T. Yoneda, "Cadherin-11-mediated interactions with bone marrow stromal/osteoblastic cells support selective colonization of breast cancer cells in bone," *International Journal of Oncology*, vol. 33, no. 1, pp. 17–24, 2008.
- [120] K. Chu, C.-J. Cheng, X. Ye et al., "Cadherin-11 promotes the metastasis of prostate cancer cells to bone," *Molecular Cancer Research*, vol. 6, no. 8, pp. 1259–1267, 2008.
- [121] S. Floor, W. C. G. Van Staveren, D. Larsimont, J. E. Dumont, and C. Maenhaut, "Cancer cells in epithelial-to-mesenchymal transition and tumor-propagating-cancer stem cells: distinct, overlapping or same populations," *Oncogene*, vol. 30, no. 46, pp. 4609–4621, 2011.
- [122] H. Kaur, P. J. Phillips-Mason, S. M. Burden-Gulley et al., "Cadherin-11, a marker of the mesenchymal phenotype, regulates glioblastoma cell migration and survival *in vivo*," *Molecular Cancer Research*, vol. 10, no. 3, pp. 293–304, 2012.
- [123] S. Kumar and V. M. Weaver, "Mechanics, malignancy, and metastasis: the force journey of a tumor cell," *Cancer and Metastasis Reviews*, vol. 28, no. 1-2, pp. 113–127, 2009.
- [124] D. Wirtz, K. Konstantopoulos, and P. C. Searson, "The physics of cancer: the role of physical interactions and mechanical forces in metastasis," *Nature Reviews Cancer*, vol. 11, no. 7, pp. 512–522, 2011.
- [125] M. J. Paszek, N. Zahir, K. R. Johnson et al., "Tensional homeostasis and the malignant phenotype," *Cancer Cell*, vol. 8, no. 3, pp. 241–254, 2005.
- [126] K. R. Levental, H. Yu, L. Kass et al., "Matrix crosslinking forces tumor progression by enhancing integrin signaling," *Cell*, vol. 139, no. 5, pp. 891–906, 2009.
- [127] J. Wels, R. N. Kaplan, S. Rafii, and D. Lyden, "Migratory neighbors and distant invaders: tumor-associated niche cells," *Genes and Development*, vol. 22, no. 5, pp. 559–574, 2008.
- [128] H. Ungefroren, S. Sebens, D. Seidl, H. Lehnert, and R. Hass, "Interaction of tumor cells with the microenvironment," *Cell Communication and Signaling*, vol. 9, article no. 18, 2011.
- [129] P. Lu, V. M. Weaver, and Z. Werb, "The extracellular matrix: a dynamic niche in cancer progression," *Journal of Cell Biology*, vol. 196, no. 4, pp. 395–406, 2012.
- [130] S. Valastyan and R. A. Weinberg, "Tumor metastasis: molecular insights and evolving paradigms," *Cell*, vol. 147, no. 2, pp. 275–292, 2011.
- [131] M. Castells, B. Thibault, J.-P. Delord, and B. Couderc, "Implication of tumor microenvironment in chemoresistance: tumor-associated stromal cells protect tumor cells from cell death," *International Journal of Molecular Sciences*, vol. 13, no. 8, pp. 9545–9571, 2012.
- [132] M. Schwarzkopf, D. Coletti, D. Sassoon, and G. Marazzi, "Muscle cachexia is regulated by a p53-PW1/Peg3-dependent pathway," *Genes and Development*, vol. 20, no. 24, pp. 3440–3452, 2006.

## Research Article

# Proliferation-Related Activity in Endothelial Cells Is Enhanced by Micropower Plasma

Kotaro Suzuki<sup>1</sup> and Daisuke Yoshino<sup>2</sup>

<sup>1</sup>Graduate School of Engineering, Tohoku University, 6-6-01 Aramaki-Aoba, Aoba, Sendai 980-8579, Japan

<sup>2</sup>Institute of Fluid Science, Tohoku University, 2-1-1 Katahira, Aoba, Sendai 980-8577, Japan

Correspondence should be addressed to Daisuke Yoshino; [yoshino.d@m.tohoku.ac.jp](mailto:yoshino.d@m.tohoku.ac.jp)

Received 16 September 2016; Accepted 20 November 2016

Academic Editor: Hideaki Fujita

Copyright © 2016 K. Suzuki and D. Yoshino. This is an open access article distributed under the Creative Commons Attribution License, which permits unrestricted use, distribution, and reproduction in any medium, provided the original work is properly cited.

Nonthermal plasma has received a lot of attention as a medical treatment technique in recent years. It can easily create various reactive chemical species (ROS) and is harmless to living body. Although plasma at gas-liquid interface has a potential for a biomedical application, the interactions between the gas-liquid plasma and living cells remain unclear. Here, we show characteristics of a micropower plasma with 0.018 W of the power input, generated at gas-liquid interface. We also provide the evidence of plasma-induced enhancement in proliferation activity of endothelial cells. The plasma produced  $\text{H}_2\text{O}_2$ ,  $\text{HNO}_2$ , and  $\text{HNO}_3$  in phosphate buffered saline containing  $\text{Mg}^{++}$  and  $\text{Ca}^{++}$  (PBS(+)), and their concentration increased linearly during 600-second discharge. The value of pH in PBS(+) against the plasma discharge time was stable at about 7.0. Temperature in PBS(+) rose monotonically, and its rise was up to 0.8°C at the bottom of a cell-cultured dish by the plasma discharge for 600 s. Short-time treatment of the plasma enhanced proliferation activity of endothelial cells. In contrast, the treatment of  $\text{H}_2\text{O}_2$  does not enhance the cell proliferation. Thus, the ROS production and the nuclear factor-kappa B (NF- $\kappa$ B) activation due to the plasma treatment might be related to enhancement of the cell proliferation. Our results may potentially provide the basis for developing the biomedical applications using the gas-liquid plasma.

## 1. Introduction

Plasma is called the fourth state of matter following solid, liquid, and gas, and it is composed of charged particles, excited particles, chemically reactive species, and neutral particles. Recently, plasma has been developed for a wide range of medical applications such as sterilization [1, 2], surface modification of a medical equipment [3], and blood coagulation [4]. They are generically known as “plasma medicine” [5]. The plasma used for medical applications is classified with two types [6]: one is thermal plasma whose temperature is around  $10^4$  K, and the other is nonthermal plasma whose temperature is around room temperature. Nonthermal plasma sources have become popular for medical applications because there is no measurable damage to living tissue.

In recent years, plasma treatments to enhance cell proliferation have attracted attention in the field of plasma

medicine, and there have been many researchers about the plasma treatments of living cells [7, 8]. It is believed that reactive oxygen species (ROS) produced by the plasma have a positive effect on the therapeutic actions. However, the interactions between nonthermal plasma and living cells are still unclear. Several types of plasma sources for biomedical applications such as plasma jets and surface discharges are generally used [9]. Plasma at gas-liquid interface also has a potential for the biomedical application because the plasma produces ROS in liquid effectively by a synergistic effect of chemical reactions in gas phase and gas-liquid interface [10–14]. However, the plasma at gas-liquid interface is not used much for the biomedical applications.

This study aims to understand characteristics of a micropower plasma generated at gas-liquid interface and to reveal responses of living cells to the plasma for development of a novel biomedical applications using the plasma. First, we measure characteristics of the micropower plasma, namely,

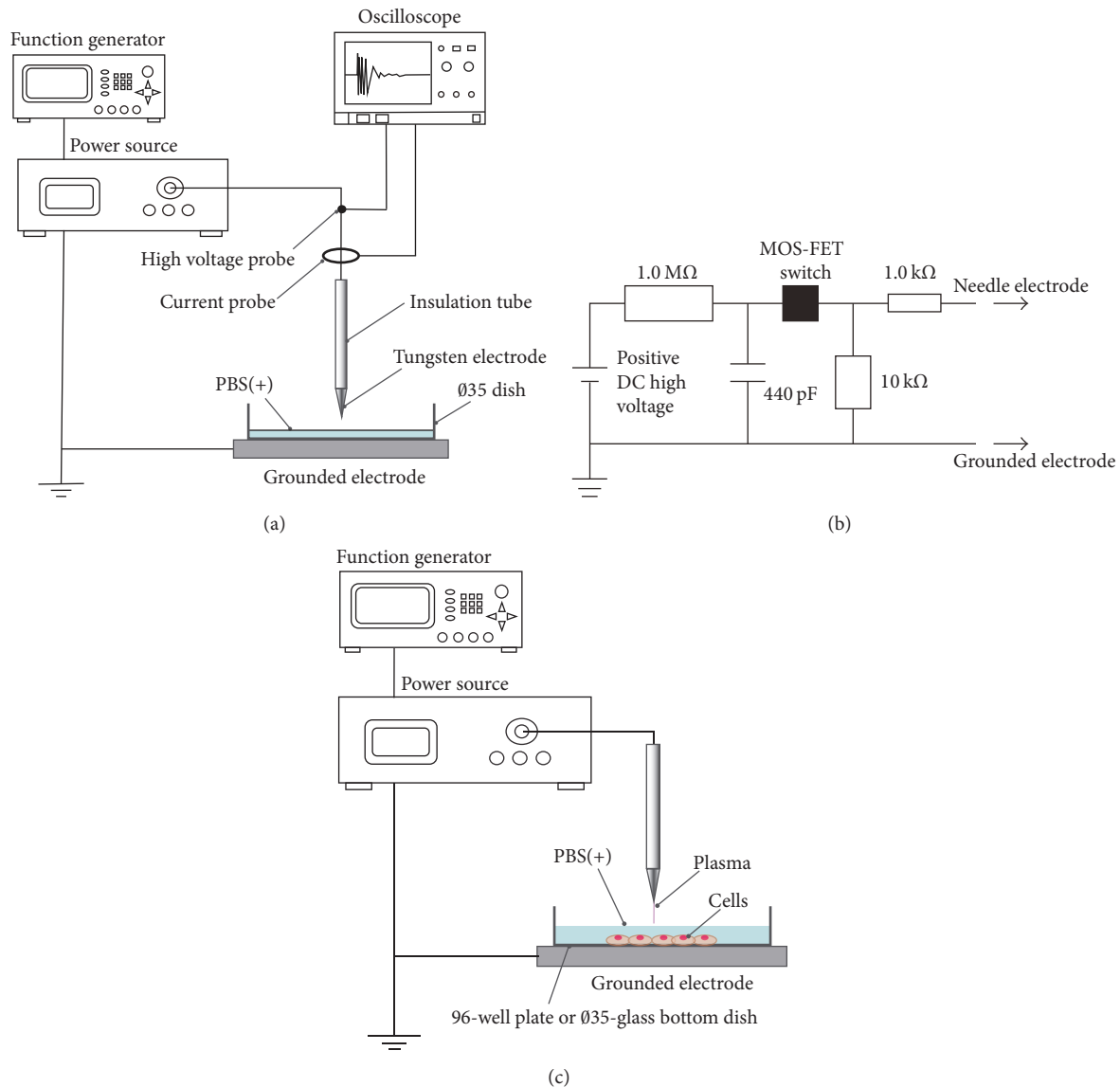


FIGURE 1: Schematics of the experimental setup (a), electric circuit in the power source (b) to generate micropower plasma, and the experimental setup to expose cells to the micropower plasma (c).

power input and emission spectra of the plasma, changes in pH and temperature in a liquid by the plasma treatment, and production of chemical species in the liquid. Secondly, we evaluate an effect of the plasma treatment on living cells focusing on the cell viability and discuss a mechanism for cellular response to the plasma treatment.

## 2. Materials and Methods

**2.1. Micropower Plasma Source.** Figure 1 shows the schematics of the experimental setup (a) and the power source (b) to generate micropower plasma. The power source consisted of a direct current (DC) power supply (HGR10-10P, Matsusada Precision Inc.), a metal-oxide-semiconductor field-effect transistor switch (MOS-FET switch; HTS 151-02,

BEHLIKE), three resistors (1.0 M $\Omega$ , 10 k $\Omega$ , and 1.0 k $\Omega$ ), and a capacitor (440 pF). The MOS-FET switch was controlled by a function generator (FG-274, TEXIO). The applied voltage and discharge current were measured using a high-voltage probe (PHV4-1221, PMK) and a current probe (FCT-028-5.0-WB, Bergoz), respectively. Waveforms were monitored using an oscilloscope (waveRunner 62Xi, Lecroy). A tungsten needle electrode (0.5 mm in diameter) covered with an insulation tube (011, TKG) was set at the center of a 35-mm diameter cell culture dish (3000-035 or 3910-35, Iwaki) or 96-well cell culture plate (353072, BD Falcon). The dish or plate was filled with 2 mL or 40  $\mu$ L, respectively, of phosphate buffered saline (PBS; 05913, Nissui) containing Mg<sup>++</sup> and Ca<sup>++</sup> (PBS(+)). The distance from a liquid surface to the tip of the electrode was 1 mm (for the 35-mm diameter dish) or 0.5 mm (for

the 96-well plate), respectively. The rectangular-wave voltage applied to the tungsten needle electrode was +5.5 kV from 0 to peak, with a frequency of 100 Hz and a duty ratio of 50%.

**2.2. Measurement of Characteristics of Micropower Plasma and Chemical Species.** Light emitted from the plasma was captured using a digital camera (D4, Nikon) equipped with a macrolens (AF Micro-Nikkor 200 mm f/4D IF-ED, Nikon). The exposure time was 10 s, ISO sensitivity was 1600, and the diaphragm of the camera was 4. Emission spectra were measured using a multichannel optical spectrometer (PMA-12, Hamamatsu Photonics). The range of measured wavelength was from 200 nm to 860 nm. The distance from the part of plasma discharge to the spectrometer was 5 cm. Temperature of the generated plasma was estimated from the vibrational and rotational temperatures of nitrogen molecule ( $N_2$ ), which were calculated with the measured spectral lines of  $N_2$ -second positive system (SPS) and an analysis software [15].

The pH of the solution was measured using a pH meter (twin pH, AS ONE). The temperature of the solution was measured using a thermocouple (T/T-E40-1, Ishikawa Trading) and a temperature controller (E5CN-HQ2, OMRON).

Concentrations of dissolved hydrogen peroxide ( $H_2O_2$ ), nitrous acid ( $HNO_2$ ), and nitric acid ( $HNO_3$ ) in the solution were measured using a water quality meter (DPM-MT, Kyoritsu Chemical-Check Laboratories). The reagent containing 4-aminoantipyrine (WAK-H2O2, Kyoritsu Chemical-Check Laboratories) or naphthylethylenediamine (WAK-NO2 or WAK-NO3, Kyoritsu Chemical-Check Laboratories) was added into the plasma-treated solution. The mixture of the plasma-treated solution and the reagent was gently shaken ten times, and the color of the mixture was then changed by the reaction between the reagent and the chemicals dissolved in the solution. The colored mixture put into the quality meter.

**2.3. Cell Culture.** Human umbilical vein endothelial cells (HUVECs; 200K-05n, Cell Applications) from the fourth to eighth passages were used for the experiments in this study. HUVECs were cultured in the 35-mm diameter dish or the 96-well plate that were precoated with 0.1% bovine gelatin (G9391, Sigma-Aldrich). HUVECs were cultured in Medium 199 (M199; 31100035, Gibco) containing 20% heat-inactivated fetal bovine serum (FBS; 12483020, Gibco), 10  $\mu$ g/L human basic fibroblast growth factor (bFGF; GF-030-3, AUSTRAL Biologicals), and 0.1% penicillin/streptomycin (P/S; 15140122, Gibco) (growth medium (GM)). After experiments, HUVECs were maintained in M199 containing 10% heat-inactivated FBS and 0.1% P/S (maintenance medium (MM)).

**2.4. Cell Viability Assay.** HUVECs were seeded into the 96-well plate at 2000 cells/well and then were incubated in the GM for 24 hours. After incubation in the MM for 1 hour, the cells were washed twice with PBS(+) to remove bFGF and FBS. The 96-well plate was filled with 40  $\mu$ L of PBS(+), and the cells were then treated with the micropower plasma, as illustrated in Figure 1(c). The distance from the liquid surface to the tip of the electrode was 0.5 mm. The

plasma irradiation time was 0, 30, 60, 90, 120, 180, 300, or 420 s. The cells were washed twice with the MM immediately after plasma treatment. After 24-hour incubation, the cells were stained with 10  $\mu$ L/well of the Cell Count Reagent SF (07553-15, Nacalai tesque) for 1 hour. Absorbance of the cells was measured at 450 nm using a microplate reader (Model 680 XR, Bio-Rad). The ratio of live cells was calculated according to the formula: ratio of viable cells = plasma-treated sample/control (nontreated sample).

**2.5. Measurement of ROS in the Plasma-Treated Cells.** HUVECs were cultured in the 35-mm diameter dish to reach 80% confluence. After incubation with 10  $\mu$ M 2',7'-dichlorodihydrofluorescein diacetate (DCFH-DA; 35845, Sigma-Aldrich) in the GM for 50 min, the GM was washed out using PBS(+). The dish was filled with 2 mL of PBS(+), and the cells were then treated with the micropower plasma. The distance from the liquid surface to the tip of the electrode was 1 mm. The plasma irradiation time was 0, 60, 180, 420, or 600 s. The cells were washed twice with PBS(+) immediately after plasma treatment. The cells were incubated in the MM for 15 min, and the fluorescent images of ROS in the cells were then observed using an inverted fluorescence microscope (Axio Observer D1; Carl Zeiss). The fluorescent intensity of ROS in the cells was evaluated with the ImageJ software (US National Institutes of Health). On the other hand, the fluorescent intensity of ROS in the plasma-treated cells was also measured using a flow cytometer (guava easyCyte™ HT, Merck Millipore). After plasma treatment, the cells were incubated in the MM for 15 min. The cells were harvested with 0.05% Trypsin-EDTA (25300054, Gibco) and spin down at 1000 rpm for 5 min. The cells were resuspended in 150  $\mu$ L of PBS(+), and the fluorescent intensity of ROS in 5000 of the cells was measured at 488 nm using the flow cytometer. As a control experiment, the cells were treated with PBS(+) containing  $H_2O_2$  (081-04215, Wako Pure Chemical Industries) for 600 s.

**2.6. Evaluation of Nuclear Factor-Kappa B (NF- $\kappa$ B) Activation.** HUVECs were cultured in the 35-mm diameter dish to reach 80% confluence. The cells were washed twice with PBS(+). The dish was filled with 2 mL of PBS(+), and the cells were then treated with the micropower plasma. The distance from the liquid surface to the tip of the electrode was 1 mm. The plasma irradiation time was 300 s. The cells were washed twice with PBS(+) immediately after plasma treatment. The cells were incubated in the MM for 0, 15, 30, and 45 min and then fixed with ice-cold methanol for 10 min at  $-20^\circ$ C. The cells were subsequently treated with 0.3% TritonX-100 (17-1315-01, Pharmacia Biotech) and 1% Block Ace (BA; UKB40, DS Pharma Biomedical) for 1 hour at room temperature for membrane permeabilization and blocking of nonspecific adsorption of antibody. They were then incubated in the rabbit NF- $\kappa$ B p65 antibody (1:300 diluted in PBS containing 1% BA, sc-372, Santa Cruz Biotechnology) for 1 hour. After washing with PBS, they were incubated in Alexa Fluor 488 goat anti-rabbit secondary antibody (1:1000 diluted in PBS, A-11034, Invitrogen) for 2 hours. Cell nucleus was stained with 1  $\mu$ g/mL 4',6-diamidino-2-phenylindole (DAPI; D1306,

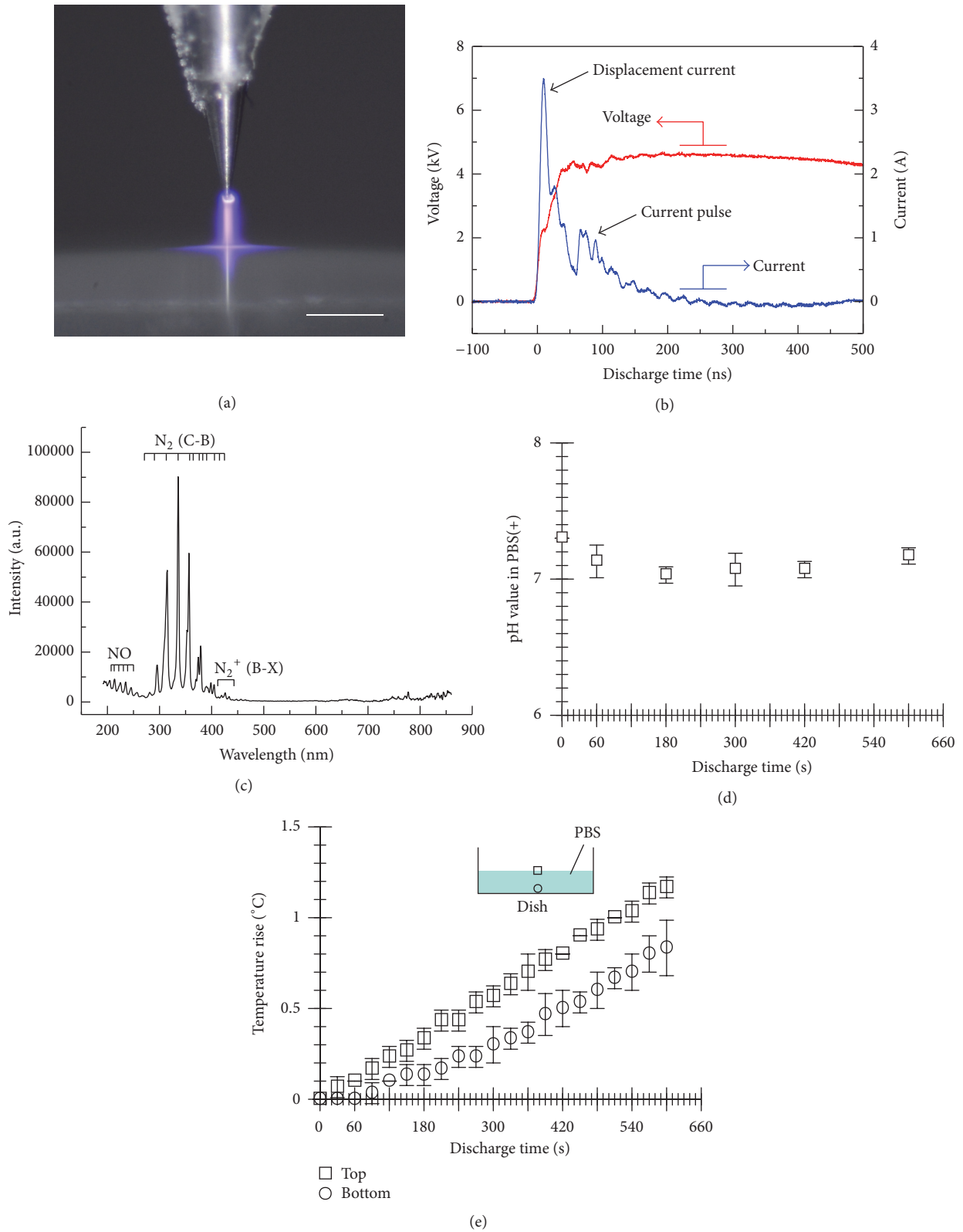


FIGURE 2: Characteristics of the micropower plasma. (a) Photograph of light emitted by the micropower plasma generated at the gas-PBS(+) interface. Bar is 500  $\mu$ m. (b) Waveforms of the applied voltage and discharge current. (c) Emission spectra of the plasma discharge at the gas-PBS(+) interface. (d) Changes in pH in the plasma-treated PBS(+) as a function of discharge time ( $n = 3$ , mean  $\pm$  SD). (e) Changes in temperature of the plasma-treated PBS(+) with the discharge time ( $n = 3$ , mean  $\pm$  SD).

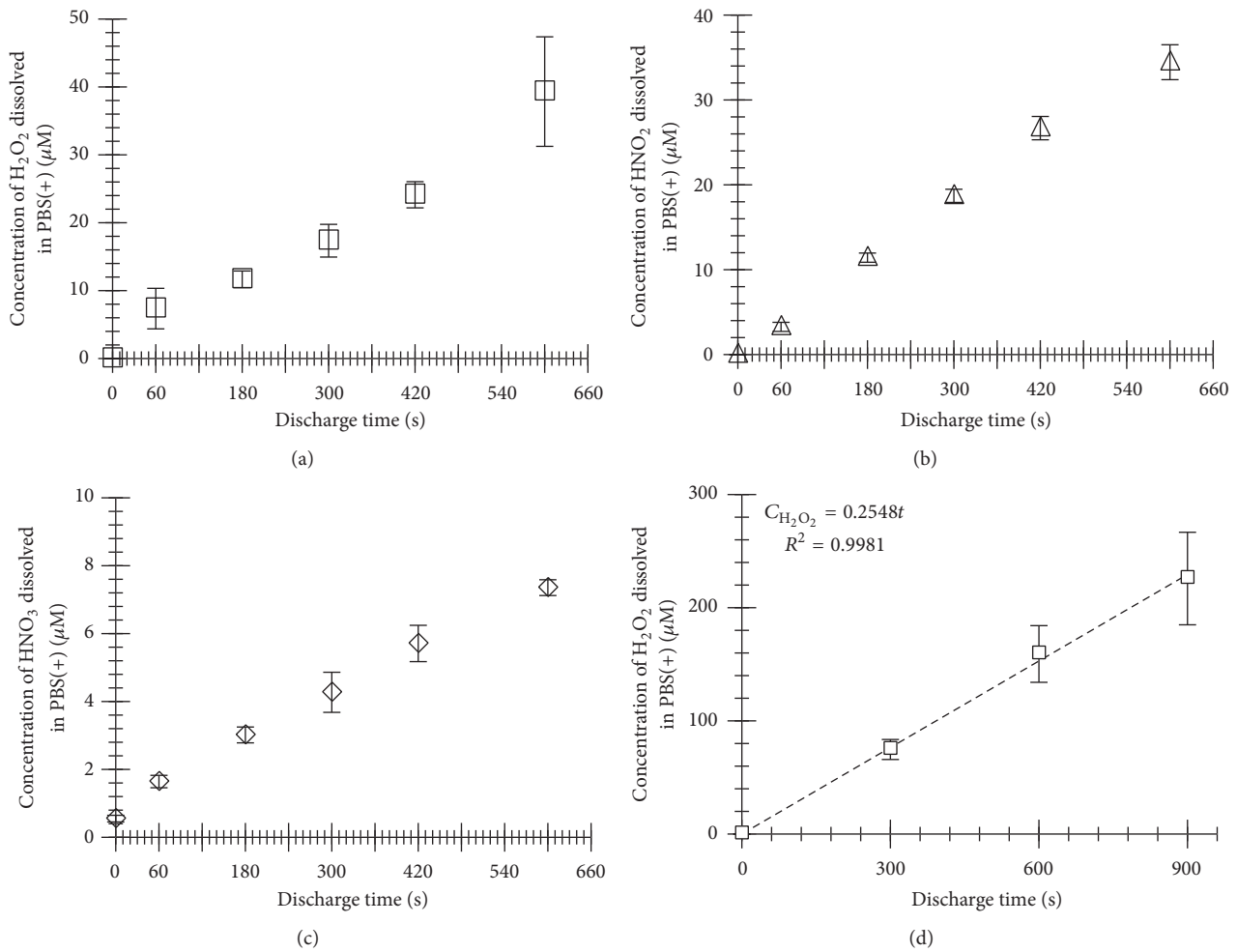


FIGURE 3: Concentrations of the dissolved H<sub>2</sub>O<sub>2</sub> (a), HNO<sub>2</sub> (b), and HNO<sub>3</sub> (c) into the plasma-treated PBS(+) in a 35-mm diameter dish or the dissolved H<sub>2</sub>O<sub>2</sub> (d) into PBS(+) in a 96-well plate, as a function of the discharge time ( $n = 3$ , mean  $\pm$  SD).

Life Technologies) for 5 min. The fluorescent images of the stained cells were observed using the inverted fluorescence microscope. Localization of NF- $\kappa$ B p65 in the cells was evaluated based on the fluorescent intensity using the ImageJ software. Percentage of NF- $\kappa$ B p65 translocated into the cell nucleus was calculated according to the formula: % of NF- $\kappa$ B p65 translocation (i.e., NF- $\kappa$ B activation) = (fluorescent intensity of NF- $\kappa$ B p65 in the cell nucleus/fluorescent intensity of NF- $\kappa$ B p65 in the whole cell)  $\times$  100. As a control experiment, the cells were treated with PBS(+) containing H<sub>2</sub>O<sub>2</sub> for 300 s. We used catalase (C9322, Sigma-Aldrich) to inhibit influence of H<sub>2</sub>O<sub>2</sub> generated by the plasma discharge on the cells.

**2.7. Statistical Analysis.** All values are shown as mean  $\pm$  standard deviation (SD) unless stated otherwise. The statistical significance was determined using an analysis of unequal variances two-tailed  $t$ -test (Welch's  $t$ -test), with significance set at  $P < 0.05$  and  $P < 0.01$ .

### 3. Results

**3.1. Characteristics of Micropower Plasma and Production of Chemical Species.** Figure 2 shows characteristics of the micropower plasma generated at the gas-liquid interface. A photograph of plasma emission at the gas-liquid interface is shown in Figure 2(a). The applied voltage rose up to +5.5 kV with a rise time of 100 ns, and 3.5 A of displacement current and about 1.2 A of the current pulse were observed, as shown in typical waveforms of the applied voltage and the discharge current (Figure 2(b)). The power input  $W$  per cycle was 0.018 W, which was calculated from the following equation:

$$W = \frac{1}{T} \int_0^T v(t) i(t) dt. \quad (1)$$

Here,  $v(t)$  and  $i(t)$  represent the applied voltage and the discharge current, respectively, and  $T$  represents the cycle length.

Figure 2(c) shows emission spectra of the plasma discharge at the gas-liquid interface. Emission peaks attributed

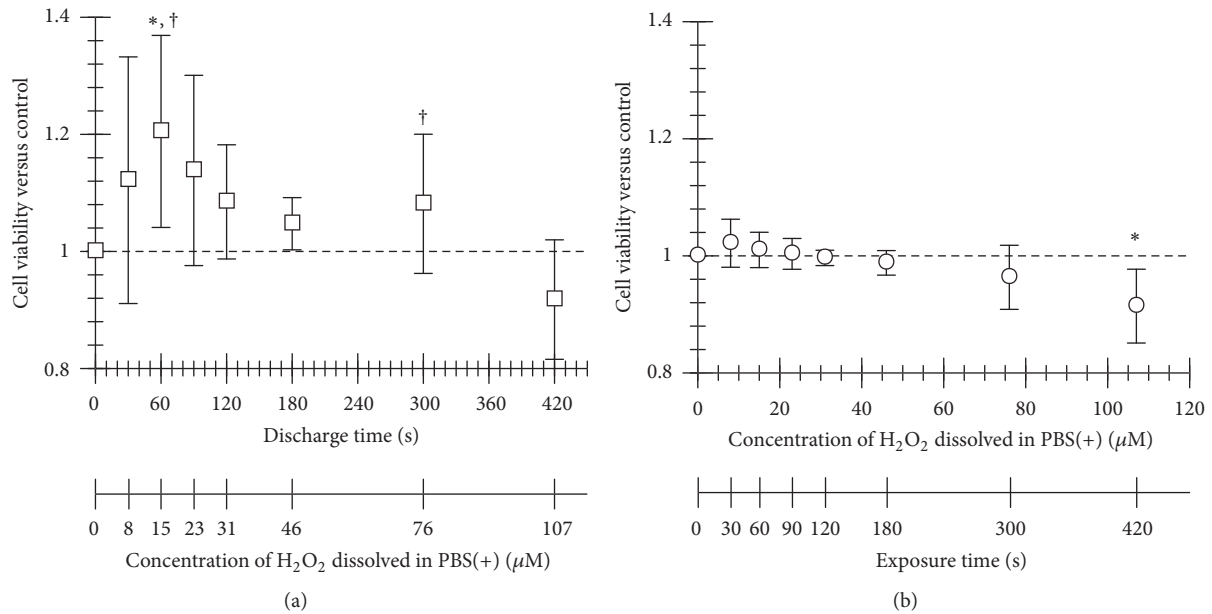


FIGURE 4: Effect of the micropower plasma treatment on proliferation in HUVECs. (a) Cell viability after the plasma treatment and 24-hour incubation ( $n = 3$ , mean  $\pm$  SD). (b) Cell viability after the treatment of H<sub>2</sub>O<sub>2</sub>, with the concentration corresponding to the plasma treatment condition and 24-hour incubation ( $n = 3$ , mean  $\pm$  SD). The viability of the cells shows a significant difference between the plasma- and H<sub>2</sub>O<sub>2</sub>-treated conditions ( $^{\dagger}P < 0.05$  versus H<sub>2</sub>O<sub>2</sub>-treated condition at the point with same time and concentration of H<sub>2</sub>O<sub>2</sub>).  $^*P < 0.05$  versus the viability before the treatment (0 s or 0  $\mu$ M).

to NO $\gamma$  (222.2~272.2 nm), N<sub>2</sub>-SPS, and N<sub>2</sub><sup>+</sup>-first negative system (FNS) (295.3~457.4 nm) were observed [16, 17]. Based on the observed emission spectra, the vibrational and rotational temperatures of N<sub>2</sub> were calculated as 0.32 eV and 0.10 eV, respectively.

The change in pH in the PBS(+) as a function of plasma discharge time is shown in Figure 2(d). The pH in the PBS(+) decreased slightly, from 7.3 to 7.0, and was maintained about 7.0 over the 600 s discharge time. The temperature at the top surface of PBS(+) and the bottom surface in the dish rose monotonically with the discharge time as shown in Figure 2(e). The temperature rises were up to 1.2°C at the top surface of PBS(+) and 0.8°C at the bottom surface in the dish, respectively, by the discharge for 600 s. The temperature at the top surface of PBS and the bottom surface in the dish rose 0.5 and 0.2°C, respectively, by 300 s of the plasma discharge.

Changes in the concentrations of H<sub>2</sub>O<sub>2</sub>, HNO<sub>2</sub>, and HNO<sub>3</sub> dissolved into the PBS(+) in the 35-mm diameter dish with plasma discharge time are shown in Figures 3(a)–3(c). The concentrations of dissolved H<sub>2</sub>O<sub>2</sub>, HNO<sub>2</sub>, and HNO<sub>3</sub> increased linearly during the plasma discharge for 600 s. Assuming the experiments using the cells cultured in 96-well plate, we also measured changes in the concentration of dissolved H<sub>2</sub>O<sub>2</sub> with the discharge time for the PBS(+) in the 96-well plate, as shown in Figure 3(d). In the case of using the 96-well plate, the concentrations of dissolved H<sub>2</sub>O<sub>2</sub> also increased linearly with the discharge time. Based on that result, we adjusted the concentration of H<sub>2</sub>O<sub>2</sub> to which the cells were exposed.

**3.2. Cell Viability, ROS in the Cells, and NF- $\kappa$ B Activation after Treatment of Micropower Plasma.** The plasma-generated H<sub>2</sub>O<sub>2</sub> is, reportedly, a key factor to induce various responses to the plasma generated at an interface between gas and liquid phases [18]. Thus, we also compared the effects of plasma treatment on the cells with that of H<sub>2</sub>O<sub>2</sub> treatment in the present study. As shown in Figure 4(a), the viability of the plasma-treated HUVECs increased and reached to the peak value by 60 s of the discharge time. Here, the concentration of H<sub>2</sub>O<sub>2</sub> dissolved in PBS(+) was 15  $\mu$ M. At this point, the viability of the cells shows a significant difference between the plasma- and H<sub>2</sub>O<sub>2</sub>-treated conditions ( $P < 0.05$ , Figures 4(a) and 4(b)). The plasma-treated condition also resulted in significant increases in the cell viability, in comparison with that of the cells before treatment ( $P < 0.05$ , Figure 4(a)). For the discharge time longer than 60 s, the viability gradually decreased down to 0.87. As a control experiment, we exposed the cells to PBS(+) containing H<sub>2</sub>O<sub>2</sub> with the concentration corresponding to that of the plasma-treated PBS(+). In contrast to the plasma-treated cells, although the viability of the cells exposed to H<sub>2</sub>O<sub>2</sub> increased slightly for the conditions of low concentrated H<sub>2</sub>O<sub>2</sub>, it decreased monotonically, as shown in Figure 4(b).

The ROS in the plasma-treated HUVECs linearly increased with the discharge time, as shown in Figures 5(a) and 5(b). The 9-fold increase in the fluorescence ROS intensity of the plasma-treated cells was found at 600 s of the discharge time, in comparison with the nontreated cells. The fluorescence intensity of ROS in the cells treated with the

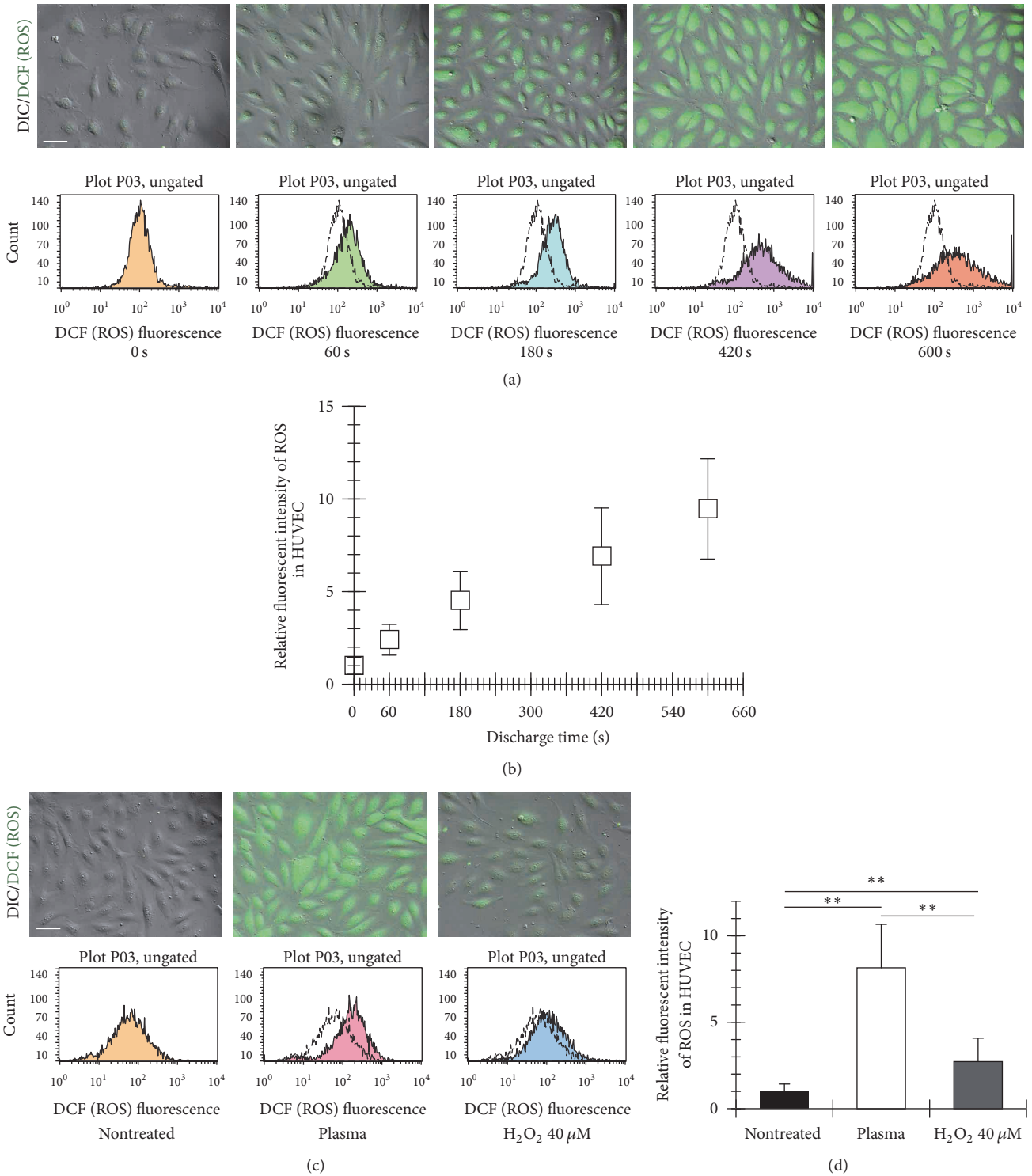


FIGURE 5: Fluorescence ROS intensity in HUVECs after the micropower plasma treatment. (a) Series of fluorescent images of ROS in the cells and representative histograms of ROS intensity from 5000 cells, measured using the flow cytometer after the plasma treatment and 15-min incubation in the MM. (b) ROS in the cells was expressed as the relative intensity. The basal value in the sample before the plasma treatment was taken as 1. The data shown were represented as mean  $\pm$  SD ( $n = 3, 148$  cells). (c) Representative fluorescent images of ROS in the cells treated with the micropower plasma and  $40 \mu\text{M}$   $\text{H}_2\text{O}_2$  for 600 s and representative histograms of ROS intensity from 5000 cells. (d) ROS in the cells treated with the micropower plasma or  $40 \mu\text{M}$   $\text{H}_2\text{O}_2$  for 600 s was expressed as the relative intensity. The basal value in the nontreated sample was taken as 1. The data shown were represented as mean  $\pm$  SD ( $n = 3, 147$  cells). The plasma treatment resulted in a significant increase in production of ROS in the cells (\*\*  $P < 0.01$  versus control and treatment of  $\text{H}_2\text{O}_2$ ).

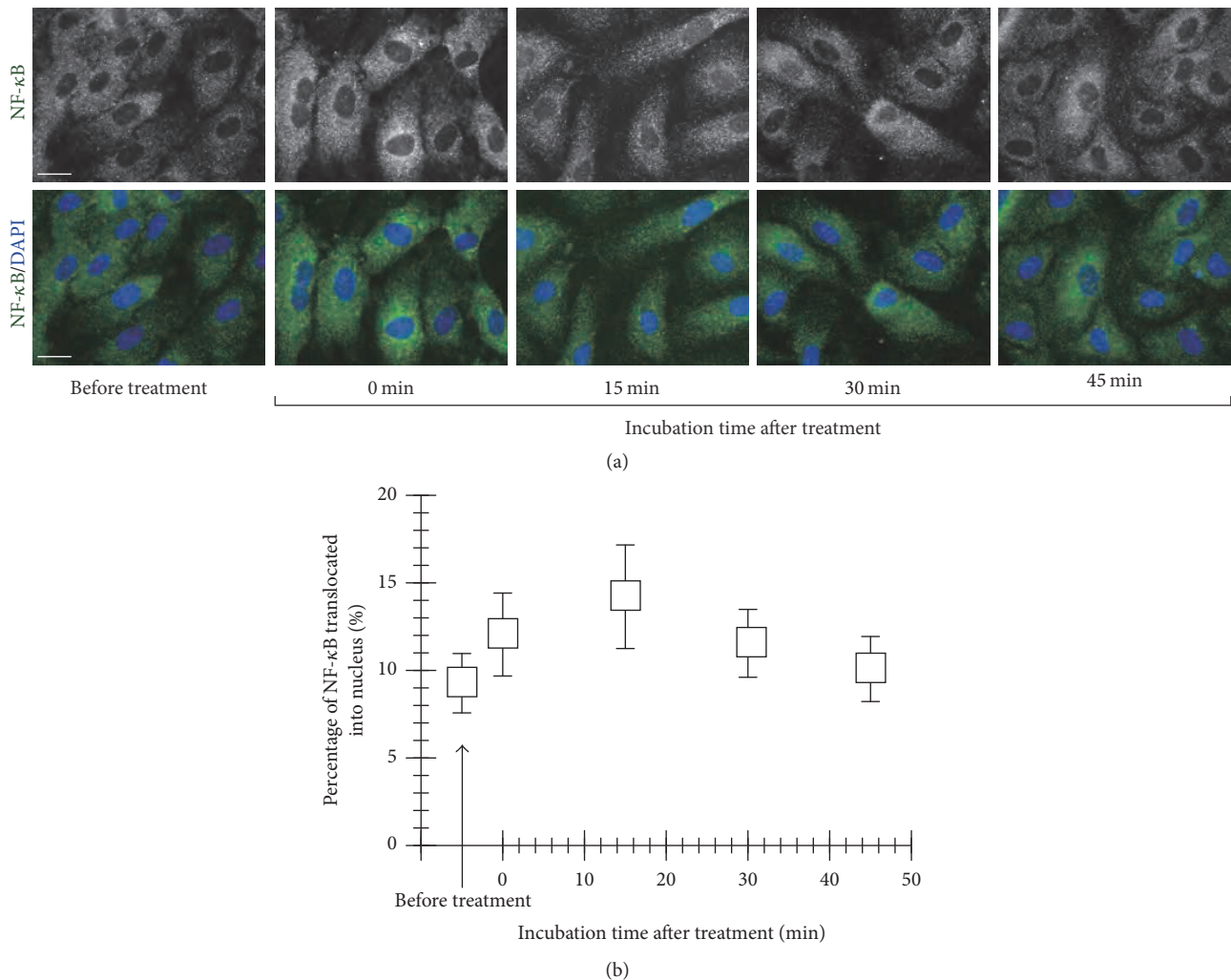


FIGURE 6: Activation of NF- $\kappa$ B in HUVECs induced by the micropower plasma treatment. (a) Series of fluorescent images of NF- $\kappa$ B in the cells after the plasma treatment for 300 s and incubation in the MM for 0, 15, 30, and 45 min. (b) Changes in percentage of NF- $\kappa$ B translocated into cell nucleus with incubation time after the plasma treatment. The data shown were represented as mean  $\pm$  SD for at least 50 cells.

plasma discharge for 600 s was 3-fold higher than that under the condition exposed to  $H_2O_2$ , as indicated in Figures 5(c) and 5(d). The concentration of  $H_2O_2$  was  $40 \mu M$ .

NF- $\kappa$ B is known to control cell death and survival decisions in cells. If the NF- $\kappa$ B is activated, the activated NF- $\kappa$ B translocates into the cell nucleus and results in the transcription of genes for cellular response such as cell death, survival, and growth [19]. Thus, focusing on translocation of NF- $\kappa$ B into the nucleus, we can evaluate activation of NF- $\kappa$ B indirectly. Based on the fluorescent images of NF- $\kappa$ B p65 in the HUVECs for 0, 15, 30, and 45-min incubations after treatment of the plasma for 300 s (Figure 6(a)), we evaluated the translocation of NF- $\kappa$ B p65 into the cell nucleus, as shown in Figure 6(b). Percentage of NF- $\kappa$ B p65 translocation into the cell nucleus reached to the peak value (14%) by 15 min after treatment of the plasma, and then it decreased down to the level equivalent to before treatment. The concentration of  $H_2O_2$  generated by the plasma discharge for 300 s was  $15 \mu M$ . Here, the nuclear translocation of NF- $\kappa$ B p65 in the

cells exposed to PBS(+) containing  $15 \mu M H_2O_2$  for 300 s was confirmed to be lower than that in the plasma-treated cells (Figure 7(a)). It shows a significant difference between the plasma- and  $H_2O_2$ -treated conditions (Figure 7(b)). In the case of decomposition of  $H_2O_2$  with 50 unit/mL catalase, the nuclear translocation of NF- $\kappa$ B p65 in the cells induced by the plasma treatment was not confirmed as shown in Figures 7(c) and 7(d). These results suggest the plasma-generated  $H_2O_2$  in PBS(+) was a main factor for the nuclear translocation of NF- $\kappa$ B p65 in the plasma-treated HUVECs.

## 4. Discussion

**4.1. Performance of the Micropower Plasma.** In the present study, we used the micropower plasma with 0.018 W of the power input per cycle. The micropower plasma was able to generate small amount of the chemical species. The concentrations of the dissolved  $H_2O_2$ ,  $HNO_2$ , and  $HNO_3$

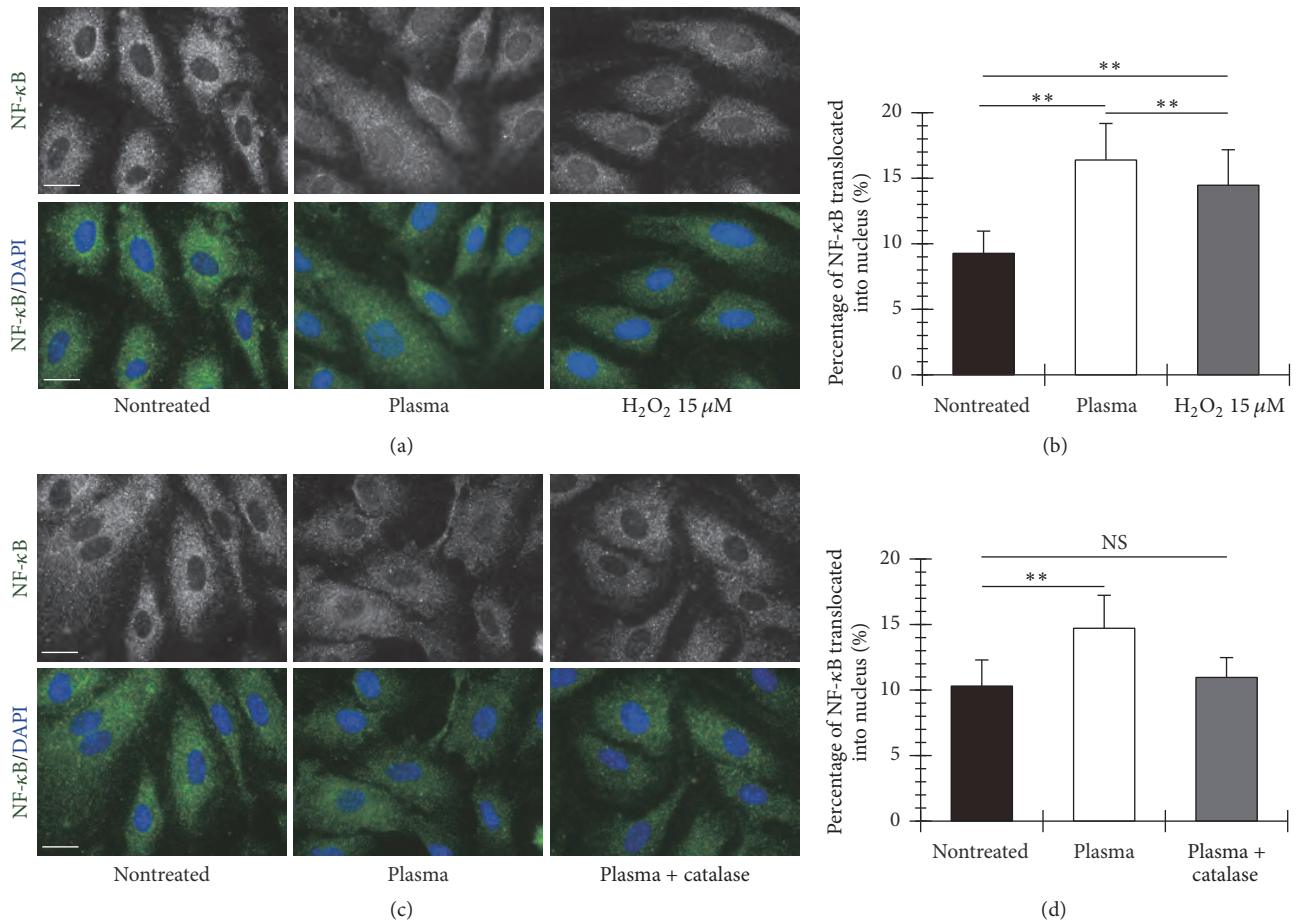


FIGURE 7: H<sub>2</sub>O<sub>2</sub> generated by the micropower plasma is required for activation of NF-κB in the HUVECs. (a) Percentage of nuclear translocation of NF-κB in the cells treated with the micropower plasma or 15 μM H<sub>2</sub>O<sub>2</sub> for 300 s. The data shown were represented as mean ± SD for at least 55 cells. The plasma treatment resulted in a significant increase in the nuclear translocation of NF-κB in the cells (\*\**P* < 0.01 versus control and treatment of H<sub>2</sub>O<sub>2</sub>). (b) Percentage of nuclear translocation of NF-κB in the cells treated with the micropower plasma with/without 50 unit/mL catalase. The data shown were represented as mean ± SD for at least 57 cells. No difference in the percentage of nuclear translocation of NF-κB was observed between the nontreated and the plasma-treated conditions when H<sub>2</sub>O<sub>2</sub> was decomposed by using catalase.

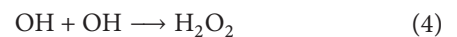
increased linearly during 600 s plasma discharge. The pH in PBS(+) showed little change after treatment of the plasma. The temperature rise in PBS(+) was up to 0.8°C at the bottom surfaces in the dish. This temperature rise is considered to have little influence on endothelial cells. This notion is supported by the report that the viability of HUVECs was not affected by heat stress at 39°C [20]. The micropower plasma can expose living cells to various reactive chemical species without harmful effects of heat and change in pH, in comparison with the plasma at the gas-liquid interface used in the previous studies [9–14].

Various chemical reactions are considered to occur during the plasma at gas-liquid interface [21, 22]. It is assumed that HNO<sub>2</sub> and HNO<sub>3</sub>, which were detected in the plasma-treated PBS(+) in this study, were generated in a gas phase and then dissolved into the PBS(+). These chemical species were formed by reacting NO and NO<sub>2</sub> with OH, as shown in the following reactions. NO and NO<sub>2</sub> were generated by

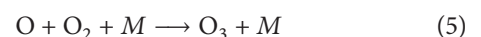
the plasma discharge in the gas phase. OH was generated by disassociation of H<sub>2</sub>O.



Here, *M* indicates the third body, which is typically N<sub>2</sub> or O<sub>2</sub>. On the other hand, H<sub>2</sub>O<sub>2</sub> was produced by the following reaction between OH groups. The OH group was generated by the disassociation of H<sub>2</sub>O due to the plasma at the gas-liquid interface [23].



In addition, the micropower plasma might produce O<sub>3</sub> according to the following reaction [24]. The oxygen atom is generated by the plasma discharge.



**4.2. Effects of Micropower Plasma on HUVECs.** The results of the present study demonstrate that the short-time treatment of the micropower plasma enhances proliferation activity of HUVECs. The treatment of H<sub>2</sub>O<sub>2</sub> with the concentration equivalent to that generated by the plasma, in contrast, does not enhance the cell proliferation. The ROS production and the NF- $\kappa$ B activation due to the plasma treatment may play important roles for enhancement of the cell proliferation. This notion is supported by the findings that there were differences in the ROS production and NF- $\kappa$ B activation, which was mainly induced by H<sub>2</sub>O<sub>2</sub>, in the cells between the plasma- and H<sub>2</sub>O<sub>2</sub>-treated conditions.

The fluorescence intensity of ROS in the cells treated with the plasma was much larger than that under the condition exposed to H<sub>2</sub>O<sub>2</sub>. Plasma is known to induce cell permeabilization [25]. The influx of the H<sub>2</sub>O<sub>2</sub> generated by the plasma into the cells was, thus, increased due to permeabilization of the cell membrane for the treatment of plasma discharge. In addition, HNO<sub>2</sub> and HNO<sub>3</sub> generated by the plasma discharge are considered to have no small effect on increase in the ROS production in the cells by the plasma treatment.

Several studies have examined enhancement of proliferation in the vascular endothelial cells by nonthermal plasma [7, 8, 26]. Most of the mechanisms by which proliferation activity of the cells is enhanced are still unclear. The present study focused on the ROS production and the following NF- $\kappa$ B activation after treatment of the plasma as the mechanism leading to the cell proliferation. NF- $\kappa$ B is known to regulate many important cellular behaviors, such as inflammatory responses, cellular growth, and apoptosis [27, 28]. Reportedly, NF- $\kappa$ B also regulates the expression of cyclin D1, which promotes cell cycle progression [29]. The activation of NF- $\kappa$ B is caused by the ROS stimulation including H<sub>2</sub>O<sub>2</sub> [30]. Increase in production of H<sub>2</sub>O<sub>2</sub> by mitochondrion is known to enhance the activation of NF- $\kappa$ B in the vascular endothelial cells [31]. These results reported in the previous studies can support our notion that the ROS production and the NF- $\kappa$ B activation due to the plasma treatment may play important roles for enhancement of the cell proliferation.

## Disclosure

The present affiliation for Kotaro Suzuki is Sumitomo Electric Industries, Ltd., 4-5-33, Kitahama, Chuo, Osaka 541-0041, Japan.

## Competing Interests

Kotaro Suzuki and Daisuke Yoshino declare that they have no conflict of interests.

## Acknowledgments

The authors thank Professor Takehiko Sato and Mr. Tomoki Nakajima (Institute of Fluid Science, Tohoku University, Japan) for technical support and their advises.

## References

- [1] G. Fridman, A. D. Brooks, M. Balasubramanian et al., "Comparison of direct and indirect effects of non-thermal atmospheric-pressure plasma on bacteria," *Plasma Processes and Polymers*, vol. 4, no. 4, pp. 370–375, 2007.
- [2] D. Yoshino, K. Nakamura, T. Nakajima, and T. Sato, "Development of low-temperature sterilization device using atmospheric pressure air plasma with circulating flow," *Mechanical Engineering Journal*, vol. 2, no. 5, 2015.
- [3] J. L. Lauer, J. L. Shohet, R. M. Albrecht et al., "Reduced adhesion of human blood platelets to polyethylene tubing by microplasma surface modification," *Journal of Applied Physics*, vol. 96, no. 8, pp. 4539–4546, 2004.
- [4] G. Fridman, M. Peddinghaus, H. Ayan et al., "Blood coagulation and living tissue sterilization by floating-electrode dielectric barrier discharge in air," *Plasma Chemistry and Plasma Processing*, vol. 26, no. 4, pp. 425–442, 2006.
- [5] G. Fridman, G. Friedman, A. Gutsol, A. B. Shekhter, V. N. Vasilets, and A. Fridman, "Applied plasma medicine," *Plasma Processes and Polymers*, vol. 5, no. 6, pp. 503–533, 2008.
- [6] T. G. Beuthe and J. S. Chang, "Ch. 9 Gas discharge phenomena," in *Handbook of Electrostatic Processes*, J. S. Chang, A. J. Kelly, and J. Crowley, Eds., Marcel Dekker, New York, NY, USA, 1995.
- [7] C. Tsutsui, T. Hirata, Y. Yokoi et al., "Effect of neoangiogenesis using micro-spot plasma," *Journal of the Institute of Electrostatics*, vol. 36, no. 4, pp. 235–240, 2012 (Japanese).
- [8] K. P. Arjunan, G. Friedman, A. Fridman, and A. M. Clyne, "Non-thermal dielectric barrier discharge plasma induces angiogenesis through reactive oxygen species," *Journal of the Royal Society Interface*, vol. 9, no. 66, pp. 147–157, 2012.
- [9] K. D. Weltmann, E. Kinde, T. von Woedtke, M. Hähnel, M. Stieber, and R. Brandenburg, "Atmospheric-pressure plasma sources: prospective tools for plasma medicine," *Pure and Applied Chemistry*, vol. 82, no. 6, pp. 1223–1237, 2010.
- [10] P. Bruggeman, E. Ribel, A. Maslani et al., "Characteristics of atmospheric pressure air discharges with a liquid cathode and a metal anode," *Plasma Sources Science and Technology*, vol. 17, no. 2, Article ID 025012, 2008.
- [11] P. Bruggeman, J. L. Walsh, D. C. Schram, C. Leys, and M. G. Kong, "Time dependent optical emission spectroscopy of sub-microsecond pulsed plasmas in air with water cathode," *Plasma Sources Science and Technology*, vol. 18, no. 4, Article ID 045023, 2009.
- [12] P. Bruggeman, L. Graham, J. Degroote, J. Vierendeels, and C. Leys, "Water surface deformation in strong electrical fields and its influence on electrical breakdown in a metal pin-water electrode system," *Journal of Physics D: Applied Physics*, vol. 40, no. 16, article 007, pp. 4779–4786, 2007.
- [13] P. Bruggeman, J. Liu, J. Degroote, M. G. Kong, J. Vierendeels, and C. Leys, "Dc excited glow discharges in atmospheric pressure air in pin-to-water electrode systems," *Journal of Physics D: Applied Physics*, vol. 41, no. 21, Article ID 215201, 2008.
- [14] T. Shimizu, Y. Iwafuchi, G. E. Morfill, and T. Sato, "Formation of thermal flow fields and chemical transport in air and water by atmospheric plasma," *New Journal of Physics*, vol. 13, Article ID 053025, 2011.
- [15] T. Sakamoto, H. Matsuura, and H. Akatsuka, "Spectroscopic study on the vibrational populations of N<sub>2</sub>C<sup>3</sup>Π and B<sup>3</sup>Π states in a microwave nitrogen discharge," *Journal of Applied Physics*, vol. 101, no. 2, Article ID 023307, 2007.

- [16] R. W. B. Pearse and A. G. Gaydon, *The Identification of Molecular Spectra*, John Wiley & Sons, New York, NY, USA, 1950.
- [17] A. Kramida, Y. Ralchenko, J. Reader, and NIST ASD Team, *NIST Atomic Spectra Database ver. 5.2*, National Institute of Standards and Technology, Gaithersburg, Md, USA, 2014.
- [18] T. Sato, M. Yokoyama, and K. Johkura, "A key inactivation factor of HeLa cell viability by a plasma flow," *Journal of Physics D: Applied Physics*, vol. 44, no. 37, Article ID 372001, 2011.
- [19] J. S. Tilstra, C. L. Clauson, L. J. Niedernhofer, and P. D. Robbins, "NF- $\kappa$ B in aging and disease," *Aging and Disease*, vol. 2, no. 6, pp. 449–465, 2011.
- [20] Z. T. Gu, H. Wang, L. Li et al., "Heat stress induces apoptosis through transcription-independent p53-mediated mitochondrial pathways in human umbilical vein endothelial cell," *Scientific Reports*, vol. 4, article 4469, 2014.
- [21] I. A. Kossyi, A. Y. Kostinsky, A. A. Matveyev, and V. P. Silakov, "Kinetic scheme of the non-equilibrium discharge in nitrogen-oxygen mixtures," *Plasma Sources Science and Technology*, vol. 1, no. 3, pp. 207–220, 1992.
- [22] A. C. Gentile and M. J. Kushner, "Reaction chemistry and optimization of plasma remediation of  $N_xO_y$  from gas streams," *Journal of Applied Physics*, vol. 78, no. 3, pp. 2074–2085, 1995.
- [23] P. Baroch, N. Saito, and O. Takai, "Special type of plasma dielectric barrier discharge reactor for direct ozonization of water and degradation of organic pollution," *Journal of Physics D: Applied Physics*, vol. 41, no. 8, Article ID 085207, 2008.
- [24] S. B. Gupta and H. Bluhm, "The potential of pulsed underwater streamer discharges as a disinfection technique," *IEEE Transactions on Plasma Science*, vol. 36, no. 4, pp. 1621–1632, 2008.
- [25] S. Sasaki, R. Honda, Y. Hokari, K. Takashima, M. Kanzaki, and T. Kaneko, "Characterization of plasma-induced cell membrane permeabilization: focus on OH radical distribution," *Journal of Physics D: Applied Physics*, vol. 49, no. 33, p. 334002, 2016.
- [26] S. Kalghatgi, G. Friedman, A. Fridman, and A. M. Clyne, "Endothelial cell proliferation is enhanced by low dose non-thermal plasma through fibroblast growth factor-2 release," *Annals of Biomedical Engineering*, vol. 38, no. 3, pp. 748–757, 2010.
- [27] M. Barkett and T. D. Gilmore, "Control of apoptosis by Rel/NF- $\kappa$ B transcription factors," *Oncogene*, vol. 18, no. 49, pp. 6910–6924, 1999.
- [28] R. E. Bellas, J. S. Lee, and G. E. Sonenshein, "Expression of a constitutive NF-kappa B-like activity is essential for proliferation of cultured bovine vascular smooth muscle cells," *The Journal of Clinical Investigation*, vol. 96, no. 5, pp. 2521–2527, 1995.
- [29] M. Hinz, D. Krappmann, A. Eichten, A. Heder, C. Scheidereit, and M. Strauss, "NF- $\kappa$ B function in growth control: regulation of cyclin D1 expression and G0/G1-to-S-phase transition," *Molecular and Cellular Biology*, vol. 19, no. 4, pp. 2690–2698, 1999.
- [30] R. Schreck, P. Rieber, and P. A. Baeuerle, "Reactive oxygen intermediates as apparently widely used messengers in the activation of the NF- $\kappa$ B transcription factor and HIV-1," *EMBO Journal*, vol. 10, no. 8, pp. 2247–2258, 1991.
- [31] Z. Ungvari, Z. Orosz, N. Labinskyy et al., "Increased mitochondrial  $H_2O_2$  production promotes endothelial NF- $\kappa$ B activation in aged rat arteries," *American Journal of Physiology—Heart and Circulatory Physiology*, vol. 293, no. 1, pp. H37–H47, 2007.

## Review Article

# The Circadian NAD<sup>+</sup> Metabolism: Impact on Chromatin Remodeling and Aging

**Yasukazu Nakahata and Yasumasa Bessho**

*Laboratory of Gene Regulation Research, Graduate School of Biological Sciences, Nara Institute of Science and Technology (NAIST), 8916-5 Takayama, Ikoma, Nara 630-0192, Japan*

Correspondence should be addressed to Yasukazu Nakahata; [yasu-nakahata@bs.naist.jp](mailto:yasu-nakahata@bs.naist.jp)

Received 7 September 2016; Accepted 30 October 2016

Academic Editor: Keiko Kawauchi

Copyright © 2016 Y. Nakahata and Y. Bessho. This is an open access article distributed under the Creative Commons Attribution License, which permits unrestricted use, distribution, and reproduction in any medium, provided the original work is properly cited.

Gene expression is known to be a stochastic phenomenon. The stochastic gene expression rate is thought to be altered by topological change of chromosome and/or by chromatin modifications such as acetylation and methylation. Changes in mechanical properties of chromosome/chromatin by soluble factors, mechanical stresses from the environment, or metabolites determine cell fate, regulate cellular functions, or maintain cellular homeostasis. Circadian clock, which drives the expression of thousands of genes with 24-hour rhythmicity, has been known to be indispensable for maintaining cellular functions/homeostasis. During the last decade, it has been demonstrated that chromatin also undergoes modifications with 24-hour rhythmicity and facilitates the fine-tuning of circadian gene expression patterns. In this review, we cover data which suggests that chromatin structure changes in a circadian manner and that NAD<sup>+</sup> is the key metabolite for circadian chromatin remodeling. Furthermore, we discuss the relationship among circadian clock, NAD<sup>+</sup> metabolism, and aging/age-related diseases. In addition, the interventions of NAD<sup>+</sup> metabolism for the prevention and treatment of aging and age-related diseases are also discussed.

## 1. Introduction

In humans, each cell has a nucleus, the diameter of which is ~10  $\mu\text{m}$ , packing approximately 2 m long DNA if stretched end to end. DNA in the nucleus is arranged at several units, from chromatin to chromosome [1, 2]. Chromosomes in the nucleus are known to be present nonrandomly, located at the spatially confined regions; for example, euchromatin prefers center and heterochromatin periphery of nucleus [2, 3]. Despite their relatively low abundance in the cell, transcription factors have to search for their target gene, usually existing in only 2 copies per cell, to activate or repress in such a spatially messy condition [4]. Such conditions make gene expression stochastic [4]. Mechanical changes of nuclear events referred to as topological changes of chromosome and further epigenetic or posttranslational changes of chromatin have been suggested to increase or decrease stochastic gene expression rate. Changing topology of chromosomes, by receiving soluble factors and also by sensing the extracellular microenvironment, can lead stem cells to differentiate into

multiple cell types [1, 2, 5–8]. Alteration of gene expression program by topological changes contributes not only to development/differentiation, but also to pathophysiological conditions such as cancer, diabetes, and aging [9].

Epigenetic events are mediated by chemical modifications of DNA and/or histones. In particular, histone modifications, such as acetylation, phosphorylation, methylation, and ubiquitination, bring about transient, nonheritable modifications in the genome, which increase or decrease the stochastic gene expression rates [10, 11]. These modifications alter stochastic gene expression rates by changing the property of chromatin surface. For example, the histone modification that involves the addition of an acetyl group neutralizes the negatively charged lysine, releasing DNA from histone, thereby facilitating recruitment of transcription activators to DNA. Many enzymes have been identified as chromatin remodeling factors such as CBP/p300 and PCAF (histone acetyltransferases, HAT), HDACs and SIRT6 (histone deacetylases), SUV39H1, and MLLs (histone methyltransferases). Epigenetic modifications of chromatin are known to be closely associated with

fate specifications of stem cells or precursor cells during embryogenesis [12]. On the other hand, differentiated cells in the adult body are also known to carry out their functions as a result of altered chromatin structure. One example of this is the rhythmic 24-hour cell-autonomous chromatin remodeling that occurs within a cell.

In this review, we discuss data suggesting that chromatin structure changes in a circadian manner and that  $\text{NAD}^+$  is the key metabolite for circadian chromatin remodeling. Furthermore, we discuss the relationship between circadian clock,  $\text{NAD}^+$  metabolism, and aging/age-related diseases. In addition, the interventions of  $\text{NAD}^+$  metabolism for the prevention and treatment of aging and age-related diseases are also discussed.

## 2. Circadian Clock

The earth's rotation period is 23 hours, 59 minutes, 4.1 seconds, or approximately 24 hours. To adjust themselves to the earth's rotation, almost all living things, including cyanobacteria, insects, fish, and mammals, have developed their endogenous clock systems, which are referred to as the "circadian clock." In mammals, circadian clock exists in all tissues of the body, including each cell [13], although there is a hierarchy among clocks. A master clock is located at the suprachiasmatic nucleus (SCN) of the anterior hypothalamus of the brain [13]. The SCN is composed of a pair of tiny nuclei (10,000 cells in each sphere), and each cell has its own circadian clock machinery and is thereby able to drive circadian rhythm cell-autonomously. The SCN receives daily light/dark information via the retinohypothalamic tract in order to entrain to the environmental conditions and transmits this information to peripheral clocks present in all other tissues in the body through hormone secretions and neuronal innervations. Although signals from the SCN are the dominant cues to entrain circadian clock in peripheral tissues, other cues such as nutrition, exercise, or pathophysiological conditions can entrain or remodel peripheral clocks [14–18]. In order to perform tissue-specific and/or interorgan functions with 24-hour rhythmicity in the body, more than 10% of all transcripts show circadian changes, and many nonoscillatory transcripts also demonstrate oscillations at protein levels due to posttranscriptional regulations or at enzymatic activity levels such as casein kinase and SIRT1 [17–23]. An interactive network of master and peripheral circadian clocks regulate many metabolic and homeostatic balances to preserve multiorgan networks, thereby keeping the organism healthy.

## 3. Molecular Clock

Molecular mechanisms of circadian clock in many model animals, such as *Drosophila melanogaster*, *Neurospora crassa*, and mammals, have been dissected, revealing that a wide array of underlying molecules are vital for circadian clocks to maintain circadian rhythmicity. Today, a complex network of interlocked transcriptional-translational feedback loops constitute a universal system of the molecular clocks in

all model animals examined to date [24]. In *Drosophila melanogaster*, for instance, transcriptional factors, CLOCK and CYCLE, activate *period* and *timeless* gene expressions, and PERIOD and TIMELESS proteins repress their own transcriptions, thereby making a transcriptional negative feedback loop. This system is very similar to mammalian and other circadian clock systems, although molecules are not evolutionarily conserved [24]. Molecular mechanisms that make up the core circadian clock in mammals consist of transcriptional factors, CLOCK, NPAS2, BMAL1, PERIOD1-2 (PER1-2), CRYPTOCHROME1-2 (CRY1-2), ROR, and REV-ERB [25]. CLOCK, NPAS2, and BMAL1 are bHLH-type transcriptional activators. BMAL1 makes a heterodimer with CLOCK or NPAS2 to activate gene expressions by binding to E-box element on the promoter of target genes. *Pers* and *Crys* are two of the CLOCK:BMAL1/NPAS2 target genes and PERs and CRYs can also heterodimerize and give feedback to repress their own transcription by binding to CLOCK:BMAL1/NPAS2 (Figure 1). However, since this repression is transient due to the decrease of *Pers* and *Crys* mRNA, repression of CLOCK:BMAL1/NPAS2 activity is released and the next cycle of this feedback loop can begin. The nuclear receptors, ROR and REV-ERB, recognize and compete for binding to the same element, RORE (ROR/REV-ERB-response element), to serve as an activator and a repressor, respectively, at target sites to drive peripheral transcriptional-translational loop that impinges on the core clock feedback loop.

## 4. Circadian Metabolites

As indicated, a wide array of cellular transcripts and proteins demonstrate a circadian pattern in many tissues, not only under the normal condition, but also under environmental or pathophysiological conditions [15, 17, 18]. For instance, high-fat diet (HFD) induces a large number of *de novo* oscillating transcripts in the mouse liver [18]. Furthermore, gene ontology analyses have revealed that a series of genes associated with metabolic processes show periodic expression with a 24-hour rhythm under both normal and pathophysiological conditions [17, 18]. Metabolomics analyses have confirmed that many metabolites, including lipids, polyamines, amino acid and glucose/glycolytic intermediates, and nicotinamide adenine dinucleotide ( $\text{NAD}^+$ ; discussed in detail later), S-adenosylmethionine (SAM), and acetyl-CoA, demonstrate a 24-hour oscillation in many tissues and cultured cells [17, 18, 26–31]. Among circadian metabolites, acetyl-CoA and SAM are acetyl and methyl donor, respectively, for histone and nonhistone proteins. Interestingly,  $\text{NAD}^+$ , another circadian metabolite, is a cosubstrate for Sirtuin family protein deacetylase, suggesting that proteins, especially histone proteins, can undergo circadian modifications in the abundance of acetyl and methyl groups.

## 5. Circadian Chromatin Remodeling

Chromatin remodeling contributes largely to the regulation of gene expression in many systems [10, 32, 33], and the

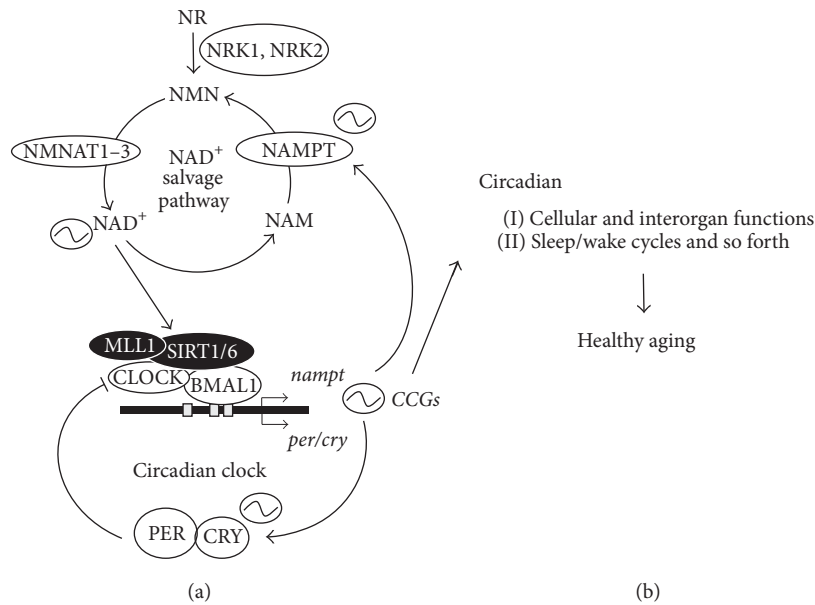


FIGURE 1: Importance of circadian clock in maintaining health and healthy aging. (a) CLOCK and BMAL1 activate an array of genes by binding to E-box elements on their promoter. *Per* and *Cry* transcripts are two of the target genes and PER/CRY repress CLOCK/BMAL1 activity to drive 24-hour rhythmicity (circadian rhythm). CCGs including *nampt* transcripts show circadian oscillations to maintain cellular, interorgan, and systemic functions, thereby contributing to healthy aging (b). CCGs: clock-controlled genes; NAD<sup>+</sup>: nicotinamide adenine dinucleotide; NAM: nicotinamide; NMN: nicotinamide mononucleotide; NR: nicotinamide riboside; NAMPT: nicotinamide phosphoribosyltransferase; NMNAT1~3: NMN adenylyltransferase 1, NMN adenylyltransferase 2, and NMN adenylyltransferase 3; NRK1 and NRK2: nicotinamide ribose kinase 1 and nicotinamide ribose kinase 2.

regulation of gene expression by circadian clock is no exception. Circadian acetylation of histone H3 lysine 9 and 14 (H3K9/14ac) was first reported to demonstrate circadian change on promoters of E-box-regulated circadian clock genes, *per1*, *per2*, and *cry1* [34]. Although p300, one of HAT, was proposed in that report to be a putative HAT for circadian H3K9/14ac, a later report demonstrated that CLOCK itself also possesses HAT activity and preferentially acetylates H3K9/14 [35]. Subsequently, it was reported that SIRT1, an NAD<sup>+</sup>-dependent Sirtuin family deacetylase, counteracts the HAT CLOCK [36]. *Sirt1*<sup>-/-</sup> cells completely ablated circadian H3K9/14ac rhythm and altered circadian gene expressions, indicating that circadian changes of chromatin property are necessary for fine-tuning circadian gene regulations (Figures 1 and 2) [36]. SIRT1 is activated by many stimuli, including low nutrition, low ATP, and exercise, and consequently it has been described as an energy and nutrition sensor [37]. Thus, SIRT1 transduces signals originated by cellular metabolites to the circadian clock.

SIRT6, another Sirtuin family deacetylase, has also been shown to control gene expressions in a circadian way. Interestingly, although SIRT6 can form a complex with CLOCK:BMAL1 similar to SIRT1, its target genes are different [38]. Whereas SIRT1 shuttles between the nucleus and the cytoplasm and preferentially regulates genes related to peptides and cofactors metabolism, SIRT6 localizes constitutively in the nucleus, especially at the euchromatin regions, and controls genes implicated in lipids and carbohydrates metabolism. This suggests that genomic partitioning by two

independent Sirtuins contributes to differential control of circadian metabolism.

While H3K9/14ac has been functionally associated with H3K4 trimethylation (H3K4me3), which is also associated with transcriptionally active genes [11], it was demonstrated in circadian clock machinery that H3K4me3 cycles with 24-hour period and follows the same phase as H3K9/14ac rhythm (Figure 2) [39]. MLL1, an H3K4-specific methyltransferase, was shown to be responsible for the rhythmic H3K4me3 and circadian gene expressions, indicating that circadian changes of chromatin property by H3K4me3 are also necessary for fine-tuning circadian gene regulations. Furthermore, it has been indicated that MLL1 is an acetylated protein and its deacetylation, following the inactivation is controlled by SIRT1 [40], suggesting that regulation of SIRT1/6 activity is the key for circadian changes of chromatin property by H3K9/14ac and H3K4me3.

## 6. Circadian NAD<sup>+</sup> Metabolism

Since SIRT1 deacetylation activity exhibits a clear circadian oscillation, intracellular NAD<sup>+</sup>, which is a cosubstrate for its activity, was assessed by LC-MS<sup>n</sup> methods. These experiments revealed that cellular NAD<sup>+</sup> amount demonstrates circadian rhythm [30]. Significantly, this oscillation has been shown to be a key regulator of rhythmic H3K9/14ac and H3K4me3 chromatin marks [30, 40]. NAD<sup>+</sup> is consumed by NAD<sup>+</sup>-consuming enzymes, Sirtuins, PARPs, and

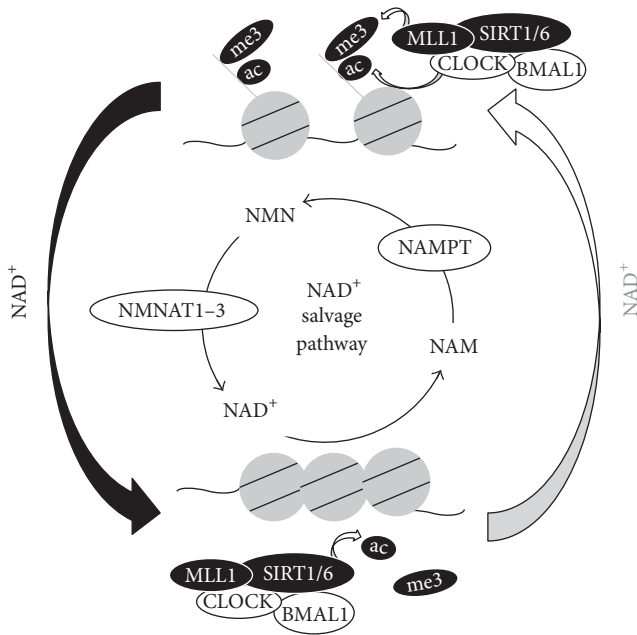


FIGURE 2: Circadian  $\text{NAD}^+$  metabolism modifies chromatin properties with a 24-hour rhythm. Circadian  $\text{NAD}^+$  metabolism controls histone modifications through acetylation and methylation processes, therefore regulating precise circadian gene expression.  $\text{NAD}^+$  with black arrow represents high  $\text{NAD}^+$  amount and  $\text{NAD}^+$  with gray arrow signifies low  $\text{NAD}^+$  amount.

CD38. These enzymes deacetylate proteins, build poly-ADP-ribosylation, and generate cyclic ADP-ribose, respectively [41]. While  $\text{NAD}^+/\text{NADH}$  redox reaction has no effect on the total amount of  $\text{NAD}^+$  and  $\text{NADH}$ , enzymatic reactions by  $\text{NAD}^+$ -consuming enzymes do decrease  $\text{NAD}^+$ , producing nicotinamide (NAM) as a common byproduct. NAM is recycled to produce  $\text{NAD}^+$  by the intracellular  $\text{NAD}^+$  salvage pathway (Figures 1 and 2), which is known to be dominant for intracellular  $\text{NAD}^+$  biosynthesis in many cells and tissues. NAM is converted to nicotinamide mononucleotide (NMN) by nicotinamide phosphoribosyltransferase (NAMPT), and then NMN is converted to  $\text{NAD}^+$  by nicotinamide mononucleotide adenylyltransferases 1–3 (NMNAT1–3) [42]. Among these enzymes, NAMPT is believed to be the rate-limiting enzyme for the  $\text{NAD}^+$  salvage pathway. Intriguingly, circadian gene expression analysis and *Nampt* promoter analysis have confirmed that *nampt* gene expression is under the regulation of circadian clock. Thus, intracellular  $\text{NAD}^+$  amount is regulated by circadian clock, oscillating with 24-hour rhythmicity [30] (Figures 1 and 2). Of note, intracellular  $\text{NAD}^+$  oscillation is in phase with SIRT1 deacetylase activity and in opposite phase of MLL1 methyltransferase activity, thereby showing that the phase of oscillatory  $\text{NAD}^+$  is opposite to that of acetylation and methylation of histone H3 (Figure 2). Interestingly, intracellular  $\text{NAD}^+$  in the liver of circadian clock deficient (*bmali*<sup>-/-</sup> or *clock* <sup>$\Delta 19/\Delta 19$</sup> ) mice and in MEF cells derived from *bmali*<sup>-/-</sup>, *clock* <sup>$\Delta 19/\Delta 19$</sup> , or *cry1*<sup>-/-/2</sup><sup>-/-</sup> mice were significantly reduced [30, 31], indicating that circadian

clock controls basal and circadian  $\text{NAD}^+$  amount. Pharmacological experiments using FK866, an NAMPT inhibitor, reduced cellular  $\text{NAD}^+$  by at least 80% and demonstrated an altered pattern of circadian gene expression [30], while CD38 knockout mice, which have high cellular  $\text{NAD}^+$ , also showed altered gene expression and locomotor activity patterns [43]. In addition, HFD, which remodeled circadian clock and completely ablated oscillations in cellular  $\text{NAD}^+$  in mouse liver, drove an altered circadian gene expression pattern [18]. These reports indicate that proper circadian  $\text{NAD}^+$  regulation is indispensable for the maintenance of circadian clock, suggesting that it is probably essential for preservation of health (discussed below).

## 7. $\text{NAD}^+$ Metabolism and Aging

Although cellular  $\text{NAD}^+$  amounts fluctuate within a short period (24-hour rhythmicity), recent findings showed that cellular  $\text{NAD}^+$  amount also fluctuates throughout the lifespan. Intracellular  $\text{NAD}^+$  has been demonstrated to decrease with aging in humans and mice tissues/cells [44–47].  $\text{NAD}^+$  amount is estimated to be around  $8.54 \pm 1.55$  ng/mg protein in human newborn (0–1 year) skin tissues but is decreased to  $2.74 \pm 0.41$  and  $1.06 \pm 0.91$  ng/mg protein in young adult (30–50 years) and elderly (>71 years) skin tissues, respectively [46]. Over the last couple of years, many papers have demonstrated that the administration of  $\text{NAD}^+$  precursor, NMN or nicotinamide riboside (NR), to old mice with low cellular  $\text{NAD}^+$  could restore  $\text{NAD}^+$  amount as well as SIRT1 activity, thereby rescuing many metabolic functions [48–52]. Furthermore, NR administration to aging mice, beginning at 2 years of age, could increase mean lifespan with concomitant improvements in maximal running times and distances, along with limb grip strength [49]. A large number of studies in mice show an association between  $\text{NAD}^+$  metabolism and aging. However, studies in humans to address that link are scarce and limited information is available regarding changes in  $\text{NAD}^+$  levels with aging, particularly in human tissues. Further studies are absolutely necessary to understand the relationship between  $\text{NAD}^+$  metabolism and aging process and whether supplementation of  $\text{NAD}^+$  has a benefit for humans against aging/age-related diseases.

While NAMPT is believed to be the enzyme controlling overall cellular  $\text{NAD}^+$  amount, via *Nampt* expression and activation [44, 47], another enzyme was recently reported to be implicated in age-dependent  $\text{NAD}^+$  depletion [53]. CD38, one of the  $\text{NAD}^+$ -consuming enzymes, increased in the liver of aged mice and has been shown to deplete  $\text{NAD}^+$  totally by degrading the  $\text{NAD}^+$  precursor, NMN, *in vivo* [53]. Further investigations are required to fully elucidate all the aspects that affect the cellular mechanisms of  $\text{NAD}^+$  reduction with aging.

## 8. Link between Aging and Circadian Clock

Like other physiological events, circadian rhythms have been reported to be attenuated with aging at multiple levels. At the

behavior level, locomotor activity rhythms, including free-running period, active mass, and amplitude, are changed with aging, thereby causing sleep fragmentation [54–56]. At the tissue and cellular levels, aging weakens or reduces the amplitude of circadian gene expression patterns [57, 58]. Age-related diseases as well as aging can therefore have adverse effects on circadian clock [59–62]. For instance, mice fed with HFD demonstrate a lengthened free-running period [63], while *db/db* mice, which are an animal model of type 2 diabetes, show attenuated locomotor activity rhythms with diminished *per2* mRNA and advanced *bmal1* oscillation [64]. CLOCK has also been reported to be upregulated in human glioma and breast cancer cells, being involved in cancer proliferation [65, 66]. While HFD induces obesity, recent papers clearly indicate that mice fed with HFD along with time-restricted feeding during active period were protected against obesity, hyperinsulinemia, hepatic steatosis, and inflammation with improvement of clock gene expression pattern [67, 68]. This suggests that maintaining circadian metabolic cycles can prevent age-related diseases and probably aging.

On the other hand, many circadian gene knockout mice exhibited accelerated aging with shortened lifespan and/or are prone to develop age-related diseases, including cancer, hypertension, and diabetes. *Bmal1*<sup>-/-</sup> mice showed a variety of age-related diseases including sarcopenia, cataracts, decrease of subcutaneous fat, organ shrinkage, dyslipidemia, arterial and venous thrombosis, and hypoinsulinaemia [69–72], with drastically short average lifespan of 37.0 ± 12.1 weeks (wk) [71]. In addition, *clock*<sup>Δ19/Δ19</sup> or *clock*<sup>-/-</sup> mice displayed age-related diseases such as hyperlipidemia, hyperleptinemia, hyperglycemia, and hypoinsulinaemia with shorter average lifespan of 100.8 ± 13.5 wk, compared to that of wild type mice (115.5 ± 18.9 wk) [70, 73]. In addition to the mouse studies, a large array of epidemiological surveys have provided evidence supporting the link between metabolic disorders, especially obesity, insulin resistance, cardiovascular disease, and cancer, and circadian disruption in humans [62, 74].

Though not yet directly tested, we speculate that circadian NAD<sup>+</sup> oscillations are diminished or missing in aged animals. The reasons are as follows: (i) as circadian gene expression patterns in aged animal has been demonstrated to be weakened or vanished [57, 58], circadian clock-dependent *Nampt* gene expression patterns may be attenuated; (ii) cellular NAD<sup>+</sup> amounts in some circadian knockout mice are significantly lower than in wild type mice [30, 31]; (iii) aged animals have much lower cellular NAD<sup>+</sup>, suggesting that even if NAD<sup>+</sup> amount still shows oscillation, its amplitude could be smaller in aged animals.

Also, since administration of NAD<sup>+</sup> precursors has shown improvements against age-related diseases and lifespan [48–52], issues to be resolved next are whether cellular NAD<sup>+</sup> rescued by NAD<sup>+</sup> precursors in old mice demonstrate an oscillation within 24 hours and improve patterns of circadian gene expressions and chromatin property. These researches will give us physiological significance of circadian NAD<sup>+</sup> oscillations.

## 9. Concluding Remarks

The accumulating evidence to date reveals the interconnection between circadian clock and aging/age-related diseases [59–62], and, as discussed in this review, NAD<sup>+</sup> metabolism has a close relationship with both the circadian clock and aging/age-related diseases. However, no direct evidence has so far demonstrated the role of NAD<sup>+</sup> as the linking hub between circadian clock and aging and age-related diseases. Therefore, this is the obvious area that remains to be explored. More work is needed to reveal how chromatin remodeling through NAD<sup>+</sup> metabolism takes place. Revealing these connections will open up multiple avenues for the understanding of aging processes and also potential therapeutic interventions.

## Competing Interests

The authors declare that they have no competing interests.

## Acknowledgments

The authors thank all the members of the Laboratory of Gene Regulation Research at NAIST for their help and advice. They also thank Drs. Kristin Eckel-Mahan and Saurabh Sahar for their careful and critical reading of this manuscript.

## References

- [1] G. Cavalli and T. Misteli, “Functional implications of genome topology,” *Nature Structural & Molecular Biology*, vol. 20, no. 3, pp. 290–299, 2013.
- [2] G. V. Shivashankar, “Mechanosignaling to the cell nucleus and gene regulation,” *Annual Review of Biophysics*, vol. 40, no. 1, pp. 361–378, 2011.
- [3] T. Misteli, “The cell biology of genomes: bringing the double helix to life,” *Cell*, vol. 152, no. 6, pp. 1209–1212, 2013.
- [4] A. Raj and A. van Oudenaarden, “Nature, nurture, or chance: stochastic gene expression and its consequences,” *Cell*, vol. 135, no. 2, pp. 216–226, 2008.
- [5] I. L. Ivanovska, J.-W. Shin, J. Swift, and D. E. Discher, “Stem cell mechanobiology: diverse lessons from bone marrow,” *Trends in Cell Biology*, vol. 25, no. 9, pp. 523–532, 2015.
- [6] F. Chowdhury, S. Na, D. Li et al., “Material properties of the cell dictate stress-induced spreading and differentiation in embryonic stem cells,” *Nature Materials*, vol. 9, pp. 82–88, 2010.
- [7] A. J. Engler, S. Sen, H. L. Sweeney, and D. E. Discher, “Matrix elasticity directs stem cell lineage specification,” *Cell*, vol. 126, no. 4, pp. 677–689, 2006.
- [8] R. McBeath, D. M. Pirone, C. M. Nelson, K. Bhadriraju, and C. S. Chen, “Cell shape, cytoskeletal tension, and RhoA regulate stem cell lineage commitment,” *Developmental Cell*, vol. 6, no. 4, pp. 483–495, 2004.
- [9] P. Isermann and J. Lammerding, “Nuclear mechanics and mechanotransduction in health and disease,” *Current Biology*, vol. 23, no. 24, pp. R1113–R1121, 2013.
- [10] T. Jenuwein and C. D. Allis, “Translating the histone code,” *Science*, vol. 293, no. 5532, pp. 1074–1080, 2001.

- [11] S. L. Berger, "The complex language of chromatin regulation during transcription," *Nature*, vol. 447, no. 7143, pp. 407–412, 2007.
- [12] M. Namihira and K. Nakashima, "Mechanisms of astrocytogenesis in the mammalian brain," *Current Opinion in Neurobiology*, vol. 23, no. 6, pp. 921–927, 2013.
- [13] S. M. Reppert and D. R. Weaver, "Coordination of circadian timing in mammals," *Nature*, vol. 418, no. 6901, pp. 935–941, 2002.
- [14] T. Doerks, R. R. Copley, J. Schultz, C. P. Ponting, and P. Bork, "Systematic identification of novel protein domain families associated with nuclear functions," *Genome Research*, vol. 12, no. 1, pp. 47–56, 2002.
- [15] C. Vollmers, S. Gill, L. DiTacchio, S. R. Pulivarthy, H. D. Le, and S. Panda, "Time of feeding and the intrinsic circadian clock drive rhythms in hepatic gene expression," *Proceedings of the National Academy of Sciences of the United States of America*, vol. 106, no. 50, pp. 21453–21458, 2009.
- [16] A. M. Schroeder and C. S. Colwell, "How to fix a broken clock," *Trends in Pharmacological Sciences*, vol. 34, no. 11, pp. 605–619, 2013.
- [17] S. Masri, T. Papagiannakopoulos, K. Kinouchi et al., "Lung adenocarcinoma distally rewires hepatic circadian homeostasis," *Cell*, vol. 165, no. 4, pp. 896–909, 2016.
- [18] K. L. Eckel-Mahan, V. R. Patel, S. De Mateo et al., "Reprogramming of the circadian clock by nutritional challenge," *Cell*, vol. 155, no. 7, pp. 1464–1478, 2013.
- [19] S. Kojima, E. L. Sher-Chen, and C. B. Green, "Circadian control of mRNA polyadenylation dynamics regulates rhythmic protein expression," *Genes & Development*, vol. 26, no. 24, pp. 2724–2736, 2012.
- [20] T. Tamaru, J. Hirayama, Y. Isojima et al., "CK2 $\alpha$  phosphorylates BMAL1 to regulate the mammalian clock," *Nature Structural and Molecular Biology*, vol. 16, no. 4, pp. 446–448, 2009.
- [21] M. E. Hughes, L. DiTacchio, K. R. Hayes et al., "Harmonics of circadian gene transcription in mammals," *PLoS Genetics*, vol. 5, no. 4, Article ID e1000442, 2009.
- [22] K.-F. Storch, O. Lipan, I. Leykin et al., "Extensive and divergent circadian gene expression in liver and heart," *Nature*, vol. 417, no. 6884, pp. 78–83, 2002.
- [23] S. Panda, M. P. Antoch, B. H. Miller et al., "Coordinated transcription of key pathways in the mouse by the circadian clock," *Cell*, vol. 109, no. 3, pp. 307–320, 2002.
- [24] S. A. Brown, E. Kowalska, and R. Dallmann, "(Re)inventing the circadian feedback loop," *Developmental Cell*, vol. 22, no. 3, pp. 477–487, 2012.
- [25] J. S. Takahashi, "Molecular components of the circadian clock in mammals," *Diabetes, Obesity and Metabolism*, vol. 17, supplement 1, pp. 6–11, 2015.
- [26] S. Sahar, S. Masubuchi, K. Eckel-Mahan et al., "Circadian control of fatty acid elongation by SIRT1 protein-mediated deacetylation of acetyl-coenzyme a synthetase 1," *Journal of Biological Chemistry*, vol. 289, no. 9, pp. 6091–6097, 2014.
- [27] H. Tsuchiya, K.-A. Da Costa, S. Lee et al., "Interactions between nuclear receptor SHP and FOXA1 maintain oscillatory homocysteine homeostasis in mice," *Gastroenterology*, vol. 148, no. 5, pp. 1012–1023.e14, 2015.
- [28] V. R. Patel, K. Eckel-Mahan, P. Sassone-Corsi, and P. Baldi, "CircadiOmics: integrating circadian genomics, transcriptomics, proteomics and metabolomics," *Nature Methods*, vol. 9, no. 8, pp. 772–773, 2012.
- [29] K. Eckel-Mahan and P. Sassone-Corsi, "Metabolism control by the circadian clock and vice versa," *Nature Structural & Molecular Biology*, vol. 16, no. 5, pp. 462–467, 2009.
- [30] Y. Nakahata, S. Sahar, G. Astarita, M. Kaluzova, and P. Sassone-Corsi, "Circadian control of the NAD<sup>+</sup> salvage pathway by CLOCK-SIRT1," *Science*, vol. 324, no. 5927, pp. 654–657, 2009.
- [31] K. M. Ramsey, J. Yoshino, C. S. Brace et al., "Circadian clock feedback cycle through NAMPT-Mediated NAD<sup>+</sup> biosynthesis," *Science*, vol. 324, no. 5927, pp. 651–654, 2009.
- [32] G. Orphanides and D. Reinberg, "A unified theory of gene expression," *Cell*, vol. 108, no. 4, pp. 439–451, 2002.
- [33] C. J. Fry and C. L. Peterson, "Chromatin remodeling enzymes: who's on first?" *Current Biology*, vol. 11, no. 5, pp. R185–R197, 2001.
- [34] J.-P. Etchegaray, C. Lee, P. A. Wade, and S. M. Reppert, "Rhythmic histone acetylation underlies transcription in the mammalian circadian clock," *Nature*, vol. 421, no. 6919, pp. 177–182, 2003.
- [35] M. Doi, J. Hirayama, and P. Sassone-Corsi, "Circadian regulator CLOCK is a histone acetyltransferase," *Cell*, vol. 125, no. 3, pp. 497–508, 2006.
- [36] Y. Nakahata, M. Kaluzova, B. Grimaldi et al., "The NAD<sup>+</sup>-dependent deacetylase SIRT1 modulates CLOCK-mediated chromatin remodeling and circadian control," *Cell*, vol. 134, no. 2, pp. 329–340, 2008.
- [37] L. Guarente, "Sirtuins, aging, and metabolism," *Cold Spring Harbor Symposia on Quantitative Biology*, vol. 76, pp. 81–90, 2011.
- [38] S. Masri, P. Rigor, M. Cervantes et al., "Partitioning circadian transcription by SIRT6 leads to segregated control of cellular metabolism," *Cell*, vol. 158, no. 3, pp. 659–672, 2014.
- [39] S. Katada and P. Sassone-Corsi, "The histone methyltransferase MLL1 permits the oscillation of circadian gene expression," *Nature Structural and Molecular Biology*, vol. 17, no. 12, pp. 1414–1421, 2010.
- [40] L. Aguilar-Arnal, S. Katada, R. Orozco-Solis, and P. Sassone-Corsi, "NAD<sup>+</sup>-SIRT1 control of H3K4 trimethylation through circadian deacetylation of MLL1," *Nature Structural & Molecular Biology*, vol. 22, no. 4, pp. 312–318, 2015.
- [41] L. R. Stein and S.-I. Imai, "The dynamic regulation of NAD metabolism in mitochondria," *Trends in Endocrinology and Metabolism*, vol. 23, no. 9, pp. 420–428, 2012.
- [42] S. Imai and L. Guarente, "It takes two to tango: NAD<sup>+</sup> and sirtuins in aging/longevity control," *Aging and Mechanisms of Disease*, vol. 2, article 16017, 2016.
- [43] S. Sahar, V. Nin, M. T. Barbosa, E. N. Chini, and P. Sassone-Corsi, "Altered behavioral and metabolic circadian rhythms in mice with disrupted NAD<sup>+</sup> oscillation," *Aging*, vol. 3, no. 8, pp. 794–802, 2011.
- [44] L. Mouchiroud, R. H. Houtkooper, N. Moullan et al., "The NAD<sup>+</sup>/sirtuin pathway modulates longevity through activation of mitochondrial UPR and FOXO signaling," *Cell*, vol. 154, no. 2, pp. 430–441, 2013.
- [45] A. P. Gomes, N. L. Price, A. J. Y. Ling et al., "Declining NAD<sup>+</sup> induces a pseudohypoxic state disrupting nuclear-mitochondrial communication during aging," *Cell*, vol. 155, no. 7, pp. 1624–1638, 2013.
- [46] H. Massudi, R. Grant, N. Braidy, J. Guest, B. Farnsworth, and G. J. Guillemin, "Age-associated changes in oxidative stress and NAD<sup>+</sup> metabolism in human tissue," *PLoS ONE*, vol. 7, no. 7, Article ID e42357, 2012.

- [47] J. Yoshino, K. F. Mills, M. J. Yoon, and S.-I. Imai, "Nicotinamide mononucleotide, a key NAD<sup>+</sup> intermediate, treats the pathophysiology of diet- and age-induced diabetes in mice," *Cell Metabolism*, vol. 14, no. 4, pp. 528–536, 2011.
- [48] K. M. Ramsey, K. F. Mills, A. Satoh, and S.-I. Imai, "Age-associated loss of Sirt1-mediated enhancement of glucose-stimulated insulin secretion in beta cell-specific Sirt1-overexpressing (BESTO) mice," *Aging Cell*, vol. 7, no. 1, pp. 78–88, 2008.
- [49] H. Zhang, D. Ryu, Y. Wu et al., "NAD<sup>+</sup> repletion improves mitochondrial and stem cell function and enhances life span in mice," *Science*, vol. 352, no. 6292, pp. 1436–1443, 2016.
- [50] S. Srivastava, "Emerging therapeutic roles for NAD<sup>+</sup> metabolism in mitochondrial and age-related disorders," *Clinical and Translational Medicine*, vol. 5, no. 1, article 25, 2016.
- [51] D. Frederick, E. Loro, L. Liu et al., "Loss of NAD homeostasis leads to progressive and reversible degeneration of skeletal muscle," *Cell Metabolism*, vol. 24, no. 2, pp. 269–282, 2016.
- [52] L. Mouchiroud, R. H. Houtkooper, and J. Auwerx, "NAD<sup>+</sup> metabolism: a therapeutic target for age-related metabolic disease," *Critical Reviews in Biochemistry and Molecular Biology*, vol. 48, no. 4, pp. 397–408, 2013.
- [53] J. Camacho-Pereira, M. Tarragó, C. Chini et al., "CD38 dictates age-related NAD decline and mitochondrial dysfunction through an SIRT3-dependent mechanism," *Cell Metabolism*, vol. 23, no. 6, pp. 1127–1139, 2016.
- [54] V. S. Valentinuzzi, K. Scarbrough, J. S. Takahashi, and F. W. Turek, "Effects of aging on the circadian rhythm of wheel-running activity in C57BL/6 mice," *American Journal of Physiology - Regulatory Integrative and Comparative Physiology*, vol. 273, no. 6, pp. R1957–R1964, 1997.
- [55] C. S. Pittendrigh and S. Daan, "Circadian oscillations in rodents: a systematic increase of their frequency with age," *Science*, vol. 186, no. 4163, pp. 548–550, 1974.
- [56] E. J. W. Van Someren, "Circadian and sleep disturbances in the elderly," *Experimental Gerontology*, vol. 35, no. 9-10, pp. 1229–1237, 2000.
- [57] S. Yamazaki, M. Straume, H. Tei, Y. Sakaki, M. Menaker, and G. D. Block, "Effects of aging on central and peripheral mammalian clocks," *Proceedings of the National Academy of Sciences of the United States of America*, vol. 99, no. 16, pp. 10801–10806, 2002.
- [58] T. Kunieda, T. Minamino, T. Katsuno et al., "Cellular senescence impairs circadian expression of clock genes in vitro and in vivo," *Circulation Research*, vol. 98, no. 4, pp. 532–539, 2006.
- [59] M. Perelis, K. M. Ramsey, and J. Bass, "The molecular clock as a metabolic rheostat," *Diabetes, Obesity and Metabolism*, vol. 17, no. 1, pp. 99–105, 2015.
- [60] S. S. Fonseca Costa and J. A. Ripperger, "Impact of the circadian clock on the aging process," *Frontiers in Neurology*, vol. 6, article 43, 2015.
- [61] V. P. Belancio, D. E. Blask, P. Deininger, S. M. Hill, and S. Michal Jazwinski, "The aging clock and circadian control of metabolism and genome stability," *Frontiers in Genetics*, vol. 5, article no. 455, 2014.
- [62] A. Ribas-Latre and K. Eckel-Mahan, "Interdependence of nutrient metabolism and the circadian clock system: importance for metabolic health," *Molecular Metabolism*, vol. 5, no. 3, pp. 133–152, 2016.
- [63] A. Kohsaka, A. D. Laposky, K. M. Ramsey et al., "High-fat diet disrupts behavioral and molecular circadian rhythms in mice," *Cell Metabolism*, vol. 6, no. 5, pp. 414–421, 2007.
- [64] T. Kudo, M. Akiyama, K. Kuriyama, M. Sudo, T. Moriya, and S. Shibata, "Night-time restricted feeding normalises clock genes and Pai-1 gene expression in the db/db mouse liver," *Diabetologia*, vol. 47, no. 8, pp. 1425–1436, 2004.
- [65] A. Li, X. Lin, X. Tan et al., "Circadian gene clock contributes to cell proliferation and migration of glioma and is directly regulated by tumor-suppressive miR-124," *FEBS Letters*, vol. 587, no. 15, pp. 2455–2460, 2013.
- [66] L. Xiao, A. K. Chang, M.-X. Zang et al., "Induction of the CLOCK gene by E2-ER $\alpha$  signaling promotes the proliferation of breast cancer cells," *PLoS ONE*, vol. 9, no. 5, article e95878, 2014.
- [67] M. Hatori, C. Vollmers, A. Zarrinpar et al., "Time-restricted feeding without reducing caloric intake prevents metabolic diseases in mice fed a high-fat diet," *Cell Metabolism*, vol. 15, no. 6, pp. 848–860, 2012.
- [68] S. Sundaram and L. Yan, "Time-restricted feeding reduces adiposity in mice fed a high-fat diet," *Nutrition Research*, vol. 36, no. 6, pp. 603–611, 2016.
- [69] S. Shimba, T. Ogawa, S. Hitosugi et al., "Deficient of a clock gene, brain and muscle arnt-like protein-1 (BMAL1), induces dyslipidemia and ectopic fat formation," *PLoS ONE*, vol. 6, no. 9, Article ID e25231, 2011.
- [70] B. Marcheiva, K. M. Ramsey, E. D. Buhr et al., "Disruption of the clock components CLOCK and BMAL1 leads to hypoinsulinaemia and diabetes," *Nature*, vol. 466, no. 7306, pp. 627–631, 2010.
- [71] R. V. Kondratov, A. A. Kondratova, V. Y. Gorbacheva, O. V. Vykhovanets, and M. P. Antoch, "Early aging and age-related pathologies in mice deficient in BMAL1, the core component of the circadian clock," *Genes and Development*, vol. 20, no. 14, pp. 1868–1873, 2006.
- [72] B. Hemmeryckx, C. E. Van Hove, P. Franssen et al., "Progression of the prothrombotic state in aging bmal1-deficient mice," *Arteriosclerosis, Thrombosis, and Vascular Biology*, vol. 31, no. 11, pp. 2552–2559, 2011.
- [73] F. W. Turek, C. Joshu, A. Kohsaka et al., "Obesity and metabolic syndrome in circadian clock mutant mice," *Science*, vol. 308, no. 5724, pp. 1043–1045, 2005.
- [74] T. Roenneberg and M. Mewrow, "The circadian clock and human health," *Current Biology*, vol. 26, no. 10, pp. R432–R443, 2016.